

COLLECTED PAPERS
ON
NANOPHOTONICS

Volume 19
August 2003 – July 2004

Professor
Motoichi OHTSU

THE UNIVERSITY OF TOKYO
Department of Electronics Engineering, School of Engineering,
7-3-1 Hongo, Bunkyo-ku, Tokyo 113-8656
Phone: +81-3-5841-1189, Fax: +81-3-5841-1140
E-mail: ohtsu@ee.t.u-tokyo.ac.jp
URL(1) <http://www.nanophotonics.info/>
URL(2) <http://uuu.ae.titech.ac.jp>

PREFACE

This issue of the *COLLECTED PAPERS ON NANOPHOTONICS* includes original papers, presentations in international conferences, review papers, and books which were published by M. OHTSU in August 2003 – July 2004. Nanophotonics has been proposed by M. Ohtsu in the year 1994. Nanophotonics is defined as a novel technology that utilizes local electromagnetic interactions between a few nanometric elements and an optical near field. Since an optical near field is free from the diffraction of light due to its size-dependent localization and size-dependent resonance features, nanophotonics enables fabrication, operation, and integration of nanometric devices (Fig.1). However, it should be noted that nanophotonics is not only to realize nanometer-sized optical technology (*quantitative innovation*). It can realize “novel functions and phenomena, which are not possible as long as propagating lights are used (*qualitative innovation*). Producing this qualitative innovation is the significance of nanophotonics, i.e., prominent advantages over conventional photonics. Due to the qualitative innovation, nanophotonics is expected to realize novel devices and systems to shift the paradigm of optical industry and market (Fig.2).

To establish nanophotonics, M. Ohtsu supervises several national projects in collaboration with industries. They are:

- (1) Localized photon project, ERATO^(a), JST (October 2003 – September 2008) . **【It has been successfully finished. Review of its research work is attached at the end of this preface.】**
- (2) Nanophotonics team, SORST^(b), JST^(c). (October 2003 – September 2008. Participating companies and an institute: Fuji Photo Film, Ricoh, Toshiba, Ushio, and NiCT^(d)).
- (3) Ohtsu-Saiki group of KAST^(e).
- (4) Nanophotonic system consortium, sponsored by KAST^(e). (October 2002-. Participating companies: Ricoh and Hoden Seimitsu Kakokenkusho).
- (5) Ultrahigh capacity optical storage project, Program for Upgrading the Telecommunications Foundation, METI^(f). (FY2002-FY2006. Participating companies: Conica Minolta, Fujitsu, Hitachi, Hitachi Maxell, Pioneer, Ricoh, Seiko Instruments, and Toshiba).
- (6) Optical near field lithography project, Leading Project, MEXT^(g). (July

2004 – March 2007. Participating company: Canon).

(7) Ultra high-density optical nodes using nanophotonics, Top-Priority Research and Development in Specific Fields, SCOPE^(h), sponsored by Ministry of Public Management, Home Affairs, Posts and Telecommunications. (FY2003-2005. Participating institute: NiCT^(d))

(a) Exploratory Research for Advanced Technology.

(b) Solution Oriented Research for Science and Technology.

(c) Japan Science and Technology Agency.

(d) National Institute of Information and Communications Technology.

(e) Kanagawa Academy of Science and Technology.

(f) Ministry of Economy, Trade, and Industry.

(g) Ministry of Education, Culture, Sports, Science, and Technology.

(h) Scientific Information and Communications R&D Promotion Program.

August 2004

Prof. Motoichi OHTSU (Dr. Eng.)

大津 元一

【上記(1)-(7)の和名】

(1) 局在フォトプロジェクト、科学技術振興機構 創造科学技術推進事業

【2003年10月～2008年9月】は終了済み。

(2) ナノフォトニクスチーム、科学技術振興機構 戦略的創造研究推進事業 継続研究課題。

【2003年10月～2008年9月。参画企業及び機関：(株)富士写真フイルム、(株)東芝、(株)ウシオ電機、(独)情報通信研究機構】

(3) (財)神奈川科学技術アカデミー、大津斉木グループ

(4) ナノ光システム研究コンソーシアム、(財)神奈川科学技術アカデミー。

【2002年10月～。参画企業：(株)リコー、(株)放電精密加工研究所】

(5) 大容量光ストレージ技術、経済産業省 情報通信基盤高度化プログラム。

【2002年度～2006年度。参画企業：(株)コニカミノルタオプト、(株)富士通、(株)日立製作所、(株)日立マクセル、(株)パイオニア、(株)リコー、(株)セイコーインスツルメンツ、(株)東芝】

(6) 近接場光リソグラフィ装置の開発、文部科学省 リーディングプロジェクト。

【2004年7月～2007年3月。参画企業：(株)キャノン】

(7) ナノフォトニクスによる超高集積光ノード技術の研究、総務省 戦略的情報通信研究開発制度 特定重点型研究開発。

【2003年度～2005年度。参画機関：(独)情報通信機構】

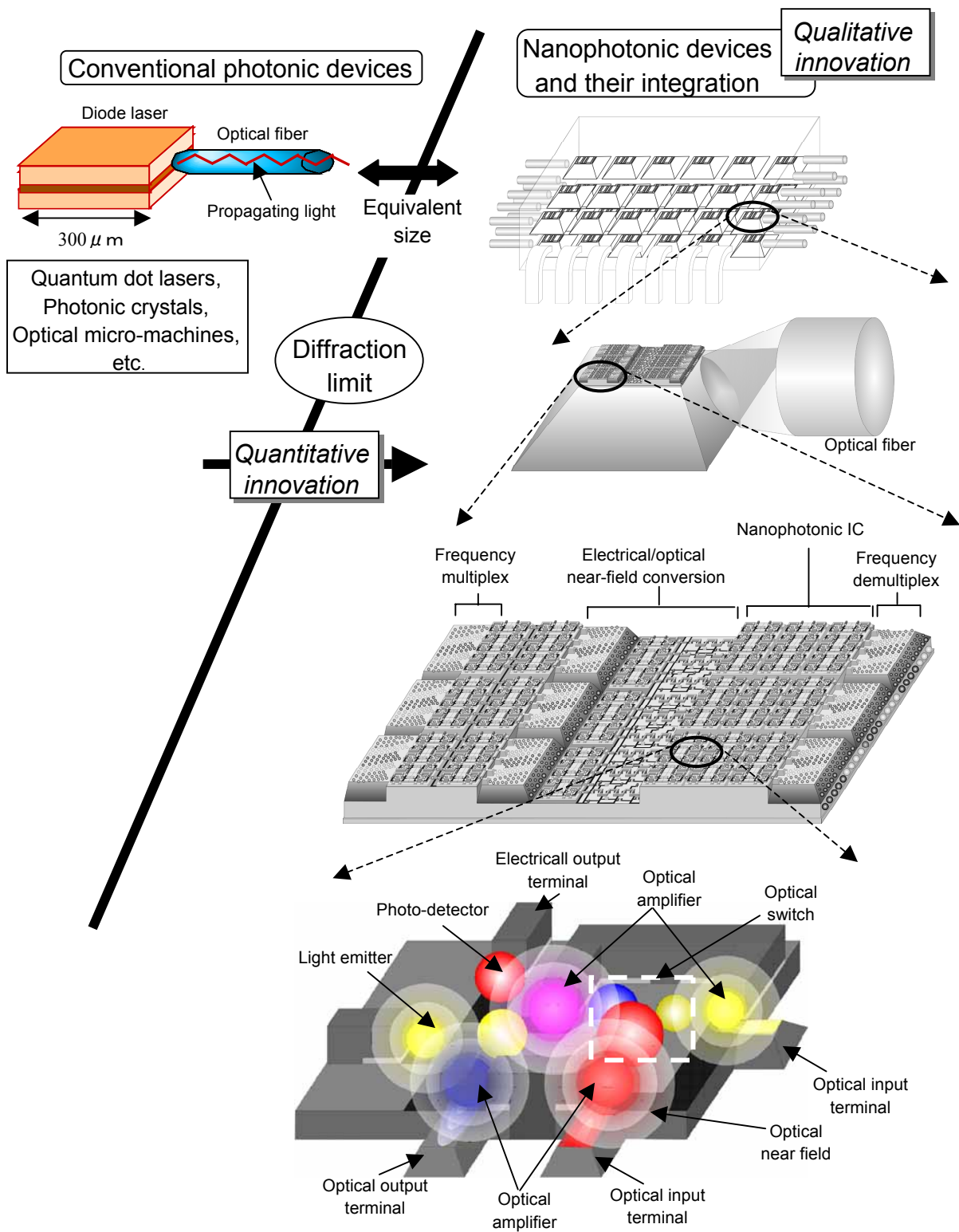


Fig.1 Concepts and structures of nanophotonic devices and their integration.

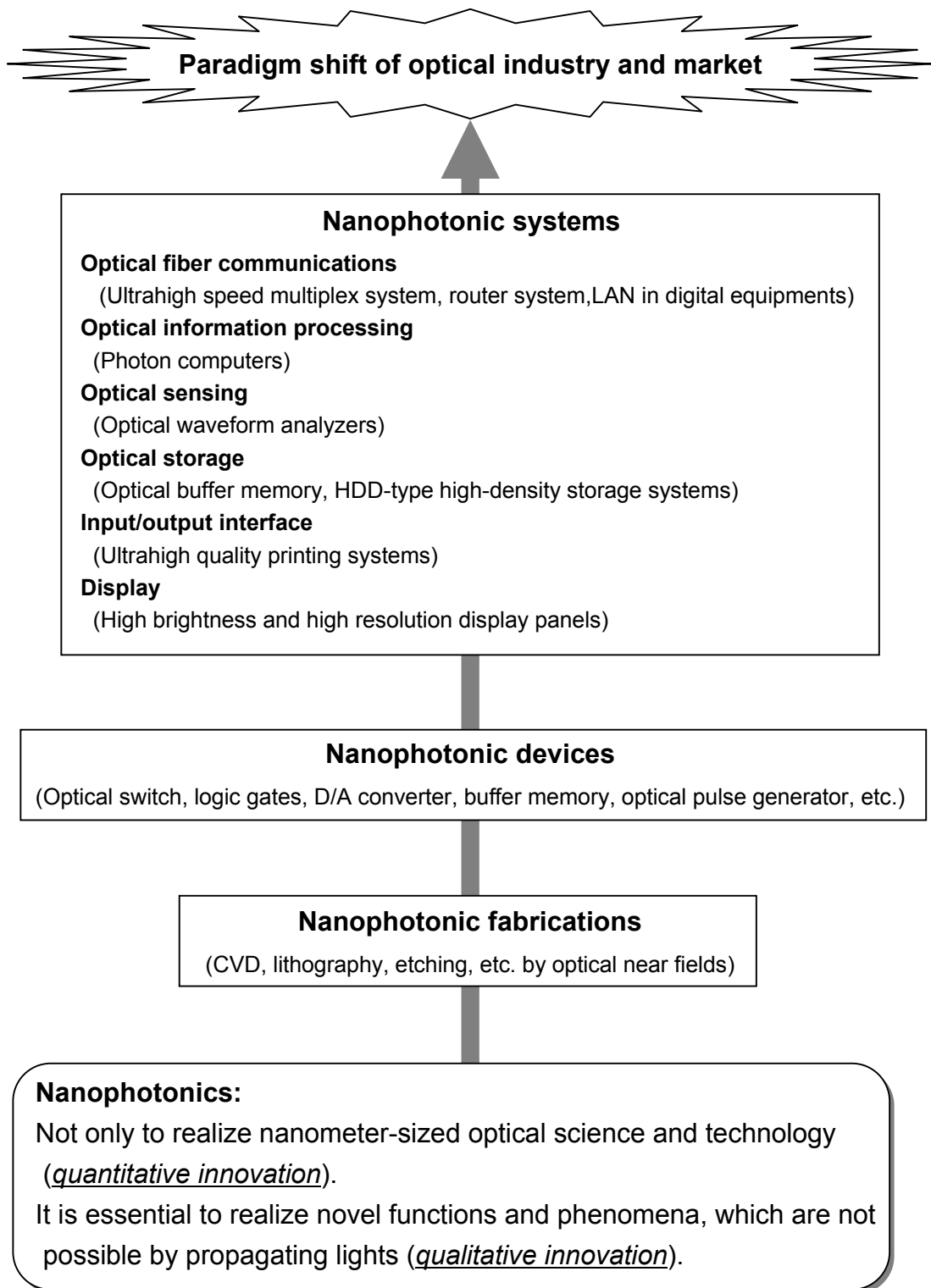


Fig.2 Possible paradigm shift by nanophotonics

LIST OF PAPERS

[(pp.XX-XX); pages in this issue of the COLLECTED PAPERS]

[I] ORIGINAL PAPERS

[1] S. Mononobe, Y. Sato, M. Ohtsu, and H. Honma, "Fabrication of a Near-Field Optical Fiber Probe Based on Electroless Nickel Plating under Ultrasonic Irradiation", *Jpn. J. Appl. Phys.*, Vol.43, No.5B, May 2004, pp.2862-2863

(pp.1-2)

[2] T-W. Kim, T. Kawazoe, S. Yamazaki, M. Ohtsu, and T. Sekiguchi, "Low-temperature orientation-selective growth and ultraviolet emission of single-crystal ZnO nanowires", *Appl. Phys. Lett.*, Vol.84, No.17, April 2004, pp.3358-3360

(pp.3-5)

[2'] T-W. Kim, T. Kawazoe, S. Yamazaki, M. Ohtsu, and T. Sekiguchi, "Low-temperature orientation-selective growth and ultraviolet emission of single-crystal ZnO nanowires", *Virtual Journal of Nanoscale Science and Technology*, Vol.9, Issue 17, May 3, 2004

(pp.6-7)

[3] S. Sangu, K. Kobayashi, A. Shojiguchi, and M. Ohtsu, "Logic and functional operations using a near-field optically coupled quantum-dot system", *Phys. Rev. B*, Vol.69, No.11, March 2004, pp.115334-1 – 115334-13

(pp.8-20)

[3'] S. Sangu, K. Kobayashi, A. Shojiguchi, and M. Ohtsu, "Logic and functional operations using a near-field optically coupled quantum-dot system", *Virtual Journal of Nanoscale Science and Technology*, Vol.9, Issue 13, April 5, 2004

(pp.21-22)

[4] H. Kubota, R. Takahashi, T.-W. Kim, T. Kawazoe, M. Ohtsu, N. Arai, M.

Yoshimura, H. Nakao, H. Furuya, Y. Mori, T. Sasaki, Y. Matsumoto, and H. Koinuma, "Combinatorial synthesis and luminescent characteristics of RECa₄O(BO₃)₃ epitaxial thin films", Applied Surface Science, Vol.223, 2004, pp.241-244

(pp.23-26)

[5] A. Shojiguchi, K. Kobayashi, S. Sangu, K. Kitahara, and M. Ohtsu, "Superradiance and Dipole Ordering of an *N*Two-Level System Interacting with Optical Near Fields", J. Phys. Soc. Jpn., Vol.72, No.11, November 2003, pp.2984-3001

(pp.27-44)

[6] T. Yatsui, S. Takubo, J. Lim, W. Nomura, M. Kouroggi, and M. Ohtsu, "Regulating the size and position of deposited Zn nanoparticles by optical near-field desorption using size-dependent resonance", Appl. Phys. Lett., Vol.83, No.9, September 2003, pp.1716-1718

(pp.45-47)

[7] S. Sangu, K. Kobayashi, T. Kawazoe, A. Shojiguchi, and M. Ohtsu, "Quantum-Coherence Effect in a Quantum Dot System Coupled by Optical Near Fields", Transactions of the Material Research Society of Japan, Vol.28, No.4, August 2003, pp.1035-1038,

(pp.48-51)

[8] A. Shojiguchi, K. Kobayashi, S. Sangu, K. Kitahara, and M. Ohtsu, "Superradiant multiple pulses from excitons interacting with optical near fields", Transactions of the Material Research Society of Japan, Vol.28, No.4, August 2003, pp.1031-1034

(pp.52-55)

[III] PRESENTATIONS IN INTERNATIONAL CONFERENCES

[1] K. Kobayashi, S. Sangu, T. Kawazoe, and M. Ohtsu, “Exciton dynamics and logic operations in a near-field optically coupled quantum-dot system”, Abstract of the 6th International Conference on Excitonic Processes in Condensed Matter, July 6-9, 2004, Cracow, Poland, (paper number O8)

(p.57)

[2] T. Yatsui, W. Nomura, and M. Ohtsu, “Plasmon polariton transfer along nano-dot coupler for optical far/near field conversion”, Technical Digest of 2004 ICO International Conference on Optics & Photonics in Technology Frontier, July 12-15, 2004, Makuhari, (paper number 12B3-4)

(pp.58-59)

[3] M. Ohtsu, “Nanophotonics: Devices, fabrications, and systems”, Technical Digest of 2004 ICO International Conference on Optics & Photonics in Technology Frontier, July 12-15, 2004, Makuhari, (paper number 13C4-2)

[Invited presentation]

(pp.60-61)

[4] S. Sangu, K. Kobayashi, and M. Ohtsu, “Nanophotonic functional devices using optical near-field energy transfer”, Technical Digest of 2004 ICO International Conference on Optics & Photonics in Technology Frontier, July 12-15, 2004, Makuhari, (paper number 13D2-19)

(pp.62-63)

[5] M. Naruse, T. Miyazaki, F. Kubota, S. Sangu, K. Kobayashi, T. Kawazoe, and M. Ohtsu, “Nanoscale matching architecture using optical near-field coupling”, Technical Digest of 2004 ICO International Conference on Optics & Photonics in Technology Frontier, July 12-15, 2004, Makuhari, (paper number 13D2-20)

(pp.64-65)

[6] T. Yatsui and M. Ohtsu, “Development of nanophotonic devices and their integration by optical near-field”, Proceedings of the 5th International

Symposium on MEMS and Nanotechnology, June 7-10, 2004, Costa Mesa, CA, pp.10-15

[Invited presentation]

(pp.66-71)

[7] T. Yatsui, J. Lim, T. Kawazoe, K. Kobayashi, M. Ohtsu, W.I. Park, and G.-C. Yi, "Observation of optical near-field energy transfer in closely spaced ZnO/ZnMgO multiple-quantum-well nanorods for nanophotonic devices", Technical Digest of Conference on Lasers and Electro-Optics, May 16-21, 2004, San Francisco, CA, (paper number CTuM4)

(pp.72-74)

[8] T. Kawazoe, R. Haga, and M. Ohtsu, "Nano-photolithography using a visible light based on the nonadiabatic near-field photochemical reaction", Technical Digest of Conference on Lasers and Electro-Optics, May 16-21, 2004, San Francisco, CA, (paper number IWA28)

(pp.75-76)

[9] T. Kawazoe, S. Maruyama, and M. Ohtsu, "Fiber optical devices using a gigantic Faraday rotation in nanometric region", Technical Digest of Conference on Lasers and Electro-Optics, May 16-21, 2004, San Francisco, CA, (paper number CWD5)

(pp.77-78)

[10] A. Neogi, H. Morkoc, A. Tackeuchi, T. Kuroda, M. Ohtsu, and T. Kawazoe, "Near field optical spectroscopy of GaN/AlN quantum dots", Technical Digest of Conference on Lasers and Electro-Optics, May 16-21, 2004, San Francisco, CA, (paper number IThM2)

(pp.79-80)

[11] T. Kawazoe, K. Kobayashi, and M. Ohtsu, "The optical nano-fountain for concentrating optical energy to a nanometric region", Technical Digest of Conference on Lasers and Electro-Optics, May 16-21, 2004, San Francisco, CA, (paper number IFC1)

(pp.81-82)

[12] T. Yatsui, W. Nomura, M. Kouroggi, and M. Ohtsu, "Plasmon polariton transfer along a nano-dot coupler for optical far/near field conversion",

Technical Digest of International Quantum Electronics Conference, May 16-21, 2004, San Francisco, CA, (paper number IFC3)

[Invited presentation]

(pp.83-85)

[13] T. Kawazoe, and M. Ohtsu, “Adiabatic and nonadiabatic nanofabrication by localized optical near fields”, Proceedings of SPIE, vol.5339, 2004, SPIE(The International Society for Optical Engineering) pp.619-630

[Symposium on Photon Processing in Microelectronics and Photonics III, Photonic West 2004, January, 24-29, 2004, San Jose, CA, (paper number 5339-85)]

[Invited presentation]

(pp.86-97)

[14] M. Ohtsu, “Nanophotonics’ Devices, fabrications, and systems”, RLNR/Tokyo-Tech 2003 International Symposium – Nanoscience and Nanotechnology on Quantum Particles”, December 15-17, 2003, Tokyo ,(paper number I-3)

[Invited presentation]

(p.98)

[15] J. Lim, T. Yatsui, and M. Ohtsu, “Fabrication of 20-nm Zn nanocrystallites by the selective photodissociation of adsorption-phase diethylzinc using a near-field optical chemical vapor deposition”, Abstracts of the 2003 Material Research Society Fall Meeting, December 1-5, 2003, Boston, (paper number M8.26)

(p.99)

[16] T. Yatsui, J. Lim, T. Kawazoe, K. Kobayashi, M. Ohtsu, W.-I. Park, and G.-C. Yi, “Observation of an optical near-field energy transfer between closely spaced ZnO/ZnMgO multiple-quantum-well nanorods for nanophotonic devices”, Abstracts of the 2003 Material Research Society Fall Meeting, December 1-5, 2003, Boston, (paper number T3.16)

(p.100)

[17] T. Yatsui and M. Ohtsu, “Nanophotonics: for size- and position-controlled nanofabrication by optical near fields”, Proceedings of

Korea-Japan Joint Symposium on Nanoengineering 2003, November 27-28, 2003, Daejeon, Korea, pp.85-88

[Invited presentation]

(pp.101-104)

[18] J. Lim, T. Yatsui, and M. Ohtsu, "Fabrication of 20-nm Zn nanocrystallites by the selective photodissociation of adsorbed diethylzinc molecules using a near-field optical chemical vapor deposition", Abstracts of International Symposium on Quantum Dots and Photonic Crystals 2003, November 17-18, 2003, Tokyo, (paper number P-11)

(p.105)

[19] R. Haga, T. Kawazoe, and M. Ohtsu, "Photolithography using a visible light based on the nonadiabatic near-field photochemical reaction", Abstracts of International Symposium on Quantum Dots and Photonic Crystals 2003, November 17-18, 2003, Tokyo, (paper number P-12)

(p.106)

[20] K. Kobayashi, S. Sangu, A. Shojiguchi, T. Kawazoe, and M. Ohtsu, "Exciton dynamics in a quantum dot system and local manipulation by optical near fields", Abstracts of International Symposium on Quantum Dots and Photonic Crystals 2003, November 17-18, 2003, Tokyo, (paper number P-25)

(p.107)

[21] S. Maruyama, T. Kawazoe, and M. Ohtsu, "Magnetic circular dichroism and large Faraday rotation of Au/Fe/Au/Fe optical fiber probe", Abstracts of International Symposium on Quantum Dots and Photonic Crystals 2003, November 17-18, 2003, Tokyo, (paper number P-26)

(p.108)

[22] M. Ohtsu, "Nanophotonics: Devices, Fabrications, and Systems", Abstract of the Seminar on Micro-, Nano- and Optical Technologies in Germany, November 10, 2003, pp.21-23

[Invited presentation]

(pp.109-111)

[23] M. Ohtsu, "Nanophotonics: Definition and true nature", Abstract of the 4th Asia-Pacific International Conference on Near-Field Optics, October

13-16, 2003, Taroko, Taiwan, p.9

[Invited presentation]

(p.112)

[24] T. Kawazoe, K. Kobayashi, and M. Ohtsu, “The optical nano-fountain, which uses energy transfer to concentrate optical energy to a 10-nm region”, Abstract of the 4th Asia-Pacific International Conference on Near-Field Optics, October 13-16, 2003, Taroko, Taiwan, p.21

(p.113)

[25] T. Yatsui, W. Nomura, M. Kouroggi, and M. Ohtsu, “Development of optical far/near field conversion devices”, Abstract of the 4th Asia-Pacific International Conference on Near-Field Optics, October 13-16, 2003, Taroko, Taiwan, p.28

(p.114)

[26] T.-W. Kim, S. Yamazaki, T. Nagira, T. Kawazoe, T. Yatsui, and M. Ohtsu, “Growth control of Ga and In nanodots by photochemical reactions for applications to group III nitrides-based nanophotonic devices”, Abstract of International Conference on Nanomaterials and Nanotechnologies, August 30 - September 6, 2003, Creta, Greece, (paper number B6 O4)

(p.115)

[27] K. Kobayashi, T. Kawazoe, and M. Ohtsu, “Characteristic mechanism of molecular dissociation and nanofabrication using optical near fields”, Proceedings of 2003 Third IEEE Conference on Nanotechnology, Vol.1, August 12-14, 2003, San Francisco, pp.271-274

(pp.116-119)

[28] S. Sangu, K. Kobayashi, A. Shojiguchi, and M. Ohtsu, “Functional operations using a near-field optically coupled quantum-dot system”, Proceedings of 2003 Third IEEE Conference on Nanotechnology, Vol.1, August 12-14, 2003, San Francisco, pp.283-286

(pp.120-123)

[29] A. Takamizawa, H. Ito, S. Yamada, and M. Ohtsu, “Cold-atom output from a near-field optical funnel”, Proceedings of 2003 Third IEEE Conference on Nanotechnology, Vol.1, August 12-14, 2003, San Francisco, pp.287-290

(pp.124-127)

[30] T. Kawazoe, K. Kobayashi, and M. Ohtsu, “Nano-optical CVD and nanophotolithography using an optical near-field nonresonant to electronic transition”, Proceedings of 2003 Third IEEE Conference on Nanotechnology, Vol.2, August 12-14, 2003, San Francisco, pp.561-564

(pp.128-131)

[31] T. Yatsui, J. Lim, T. Kawazoe, K. Kobayashi, M. Ohtsu, W.I. Park, and G.-C. Yi, “Observation of an optical near-field energy transfer in closely spaced ZnO/ZnMgO multiple-quantum-well nanorods for nanophotonic devices“, Proceedings of 2003 Third IEEE Conference on Nanotechnology, Vol.2, August 12-14, 2003, San Francisco, pp.585-587

(pp.132-134)

[III] REVIEW PAPERS

[1] T. Yatsui and M. Ohtsu, "Nanophotonics: Size- and position-controlled nanofabrication using optical near field", J. Photographical Soc. Jpn., Vol.67, No.3, June 2004, pp.281-287

【八井崇、大津元一、「ナノフォトニクス：近接場光による寸法・位置制御ナノ光加工」、日本写真学会誌、第67巻、第3号、2004年6月、pp.281-287】
(pp.135-141)

[2] M. Ohtsu, "What are optical near fields?", O plus E, Vol.26, No.4, April 2004, pp.372-377

【大津元一、「近接場光とは何か?」、O plus E、第26巻、第4号、2004年4月、pp.372-377】
(pp.142-147)

[3] K. Kobayashi, S. Sangu, and M. Ohtsu, "Optical near fields as an electron-photon interaction system in nanometric space", O plus E, Vol.26, No.4, April 2004, pp.406-411

【小林潔、三宮俊、大津元一、「ナノ領域の電子-光子相互作用システムとしての近接場光」、O plus E、第26巻、第4号、2004年4月、pp.406-411】

(pp.148-153)

[4] T. Yatsui, W. Nomura, and M. Ohtsu, "Plasmon-polariton nanophotonic integrated circuits", J. Opt. Soc. Jpn. Vol.33, No.3, March 2004, pp.174-176

【八井崇、野村航、大津元一、「プラズモン・ポラリトンナノ光回路」、光学、第33巻、第3号、2004年3月、pp.174-176】

(pp.154-156)

[5] M. Ohtsu, T. Kawazoe, and T. Yatsui, "Nanophotonic fabrication: Paradigm shift of optical fabrication", O plus E, Vol.25, No.12, December 2003, pp.1369-1374

【大津元一、川添忠、八井崇、「ナノ光加工：光加工のパラダイムシフト」、O plus E、第25巻、第12号、2003年12月、pp.1369-1374】

(pp.157-161)

[6] M. Ohtsu, "What are optical near fields?", J. Jpn. Soc. For Analytical Chemistry, No.12, December 2003, pp.716-721

【大津元一、「近接場光とは何か」、ぶんせき、第12号、2003年12月、pp.716-721】

(pp.162-167)

[IV] PUBLISHED BOOKS

[1] M. Ohtsu and K. Kobayashi, *Optical Near Fields*, Springer Verlag, Berlin, 2004, (205 pages)

(pp.169-177)

[2] M. Ohtsu (ed.), *Progreess in Nano-Electro-Optics II*, Springer Verlag, Berlin, 2004, (190 pages)

(pp.178-186)

[3] M. Ohtsu, “Principles and applications of optical near fields”, in *Nanoelectronics*, ed. By H. Sakaki and N. Yokoyama, Ohm-sha Tokyo, 2004, pp.211-234

【大津元一、「近接場光学の原理、近接場光を用いたナノフォトニクスの展開」、ナノエレクトロニクス、(榊裕之、横山直樹共編)、オーム社、東京、2004年、pp.211-234】

[4] M. Ohtsu (ed.), *Progreess in Nano-Electro-Optics I*, Springer Verlag, Berlin, 2003, (161 pages)

(pp.187-194)

[5] M. Fukui and M. Ohtsu, *Fundamentals of optical nanotechnology*, Ohm-sha, Tokyo, 2003, (207 pages)

【福井萬壽夫、大津元一、「光ナノテクノロジーの基礎」、オーム社、東京、(207ページ)】

[6] M. Ohtsu(ed.), *Challenges to Nanophotonics*, Yoneda-publishers, Chiba, , 2003, (188 pages)

【大津元一(監修)、「ナノフォトニクスへの挑戦」、米田出版、東京、2003, (188ページ)】

[7] M. Ohtsu, “Near field optical technologies: From imaging/diagnostics to nano-fabrication/atom manipulation”, in *Hyper-Structured Molecules III*, ed. by H. Sasabe, Taylor & Francis, London and New York, 2002, pp.1-30

[V] AWARDS

[1] S. Yamazaki, Imoto Special Award for the poster paper presented at the 48th Young Scientists School of Material Science, Jpn. Soc. Phys.. August 14, 2003,

【山崎俊輔、井元先生特別賞、日本物理学会 第48回物性若手夏の学校、2003年8月14日】

MEMBERS

(From April 1, 2004)

*[I] THE UNIVERSITY OF TOKYO**

Professor

Motoichi OHTSU

(Dr. Eng.)

Graduate Students (Doctor Candidates)

Wataru NOMURA

Graduate Students (Master Course)

Kokoro KITAMURA

Undergraduate Students

Hiroki YONEMITSU

Yuuki NAKAJIMA

Secretary

Sachiyo KOJIMA

- (*) Department of Electronics Engineering, School of Engineering,
The University of Tokyo
7-3-1 Hongo, Bunkyo-ku, Tokyo 113-8656
Phone: +81-3-5841-1189, Fax: +81-3-5841-1140
E-mail: ohtsu@ee.t.u-tokyo.ac.jp

東京大学大学院工学系研究科電子工学専攻

〒113-8656 東京都文京区本郷 7-3-1

Phone: 03-5841-1189, Fax: 03-5841-1140

E-mail: ohtsu@ee.t.u-tokyo.ac.jp

[III] TOKYO INSTITUTE OF TECHNOLOGY*

Graduate Students (Doctor Candidates)

Yoshinobu NAKAYAMA

Jungshik LIM

Graduate Students (Master Course)

Kazunori KOBAYASHI

Takashi NAGIRA

Secretary

Kaoru OGURA

- (*) Interdisciplinary Graduate School of Science and Engineering,
Tokyo Institute of Technology
4259 Nagatsuta-cho, Midori-ku, Yokohama 226-8502
Phone: +81-45-924-5455, Fax: +81-45-924-5599

東京工業大学大学院総合理工学研究科電子機能システム専攻
〒226-8502 横浜市緑区長津田町 4259

Phone: 045-924-5455, Fax: 045-924-5599

**[III] NANOPHOTONICS TEAM*,
SORST,
JAPAN SCIENCE AND TECHNOLOGY AGENCY**

Researchers

Tadashi KAWAZOE (Dr. Sci.)

Takashi YATSUI (Dr. Eng.)

Managers

Akiyoshi ORIDE

Secretaries

Tomoko TOTAKE

(*) Nanophotonics Team,
Japan Science and Technology Agency
4th-floor, Tenko Building #17
687-1 Tsuruma, Machida-shi, Tokyo 194-0004
Phone: +81-42-7888-6030, Fax: +81-42-788-6031

(独) 科学技術振興機構 ナノフォトンクスチーム
〒194-0004 東京都町田市鶴間 687-1
第 17 天幸ビル 4 階
Phone: 042-7888-6030, Fax: 042-788-6031

[IV] KANAGAWA ACADEMY OF SCIENCE AND TECHNOLOGY*

Full-Time Researchers

Shuji MONONOBE

(Dr. Eng.)

Secretary

Kazumi NAKAHARA

- (*) Ohtsu-Saiki group,
Kanagawa Academy of Science and Technology
KSP East, Rm.408,
3-2-1 Sakado, Takatsu-ku, Kawasaki 213-0012
Phone: +81-44-819-2075, Fax: +81-44-819-2072

(財) 神奈川科学技術アカデミー 光科学重点研究室
大津齊木グループ

〒213-0012 川崎市高津区坂戸 3-2-1

194-0004 東京都町田市鶴間 687-1

KSP 東棟、408 号室

Phone: 044-819-2075,

Fax: 044-819-2072

LIST OF PAPERS

[(pp.XX-XX); pages in this issue of the COLLECTED PAPERS]

[I] ORIGINAL PAPERS

[1] S. Mononobe, Y. Sato, M. Ohtsu, and H. Honma, "Fabrication of a Near-Field Optical Fiber Probe Based on Electroless Nickel Plating under Ultrasonic Irradiation", Jpn. J. Appl. Phys., Vol.43, No.5B, May 2004, pp.2862-2863

(pp.1-2)

[2] T-W. Kim, T. Kawazoe, S. Yamazaki, M. Ohtsu, and T. Sekiguchi, "Low-temperature orientation-selective growth and ultraviolet emission of single-crystal ZnO nanowires", Appl. Phys. Lett., Vol.84, No.17, April 2004, pp.3358-3360

(pp.3-5)

[2'] T-W. Kim, T. Kawazoe, S. Yamazaki, M. Ohtsu, and T. Sekiguchi, "Low-temperature orientation-selective growth and ultraviolet emission of single-crystal ZnO nanowires", Virtual Journal of Nanoscale Science and Technology, Vol.9, Issue 17, May 3, 2004

(pp.6-7)

[3] S. Sangu, K. Kobayashi, A. Shojiguchi, and M. Ohtsu, "Logic and functional operations using a near-field optically coupled quantum-dot system", Phys. Rev. B, Vol.69, No.11, March 2004, pp.115334-1 – 115334-13

(pp.8-20)

[3'] S. Sangu, K. Kobayashi, A. Shojiguchi, and M. Ohtsu, "Logic and functional operations using a near-field optically coupled quantum-dot system", Virtual Journal of Nanoscale Science and Technology, Vol.9, Issue 13, April 5, 2004

(pp.21-22)

[4] H. Kubota, R. Takahashi, T.-W. Kim, T. Kawazoe, M. Ohtsu, N. Arai, M.

Yoshimura, H. Nakao, H. Furuya, Y. Mori, T. Sasaki, Y. Matsumoto, and H. Koinuma, "Combinatorial synthesis and luminescent characteristics of $\text{RECa}_4\text{O}(\text{BO}_3)_3$ epitaxial thin films", Applied Surface Science, Vol.223, 2004, pp.241-244

(pp.23-26)

[5] A. Shojiguchi, K. Kobayashi, S. Sangu, K. Kitahara, and M. Ohtsu, "Superradiance and Dipole Ordering of an N Two-Level System Interacting with Optical Near Fields", J. Phys. Soc. Jpn., Vol.72, No.11, November 2003, pp.2984-3001

(pp.27-44)

[6] T. Yatsui, S. Takubo, J. Lim, W. Nomura, M. Kouroggi, and M. Ohtsu, "Regulating the size and position of deposited Zn nanoparticles by optical near-field desorption using size-dependent resonance", Appl. Phys. Lett., Vol.83, No.9, September 2003, pp.1716-1718

(pp.45-47)

[7] S. Sangu, K. Kobayashi, T. Kawazoe, A. Shojiguchi, and M. Ohtsu, "Quantum-Coherence Effect in a Quantum Dot System Coupled by Optical Near Fields", Transactions of the Material Research Society of Japan, Vol.28, No.4, August 2003, pp.1035-1038,

(pp.48-51)

[8] A. Shojiguchi, K. Kobayashi, S. Sangu, K. Kitahara, and M. Ohtsu, "Superradiant multiple pulses from excitons interacting with optical near fields", Transactions of the Material Research Society of Japan, Vol.28, No.4, August 2003, pp.1031-1034

(pp.52-55)

[III] PRESENTATIONS IN INTERNATIONAL CONFERENCES

[1] K. Kobayashi, S. Sangu, T. Kawazoe, and M. Ohtsu, “Exciton dynamics and logic operations in a near-field optically coupled quantum-dot system”, Abstract of the 6th International Conference on Excitonic Processes in Condensed Matter, July 6-9, 2004, Cracow, Poland, (paper number O8)

(p.57)

[2] T. Yatsui, W. Nomura, and M. Ohtsu, “Plasmon polariton transfer along nano-dot coupler for optical far/near field conversion”, Technical Digest of 2004 ICO International Conference on Optics & Photonics in Technology Frontier, July 12-15, 2004, Makuhari, (paper number 12B3-4)

(pp.58-59)

[3] M. Ohtsu, “Nanophotonics: Devices, fabrications, and systems”, Technical Digest of 2004 ICO International Conference on Optics & Photonics in Technology Frontier, July 12-15, 2004, Makuhari, (paper number 13C4-2)

[Invited presentation]

(pp.60-61)

[4] S. Sangu, K. Kobayashi, and M. Ohtsu, “Nanophotonic functional devices using optical near-field energy transfer”, Technical Digest of 2004 ICO International Conference on Optics & Photonics in Technology Frontier, July 12-15, 2004, Makuhari, (paper number 13D2-19)

(pp.62-63)

[5] M. Naruse, T. Miyazaki, F. Kubota, S. Sangu, K. Kobayashi, T. Kawazoe, and M. Ohtsu, “Nanoscale matching architecture using optical near-field coupling”, Technical Digest of 2004 ICO International Conference on Optics & Photonics in Technology Frontier, July 12-15, 2004, Makuhari, (paper number 13D2-20)

(pp.64-65)

[6] T.Yatsui and M. Ohtsu, “Development of nanophotonic devices and their integration by optical near-field”, Proceedings of the 5th International Symposium on MEMS and Nanotechnology, June 7-10, 2004, Costa Mesa, CA, pp.10-15

[Invited presentation]

(pp.66-71)

[7] T. Yatsui, J. Lim, T. Kawazoe, K. Kobayashi, M. Ohtsu, W.I. Park, and G.-C. Yi, “Observation of optical near-field energy transfer in closely spaced ZnO/ZnMgO multiple-quantum-well nanorods for nanophotonic devices”, Technical Digest of Conference on Lasers and Electro-Optics, May 16-21, 2004, San Francisco, CA, (paper number CTuM4)

(pp.72-74)

[8] T. Kawazoe, R. Haga, and M. Ohtsu, “Nano-photolithography using a visible light based on the nonadiabatic near-field photochemical reaction”, Technical Digest of Conference on Lasers and Electro-Optics, May 16-21, 2004, San Francisco, CA, (paper number IWA28)

(pp.75-76)

[9] T. Kawazoe, S. Maruyama, and M. Ohtsu, “Fiber optical devices using a gigantic Faraday rotation in nanometric region”, Technical Digest of Conference on Lasers and Electro-Optics, May 16-21, 2004, San Francisco, CA, (paper number CWD5)

(pp.77-78)

[10] A. Neogi, H. Morkoc, A. Tackeuchi, T. Kuroda, M. Ohtsu, and T. Kawazoe, “Near field optical spectroscopy of GaN/AlN quantum dots”, Technical Digest of Conference on Lasers and Electro-Optics, May 16-21, 2004, San Francisco, CA, (paper number IThM2)

(pp.79-80)

[11] T. Kawazoe, K. Kobayashi, and M. Ohtsu, “The optical nano-fountain for concentrating optical energy to a nanometric region”, Technical Digest of Conference on Lasers and Electro-Optics, May 16-21, 2004, San Francisco, CA, (paper number IFC1)

(pp.81-82)

[12] T. Yatsui, W. Nomura, M. Kouroggi, and M. Ohtsu, “Plasmon polariton transfer along a nano-dot coupler for optical far/near field conversion”, Technical Digest of International Quantum Electronics Conference, May 16-21, 2004, San Francisco, CA, (paper number IFC3)

[Invited presentation]

(pp.83-85)

[13] T. Kawazoe, and M. Ohtsu, “Adiabatic and nonadiabatic nanofabrication by localized optical near fields”, Proceedings of SPIE, vol.5339, 2004, SPIE(The International Society for Optical Engineering) pp.619-630

[Symposium on Photon Processing in Microelectronics and Photonics III, Photonic West 2004, January, 24-29, 2004, San Jose, CA, (paper number 5339-85)]

[Invited presentation]

(pp.86-97)

[14] M. Ohtsu, “Nanophotonics’ Devices, fabrications, and systems”, RLNR/Tokyo-Tech 2003 International Symposium – Nanoscience and Nanotechnology on Quantum Particles”, December 15-17, 2003, Tokyo ,(paper number I-3)

[Invited presentation]

(p.98)

[15] J. Lim, T. Yatsui, and M. Ohtsu, “Fabrication of 20-nm Zn nanocrystallites by the selective photodissociation of adsorption-phase diethylzinc using a near-field optical chemical vapor deposition”, Abstracts of the 2003 Material Research Society Fall Meeting, December 1-5, 2003, Boston, (paper number M8.26)

(p.99)

[16] T. Yatsui, J. Lim, T. Kawazoe, K. Kobayashi, M. Ohtsu, W.-I. Park, and G-C. Yi, “Observation of an optical near-field energy transfer between closely spaced ZnO/ZnMgO multiple-quantum-well nanorods for nanophotonic devices”, Abstracts of the 2003 Material Research Society Fall Meeting, December 1-5, 2003, Boston, (paper number T3.16)

(p.100)

[17] T. Yatsui and M. Ohtsu, "Nanophotonics: for size- and position-controlled nanofabrication by optical near fields", Proceedings of Korea-Japan Joint Symposium on Nanoengineering 2003, November 27-28, 2003, Daejeon, Korea, pp.85-88

[Invited presentation]

(pp.101-104)

[18] J. Lim, T. Yatsui, and M. Ohtsu, "Fabrication of 20-nm Zn nanocrystallites by the selective photodissociation of adsorbed diethylzinc molecules using a near-field optical chemical vapor deposition", Abstracts of International Symposium on Quantum Dots and Photonic Crystals 2003, November 17-18, 2003, Tokyo, (paper number P-11)

(p.105)

[19] R. Haga, T. Kawazoe, and M. Ohtsu, "Photolithography using a visible light based on the nonadiabatic near-field photochemical reaction", Abstracts of International Symposium on Quantum Dots and Photonic Crystals 2003, November 17-18, 2003, Tokyo, (paper number P-12)

(p.106)

[20] K. Kobayashi, S. Sangu, A. Shojiguchi, T. Kawazoe, and M. Ohtsu, "Exciton dynamics in a quantum dot system and local manipulation by optical near fields", Abstracts of International Symposium on Quantum Dots and Photonic Crystals 2003, November 17-18, 2003, Tokyo, (paper number P-25)

(p.107)

[21] S. Maruyama, T. Kawazoe, and M. Ohtsu, "Magnetic circular dichroism and large Faraday rotation of Au/Fe/Au/Fe optical fiber probe", Abstracts of International Symposium on Quantum Dots and Photonic Crystals 2003, November 17-18, 2003, Tokyo, (paper number P-26)

(p.108)

[22] M. Ohtsu, "Nanophotonics: Devices, Fabrications, and Systems", Abstract of the Seminar on Micro-, Nano- and Optical Technologies in Germany, November 10, 2003, pp.21-23

[Invited presentation]

(pp.109-111)

[23] M. Ohtsu, “Nanophotonics: Definition and true nature”, Abstract of the 4th Asia-Pacific International Conference on Near-Field Optics, October 13-16, 2003, Taroko, Taiwan, p.9

[Invited presentation]

(p.112)

[24] T. Kawazoe, K. Kobayashi, and M. Ohtsu, “The optical nano-fountain, which uses energy transfer to concentrate optical energy to a 10-nm region”, Abstract of the 4th Asia-Pacific International Conference on Near-Field Optics, October 13-16, 2003, Taroko, Taiwan, p.21

(p.113)

[25] T. Yatsui, W. Nomura, M. Kouroggi, and M. Ohtsu, “Development of optical far/near field conversion devices”, Abstract of the 4th Asia-Pacific International Conference on Near-Field Optics, October 13-16, 2003, Taroko, Taiwan, p.28

(p.114)

[26] T.-W. Kim, S. Yamazaki, T. Nagira, T. Kawazoe, T. Yatsui, and M. Ohtsu, “Growth control of Ga and In nanodots by photochemical reactions for applications to group III nitrides-based nanophotonic devices”, Abstract of International Conference on Nanomaterials and Nanotechnologies, August 30 - September 6, 2003, Creta, Greece, (paper number B6 O4)

(p.115)

[27] K. Kobayashi, T. Kawazoe, and M. Ohtsu, “Characteristic mechanism of molecular dissociation and nanofabrication using optical near fields”, Proceedings of 2003 Third IEEE Conference on Nanotechnology, Vol.1, August 12-14, 2003, San Francisco, pp.271-274

(pp.116-119)

[28] S. Sangu, K. Kobayashi, A. Shojiguchi, and M. Ohtsu, “Functional operations using a near-field optically coupled quantum-dot system”, Proceedings of 2003 Third IEEE Conference on Nanotechnology, Vol.1, August 12-14, 2003, San Francisco, pp.283-286

(pp.120-123)

[29] A. Takamizawa, H. Ito, S. Yamada, and M. Ohtsu, “Cold-atom output from a near-field optical funnel”, Proceedings of 2003 Third IEEE

Conference on Nanotechnology, Vol.1, August 12-14, 2003, San Francisco, pp.287-290

(pp.124-127)

[30] T. Kawazoe, K. Kobayashi, and M. Ohtsu, “Nano-optical CVD and nanophotolithography using an optical near-field nonresonant to electronic transition”, Proceedings of 2003 Third IEEE Conference on Nanotechnology, Vol.2, August 12-14, 2003, San Francisco, pp.561-564

(pp.128-131)

[31] T. Yatsui, J. Lim, T. Kawazoe, K. Kobayashi, M. Ohtsu, W.I. Park, and G.-C. Yi, “Observation of an optical near-field energy transfer in closely spaced ZnO/ZnMgO multiple-quantum-well nanorods for nanophotonic devices“, Proceedings of 2003 Third IEEE Conference on Nanotechnology, Vol.2, August 12-14, 2003, San Francisco, pp.585-587

(pp.132-134)

[III] REVIEW PAPERS

[1] T. Yatsui and M. Ohtsu, “Nanophotonics: Size- and position-controlled nanofabrication using optical near field”, J. Photographical Soc. Jpn., Vol.67, No.3, June 2004, pp.281-287

【八井崇、大津元一、「ナノフォトニクス：近接場光による寸法・位置制御ナノ光加工」、日本写真学会誌、第67巻、第3号、2004年6月、pp.281-287】
(pp.135-141)

[2] M. Ohtsu, “What are optical near fields?”, O plus E, Vol.26, No.4, April 2004, pp.372-377

【大津元一、「近接場光とは何か?」、O plus E、第26巻、第4号、2004年4月、pp.372-377】

(pp.142-147)

[3] K. Kobayashi, S. Sangu, and M. Ohtsu, “Optical near fields as an electron-photon interaction system in nanometric space”, O plus E, Vol.26, No.4, April 2004, pp.406-411

【小林潔、三宮俊、大津元一、「ナノ領域の電子-光子相互作用システムとしての近接場光」、O plus E、第26巻、第4号、2004年4月、pp.406-411】

(pp.148-153)

[4] T. Yatsui, W. Nomura, and M. Ohtsu, “Plasmon-polariton nanophotonic integrated circuits”, J. Opt. Soc. Jpn. Vol.33, No.3, March 2004, pp.174-176

【八井崇、野村航、大津元一、「プラズモン・ポラリトンナノ光回路」、光学、第33巻、第3号、2004年3月、pp.174-176】

(pp.154-156)

[5] M. Ohtsu, T. Kawazoe, and T. Yatsui, “Nanophotonic fabrication: Paradigm shift of optical fabrication”, O plus E, Vol.25, No.12, December 2003, pp.1369-1374

【大津元一、川添忠、八井崇、「ナノ光加工：光加工のパラダイムシフト」、O plus E、第25巻、第12号、2003年12月、pp.1369-1374】

(pp.157-161)

[6] M. Ohtsu, “What are optical near fields?”, J. Jpn. Soc. For Analytical Chemistry, No.12, December 2003, pp.716-721

【大津元一、「近接場光とは何か」、ぶんせき、第12号、2003年12月、pp.716-721】

(pp.162-167)

[IV] PUBLISHED BOOKS

[1] M. Ohtsu and K. Kobayashi, *Optical Near Fields*, Springer Verlag, Berlin, 2004, (205 pages)

(pp.169-177)

[2] M. Ohtsu (ed.), *Progreess in Nano-Electro-Optics II*, Springer Verlag, Berlin, 2004, (190 pages)

(pp.178-186)

[3] M. Ohtsu, “Principles and applications of optical near fields”, in *Nanoelectronics*, ed. By H. Sakaki and N. Yokoyama, Ohm-sha Tokyo, 2004, pp.211-234

【大津元一、「近接場光学の原理、近接場光を用いたナノフォトニクスの展開」、ナノエレクトロニクス、(榊裕之、横山直樹共編)、オーム社、東京、2004年、pp.211-234】

[4] M. Ohtsu (ed.), *Progreess in Nano-Electro-Optics I*, Springer Verlag, Berlin, 2003, (161 pages)

(pp.187-194)

[5] M. Fukui and M. Ohtsu, *Fundamentals of optical nanotechnology*, Ohm-sha, Tokyo, 2003, (207 pages)

【福井萬壽夫、大津元一、「光ナノテクノロジーの基礎」、オーム社、東京、(207ページ)】

[6] M. Ohtsu(ed.), *Challenges to Nanophotonics*, Yoneda-publishers, Chiba, , 2003, (188 pages)

【大津元一（監修）、「ナノフォトニクスへの挑戦」、米田出版、東京、2003、（188ページ）】

[7] M. Ohtsu, “Near field optical technologies: From imaging/diagnostics to nano-fabrication/atom manipulation”, in *Hyper-Structured Molecules III*, ed. by H. Sasabe, Taylor & Francis, London and New York, 2002, pp.1-30

[V] AWARDS

[1] S. Yamazaki, Imoto Special Award for the poster paper presented at the 48th Young Scientists School of Material Science, Jpn. Soc. Phys.. August 14, 2003,

【山崎俊輔、井元先生特別賞、日本物理学会 第48回物性若手夏の学校、2003年8月14日】

[I] ORIGINAL PAPERS



Fabrication of a Near-Field Optical Fiber Probe Based on Electroless Nickel Plating under Ultrasonic Irradiation

Shuji MONONOBE^{1,2,*}, Yuichi SAITO³, Motoichi OHTSU^{2,4} and Hideo HONMA³

¹Kunitake “Organization and Function” Research Area, PRESTO, Japan Science and Technology Agency, Japan

²Kanagawa Academy of Science and Technology, KSP East 408, 3-2-1 Sakado, Takatsu, Kawasaki 213-0012, Japan

³Faculty of Engineering, Kanto Gakuin University, Mitsuurahigashi, Yokohama 236-8501, Japan

⁴Interdisciplinary Graduate School of Science and Engineering, Tokyo Institute of Technology, Yokohama 226-8502, Japan

(Received November 25, 2003; revised February 8, 2004; accepted February 12, 2004; published May 28, 2004)

We present a method of fabricating a near-field optical probe with a nickel film whose thickness gradually decreases to a few tens of nanometers toward the apex. This method involves etching an optical fiber and electroless nickel plating with ultrasonic agitation. Using 1 MHz ceramic transducers, we have reproducibly fabricated the probe with a tip diameter of less than 40 nm. This reproducibility is high compared to those for Langevin-type transducers. [DOI: 10.1143/JJAP.43.2862]

KEYWORDS: electroless plating, metallization, ultrasonic wave, optical fiber, SNOM, NSOM, etching

Recently, a scanning near-field optical microscope (SNOM)^{1,2)} employing a tapered probe and shear-force feedback technique, which provides simultaneous topographic and SNOM imaging, has been widely applied to super-resolution imaging and local spectroscopy. To obtain highly resolved SNOM images, the tapered probe should be coated with a submicrometer-thick metal except for the apex region. Further, the probe tip must have a small diameter of a few tens of nanometers to perform high resolution shear-force imaging. To develop a high resolution SNOM/shear-force microscope, we recently proposed a novel metallized fiber probe³⁾ with a tiny tip as shown in Fig. 1(a), where the inset illustrates the magnified apex region of the probe. The metal coating thickness gradually decreases to a few tens of nanometers toward the apex. To realize such probes, we have developed a method based on size-dependent electroless nickel plating under ultrasonic irradiation. Since the plating activity is affected by the concentration of dissolved oxygen (DO), the ultrasonic power density must be controlled to keep the local DO concentration near the apex region higher than those of the other regions of the probe. In this paper, we present a novel method of probe fabrication and discuss the reproducibilities for two different ultrasonic generators which have ceramic transducers and Langevin-type transducers.

This method consists of fiber etching, surface activation, and electroless plating with ultrasonic agitation. First, a GeO₂-doped fiber with a core diameter of 2 μm and an index difference of 2% was consecutively etched by two buffered HF solutions with volume ratios of 40%NH₄F:50%HF:H₂O = 1.7:1:1 for 80 min and in 10:1:1 for 120 min at 25°C. The obtained fiber probe has a conical tapered core protruding from the flat clad end with a diameter of 25 μm. The cone angle is $\theta = 20^\circ$, and the apex diameter is less than 10 nm. Next, the fiber probe was consecutively immersed in 0.8 g dm⁻³-SnCl₂ solution for 3 min and in 5 mg dm⁻³-PdCl₂ solution for 3 min. This activation process was repeated twice. Figure 1(b) schematically shows the plating unit for metallization of the probe. The plating bath composition is summarized in Table I. Figure 1(c) shows an ultrasonic generator (Honda Electronics, W357 HP) with four ceramic transducers, which radiates directional 1 MHz

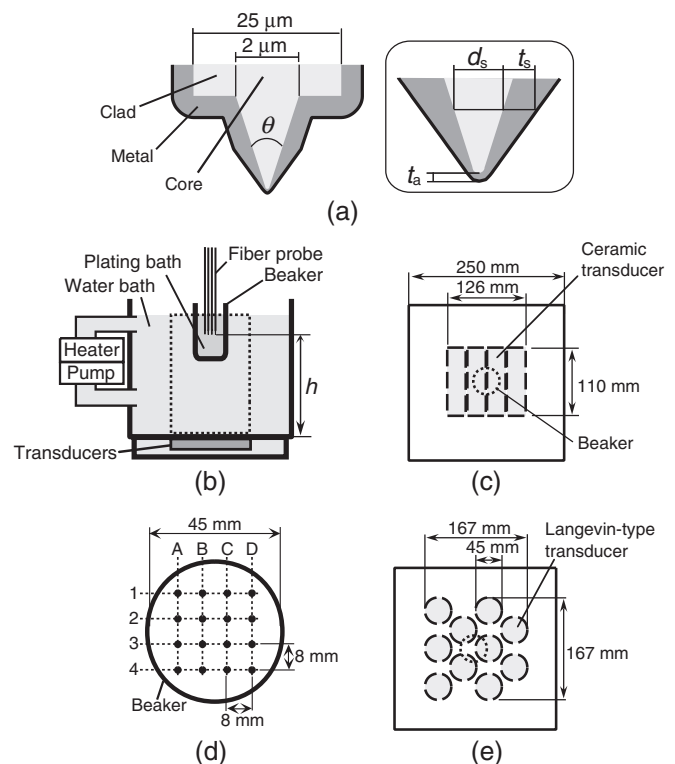


Fig. 1. (a) Schematic design of the near-field optical fiber probe having a metal film whose thickness gradually decreases toward the apex. Here, the body and portions with fiber diameters of more than the optical wavelength size have fairly thick thicknesses in comparison to the skin depth. θ is the cone angle of the tapered fiber. The inset shows the magnified apex region. d_s and t_s are defined as the fiber diameter and radial thickness in the same cross-section, respectively. t_a is the thickness of metal covering the apex. (b) Schematic explanation of electroless plating unit with an ultrasonic generator. Here, $h = 220$ mm. Top view illustrations of (c) the 1 MHz ultrasonic generator, (d) sixteen probes in the plating bath, and (e) 100 kHz ultrasonic generator.

Table I. Composition of the nickel plating bath.

NiSO ₄ ·6H ₂ O	0.1 mol·dm ⁻³
CH ₃ COONH ₄	0.4 mol·dm ⁻³
NaPH ₂ O ₂ ·H ₂ O	0.2 mol·dm ⁻³
pH	5.0
Temperature	60°C

*E-mail address: mononobe@net.ksp.or.jp

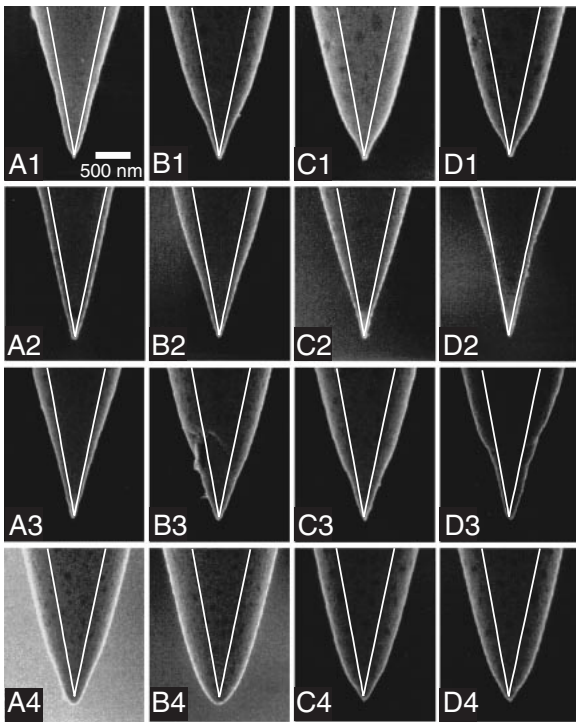


Fig. 2. SEM images of the nickel-coated probes, fabricated by the plating unit with 1 MHz ceramic transducers. The symbol sets represent the horizontal and vertical positions of the probes at the plating, defined as in Fig. 1(d).

ultrasonic waves. Due to the high directivity, the ultrasonic energy is strongly confined within the region indicated by the dotted rectangle. We plated a set of 16 tapered fibers for 15 min while applying an electric power of approximately 300 W to the transducers with a total area of $126 \text{ mm} \times 110 \text{ mm}$. For this plating, we made the delay time between the start of plating and the start of ultrasonic agitation around five seconds. Figure 1(d) schematically shows the lateral positions of the 16 probes in the plating bath. Here, the positions are indicated by the closed circles, which are denoted as ij (where $i = A - D$ and $j = 1 - 4$). Figure 1(e) shows another generator (Honda electronics, W-100-HF MKII) with 100 kHz Langevin-type transducers.

Figure 2 shows a set of scanning electron micrographs (SEM) of the 16 probes, where the dotted lines represent the cross-sectional profiles of the tapered fibers. These nickel-coated probes have a tip diameter of less than 40 nm. The nickel thicknesses covering the apices of the fiber were estimated to be $t_a < 20 \text{ nm}$. To evaluate the decreasing thickness profiles, we estimated the radial thickness t_s for a cross-sectional fiber diameter of $d_s = 200 \text{ nm}$. The average and deviation of the 16 probes take comparable values of 130 nm and 72 nm, respectively. For probes B2, B3, C2, and C3, we obtained a reduced deviation of 17 nm for an average of 90 nm. This result indicates that the probe was fabricated with high reproducibility by plating in the inner square with an area of $8 \text{ mm} \times 8 \text{ mm}$. The thickness ratio t_a/t_s depends on the ultrasonic power density and is minimized at an electric power of 225–300 W. The nickel thickness profile can be controlled by varying the etching time for the electric power.

Furthermore, we applied this method to another set of 16

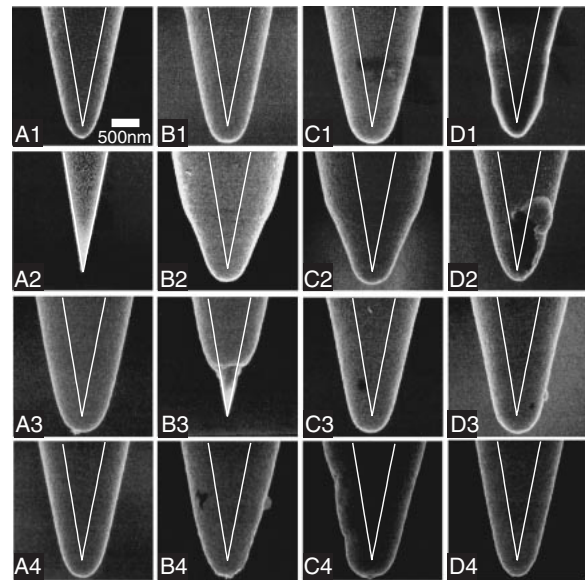


Fig. 3. SEM images of the 16 nickel-coated probes, plated at 55°C by the unit with the 100 kHz Langevin-type transducers. The symbol sets as in Fig. 2.

tapered fibers by using the 100 kHz ultrasonic generator (Fig. 1(e)). This generator based on Langevin-type transducers supplies the ultrasonic energy to the whole water and plating bath. Figure 3 shows the SEM images of the 16 obtained probes in the conditions of the maximum electric power of 300 W and a bath temperature of 55°C . Although probes A2 and B3 have an uncoated tapered portion and a protruding tip from a nickel film, respectively, such tips could not be reproducibly fabricated in the same positions. The other 14 probes were entirely coated with fairly thick nickel. We considered this low reproducibility attributable the spatial and temporal variations of the ultrasonic power density. Furthermore, several tapered fibers were plated using a commercial ultrasonic cleaner with a 45 kHz Langevin-type transducer. The electric power and bath temperature were 100 W and 55°C , respectively. Some of the obtained probes were uncoated and entirely coated. These results show that it is difficult to produce the metallized probe with a tiny tip diameter by plating units based on Langevin-type transducers. We consider that the reproducibility of the plating process is mainly affected by the spatial and temporal power density variations rather than by the ultrasonic frequency.

In summary, we developed an electroless nickel plating unit with 1 MHz ceramic transducers and successfully fabricated a metallized probe tip with a diameter of less than 40 nm for SNOM/shear-force microscopy. In comparison to Langevin-type transducers, it was found that ceramic transducers with directional ultrasonic radiation are effective for improving the reproducibility of this plating method.

- 1) *Near-field Optics*, eds. D. W. Pohl and D. Coujorn (Kluwer, Dordrecht, 1993) NATO ASI Series E, Vol. 242.
- 2) *Near-field Nano/Atom Optics and Technology*, ed. M. Ohtsu (Springer-Verlag, Tokyo, 1998).
- 3) S. Mononobe, M. Ohtsu, T. Matsumoto and T. Saiki: U. S. Patent 5812724 (1998).

Low-temperature orientation-selective growth and ultraviolet emission of single-crystal ZnO nanowires

Tae-Won Kim^{a)} and Tadashi Kawazoe

Ohtsu Localized Photon Project, Exploratory Research for Advanced Technology (ERATO), Japan Science and Technology Corporation, 687-1, Tsuruma, Machida, Tokyo 194-0004, Japan

Shunsuke Yamazaki and Motoichi Ohtsu^{b)}

Interdisciplinary Graduate School of Science and Engineering, Tokyo Institute of Technology, Yokohama, Kanagawa 226-8502, Japan

Takashi Sekiguchi

Nanomaterials Laboratory, National Institute for Materials Science, Tsukuba 305-0047, Japan

(Received 26 November 2003; accepted 1 March 2004)

We fabricated single-crystal ZnO nanowires at a low temperature of 500 °C without using any metal catalysts via the simple thermal oxidation of metallic Zn precursors. Scanning electron microscopy and high-resolution transmission electron microscopy (HRTEM) studies showed that the ZnO nanowires with orientation-selectivity grew laterally along the sides of the hexagonal-shaped ZnO matrix transformed from the metallic Zn precursors. It was found that the nanowires grew along the $\langle 11\bar{2}0 \rangle$ direction and were single crystals by HRTEM study. Typically, the lengths of the ZnO nanowires ranged from 0.5 to 3 μm and their mean diameter was 20 ± 5 nm. Photoluminescence and cathodoluminescence measurements at room temperature showed a strong ultraviolet emission peak with negligibly weak green emissions, confirming that the individual ZnO nanowire was of excellent optical quality. Based on these results, we conclude that the simple thermal oxidation of metal Zn precursors is a useful, feasible approach for fabricating high-quality one-dimensional ZnO nanostructures for integration into nanophotonic integrated circuits. © 2004 American Institute of Physics. [DOI: 10.1063/1.1723696]

ZnO, which has a wide band gap of 3.35 eV and a large excitonic binding energy of ~ 60 meV, is a promising material for ultraviolet (UV) photonic devices. There have been many attempts to synthesize one-dimensional (1D) ZnO nanostructures, using chemical vapor deposition,¹ thermal evaporation,² and catalysis-assisted vapor–liquid–solid (VLS) growth.³ Room temperature (RT) UV lasing using 1D ZnO nanostructures and/or epitaxial film has recently been reported.^{3,4} However, most established fabrication methods require a high temperature above ~ 1000 °C. Such high temperature is disadvantageous in the fabrication of nanophotonic integrated circuits (ICs) because the precise control in the size and position of nanomaterial would be disturbed due to thermal drift.⁵ The fabrication of nanophotonic ICs requires accuracy in size and positioning as high as a few nanometers in order to transfer size-dependent nanometer-localized optical near-fields from one nanodot to another.^{6–10} Therefore, a low process temperature is required to fabricate nanophotonic ICs. Moreover, most of the 1D ZnO nanostructures fabricated using the abovementioned methods were grown vertically on substrates with *c*-axis orientation. From the viewpoint of a nanophotonic ICs, however, lateral growth of

1D ZnO nanostructures without a catalysis metal at the tip is needed because such structures can be used as nanometric waveguides to interconnect the components fabricated on a substrate. We have established a deposition method of size- and position-controlled nanometric Zn and ZnO nanodots by the photodissociation of metalorganic precursors using an optical near-field.^{11,12}

Here, we report the lateral growth of ZnO nanowires with orientation-selectivity using a simple method, which involves the thermal oxidation of predeposited-hexagonal Zn nanoplates. ZnO nanowires were grown by the thermal oxidation of predeposited-hexagonal Zn nanoplates on $\text{CaF}_2(111)$ substrate with no metal catalyst. Hexagonal Zn nanoplates formed on $\text{CaF}_2(111)$ substrate via the thermal evaporation of metallic Zn powder (Furuuchi Chemical Co., 99.999%). The sample was oxidized at 380–950 °C for 1 h, in air.¹³ After thermal oxidation, the substrate surface was covered with a thin white material. The morphology of the nanowires and precursors was analyzed using scanning electron microscopy (SEM) (Hitachi, HT-4700). High-resolution transmission electron microscopy (HRTEM) characterization of the nanowires was performed using an Hitachi HF-2000 operated at 200 kV. Photoluminescence (PL) measurements were made at room temperature using a continuous-wave He–Cd laser ($\lambda = 325$ nm) as the excitation source for optical characterization of the nanowires. Additionally, a monochromatic cathodoluminescence (CL) image of a single ZnO nanowire was taken at room temperature using a high-resolution SEM (Hitachi, HT-4200), equipped with a CL sys-

^{a)} Author to whom correspondence should be addressed. Present address: Kanagawa Academy of Science and Technology, KSP East 301, 3-2-1 Sakado, Takatsu, Kawasaki, Kanagawa 213-0012, Japan; electronic mail: twkim90@ksp.or.jp

^{b)} Also at: Ohtsu Localized Photon Project, Exploratory Research for Advanced Technology (ERATO), Japan Science and Technology Corporation, 687-1, Tsuruma, Machida, Tokyo 194-0004, Japan

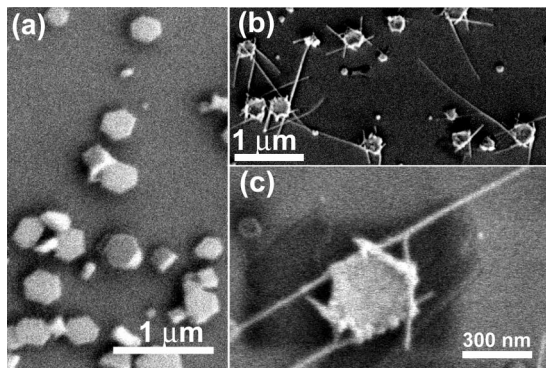


FIG. 1. SEM images of as-deposited metallic Zn precursors on CaF₂(111) substrate (a) and ZnO nanowires with hexagonal ZnO nanoplates formed after thermal oxidation at 500 °C (b), with a high-magnification image of (b).

tem (Jobin Yvon, Triax320), operated at an acceleration voltage of 5 kV and a sample current of 120 pA.

SEM images of as-deposited hexagonal Zn nanoplates and ZnO nanostructures after thermal oxidation at 500 °C for 1 h are shown in Figs. 1(a)–1(c), respectively. Before thermal oxidation, well-defined hexagonal Zn nanoplates were clearly observed on CaF₂(111) substrate, accompanied by a few rectangular ones. The diameters ranged from 200 to 600 nm and their typical thickness was 60 ± 10 nm. After thermal oxidation, many thin ZnO nanowires that grew laterally at the apexes of the hexagonal ZnO nanoplates were observed, and the edges of the hexagonal plates swelled as they incorporated oxygen [see Figs. 1(b) and 1(c)]. Note that the growth direction of each ZnO nanowire showed a specific orientation relationship with the hexagonal ZnO nanoplates (discussed below). As shown in Fig. 1(c), the ZnO nanowires grow along the sides of the hexagonal ZnO nanoplates. Typically, the lengths of the ZnO nanowires ranged from 0.5 to 3 μm and their mean diameter was 20 ± 5 nm. The length and diameter of the ZnO nanowires were easily controlled by the thermal oxidation conditions, mainly by oxidation time and temperature. Preliminary experiments for controlling the size and length of the ZnO nanowire showed that the mean diameters ranged from 10 ± 3 to 30 ± 7 nm as the oxidation temperature changed from 420 to 650 °C, while dramatic change was observed for the typical lengths of the nanowire; the typical length ranged from 20 to 30 nm at 420 °C, but from 0.5 to 5 μm at 650 °C. Details of the growth mechanism will be described elsewhere.¹³

Transmission electron microscopy (TEM) was used to investigate the microstructure of the ZnO nanowires. Figure 2(a) shows the representative morphology of ZnO nanowires grown from hexagonal ZnO nanoplates, although the edge of the ZnO nanoplate appears dark due to its thickness. The bright-field TEM image clearly shows that individual ZnO nanowires without a catalysis particle on the tip grew near the apexes of the hexagonal ZnO nanoplates, and their growth paralleled the sides of the hexagonal ZnO. The inset shows the selected-area electron diffraction pattern (SAED) of a hexagonal ZnO nanoplate. This indicates that the hexagonal ZnO nanoplates are *c*-axis orientated on the substrate, confirming their single-crystal wurtzite structure. Figures 2(b)–2(c) show HRTEM images of a single ZnO nanowire taken at points *1 and *2 in Fig. 2(a), respectively. The di-

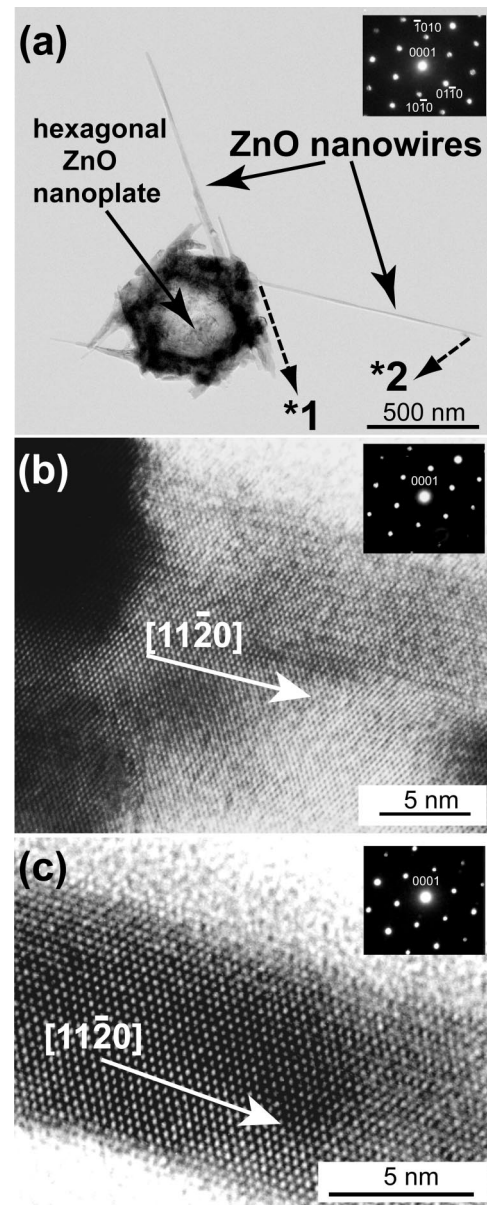


FIG. 2. (a) TEM image of a representative ZnO nanowire grown from a hexagonal ZnO nanoplate. The inset shows the SAED pattern obtained at the center of the ZnO nanoplate, indicating the *c*-axis alignment of the nanoplate. *1 and *2 in the figure denote the positions used for the HRTEM measurement. (b) HRTEM image and the corresponding SAED pattern (inset) of a single ZnO nanowire taken at position *1. (c) HRTEM image and the corresponding SAED pattern (inset) of a single ZnO nanowire taken at position *2.

ameter of the ZnO nanowire was 20 nm near the lower part of the ZnO stem and 7 nm near the tip. Figure 2(b) shows that the nanowire grew from the edge of the ZnO matrix (i.e., the apex of a hexagonal ZnO nanoplate) with the same lattice arrangement. The SAED pattern shown in the inset confirmed the single-crystal nature of the ZnO nanowire and the growth direction of $\langle 11\bar{2}0 \rangle$. Similarly, a HRTEM image taken near the tip also shows a clear lattice arrangement [see Fig. 2(c)]. These results indicate that the ZnO nanowires grown using our method are essentially defect-free single crystals. In addition, the SAED patterns shown in Figs. 2(b) and 2(c) confirm that the *c* axis of the ZnO nanowire is aligned with that of the hexagonal ZnO nanoplate and that the growth direction of individual ZnO nanowires is

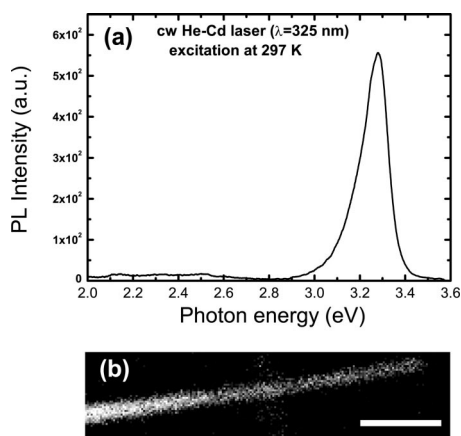


FIG. 3. (a) PL spectrum of ZnO nanowires measured at room temperature. There is dominant UV emission at 3.28 eV and very weak green emission from 2.0 to 2.6 eV. (b) A typical monochromatic CL image of a single ZnO nanowire with a diameter of 50 nm measured at RT for emission at 380 nm (~ 3.26 eV). The scale bar is 150 nm.

[11 $\bar{2}$ 0] direction, unlike ZnO nanowires grown using established methods, in which ZnO nanowires grew along the [0001] direction.^{1,3} In contrast to other methods, our ZnO nanowires are formed by the phase transformation of pre-deposited metallic Zn into ZnO via a thermal oxidation process with no metal catalysis. Since the melting point of Zn and Zn suboxide (ZnO_x , here $x < 1$) is approximately 419 °C,² liquid phase Zn or ZnO_x should first form at the early stage of heating. Therefore, the liquid phase plays an important role in the nucleation of ZnO nanowires, instead of an alloy liquid as occurs in catalytic VLS growth. The SEM image shown in Fig. 1(c) and the TEM image shown in Fig. 2(a) show that ZnO nanowires preferentially form at each apex of a hexagonal ZnO nanoplate. This demonstrates that the liquid phase of Zn or ZnO_x formed at the apexes acts as a nucleation site for the ZnO nanowires. Furthermore, one can readily suppose that vapor phase Zn exists under our experimental conditions (~ 500 °C) due to its high vapor pressure. During nanowire growth, the liquid phase promotes the fusion of Zn vapor and oxygen at the end of the ZnO nanowires, leading to the growth of single-crystal ZnO nanowires via further oxidation. We postulate that pre-deposited-Zn precursors aligned along the c -axis and the liquid phase formed near the apexes of the hexagonal ZnO nanoplates are crucial for the lateral growth and growth direction selectivity observed in this study.

To characterize the luminescence properties of the ZnO nanowires, we carried out PL measurement using a He–Cd laser (325 nm) as the excitation light and CL measurement at RT. Figure 3(a) shows the PL spectrum of the ZnO nanowires at RT. A dominant UV emission peak was seen at 3.28 eV with very weak green emissions from 2.0 to 2.6 eV. The UV emissions are attributed to free-exciton recombination at the near-band edge.^{14,15} In contrast to the UV emissions, the green emissions, brought about by intrinsic defects in the ZnO,¹⁶ are much weaker. Note that our nanowires show very weak green emissions, while the 1D ZnO nanostructures reported previously show very intense green emissions.^{2,17,18} We believe that the difference is due to the much lower process temperature in our method (500 vs ~ 1000 °C). At high

temperatures, the formation of intrinsic defects, such as oxygen vacancy or trap states, is enhanced, resulting in the considerable green emissions. In addition, as verified by the HR-TEM investigation, the individual ZnO nanowires were almost defect free and were single crystals. Therefore, the excellent optical properties demonstrated by PL and the defect-free single-crystal nature shown by HRTEM indicate that our ZnO nanowires are of high quality. Nevertheless, the PL data are insufficient to verify the high quality of the ZnO nanowires due to the contribution of the hexagonal ZnO nanoplates. To verify the excellent luminescent properties of the individual ZnO nanowire, we measured the CL of a single ZnO nanowire at RT. Figure 3(b) shows a typical monochromatic CL image of a single ZnO nanowire with a diameter of 50 nm measured at RT for emissions at 380 nm (~ 3.26 eV), which are attributed to free-exciton emissions.¹⁹ The green emissions around 520 nm (~ 2.38 eV) measured at the same position were almost negligible. Most ZnO nanowires tended to show very strong UV emissions at 3.26 eV, with negligible green emissions.

In conclusion, we fabricated single-crystal ZnO nanowires at a low temperature of 500 °C without using any metal catalysts via the simple thermal oxidation of metallic Zn precursors. SEM and HRTEM studies showed that the ZnO nanowires grew laterally with orientation selectivity along the sides of the hexagonal-shaped ZnO nanoplate. Furthermore, HRTEM revealed that the nanowires grew along the $\langle 11\bar{2}0 \rangle$ direction and were single crystals. PL and CL measurements at RT showed a strong UV emission peak with very weak green emissions, confirming that the individual ZnO nanowire was of excellent optical quality.

- ¹J.-J. Wu and S.-C. Liu, *Adv. Mater. (Weinheim, Ger.)* **14**, 215 (2002).
- ²B. D. Yao, Y. F. Chan, and N. Wang, *Appl. Phys. Lett.* **81**, 757 (2002).
- ³M. H. Huang, S. Mao, H. Feick, H. Yan, Y. Wu, H. Kind, E. Weber, R. Russo, and P. Yang, *Science* **292**, 1897 (2001).
- ⁴D. M. Bagnall, Y. F. Chen, Z. Zhu, T. Yao, S. Koyama, M. Y. Shen, and T. Goto, *Appl. Phys. Lett.* **70**, 2230 (1997).
- ⁵M. Ohtsu, K. Kobayashi, T. Kawazoe, S. Sangu, and T. Yatsui, *IEEE J. Sel. Top. Quantum Electron.* **8**, 839 (2002).
- ⁶T. Kawazoe, K. Kobayashi, J. Lim, Y. Narita, and M. Ohtsu, *Phys. Rev. Lett.* **88**, 067404 (2002).
- ⁷K. Kobayashi, S. Sangu, H. Ito, and M. Ohtsu, *Phys. Rev. A* **63**, 013806 (2001).
- ⁸S. Sangu, K. Kobayashi, A. Shojiguchi, T. Kawazoe, and M. Ohtsu, *J. Appl. Phys.* **93**, 2937 (2003).
- ⁹T. Yatsui, M. Kourogi, and M. Ohtsu, *Appl. Phys. Lett.* **79**, 4583 (2001).
- ¹⁰T. Kawazoe, K. Kobayashi, S. Sangu, and M. Ohtsu, *Appl. Phys. Lett.* **82**, 2957 (2003).
- ¹¹T. Yatsui, T. Kawazoe, M. Ueda, Y. Yamamoto, M. Kourogi, and M. Ohtsu, *Appl. Phys. Lett.* **81**, 3651 (2002).
- ¹²T. Yatsui, S. Takubo, J. Lim, W. Nomura, M. Kourogi, and M. Ohtsu, *Appl. Phys. Lett.* **83**, 1716 (2003).
- ¹³T.-W. Kim, T. Kawazoe, S. Yamazaki, and M. Ohtsu (unpublished).
- ¹⁴W. I. Park, G.-C. Yi, M. Y. Kim, and S. J. Pennycook, *Adv. Mater. (Weinheim, Ger.)* **14**, 1841 (2002).
- ¹⁵D. M. Bagnall, Y. F. Chen, Z. Zhu, T. Yao, M. Y. Shen, and T. Goto, *Appl. Phys. Lett.* **73**, 1038 (1998).
- ¹⁶K. Vanheusden, W. L. Warren, C. H. Seager, D. K. Tallant, J. A. Voigt, and B. E. Gnade, *J. Appl. Phys.* **79**, 7983 (1996).
- ¹⁷M. H. Huang, Y. Wu, H. Feick, N. Tran, E. Weber, and P. Yang, *Adv. Mater. (Weinheim, Ger.)* **13**, 113 (2001).
- ¹⁸Y. B. Li, Y. Bando, T. Sato, and K. Kurashima, *Appl. Phys. Lett.* **81**, 144 (2002).
- ¹⁹H. C. Ong, A. S. K. Li, and G. T. Du, *Appl. Phys. Lett.* **78**, 2667 (2001).

Logic and functional operations using a near-field optically coupled quantum-dot systemSuguru Sangu,^{1,2,*} Kiyoshi Kobayashi,¹ Akira Shojiguchi,¹ and Motoichi Ohtsu^{1,3}¹ERATO Localized Photon Project, Japan Science and Technology Agency, 687-1 Tsuruma, Machida, Tokyo 194-0004, Japan²Research and Development Center, Ricoh Company, Limited, 16-1 Shinei-cho, Tsuzuki-ku, Yokohama, Kanagawa 224-0035, Japan³Interdisciplinary Graduate School of Science and Engineering, Tokyo Institute of Technology, 4259 Nagatsuta-cho, Midori-ku, Yokohama, Kanagawa 226-8502, Japan

(Received 11 September 2003; revised manuscript received 18 November 2003; published 26 March 2004)

This paper investigates the exciton dynamics in a three-quantum-dot system coupled via an optical near field. The system consists of two identical quantum dots coupled coherently (the coherent operation part) and a third quantum dot with exciton sublevels (the output part). It provides certain characteristic functional operations depending on the initial excitation, as well as symmetry of the coupling strengths or the spatial arrangement. First, we analytically obtain the coupling strength between two quantum dots via an optical near field and give a numerical estimation for a CuCl quantum-cube system. Then, a resonance condition between the two parts is shown; this depends on the initial excitation in the coherent operation part. Using this condition, which can be realized by adjusting the energy level of a quantum dot in the output part, AND- and XOR-logic operations can be demonstrated in a symmetrically arranged quantum-dot system. We also discuss how the asymmetry of the system affects the energy transfer through certain coupled states in the coherent operation part that would be forbidden in a symmetrically arranged system. Although the asymmetry degrades the signal contrast for logic operations, it is expected to open up new techniques for novel device technologies where quantum entangled states are mediated in the operations.

DOI: 10.1103/PhysRevB.69.115334

PACS number(s): 73.21.La, 42.79.Ta, 71.35.Gg

I. INTRODUCTION

The miniaturization of the constituents of conventional photonic devices will reach a barrier in the near future as the device integration progresses. A $10^4 \times 10^4$ matrix switch will be required to realize the necessary high data transmission rates, which are expected to reach 40 TB/s by 2015,¹ and the size of each element will become less than 100 nm, far below the diffraction limit of light. In order to overcome this barrier, *nanophotonics*, in which local electromagnetic interactions between nanometric materials and an optical near field are utilized,² must be promising technology. Since an optical near field is not limited by the diffraction of light, this technology is expected to enable signal transfer and control in nanometric device elements.

The characteristic features of an optical near field can be utilized to achieve functional operations in nanophotonic devices, which are discussed in this paper. One such feature is the high spatial localization, which enables us to access individual nanometric elements in devices that are smaller than the diffraction limit of light. This feature is widely used in scanning near-field optical microscopy and spectroscopy³ for nanometric structures,⁴⁻⁶ single molecules,⁷ and biological specimens.⁸ On the basis of the spatial localization of an optical near field, an interesting phenomenon of dipole-forbidden energy transfer has been observed experimentally in a semiconductor quantum-dot system.⁹ Several theoretical studies of a few quantum-dot systems related to optical near-field techniques have been reported¹⁰ and the dipole-forbidden transition has been also expected^{11,12} by considering nonlocal susceptibility and a highly localized optical field. Another characteristic feature of an optical near field is the anomalous dispersion relation due to the coupling between the photon and the material excitation.¹³ This can

bring about collective dynamics inherent in optical near-field interactions in a system consisting of several nanometric materials.^{14,15}

In this paper, we propose functional devices which consist of several quantum dots coupled via an optical near field. For device operations, unidirectional signal transfer from input to output terminals must occur. We previously proposed using several quantum dots to form the fundamental blocks of a nanophotonic device, in which the discrete energy levels resonantly couple with each other via an optical near field. Intra-sublevel relaxation due to exciton-phonon coupling in a quantum dot guarantees unidirectional energy transfer. A nanophotonic switch has been studied both experimentally¹⁶ and theoretically^{17,18} using such a coupled quantum-dot system, and a switch was recently demonstrated using CuCl quantum cubes.¹⁶ In such nanophotonic devices using the resonant energy transfer, quantum coherence survives for a short period of time; afterwards, the excitation moves in a lower-energy state.¹⁹ The proposed coupled quantum-dot system consists of two characteristic parts similar to the nanophotonic switch mentioned above: one is the portion of the near-field optically coupled nanometric materials that maintains quantum coherence, which we call the *coherent operation part*; and the other determines certain final states with dissipation or decoherence, which we call the *output part*. This paper focuses on taking full advantage of these coherent and defined output parts to achieve functional operations. As a typical example, we consider the three-quantum-dot system illustrated in Fig. 1, where the excitons are carriers for the signal transfer. In the system, two identical quantum dots (QD-A and -B) are resonantly coupled with each other via an optical near field.

Various authors have investigated the coupling properties and dynamics in a pair of quantum dots. For example, the

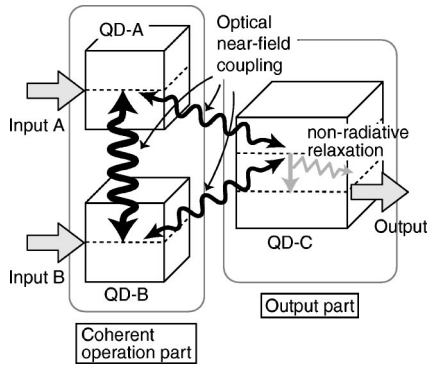


FIG. 1. Illustration of a three-quantum-dot system that consists of two identical two-level dots (QD-A and -B) and a three-level dot (QD-C). Since the coupling between QD-A and -B is stronger than that between QD-A and C (QD-B and -C), the system is divided into two parts: a coherent operation part with optical nutation, and an output part with a dissipation process.

energy shift due to exciton-exciton or Coulomb interactions between electrons and holes has been evaluated theoretically to process quantum information,^{20,21} and a controlled-NOT logic gate has been proposed using the energy shift.²² In these studies, excitons or qubits were controlled by two-color laser pulses of far-field light. As a similar subject to this paper, Quiroga and Johnson²³ theoretically discussed the dynamics in two- and three-quantum-dot systems and presented a way to prepare both quantum Bell and Greenberger-Horne-Zeilinger entangled states, by using far-field light, which allows only global excitation of two and three quantum dots with spatially symmetric arrangement. By contrast, we deal with coupled quantum-dot systems arranged symmetrically and asymmetrically, which are individually excited by the optical near field, and the intra-sublevel relaxation is also considered for the unidirectional energy transfer. Note that the excitation in each quantum dot can be prepared individually owing to the spatial localization of the optical near field. The exciton dynamics driven by the optical near field has been investigated in the case of a coupled two-quantum-dot system with a relaxation process.¹⁷ The energy transfer between two quantum dots is expressed as a Förster process,²⁴ and the nutation of excitation occurs in the strongly coupled or resonant energy levels, corresponding to the coherent operation part in our system. For the short period before relaxation, certain coherently coupled states appear in the coherent operation part, depending on the initial excitation. In order to prepare the initial excitation, the shorter excitation time in the individual quantum dot than the energy-transfer time between two identical quantum dots is necessary, where the excitation time is inversely proportional to the optical near-field intensity. The energy-transfer time or coupling strength via an optical near field can be controlled by adjusting interdot spacings. The population in the coherently coupled states can be transferred to the third quantum dot (QD-C) if the energy level of QD-C is adjusted to couple resonantly with the entangled states in the coherent operation part. If this happens, QD-C operates as the output part, which involves an intra-sublevel relaxation process due to the

exciton-phonon interaction. In this manner, unidirectional energy or signal transfer is satisfied.

This paper examines the exciton dynamics in this system illustrated in Fig. 1 using density-matrix formalism. The dynamics of the system can be determined analytically when three quantum dots are arranged symmetrically. AND- and XOR-logic operations can also be demonstrated by adjusting the energy configuration in this three-quantum-dot system. The asymmetry due to the coupling strength of the quantum-dot pairs via an optical near field or quantum-dot arrangement also plays an important role in the exciton dynamics. We find that an asymmetric arrangement permits energy transfer from the coherent operation part to the output part via a certain quantum entangled state, the so-called “dark state”²⁵ in a symmetric system. This characteristic feature due to the spatial arrangement may be useful for detection of quantum entangled state. Here, note that these logic and functional operations are in the irreversible process, although quantum entangled states are partially mediated to sort out the initial excitations. This resembles quantum information processing, however, we do not need long coherence time as the quantum computation requires. Regarding quantum information processing with dissipation or decoherence, there are several reports which are discussed such as tolerance and decoherence-free operations.^{26,27}

This paper is organized as follows. Section II derives the optical near-field coupling between two energy levels in two quantum dots and shows the existence of dipole-forbidden energy transfer mediated by an optical near field. The coupling strength is also estimated numerically and is used to discuss the exciton dynamics in a three-quantum-dot system. Section III is devoted to the formulation of the exciton dynamics in the relevant system using density-matrix formalism. Here, we present the “selective” energy transfer from the coherent operation part to the output part. Based on this feature, we show that logic operations can be realized in a symmetrically arranged quantum-dot system. Section IV discusses the effects of the asymmetry using the numerical exciton dynamics results. Finally, concluding remarks are given in Sec. V.

II. OPTICAL NEAR-FIELD COUPLING

In this section, we formulate an optical near-field coupling between two quantum dots using the multipolar QED Hamiltonian^{28,29} in the dipole approximation, $\boldsymbol{\mu} \cdot \mathbf{D}$, where $\boldsymbol{\mu}$ and \mathbf{D} represent the transition dipole moment and electric displacement field, respectively. There are several advantages to use the multipolar QED Hamiltonian instead of the minimal coupling Hamiltonian $\mathbf{p} \cdot \mathbf{A}$, \mathbf{p} being the electronic momentum and \mathbf{A} the vector potential; first of all, the multipolar QED Hamiltonian does not contain any explicit intermolecular or inter-quantum-dot Coulomb interactions in the interaction Hamiltonian and entire contribution to the fully retarded result originates from exchange of transverse photons, while in the minimal coupling, the intermolecular interactions arise both from exchange of transverse photons, which include static components, and from instantaneous intermolecular electrostatic interactions.³⁰ Second, it clarifies

physical interpretation of the dipole-forbidden transition via the optical near field as discussed below. Basic ideas in the formulation are to express internal electronic structures in a quantum dot regarding them as collection of local dipoles and to investigate the interactions between nanometric materials and spatially varied optical near fields. We can also depict multipoles for a single quantum dot by using an effective-mass approximation. Such theoretical approach has been already published³¹ where the enhancement of electric quadrupole coupling was pointed out by assuming steep variation of electric field due to the optical near field. This phenomenon is equivalent to our result of the dipole-forbidden transition, but the field variation in our theoretical formulation is caused by the coupling between the local dipoles in the neighboring quantum-dot pair [see Fig. 2(b)].

In the following sections, we present the interaction Hamiltonian in second-quantized form in terms of electron basis functions satisfying the quantum-dot boundary conditions, as well as transition dipole moments of excitons, and derive an optical near-field coupling on the basis of the projection operator method we previously proposed.

A. Interaction Hamiltonian

According to the dipole coupling in the multipolar Hamiltonian, the interaction between photons and nanometric materials can be written as²⁹

$$\hat{H}_{\text{int}} = - \int \psi^\dagger(\mathbf{r}) \boldsymbol{\mu}(\mathbf{r}) \psi(\mathbf{r}) \cdot \hat{\mathbf{D}}(\mathbf{r}) d\mathbf{r}, \quad (1)$$

where $\psi^\dagger(\mathbf{r})$ and $\psi(\mathbf{r})$ denote field operators for electron creation and annihilation, respectively, and the dipole moment and the second-quantized electric displacement vector at position \mathbf{r} are expressed as $\boldsymbol{\mu}(\mathbf{r})$ and $\hat{\mathbf{D}}(\mathbf{r})$, respectively. In a quantum dot, the electron field operators should be expanded in terms of basis functions $\phi_{\nu n}(\mathbf{r})$ that satisfy the electron boundary conditions in a quantum dot, which is analogous to those in bulk materials where the Bloch functions satisfying periodic boundary condition are used. The field operators are given by

$$\psi(\mathbf{r}) = \sum_{\nu=c,v} \sum_{\mathbf{n}} \hat{c}_{\nu n} \phi_{\nu n}(\mathbf{r}), \quad \psi^\dagger(\mathbf{r}) = \sum_{\nu=c,v} \sum_{\mathbf{n}} \hat{c}_{\nu n}^\dagger \phi_{\nu n}^*(\mathbf{r}), \quad (2)$$

where $\hat{c}_{\nu n}^\dagger$ and $\hat{c}_{\nu n}$ represent the creation and annihilation operators for the electrons specified by (ν, \mathbf{n}) , respectively, and the indices $\nu=c, v$ denote the conduction and valence bands. The discrete energy levels in the quantum dot are labeled \mathbf{n} . The basis functions satisfy the following completeness condition, as well as orthonormalization:

$$\sum_{\nu=c,v} \sum_{\mathbf{n}} \phi_{\nu n}^*(\mathbf{r}) \phi_{\nu n}(\mathbf{r}') = \delta(\mathbf{r}-\mathbf{r}'). \quad (3)$$

Simultaneously, we express the electric displacement vector $\hat{\mathbf{D}}(\mathbf{r})$ using exciton-polariton creation and annihilation operators $(\hat{\xi}_k^\dagger, \hat{\xi}_k)$, where branch suffix of the exciton-polariton is suppressed by taking only an upper branch. We consider

exciton-polaritons because a nanometric system in a near-field optical environment is always surrounded by macroscopic materials, such as the substrate, matrix, fiber probe, and so on. Previously,^{13,32} we proposed an effective interaction for such a nanometric system mediated by exciton-polaritons that are expressed in mixed states between photons and macroscopic material excitations instead of free photons. We showed that such a treatment provides a good description of the characteristics of an optical near field.³³ Using this, the electric displacement vector $\hat{\mathbf{D}}(\mathbf{r})$ in Eq. (1) can be written as³⁴

$$\hat{\mathbf{D}}(\mathbf{r}) = i \sqrt{\frac{2\pi}{V}} \sum_{\mathbf{k}} \sum_{\lambda=1}^2 \mathbf{e}_\lambda(\mathbf{k}) f(k) (\hat{\xi}_k e^{i\mathbf{k}\cdot\mathbf{r}} - \hat{\xi}_k^\dagger e^{-i\mathbf{k}\cdot\mathbf{r}}), \quad (4)$$

with

$$f(k) = \frac{\hbar c k}{\sqrt{E(k)}} \sqrt{\frac{E^2(k) - E_m^2}{2E^2(k) - E_m^2 - \hbar^2 c^2 k^2}}, \quad (5)$$

where \hbar , V , $\mathbf{e}_\lambda(\mathbf{k})$, and \mathbf{k} are the Dirac constant, the quantization volume, the unit polarization vector, and the wave vector of the exciton-polaritons, respectively. Here we assume $\mathbf{e}_\lambda(\mathbf{k})$ as real. The speed of light in a vacuum is c , and the exciton-polariton energy with a wave vector \mathbf{k} and the macroscopic material excitation energy are $E(k)$ and E_m , respectively. Substituting Eqs. (2) and (4) into Eq. (1) gives the interaction Hamiltonian in the second-quantized representation as

$$\hat{H}_{\text{int}} = \sum_{\nu\nu'\mathbf{n}'\mathbf{k}\lambda} (\hat{c}_{\nu n}^\dagger \hat{c}_{\nu'\mathbf{n}'} \hat{\xi}_k g_{\nu\nu'\mathbf{n}'\mathbf{k}\lambda} - \hat{c}_{\nu n}^\dagger \hat{c}_{\nu'\mathbf{n}'} \hat{\xi}_k^\dagger g_{\nu\nu'\mathbf{n}'-k\lambda}), \quad (6)$$

with

$$g_{\nu\nu'\mathbf{n}'\mathbf{k}\lambda} = -i \sqrt{\frac{2\pi}{V}} f(k) \int \phi_{\nu n}^*(\mathbf{r}) \times [\boldsymbol{\mu}(\mathbf{r}) \cdot \mathbf{e}_\lambda(\mathbf{k})] e^{i\mathbf{k}\cdot\mathbf{r}} \phi_{\nu'\mathbf{n}'}(\mathbf{r}) d\mathbf{r}. \quad (7)$$

B. Transition moments for exciton states

In order to describe the creation and annihilation of excitons in a quantum dot, it is convenient to use the Wannier representation in which electrons are localized in an atomic site \mathbf{R} . Then, the electron field operators can be expanded using the Wannier functions $w_{\nu\mathbf{R}}(\mathbf{r})$ instead of $\phi_{\nu n}(\mathbf{r})$,

$$\psi(\mathbf{r}) = \sum_{\nu=c,v} \sum_{\mathbf{R}} \hat{c}_{\nu\mathbf{R}} w_{\nu\mathbf{R}}(\mathbf{r}), \quad \psi^\dagger(\mathbf{r}) = \sum_{\nu=c,v} \sum_{\mathbf{R}} \hat{c}_{\nu\mathbf{R}}^\dagger w_{\nu\mathbf{R}}^*(\mathbf{r}), \quad (8)$$

where $\hat{c}_{\nu\mathbf{R}}^\dagger$ and $\hat{c}_{\nu\mathbf{R}}$ denote the creation and annihilation operators of electrons at site \mathbf{R} in the energy band ν . These operators in the Wannier representation are written in terms of $\hat{c}_{\nu n}$ in Eq. (2) as follows:

$$\begin{aligned}\hat{c}_{\nu\mathbf{R}} &= \sum_{\nu'=c,v} \sum_{\mathbf{n}} \hat{c}_{\nu'n} \int w_{\nu\mathbf{R}}^*(\mathbf{r}) \phi_{\nu'n}(\mathbf{r}) d\mathbf{r}, \\ \hat{c}_{\nu\mathbf{R}}^\dagger &= \sum_{\nu'=c,v} \sum_{\mathbf{n}} \hat{c}_{\nu'n}^\dagger \int w_{\nu\mathbf{R}}(\mathbf{r}) \phi_{\nu'n}^*(\mathbf{r}) d\mathbf{r}.\end{aligned}\quad (9)$$

When we assume excitons in the weak-confinement regime, i.e., an exciton Bohr radius to be smaller than the quantum-dot size, the exciton states in a quantum dot specified by the quantum number \mathbf{m} and μ can be described by superposition of the excitons in the Wannier representation as³⁵

$$\begin{aligned}|\Phi_{m\mu}\rangle &= \sum_{\mathbf{R},\mathbf{R}'} F_m(\mathbf{R}_{\text{c.m.}}) \varphi_\mu(\boldsymbol{\beta}) \hat{c}_{c\mathbf{R}'}^\dagger \hat{c}_{v\mathbf{R}} |\Phi_g\rangle, \\ &= \sum_{\mathbf{R},\mathbf{R}'} F_m(\mathbf{R}_{\text{c.m.}}) \varphi_\mu(\boldsymbol{\beta}) \sum_{n,n'} h_{\mathbf{R}n\mathbf{R}'n'} \hat{c}_{cn}^\dagger \hat{c}_{vn'} |\Phi_g\rangle,\end{aligned}\quad (10)$$

where $F_m(\mathbf{R}_{\text{c.m.}})$ and $\varphi_\mu(\boldsymbol{\beta})$ denote the envelope functions for the center of mass and relative motions of the excitons, respectively. These are $\mathbf{R}_{\text{c.m.}} = (m_e \mathbf{R}' + m_h \mathbf{R}) / (m_e + m_h)$ and $\boldsymbol{\beta} = \mathbf{R}' - \mathbf{R}$, where m_e and m_h are the effective masses of the electrons and holes. The overlap integrals $h_{\mathbf{R}n\mathbf{R}'n'}$ are defined as

$$h_{\mathbf{R}n\mathbf{R}'n'} = \int \int w_{v\mathbf{R}}^*(\mathbf{r}_2) w_{c\mathbf{R}'}(\mathbf{r}_1) \phi_{cn}^*(\mathbf{r}_1) \phi_{vn'}(\mathbf{r}_2) d\mathbf{r}_1 d\mathbf{r}_2.\quad (11)$$

The sum of ν' in Eq. (9) is determined automatically as \hat{c}_{cn}^\dagger and $\hat{c}_{vn'}$ because the valence band is fully occupied in the initial ground state $|\Phi_g\rangle$. Using Eqs. (6) and (10), the transition moment from the exciton state to the ground state is obtained as

$$\begin{aligned}\langle \Phi_g | \hat{H}_{\text{int}} | \Phi_{m\mu} \rangle &= \sum_{n_1, n_2} \sum_{\mathbf{R}, \mathbf{R}'} F_m(\mathbf{R}_{\text{c.m.}}) \varphi_\mu(\boldsymbol{\beta}) \\ &\quad \times \sum_{\mathbf{k}} \sum_{\lambda=1}^2 (\hat{\xi}_{\mathbf{k}} g_{vn_1cn_2k\lambda} - \hat{\xi}_{\mathbf{k}}^\dagger g_{vn_1cn_2-k\lambda}) \\ &\quad \times h_{\mathbf{R}n_2\mathbf{R}'n_1},\end{aligned}\quad (12)$$

where we use the following relation:

$$\langle \Phi_g | \hat{c}_{vn_1}^\dagger \hat{c}_{cn_2} \hat{c}_{cn_3}^\dagger \hat{c}_{vn_4} | \Phi_g \rangle = \delta_{n_1n_4} \delta_{n_2n_3}.\quad (13)$$

In addition, with the help of the completeness and orthonormalization of $\phi_{\nu\mathbf{m}}(\mathbf{r})$ [see Eq. (3)], we can simplify the product of g and h as

$$\begin{aligned}\sum_{n_1, n_2} g_{vn_1cn_2k\lambda} h_{\mathbf{R}n_2\mathbf{R}'n_1} \\ = -i \sqrt{\frac{2\pi}{V}} f(k) \int w_{v\mathbf{R}}^*(\mathbf{r}) \boldsymbol{\mu}(\mathbf{r}) w_{c\mathbf{R}'}(\mathbf{r}) \cdot \mathbf{e}_\lambda(\mathbf{k}) e^{i\mathbf{k}\cdot\mathbf{r}} d\mathbf{r} \\ \approx -i \sqrt{\frac{2\pi}{V}} f(k) [\boldsymbol{\mu}_{cv} \cdot \mathbf{e}_\lambda(\mathbf{k})] e^{i\mathbf{k}\cdot\mathbf{R}} \delta_{\mathbf{R}\mathbf{R}'},\end{aligned}\quad (14)$$

where the transformation of the spatial integral in the first line of Eq. (14) into the sum of the unit cells and the spatial localization of the Wannier functions provides $\delta_{\mathbf{R}\mathbf{R}'}$ in the second line. The transition dipole moment for each unit cell is defined as

$$\boldsymbol{\mu}_{cv} = \int_{\text{UC}} w_{v\mathbf{R}}^*(\mathbf{r}) \boldsymbol{\mu}(\mathbf{r}) w_{c\mathbf{R}}(\mathbf{r}) d\mathbf{r}.\quad (15)$$

We assume that the transition dipole moment is the same as that of the bulk material, independent of the site \mathbf{R} , and that the electric displacement vector is uniform at each site. Finally, Eq. (12) is reduced to

$$\begin{aligned}\langle \Phi_g | \hat{H}_{\text{int}} | \Phi_{m\mu} \rangle &= -i \sqrt{\frac{2\pi}{V}} \sum_{\mathbf{R}} \sum_{\mathbf{k}} \sum_{\lambda=1}^2 f(k) \\ &\quad \times [\boldsymbol{\mu}_{cv} \cdot \mathbf{e}_\lambda(\mathbf{k})] F_m(\mathbf{R}) \varphi_\mu(0) \\ &\quad \times (\hat{\xi}_{\mathbf{k}} e^{i\mathbf{k}\cdot\mathbf{R}} - \hat{\xi}_{\mathbf{k}}^\dagger e^{-i\mathbf{k}\cdot\mathbf{R}}).\end{aligned}\quad (16)$$

Here, we note that the exciton-polariton field expanded by the plane wave with the wave vector \mathbf{k} depends on the site \mathbf{R} in the quantum dot because we do not apply the long-wave approximation that is usually used for far-field light.

C. Optical near-field coupling

To derive the coupling strength between two quantum dots due to the optical near-field interaction, we use the projection operator method, which was reported in detail in our previous paper.³² In this method, the eigenstates of a total optical near-field system are divided into two subspaces: a relevant P space constructed from the two energy levels for each quantum dot and the exciton-polariton vacuum state, and an irrelevant Q space that is complementary to the P space and includes exciton-polariton states. Using this formulation, the coupling strength is given to the lowest order as

$$\begin{aligned}\hbar U &= \sum_m \langle \Psi_f^P | \hat{H}_{\text{int}} | m^Q \rangle \langle m^Q | \hat{H}_{\text{int}} | \Psi_i^P \rangle \\ &\quad \times \left(\frac{1}{E_{0i}^P - E_{0m}^Q} + \frac{1}{E_{0f}^P - E_{0m}^Q} \right),\end{aligned}\quad (17)$$

where E_{0i}^P , E_{0f}^P , and E_{0m}^Q represent the eigenenergies of the unperturbed Hamiltonian for the initial and final states in P space and the intermediate state in Q space, respectively. Since we focus on the interdot interaction of Eq. (17), we set the initial and final states in P space to $|\Psi_i^P\rangle$

$=|\Phi_{m\mu}^A\rangle|\Phi_g^B\rangle|0\rangle$ and $|\Psi_f^P\rangle=|\Phi_g^A\rangle|\Phi_{m'\mu'}^B\rangle|0\rangle$. Then, the intermediate states in Q space that involve exciton-polaritons with the wave vector \mathbf{k} are utilized for the energy transfer from one quantum dot to the other, according to $|m^Q\rangle=|\Phi_g^A\rangle|\Phi_g^B\rangle|\mathbf{k}\rangle$ and $|\Phi_{m\mu}^A\rangle|\Phi_{m'\mu'}^B\rangle|\mathbf{k}\rangle$. The superscripts A and B are used to label two quantum dots. Substituting Eq. (16), one can rewrite Eq. (17) as

$$\hbar U = \varphi_{\mu}^A(0)\varphi_{\mu'}^{B*}(0) \int \int F_m^A(\mathbf{R}_A)F_{m'}^{B*}(\mathbf{R}_B)[Y_A(\mathbf{R}_A-\mathbf{R}_B) + Y_B(\mathbf{R}_A-\mathbf{R}_B)]d\mathbf{R}_Ad\mathbf{R}_B, \quad (18)$$

where the sum of \mathbf{R}_α ($\alpha=A,B$) in Eq. (16) is transformed to the integral form. The functions $Y_\alpha(\mathbf{R}_{AB})$, which connect the spatially isolated two envelope functions $F_m^A(\mathbf{R}_A)$ and $F_{m'}^B(\mathbf{R}_B)$, are defined as

$$Y_\alpha(\mathbf{R}_{AB}) = -\frac{1}{4\pi^2} \sum_{\lambda=1}^2 \int [\boldsymbol{\mu}_{cv}^A \cdot \hat{\mathbf{e}}_\lambda(\mathbf{k})][\boldsymbol{\mu}_{cv}^B \cdot \hat{\mathbf{e}}_\lambda(\mathbf{k})]f^2(k) \times \left(\frac{e^{i\mathbf{k}\cdot\mathbf{R}_{AB}}}{E(k)+E_\alpha} + \frac{e^{-i\mathbf{k}\cdot\mathbf{R}_{AB}}}{E(k)-E_\alpha} \right) d\mathbf{k}, \quad (19)$$

where $\mathbf{R}_{AB}=\mathbf{R}_A-\mathbf{R}_B$ is used. In order to obtain an explicit functional form of $Y_\alpha(\mathbf{R}_{AB})$, we apply the effective-mass approximation to the exciton-polaritons,

$$E(k) = \frac{\hbar^2 k^2}{2m_p} + E_m, \quad (20)$$

where m_p is the exciton-polariton effective mass. Using this approximation, Eq. (19) can be transformed into

$$Y_\alpha(\mathbf{R}_{AB}) = (\boldsymbol{\mu}_{cv}^A \cdot \boldsymbol{\mu}_{cv}^B) \left[W_{\alpha+} e^{-\Delta_{\alpha+} R_{AB}} \left(\frac{\Delta_{\alpha+}^2}{R_{AB}} + \frac{\Delta_{\alpha+}}{R_{AB}^2} + \frac{1}{R_{AB}^3} \right) - W_{\alpha-} e^{-\Delta_{\alpha-} R_{AB}} \left(\frac{\Delta_{\alpha-}^2}{R_{AB}} + \frac{\Delta_{\alpha-}}{R_{AB}^2} + \frac{1}{R_{AB}^3} \right) \right] - (\boldsymbol{\mu}_{cv}^A \cdot \hat{\mathbf{R}}_{AB})(\boldsymbol{\mu}_{cv}^B \cdot \hat{\mathbf{R}}_{AB}) \left[W_{\alpha+} e^{-\Delta_{\alpha+} R_{AB}} \times \left(\frac{\Delta_{\alpha+}^2}{R_{AB}} + \frac{3\Delta_{\alpha+}}{R_{AB}^2} + \frac{3}{R_{AB}^3} \right) - W_{\alpha-} e^{-\Delta_{\alpha-} R_{AB}} \left(\frac{\Delta_{\alpha-}^2}{R_{AB}} + \frac{3\Delta_{\alpha-}}{R_{AB}^2} + \frac{3}{R_{AB}^3} \right) \right], \quad (21)$$

where R_{AB} and $\hat{\mathbf{R}}_{AB}$ are the absolute value $|\mathbf{R}_{AB}|$ and the unit vector defined by \mathbf{R}_{AB}/R_{AB} , respectively. The weight coefficients $W_{\alpha\pm}$ and decay constants $\Delta_{\alpha\pm}$ are given by

$$W_{\alpha\pm} = \frac{E_p}{E_\alpha} \frac{(E_m - E_\alpha)(E_m + E_\alpha)}{(E_m - E_p \mp E_\alpha)(E_m \pm E_\alpha) - E_m^2/2}, \quad \Delta_{\alpha\pm} = \frac{1}{\hbar c} \sqrt{E_p(E_m \pm E_\alpha)}, \quad (22)$$

where the exciton-polariton effective mass is rewritten as $E_p = m_p c^2$. Since the dipole moments $\boldsymbol{\mu}_{cv}^A$ and $\boldsymbol{\mu}_{cv}^B$ are not determined as fixed values, we assume that they are parallel, and take a rotational average of Eq. (21). Therefore, $\langle (\boldsymbol{\mu}_{cv}^A \cdot \hat{\mathbf{R}}_{AB})(\boldsymbol{\mu}_{cv}^B \cdot \hat{\mathbf{R}}_{AB}) \rangle = \mu_{cv}^A \mu_{cv}^B / 3$ with $\mu_{cv}^\alpha = |\boldsymbol{\mu}_{cv}^\alpha|$, and we obtain the final form of the function $Y_\alpha(\mathbf{R}_{AB})$ as

$$Y_\alpha(\mathbf{R}_{AB}) = \frac{2\mu_{cv}^A \mu_{cv}^B}{3R_{AB}} (W_{\alpha+} \Delta_{\alpha+}^2 e^{-\Delta_{\alpha+} R_{AB}} - W_{\alpha-} \Delta_{\alpha-}^2 e^{-\Delta_{\alpha-} R_{AB}}). \quad (23)$$

Equation (23) is the sum of two Yukawa functions with a short and long interaction range (heavy and light effective mass) given by the second equation in Eq. (22). We can estimate the coupling strength between two quantum dots from the analytic form of the interaction potential given by Eqs. (18) and (23), and we can show the existence of dipole-forbidden energy transfer driven by the optical near-field coupling, as discussed in the following section.

D. Numerical results

In this section, we give typical values of the coupling strength of $\hbar U$ in Eq. (18) using an example of CuCl quantum cubes embedded in a NaCl matrix. Due to the effect of size confinement, the center-of-mass motion and relative motion for an exciton in a CuCl quantum cube are³⁵

$$F_m^\alpha(\mathbf{R}_\alpha) = \left(\frac{2}{L_\alpha} \right)^{3/2} \sin\left(\frac{\pi m_x x_\alpha}{L_\alpha} \right) \sin\left(\frac{\pi m_y y_\alpha}{L_\alpha} \right) \sin\left(\frac{\pi m_z z_\alpha}{L_\alpha} \right), \quad \varphi_{1s}(r) = \frac{1}{\sqrt{\pi a^3}} e^{-r/a}, \quad (24)$$

respectively, where the atomic site and the quantum number are represented by $\mathbf{R}_\alpha = (x_\alpha, y_\alpha, z_\alpha)$ with $\alpha=A,B$ and $\mathbf{m} = (m_x, m_y, m_z)$ with $m_x, m_y, m_z = 1, 2, 3, \dots$. The variables L_α and a denote a width of the quantum cube and the Bohr radius of the exciton, respectively. Here, we assume relative motion in the $1s$ state. The coupling strength is obtained numerically by substituting Eqs. (23) and (24) into Eq. (18). In Fig. 2(a), the calculation results are plotted as a function of the intercube distance. The curve with square dots represents the coupling between the dipole-active exciton levels, i.e., $\mathbf{m}=\mathbf{m}'=(1,1,1)$, in two quantum cubes. When we set the intercube distance and a width of the quantum cubes as $d=5$ nm and $L_A=L_B=10$ nm, respectively, which corresponds to the resonant coupling between QD-A and -B in Fig. 1, the coupling strength is about $89 \mu\text{eV}$ ($U^{-1}=7.4$ ps). The curve with circular dots is the result for $\mathbf{m}=(1,1,1)$ and $\mathbf{m}'=(2,1,1)$. For conventional far-field light, $\mathbf{m}'=(2,1,1)$ is the dipole-forbidden exciton level, and it follows that the optical near-field interaction inherently involves such a transition because of the finite interaction range. Figure 2(b) is a schematic illustration of the dipole-forbidden transition, in which the optical near field enables to excite the local dipoles at the near side in a quantum dot with dipole-forbidden level for far-field light. This coupling

strength is estimated from Fig. 2(a) as $\hbar U = 37 \mu\text{eV}$ ($U^{-1} = 17.7$ ps) for $d = 5$ nm, and $\hbar U = 14 \mu\text{eV}$ ($U^{-1} = 46.9$ ps) for $d = 15$ nm, where the cube sizes are set as $L_A = 10$ nm and $L_B = 14.1$ nm to realize resonant energy transfer between the two quantum cubes. The coupling strength ($m \neq m'$) is approximately half that of $m = m'$ at the same intercube distance, but it is strong enough for our proposed nanophotonic devices. For functional operations, the difference between the coupling strengths can be used to divide the system into two parts, i.e., the coherent operation and the output parts. Therefore, in the following discussion of the functional operations, we use $d = 5$ nm as the values of the coupling strength between QD-A and B, and $d = 15$ nm for that between QD-A and C or QD-B and C.

III. EXCITON DYNAMICS AND THEIR APPLICATION TO FUNCTIONAL OPERATIONS

A. Symmetric and antisymmetric states

In this section, we discuss the exciton dynamics in a symmetrically arranged three-quantum-dot system, as shown in Fig. 1. The asymmetric effects on the dynamics are considered in the subsequent section. From the symmetry of the system, the following bases are suitable for describing the dynamics using the smallest number of density-matrix elements³⁶:

$$\begin{aligned} |S_1\rangle &= \frac{1}{\sqrt{2}}(|A^*BC_1C_2\rangle + |AB^*C_1C_2\rangle), \\ |A_1\rangle &= \frac{1}{\sqrt{2}}(|A^*BC_1C_2\rangle - |AB^*C_1C_2\rangle), \\ |P'_1\rangle &= |ABC_1C_2^*\rangle, \quad |P_1\rangle = |ABC_1^*C_2\rangle. \end{aligned} \quad (25)$$

One-exciton state describes the condition whereby an exciton exists in either one of the three quantum dots. The ground and exciton states in each quantum dot, written using $|\Phi_g^\alpha\rangle$ and $|\Phi_{m(1,s)}^\alpha\rangle$ in the preceding section, are represented here simply as A , B , C_i ($i = 1, 2$), and A^* , B^* , C_i^* , respectively. Similarly, a *two-exciton state* indicates that two excitons stay in the system. The suitable bases for the two-exciton states without occupation of the lower energy level in QD-C are expressed as

$$\begin{aligned} |S'_2\rangle &= \frac{1}{\sqrt{2}}(|A^*BC_1C_2^*\rangle + |AB^*C_1C_2^*\rangle), \\ |A'_2\rangle &= \frac{1}{\sqrt{2}}(|A^*BC_1C_2^*\rangle - |AB^*C_1C_2^*\rangle), \\ |P'_2\rangle &= |A^*B^*C_1C_2\rangle, \end{aligned} \quad (26)$$

and those with occupation of the lower energy level are expressed as

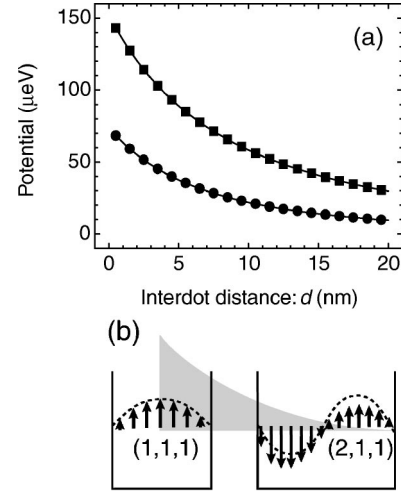


FIG. 2. (a) Optical near-field interaction potential for pairs of CuCl quantum cubes embedded in a NaCl matrix. The curves shown with square and circular dots correspond to quantum numbers for the exciton center-of-mass motion $m = m' = (1, 1, 1)$, and $m = (1, 1, 1)$ and $m' = (2, 1, 1)$, respectively. The energy level $m' = (2, 1, 1)$ is a dipole-forbidden state for conventional far-field light. The parameters are set to $E_A = E_B = 3.22$ eV, $E_m = 6.9$ eV, $\mu_{cv}^A = \mu_{cv}^B = 1.73 \times 10^{-2}$ (eV nm^3)^{1/2}, $L_A = 10$ nm, $L_B = 10$ and 14.1 nm [$m' = (1, 1, 1)$ and $(2, 1, 1)$], and $a = 0.67$ nm. (b) Schematic illustration of a transition between dipole-allowed and dipole-forbidden states via the optical near-field coupling. Steeply gradient optical near field enables to excite near side local dipoles in a quantum dot with dipole-forbidden $(2, 1, 1)$ level.

$$\begin{aligned} |S_2\rangle &= \frac{1}{\sqrt{2}}(|A^*BC_1^*C_2\rangle + |AB^*C_1^*C_2\rangle), \\ |A_2\rangle &= \frac{1}{\sqrt{2}}(|A^*BC_1^*C_2\rangle - |AB^*C_1^*C_2\rangle), \end{aligned}$$

$$|P_2\rangle = |ABC_1^*C_2^*\rangle, \quad (27)$$

where $|S\rangle$ and $|A\rangle$ represent symmetric and antisymmetric states in the coherent operation part, respectively, and the subscripts 1 and 2 on the left-hand sides in Eqs. (25), (26), and (27) denote the one- and two-exciton states, respectively. In the following, we use these bases to evaluate the exciton dynamics in the three-quantum-dot system.

B. Equations of motion and coupling properties

Based on the results of optical near-field coupling in Sec. II, a model Hamiltonian for the system \hat{H} is given by

$$\begin{aligned} \hat{H} &= \hat{H}_0 + \hat{H}_{\text{int}}, \\ \hat{H}_0 &= \hbar\Omega\hat{A}^\dagger\hat{A} + \hbar\Omega\hat{B}^\dagger\hat{B} + \hbar\sum_{i=1}^2\Omega_{C_i}\hat{C}_i^\dagger\hat{C}_i, \end{aligned}$$

$$\hat{H}_{\text{int}} = \hbar U(\hat{A}^\dagger\hat{B} + \hat{B}^\dagger\hat{A}) + \hbar U'(\hat{B}^\dagger\hat{C}_2 + \hat{C}_2^\dagger\hat{B} + \hat{C}_2^\dagger\hat{A} + \hat{A}^\dagger\hat{C}_2), \quad (28)$$

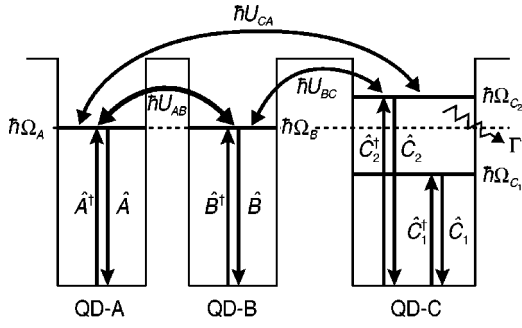


FIG. 3. Schematic drawing of exciton creation and annihilation operators and the energy-transfer process in a three-quantum-dot system. The optical near-field couplings for the quantum-dot pairs are represented by U_{AB} for QD-A and -B, U_{BC} for QD-B and -C, and U_{CA} for QD-C and -A. The nonradiative relaxation constant due to exciton-phonon coupling is denoted by Γ .

where the definitions of the creation and annihilation operators, $(\hat{A}^\dagger, \hat{A})$, $(\hat{B}^\dagger, \hat{B})$, and $(\hat{C}_i^\dagger, \hat{C}_i)$, are shown schematically in Fig. 3. The eigenfrequencies for QD-A and -B are set to $\Omega_A = \Omega_B \equiv \Omega$, and the optical near-field coupling for the symmetric system is denoted as $U_{AB} \equiv U$ and $U_{BC} = U_{CA} \equiv U'$. The equation of motion for the density operator of the quantum-dot system, $\hat{\rho}(t)$, is expressed using the Born-Markov approximation³⁷ as

$$\begin{aligned} \dot{\hat{\rho}}(t) = & -\frac{i}{\hbar} [\hat{H}_0 + \hat{H}_{\text{int}}, \hat{\rho}(t)] + \frac{\Gamma}{2} \{2\hat{C}_1^\dagger \hat{C}_2 \hat{\rho}(t) \hat{C}_2^\dagger \hat{C}_1 \\ & - \hat{C}_2^\dagger \hat{C}_1 \hat{C}_1^\dagger \hat{C}_2 \hat{\rho}(t) - \hat{\rho}(t) \hat{C}_2^\dagger \hat{C}_1 \hat{C}_1^\dagger \hat{C}_2\}, \end{aligned} \quad (29)$$

where the nonradiative relaxation constant due to exciton-phonon coupling is denoted as Γ . The radiative relaxation due to exciton-free photon coupling is omitted because the time scale of the optical near-field coupling and the exciton-phonon coupling is much faster than the radiative lifetime, which is of the order of a few nanoseconds. Taking matrix elements of Eq. (29) in terms of Eqs. (25) and (26) after substituting Eq. (28) into Eq. (29), we obtain the following simultaneous differential equations:

$$\begin{aligned} \dot{\rho}_{S_1, S_1}(t) &= i\sqrt{2}U' \{\rho_{S_1, P_1'}(t) - \rho_{P_1', S_1}(t)\}, \\ \dot{\rho}_{S_1, P_1'}(t) &= \left\{ i(\Delta\Omega - U) - \frac{\Gamma}{2} \right\} \rho_{S_1, P_1'}(t) + i\sqrt{2}U' \{\rho_{S_1, S_1}(t) \\ & \quad - \rho_{P_1', P_1'}(t)\}, \\ \dot{\rho}_{P_1', S_1}(t) &= \left\{ -i(\Delta\Omega - U) - \frac{\Gamma}{2} \right\} \rho_{P_1', S_1}(t) - i\sqrt{2}U' \{\rho_{S_1, S_1}(t) \\ & \quad - \rho_{P_1', P_1'}(t)\}, \\ \dot{\rho}_{P_1', P_1'}(t) &= -i\sqrt{2}U' \{\rho_{S_1, P_1'}(t) - \rho_{P_1', S_1}(t)\} - \Gamma \rho_{P_1', P_1'}(t), \\ \dot{\rho}_{P_1, P_1}(t) &= \Gamma \rho_{P_1, P_1}(t), \end{aligned} \quad (30)$$

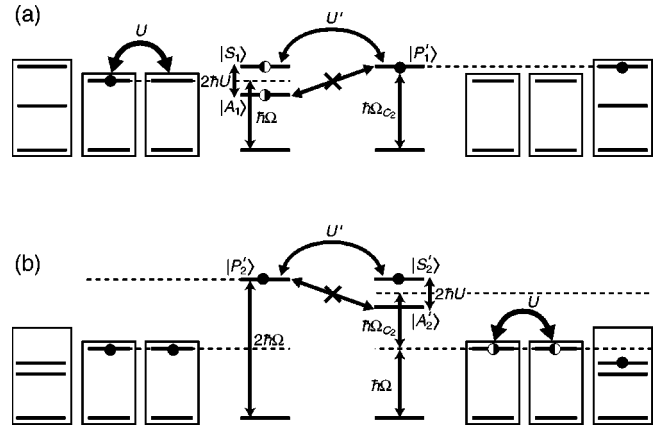


FIG. 4. Schematic explanation of selective energy transfer for (a) one- and (b) two-exciton states. The left and right illustrations represent the initial and final states, respectively. The energy transfer between states $|A\rangle$ and $|P\rangle$ is forbidden because of symmetry. Therefore, the resonance conditions for the energy transfer between states $|S\rangle$ and $|P\rangle$ are $\hbar(\Omega + U) = \hbar\Omega_{C_2}$ ($\Delta\Omega = U$) for a one-exciton state and $2\hbar\Omega = \hbar(\Omega + \Omega_{C_2} + U)$ ($\Delta\Omega = -U$) for a two-exciton state.

and

$$\begin{aligned} \dot{\rho}_{S_2', S_2'}(t) &= i\sqrt{2}U' \{\rho_{S_2', P_2'}(t) - \rho_{P_2', S_2'}(t)\} - \Gamma \rho_{S_2', S_2'}(t), \\ \dot{\rho}_{S_2', P_2'}(t) &= \left\{ -i(\Delta\Omega + U) - \frac{\Gamma}{2} \right\} \rho_{S_2', P_2'}(t) \\ & \quad + i\sqrt{2}U' \{\rho_{S_2', S_2'}(t) - \rho_{P_2', P_2'}(t)\}, \\ \dot{\rho}_{P_2', S_2'}(t) &= \left\{ i(\Delta\Omega + U) - \frac{\Gamma}{2} \right\} \rho_{P_2', S_2'}(t) \\ & \quad - i\sqrt{2}U' \{\rho_{S_2', S_2'}(t) - \rho_{P_2', P_2'}(t)\}, \\ \dot{\rho}_{P_2', P_2'}(t) &= -i\sqrt{2}U' \{\rho_{S_2', P_2'}(t) - \rho_{P_2', S_2'}(t)\}, \end{aligned} \quad (31)$$

where the density-matrix element $\langle \alpha | \hat{\rho}(t) | \beta \rangle$ is abbreviated $\rho_{\alpha, \beta}(t)$ and the energy difference $\Omega_{C_2} - \Omega$ is replaced by $\Delta\Omega$. The equations of motion in terms of the bases of Eq. (27) are not shown, but are derived similarly. Although other matrix elements related to the antisymmetric states $|A\rangle$ also appear in the equations of motion, they are decoupled from the above equations and do not affect the exciton dynamics of the symmetric states.

States $|S_1\rangle$ and $|P_1'\rangle$ or $|S_2'\rangle$ and $|P_2'\rangle$ are coherently coupled with each other, as shown by Eqs. (30) and (31). Moreover, it is noteworthy that the energy difference in Eqs. (30) and (31) makes opposite contributions to the one- and two-exciton dynamics as $\Delta\Omega - U$ and $\Delta\Omega + U$, respectively. This coupling property can be explained by considering the energy levels of a coupled system constructed from three quantum dots. Figure 4(a) shows the energy levels of a coupled system for one-exciton states. The upper and lower energy levels are split by the optical near-field coupling $\hbar U$,

corresponding to the states $|S_1\rangle$ and $|A_1\rangle$, respectively. This is confirmed by evaluating the expectation values, i.e., $\langle S_1|\hat{H}|S_1\rangle > \langle A_1|\hat{H}|A_1\rangle$. A filled circle indicates that an exciton occupies the corresponding energy level, while a semi-circle indicates that an exciton exists in the energy level in either QD-A or -B with a certain probability. In order to realize the resonant energy transfer into the output part via state $|P'_1\rangle$, we must set the energy level in QD-C as $\Delta\Omega = U$ to satisfy the resonance condition of states $|S_1\rangle$ and $|P'_1\rangle$. This is because the matrix element $\langle P'_1|\hat{H}_{\text{int}}|A_1\rangle$ is zero, so that this transition is forbidden in symmetric systems. For the two-exciton states, one exciton is always transferred from state $|P'_2\rangle$ to states $|S_2\rangle$ and $|P_2\rangle$ via state $|S'_2\rangle$. Figure 4(b) shows the energy levels of a coupled system for states $|P'_2\rangle$ and $|S'_2\rangle$. In this case, the center of the energy splitting due to the optical near-field coupling becomes $\hbar(\Omega + \Omega_{C_2})$. Therefore, the resonance condition of states $|P'_2\rangle$ and $|S'_2\rangle$ can be fulfilled when $\Delta\Omega = -U$ is satisfied. Here, note that the coupling between states $|P'_2\rangle$ and $|A'_2\rangle$ is also forbidden by $\langle A'_2|\hat{H}_{\text{int}}|P'_2\rangle = 0$. These characteristic energy transfers allow us to pick up selective information about either the one- or two-exciton states, i.e., information about the initial exciton populations in the coherent operation part. The results are utilized for the functional logic operations as discussed below.

C. Dynamics and logic operations

Analytic solutions of Eqs. (30) and (31) for typical initial conditions can be obtained readily with the help of Laplace transforms. The output population for the one-exciton state can be written as

$$\begin{aligned} \rho_{P_1, P_1}(t) &= \Gamma \int_0^t \rho_{P'_1, P'_1}(t') dt' \\ &= \frac{1}{2} + \frac{4U'^2}{\omega_+^2 - \omega_-^2} \{ \cos \phi_+ \cos(\omega_+ t + \phi_+) \\ &\quad - \cos \phi_- \cos(\omega_- t + \phi_-) \} e^{-(\Gamma/2)t}, \end{aligned} \quad (32)$$

with

$$\begin{aligned} \omega_{\pm} &= \frac{1}{\sqrt{2}} [(\Delta\Omega - U)^2 + W_+ W_- \\ &\quad \pm \sqrt{\{(\Delta\Omega - U)^2 + W_+^2\} \{(\Delta\Omega - U)^2 + W_-^2\}}]^{1/2}, \\ \phi_{\pm} &= \tan^{-1} \left(\frac{2\omega_{\pm}}{\Gamma} \right), \\ W_{\pm} &= 2\sqrt{2}U' \pm \frac{\Gamma}{2}, \end{aligned} \quad (33)$$

for the initial condition $\rho_{S_1, S_1}(0) = \rho_{A_1, A_1}(0) = \rho_{S_1, A_1}(0) = \rho_{A_1, S_1}(0) = 1/2$, which corresponds to the condition $\langle A^* B C_1 C_2 | \hat{\rho}(t) | A^* B C_1 C_2 \rangle = 1$ and otherwise zero. Solutions for the two-exciton states can be obtained from an

equation similar to Eq. (32), except for the sign of U , i.e., with the resonance conditions inverted. The probability of an exciton occupying the lower energy level in QD-C is

$$\begin{aligned} &\rho_{S_2, S_2}(t) + \rho_{P_2, P_2}(t) \\ &= \Gamma \int_0^t \rho_{S'_2, S'_2}(t') dt' \\ &= 2 \left[\frac{1}{2} + \frac{4U'^2}{\omega_+'^2 - \omega_-'^2} \{ \cos \phi_+' \cos(\omega_+' t + \phi_+') \right. \\ &\quad \left. - \cos \phi_-' \cos(\omega_-' t + \phi_-') \} e^{-(\Gamma/2)t} \right], \end{aligned} \quad (34)$$

with

$$\begin{aligned} \omega'_{\pm} &= \frac{1}{\sqrt{2}} [(\Delta\Omega + U)^2 + W_+ W_- \\ &\quad \pm \sqrt{\{(\Delta\Omega + U)^2 + W_+^2\} \{(\Delta\Omega + U)^2 + W_-^2\}}]^{1/2}, \\ \phi'_{\pm} &= \tan^{-1} \left(\frac{2\omega'_{\pm}}{\Gamma} \right), \end{aligned} \quad (35)$$

where the factor 2 in Eq. (34) comes from the initial conditions for the two-exciton state, i.e., $\rho_{P'_2, P'_2}(0) = 1$ and otherwise zero.

We will now discuss the characteristic behaviors described by Eqs. (32) and (34) using a CuCl quantum-cube system that has the coupling strengths calculated in Sec. II: $\hbar U = 89 \mu\text{eV}$ and $\hbar U' = 14 \mu\text{eV}$. Figure 5(a) shows the temporal evolution of the output population $\rho_{P_1, P_1}(t)$ for some energy differences $\Delta\Omega$. The fastest energy transfer is observed for the condition $\Delta\Omega = U$ (dotted curve), where the population can reach half of the maximum value. This is because the coherent operation part couples with the output part in the one-exciton state via states $|S_1\rangle$ and $|P'_1\rangle$. However, state $|S_1\rangle$ is not fully occupied when we set the initial condition so that only one quantum cube is excited independently. In other words, state $|A_1\rangle$, which decouples state $|P'_1\rangle$ in a symmetric system, is excited simultaneously, and the population remains in the same state $|A_1\rangle$ without temporal evolution. Conversely, for two-exciton states [Fig. 5(b)], the energy transfer occurs under the resonance condition $\Delta\Omega = -U$ and the population can reach unity because the initial state $|P'_2\rangle$ is independent of state $|A'_2\rangle$.

The steepness of the resonance determines the contrast of the output signal. In Fig. 6, the population at $t = 100$ ps, which is the time until energy transfer is almost completed under resonance conditions $\Delta\Omega = \pm U$, is plotted as a function of the energy difference $\Delta\Omega$ for the one- and two-exciton states, as shown by the solid and dashed curves, respectively. We clearly find that two types of switching operations can be realized by choosing the appropriate energy difference $\Delta\Omega = \pm U$. From Eqs. (32) and (34), narrow

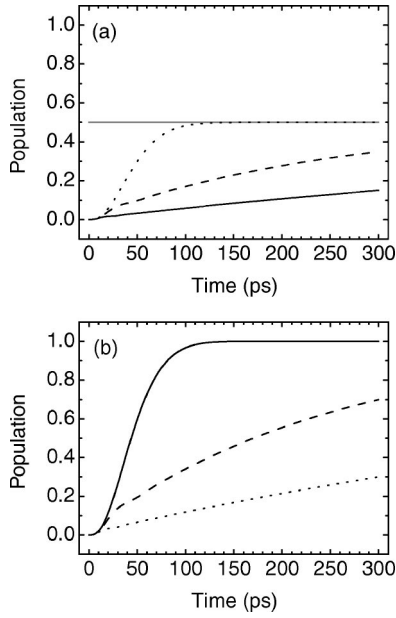


FIG. 5. Temporal evolution of the output populations for (a) one- and (b) two-exciton states. The solid, dashed, and dotted curves represent the results for the energy difference $\Delta\Omega = -U$, 0 , and U , respectively. The parameters are set to $\hbar U = 89 \mu\text{eV}$, $\hbar U' = 14 \mu\text{eV}$, and $\Gamma^{-1} = 10 \text{ ps}$. The output population for the one-exciton state does not exceed a value of 0.5 (the horizontal gray line) because of the initial conditions.

peaks are obtained when $W_+ \ll 1$ and $W_- = 0$, i.e., $2\sqrt{2}U' \sim \Gamma/2 \ll 1$. In this case, a high contrast logic operation can be achieved.

These results are summarized in Table I, which shows the logic operations inherent in nanophotonic devices using typical coherent process and the process with decoherence that occur in a quantum-dot system. The system behaves as an AND-logic gate when the energy difference is set to $\Delta\Omega = -U$, and the system provides an XOR-like-logic operation when $\Delta\Omega = U$. The value 0.5 indicates that the signal can be detected at a 1/2 probability level. As explained in the Introduction, these operations are different from the quantum logic, and long quantum coherence time is unnecessary. The

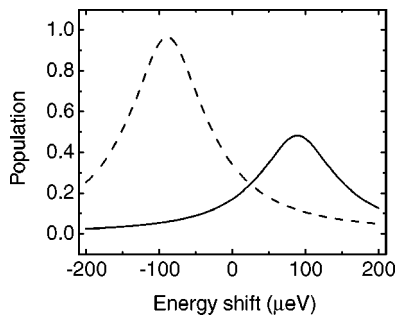


FIG. 6. Variation in the output populations at a fixed time of $t = 100 \text{ ps}$ as a function of the energy difference $\Delta\Omega$. The solid and dashed curves represent the one- and two-exciton states, respectively. The optical near-field coupling strengths $\hbar U$ and $\hbar U'$ and the nonradiative relaxation constant Γ have the same values as in Fig. 5.

TABLE I. Relationship between the input and output populations for the energy difference $\Delta\Omega = \pm U$.

A	Input		Output: C	
	B	$\Delta\Omega = -U$	$\Delta\Omega = U$	
0	0	0	0	
1	0	0	0.5	
0	1	0	0.5	
1	1	1	0	

critical limit of these logic gates is determined by the following condition; the energy-transfer time from the coherent operation part to the output part, which is estimated about 50 ps for the CuCl quantum-cube system, is enough shorter than the radiative lifetime ($\sim 1 \text{ ns}$) of excitons in each quantum dot.

IV. EFFECTS OF ASYMMETRY ON EXCITON DYNAMICS

It is valuable to examine the exciton dynamics in an asymmetrically arranged quantum-dot system to estimate the fabrication tolerance for the system described above and to propose further functional operations inherent in nanophotonic devices. In this section, we demonstrate the effects of asymmetry numerically. In addition, we comment on a positive use of these effects, i.e., the possibility of accessing quantum entangled states depending on the prepared initial excitation in a quantum-dot system. The simultaneous differential equations in an asymmetric system are given in part by

$$\begin{aligned}
 \dot{\rho}_{S_1, S_1}(t) &= i\sqrt{2}\bar{U}'[\rho_{S_1, P_1'}(t) - \rho_{P_1', S_1}(t)] + i\Delta\Omega_{AB}[\rho_{S_1, A_1}(t) \\
 &\quad - \rho_{A_1, S_1}(t)], \\
 \dot{\rho}_{S_1, P_1'}(t) &= \left\{ i(\Delta\Omega - U) - \frac{\Gamma}{2} \right\} \rho_{S_1, P_1'}(t) + i\sqrt{2}\bar{U}'[\rho_{S_1, S_1}(t) \\
 &\quad - \rho_{P_1', P_1'}(t)] - i\sqrt{2}\Delta U' \rho_{S_1, A_1}(t) \\
 &\quad - i\Delta\Omega_{AB} \rho_{A_1, P_1'}(t), \\
 \dot{\rho}_{A_1, A_1}(t) &= i\sqrt{2}\Delta U'[\rho_{P_1', A_1}(t) - \rho_{A_1, P_1'}(t)] \\
 &\quad - i\Delta\Omega_{AB}[\rho_{S_1, A_1}(t) - \rho_{A_1, S_1}(t)], \\
 \dot{\rho}_{A_1, P_1'}(t) &= \left\{ i(\Delta\Omega + U) - \frac{\Gamma}{2} \right\} \rho_{A_1, P_1'}(t) + i\sqrt{2}\bar{U}' \rho_{A_1, S_1}(t) \\
 &\quad - i\sqrt{2}\Delta U'[\rho_{A_1, A_1}(t) - \rho_{P_1', P_1'}(t)] \\
 &\quad - i\Delta\Omega_{AB} \rho_{S_1, P_1'}(t), \tag{36}
 \end{aligned}$$

for the one-exciton states, and

$$\begin{aligned}
\dot{\rho}_{S'_2, S'_2}(t) &= -\Gamma \rho_{S'_2, S'_2}(t) + i\sqrt{2}\bar{U}'[\rho_{S'_2, P'_2}(t) - \rho_{P'_2, S'_2}(t)] \\
&\quad + i\Delta\Omega_{AB}[\rho_{S'_2, A'_2}(t) - \rho_{A'_2, S'_2}(t)], \\
\dot{\rho}_{S'_2, P'_2}(t) &= \left\{ -i(\Delta\Omega + U) - \frac{\Gamma}{2} \right\} \rho_{S'_2, P'_2}(t) + i\sqrt{2}\bar{U}'[\rho_{S'_2, S'_2}(t) \\
&\quad - \rho_{P'_2, P'_2}(t)] + i\sqrt{2}\Delta U' \rho_{S'_2, A'_2}(t) \\
&\quad - i\Delta\Omega_{AB} \rho_{A'_2, P'_2}(t), \\
\dot{\rho}_{A'_2, A'_2}(t) &= -\Gamma \rho_{A'_2, A'_2}(t) - i\sqrt{2}\Delta U'[\rho_{P'_2, A'_2}(t) - \rho_{A'_2, P'_2}(t)] \\
&\quad - i\Delta\Omega_{AB}[\rho_{S'_2, A'_2}(t) - \rho_{A'_2, S'_2}(t)], \\
\dot{\rho}_{A'_2, P'_2}(t) &= \left\{ -i(\Delta\Omega - U) - \frac{\Gamma}{2} \right\} \rho_{A'_2, P'_2}(t) + i\sqrt{2}\bar{U}' \rho_{A'_2, S'_2}(t) \\
&\quad + i\sqrt{2}\Delta U'[\rho_{A'_2, A'_2}(t) - \rho_{P'_2, P'_2}(t)] \\
&\quad - i\Delta\Omega_{AB} \rho_{S'_2, P'_2}(t), \tag{37}
\end{aligned}$$

for the two-exciton states. Here, we only present the equations that differ from Eqs. (30) and (31) (see the Appendix for more details), and we redefine the parameters $\Delta\Omega = \Omega_{C_2} - (\Omega_A + \Omega_B)/2$, $\Delta\Omega_{AB} = \Omega_A - \Omega_B$, $\bar{U}' = (U_{BC} + U_{CA})/2$, and $\Delta U' = (U_{BC} - U_{CA})/2$. In the asymmetric system, the exciton dynamics between states $|S\rangle$ and $|P\rangle$ do not change, provided the coupling strength U' for a symmetric system is replaced by the average value \bar{U}' in Eqs. (36) and (37). The main difference is that the matrix elements for states $|A\rangle$ can couple with states $|S\rangle$ and $|P\rangle$ in an asymmetric system, while these are decoupled in a symmetric system. Two types of coupling emerge in an asymmetric system: one originates from the energy difference $\Delta\Omega_{AB}$ between QD-A and -B, and the other comes from the arrangement of the three quantum dots, which is expressed using the parameter $\Delta U'$. Previously,¹⁷ we discussed the influence of the energy difference on the exciton dynamics in a two-quantum-dot system that mainly degrades the signal contrast. Here, we focus on the effects of asymmetry due to the arrangement of each quantum dot, assuming $\Delta\Omega_{AB} = 0$.

In order to examine the effects of the quantum-dot arrangement, the average coupling strength \bar{U}' is fixed so that states $|S\rangle$ and $|P\rangle$ maintain the same temporal evolution that was found in the symmetric system. Then, the difference between the coupling strengths $\Delta U'$ varies from 0 to $\pm U$, where the exciton dynamics are independent of the sign of $\Delta U'$. Therefore, an asymmetry factor is defined by the ratio of $|\Delta U'|$ to \bar{U}' , varying from 0 (symmetry) to 1 (maximum amount of asymmetry).

Figure 7 presents the temporal evolution of the output population for the energy difference $\Delta\Omega = -U$ (an AND-logic gate case) with and without an asymmetric arrangement. For the one-exciton state [Fig. 7(a)], the asymmetric arrangement strongly affects the exciton dynamics, and the OFF state in the AND-gate operation is no longer valid be-

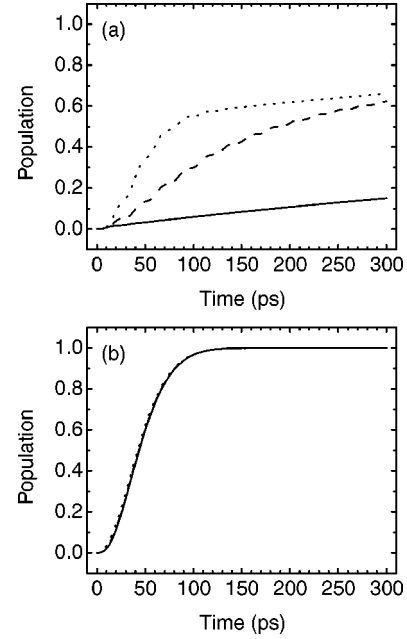


FIG. 7. Temporal evolution of the output populations where the energy difference is set to $\Delta\Omega = -U$ ($\hbar U = 89 \mu\text{eV}$). Parts (a) and (b) show the populations for one- and two-exciton states, respectively. The solid, dashed, and dotted curves represent the results for asymmetry factors $|\Delta U'|/\bar{U}' = 0, 0.5$, and 1.0 , respectively, where the average coupling strength is set to $\hbar \bar{U}' = 14 \mu\text{eV}$. In part (b), the three curves are almost identical.

cause the off-resonance condition for the energy transfer between states $|S_1\rangle$ and $|P'_1\rangle$ acts oppositely to the resonance condition between states $|A_1\rangle$ and $|P'_1\rangle$. This is evident in Eq. (36), for example, by comparing the matrix elements $\rho_{S_1, P'_1}(t)$ with $\rho_{A_1, P'_1}(t)$. Therefore, in the one-exciton state, the exciton population is very sensitive to the asymmetric arrangement. By contrast, the two-exciton state is not influenced by the quantum-dot arrangement [see Fig. 7(b)]. We also observe small and high-frequency oscillations for the dashed and dotted curves ($|\Delta U'|/\bar{U}' = 0.5$ and 1.0) in Fig. 7(a). These come from the coherence between states $|S_1\rangle$ and $|A_1\rangle$ which can be seen in the equations of motion of $\rho_{S_1, A_1}(t)$ and $\rho_{A_1, S_1}(t)$ [see Eq. (A1)]. Since the coherence is always excited by mediating state $|P'_1\rangle$ and the state $|P'_1\rangle$ has a short lifetime dominated by the relaxation constant Γ , the oscillations have no relation to the population dynamics. Figure 8 shows the variation in the output population at $t = 100$ ps as a function of the asymmetry factor $|\Delta U'|/\bar{U}'$. From this figure, it follows that the asymmetry only affects the one-exciton state, where it breaks the OFF state in the logic gate, as shown by the curve with squares, and the signal contrast decreases with increasing asymmetry.

Conversely, for the XOR-logic gate ($\Delta\Omega = U$), the two-exciton states correspond to the off-resonant states in the symmetric system. Therefore, the excitation is transferred to the output energy level in QD-C as the asymmetry factor increases, as shown in Fig. 9(b). Similarly, the variation in the output population with the asymmetry factor is plotted in

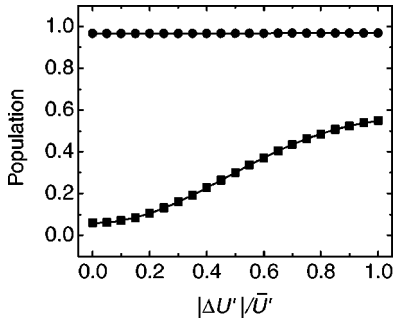


FIG. 8. Variation in the output populations at a fixed time of $t = 100$ ps as a function of the asymmetry factor, where the energy difference is set to $\Delta\Omega = -U$ ($\hbar U = 89 \mu\text{eV}$) and an average coupling strength of $\hbar\bar{U}' = 14 \mu\text{eV}$ is used. The curves shown with square and circular dots represent the one- and two-exciton states, respectively. Only the exciton population in the one-exciton state is modified by increasing the asymmetry factor.

Fig. 10, where the time is fixed at $t = 100$ ps. The figure shows that the XOR-logic operation in the symmetric system is reversed when the asymmetry factor exceeds 0.5 because a one-exciton state can occupy the initial state of $|S_1\rangle$ with a probability of 1/2, as shown in Sec. III. Consequently, the output population also reaches a probability of 1/2. This is also valid in the asymmetric system. However, the asymmetric arrangement enables coupling of the two-exciton states $|P_2'\rangle$ and $|A_2'\rangle$. State $|P_2'\rangle$ can be fully excited in the initial stage, so the output population reaches a unit value via states $|A_2'\rangle$. This exceeds the output population 0.5 for a one-exciton state with a larger amount of asymmetry.

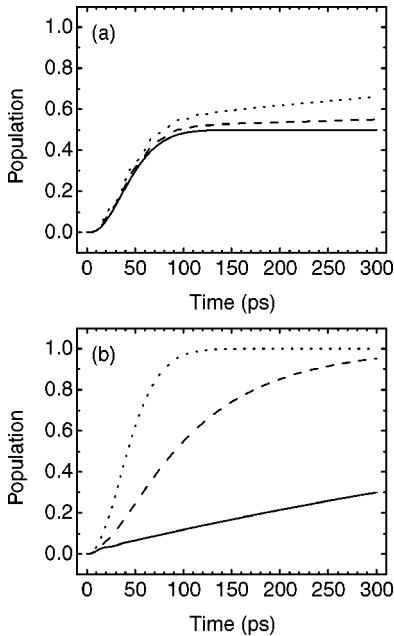


FIG. 9. Temporal evolution of the output populations for the energy difference of $\Delta\Omega = U$ ($\hbar U = 89 \mu\text{eV}$). Parts (a) and (b) show the populations for the one- and two-exciton states, respectively. The solid, dashed, and dotted curves represent the results for asymmetry factors $|\Delta U'|/\bar{U}' = 0, 0.5,$ and $1.0,$ respectively, where the average coupling strength is set to $\hbar\bar{U}' = 14 \mu\text{eV}$.

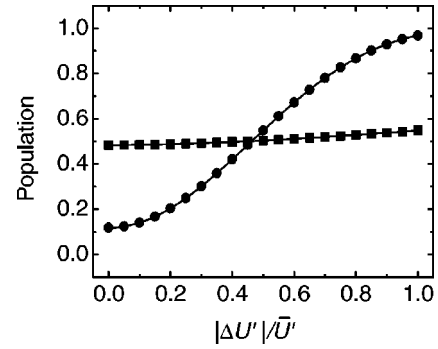


FIG. 10. Variation in the output populations at the fixed time of $t = 100$ ps as a function of the asymmetry factor, where the energy difference is set to $\Delta\Omega = U$ ($\hbar U = 89 \mu\text{eV}$) and an average coupling strength of $\hbar\bar{U}' = 14 \mu\text{eV}$ is used. The curves shown with square and circular dots represent the one- and two-exciton states, respectively. The exciton population in the two-exciton state exceeds that of the one-exciton state when the asymmetry factor $|\Delta U'|/\bar{U}'$ exceeds 0.5, so the XOR-logic operation is reversed.

An asymmetric system can also be applied to inherent nanophotonic functions. As mentioned above, the effect of asymmetry is based on coupling to states $|A\rangle$, which are similar to the so-called “dark states” in an asymmetric system.²⁵ In other words, the populations of states $|S\rangle$ and $|A\rangle$ can be chosen selectively by adjusting the arrangement of some of the quantum dots. Note that both states are expressed by the superposition of eigenstates in isolated (non-interacting) quantum dots. Therefore, a system composed of three quantum dots cannot only select information that depends on the initially prepared excitations, but also information that reflects the initial quantum entangled states in the coherent operation part. From this perspective, such nanophotonic devices are useful in connecting quantum devices as a detector and interface devices which identify occupation probability of the quantum entangled states in an input signal.

V. CONCLUSIONS

This paper proposed nanophotonic inherent operations using a three-quantum-dot system. Such a system consists of a coherent operation part and an incoherent output part. The exciton state in the coherent operation part can be read selectively by adjusting the energy level in an output quantum dot or the size of the quantum dot. First, we derived the coupling strength induced by an optical near field and showed that optical near-field coupling enables us to access dipole-forbidden energy levels for conventional far-field light. Then, we derived the equations of motion for the exciton dynamics in a symmetric system to discuss the coupling properties between the coherent operation part and the output part. Initially prepared one- and two-exciton states couple resonantly with the output part due to the optical near-field coupling when the energy level in the third quantum dot is set higher than one and lower than in the other identical quantum dots. This feature is applicable to logic operations. Using analytical solutions, we showed that the

system operates as an AND-logic gate when the energy difference is $\Delta\Omega = -U$, and it operates as an XOR-logic gate when $\Delta\Omega = U$. Furthermore, we examined the effects of asymmetry due to the arrangement of quantum dots numerically. The asymmetry allows coupling between states $|A\rangle$ and $|P\rangle$, and $|A\rangle$ and $|S\rangle$; these states are decoupled in the symmetric system. Although the asymmetric arrangement decreases the signal contrast in the AND- and XOR-logic operations, it introduces a technique to manipulate the information about quantum entangled states or quantum coherence by adjusting the quantum-dot arrangement. In conclusion, we proposed functional operations (AND- and XOR-logic gates)

using a near-field optically coupled quantum-dot system and characteristic device operations inherent in nanophotonics, including coherent and dissipative process. Such a system opens up a different way to nanoscale science and technology.

ACKNOWLEDGMENTS

The authors thank Dr. T. Kawazoe (Japan Science and Technology Agency) for kindly providing experimental information about CuCl quantum dots and the dynamics driven by optical near-field interactions.

APPENDIX: EQUATIONS OF MOTION IN AN ASYMMETRIC SYSTEM

The equations of motion for density-matrix elements in an asymmetric system are derived using the bases described in Eqs. (25) and (26) for one-exciton states,

$$\begin{aligned}
\dot{\rho}_{S_1, S_1}(t) &= i\sqrt{2}\bar{U}'[\rho_{S_1, P_1}(t) - \rho_{P_1, S_1}(t)] + i\Delta\Omega_{AB}[\rho_{S_1, A_1}(t) - \rho_{A_1, S_1}(t)], \\
\dot{\rho}_{S_1, P_1}(t) &= \left\{ i(\Delta\Omega - U) - \frac{\Gamma}{2} \right\} \rho_{S_1, P_1}(t) + i\sqrt{2}\bar{U}'[\rho_{S_1, S_1}(t) - \rho_{P_1, P_1}(t)] - i\sqrt{2}\Delta U' \rho_{S_1, A_1}(t) - i\Delta\Omega_{AB}\rho_{A_1, P_1}(t), \\
\dot{\rho}_{P_1, S_1}(t) &= \left\{ -i(\Delta\Omega - U) - \frac{\Gamma}{2} \right\} \rho_{P_1, S_1}(t) - i\sqrt{2}\bar{U}'[\rho_{S_1, S_1}(t) - \rho_{P_1, P_1}(t)] + i\sqrt{2}\Delta U' \rho_{A_1, S_1}(t) + i\Delta\Omega_{AB}\rho_{P_1, A_1}(t), \\
\dot{\rho}_{P_1, P_1}(t) &= -\Gamma\rho_{P_1, P_1}(t) - i\sqrt{2}\bar{U}'[\rho_{S_1, P_1}(t) - \rho_{P_1, S_1}(t)] - i\Delta U'[\rho_{P_1, A_1}(t) - \rho_{A_1, P_1}(t)], \\
\dot{\rho}_{P_1, A_1}(t) &= \left\{ -i(\Delta\Omega + U) - \frac{\Gamma}{2} \right\} \rho_{P_1, A_1}(t) - i\sqrt{2}\bar{U}'\rho_{S_1, A_1}(t) + i\sqrt{2}\Delta U'[\rho_{A_1, A_1}(t) - \rho_{P_1, P_1}(t)] + i\Delta\Omega_{AB}\rho_{P_1, S_1}(t), \\
\dot{\rho}_{A_1, P_1}(t) &= \left\{ i(\Delta\Omega + U) - \frac{\Gamma}{2} \right\} \rho_{A_1, P_1}(t) + i\sqrt{2}\bar{U}'\rho_{A_1, S_1}(t) - i\sqrt{2}\Delta U'[\rho_{A_1, A_1}(t) - \rho_{P_1, P_1}(t)] - i\Delta\Omega_{AB}\rho_{S_1, P_1}(t), \\
\dot{\rho}_{S_1, A_1}(t) &= -i2U\rho_{S_1, A_1}(t) - i\sqrt{2}\bar{U}'\rho_{P_1, A_1}(t) - i\sqrt{2}\Delta U'\rho_{S_1, P_1}(t) + i\Delta\Omega_{AB}[\rho_{S_1, S_1}(t) - \rho_{A_1, A_1}(t)], \\
\dot{\rho}_{A_1, S_1}(t) &= i2U\rho_{A_1, S_1}(t) + i\sqrt{2}\bar{U}'\rho_{A_1, P_1}(t) + i\sqrt{2}\Delta U'\rho_{P_1, S_1}(t) - i\Delta\Omega_{AB}[\rho_{S_1, S_1}(t) - \rho_{A_1, A_1}(t)], \\
\dot{\rho}_{A_1, A_1}(t) &= i\sqrt{2}\Delta U'[\rho_{P_1, A_1}(t) - \rho_{A_1, P_1}(t)] - i\Delta\Omega_{AB}[\rho_{S_1, A_1}(t) - \rho_{A_1, S_1}(t)], \tag{A1}
\end{aligned}$$

where $\Delta\Omega = \Omega_{C_2} - (\Omega_A + \Omega_B)/2$, $\Delta\Omega_{AB} = \Omega_A - \Omega_B$, $\bar{U}' = (U_{BC} + U_{CA})/2$, and $\Delta U' = (U_{BC} - U_{CA})/2$. For two-exciton states,

$$\begin{aligned}
\dot{\rho}_{S_2', S_2'}(t) &= -\Gamma\rho_{S_2', S_2'}(t) + i\sqrt{2}\bar{U}'[\rho_{S_2', P_2'}(t) - \rho_{P_2', S_2'}(t)] + i\Delta\Omega_{AB}[\rho_{S_2', A_2'}(t) - \rho_{A_2', S_2'}(t)], \\
\dot{\rho}_{S_2', P_2'}(t) &= \left\{ -i(\Delta\Omega + U) - \frac{\Gamma}{2} \right\} \rho_{S_2', P_2'}(t) + i\sqrt{2}\bar{U}'[\rho_{S_2', S_2'}(t) - \rho_{P_2', P_2'}(t)] + i\sqrt{2}\Delta U'\rho_{S_2', A_2'}(t) - i\Delta\Omega_{AB}\rho_{A_2', P_2'}(t), \\
\dot{\rho}_{P_2', S_2'}(t) &= \left\{ i(\Delta\Omega + U) - \frac{\Gamma}{2} \right\} \rho_{P_2', S_2'}(t) - i\sqrt{2}\bar{U}'[\rho_{S_2', S_2'}(t) - \rho_{P_2', P_2'}(t)] - i\sqrt{2}\Delta U'\rho_{A_2', S_2'}(t) + i\Delta\Omega_{AB}\rho_{P_2', A_2'}(t), \\
\dot{\rho}_{P_2', P_2'}(t) &= -i\sqrt{2}\bar{U}'[\rho_{S_2', P_2'}(t) - \rho_{P_2', S_2'}(t)] + i\sqrt{2}\Delta U'[\rho_{P_2', A_2'}(t) - \rho_{A_2', P_2'}(t)],
\end{aligned}$$

$$\begin{aligned}
\dot{\rho}_{A'_2, P'_2}(t) &= \left\{ -i(\Delta\Omega - U) - \frac{\Gamma}{2} \right\} \rho_{A'_2, P'_2}(t) + i\sqrt{2}\bar{U}' \rho_{A'_2, S'_2}(t) + i\sqrt{2}\Delta U' [\rho_{A'_2, A'_2}(t) - \rho_{P'_2, P'_2}(t)] - i\Delta\Omega_{AB} \rho_{S'_2, P'_2}(t), \\
\dot{\rho}_{P'_2, A'_2}(t) &= \left\{ i(\Delta\Omega - U) - \frac{\Gamma}{2} \right\} \rho_{P'_2, A'_2}(t) - i\sqrt{2}\bar{U}' \rho_{S'_2, A'_2}(t) - i\sqrt{2}\Delta U' [\rho_{A'_2, A'_2}(t) - \rho_{P'_2, P'_2}(t)] + i\Delta\Omega_{AB} \rho_{P'_2, S'_2}(t), \\
\dot{\rho}_{S'_2, A'_2}(t) &= (-i2U - \Gamma) \rho_{S'_2, A'_2}(t) - i\sqrt{2}\bar{U}' \rho_{P'_2, A'_2}(t) + i\sqrt{2}\Delta U' \rho_{S'_2, P'_2}(t) + i\Delta\Omega_{AB} [\rho_{S'_2, S'_2}(t) - \rho_{A'_2, A'_2}(t)], \\
\dot{\rho}_{A'_2, S'_2}(t) &= (i2U - \Gamma) \rho_{A'_2, S'_2}(t) + i\sqrt{2}\bar{U}' \rho_{A'_2, P'_2}(t) - i\sqrt{2}\Delta U' \rho_{P'_2, S'_2}(t) - i\Delta\Omega_{AB} [\rho_{S'_2, S'_2}(t) - \rho_{A'_2, A'_2}(t)], \\
\dot{\rho}_{A'_2, A'_2}(t) &= -\Gamma \rho_{A'_2, A'_2}(t) - i\sqrt{2}\Delta U' [\rho_{P'_2, A'_2}(t) - \rho_{A'_2, P'_2}(t)] - i\Delta\Omega_{AB} [\rho_{S'_2, A'_2}(t) - \rho_{A'_2, S'_2}(t)]. \tag{A2}
\end{aligned}$$

*Electronic address: suguru.sangu@nts.rioh.co.jp

¹M. Ohtsu, in *Near-Field Optics: Principles and Applications*, edited by X. Zhu and M. Ohtsu (World Scientific, Singapore, 2000), pp. 1–8.

²M. Ohtsu, K. Kobayashi, T. Kawazoe, S. Sangu, and T. Yatsui, *IEEE J. Sel. Top. Quantum Electron.* **8**, 839 (2002).

³*Near-Field Nano/Atom Optics and Technology*, edited by M. Ohtsu (Springer-Verlag, Tokyo, 1998).

⁴K. Matsuda, K. Ikeda, T. Saiki, H. Tsuchiya, H. Saito, and K. Nishi, *Phys. Rev. B* **63**, 121304 (2001).

⁵K. Matsuda, T. Saiki, S. Nomura, M. Mihara, Y. Aoyagi, S. Nair, and T. Takagahara, *Phys. Rev. Lett.* **91**, 177401 (2003).

⁶T. Yatsui, M. Kurogi, and M. Ohtsu, *Appl. Phys. Lett.* **79**, 4583 (2001).

⁷N. Hosaka and T. Saiki, *J. Microsc.* **202**, 362 (2001).

⁸R.U. Maheswari, S. Mononobe, K. Yoshida, M. Yoshimoto, and M. Ohtsu, *Jpn. J. Appl. Phys., Part 1* **38**, 6713 (1999).

⁹T. Kawazoe, K. Kobayashi, J. Lim, Y. Narita, and M. Ohtsu, *Phys. Rev. Lett.* **88**, 067404 (2002).

¹⁰C.D. Simserides, U. Hohenester, G. Goldoni, and E. Molinari, *Phys. Rev. B* **62**, 13 657 (2000).

¹¹K. Cho, Y. Ohfuti, and K. Arima, *Surf. Sci.* **363**, 378 (1996).

¹²G.W. Bryant, *Appl. Phys. Lett.* **72**, 768 (1998).

¹³K. Kobayashi and M. Ohtsu, *J. Microsc.* **194**, 249 (1999).

¹⁴A. Shojiguchi, K. Kobayashi, S. Sangu, K. Kitahara, and M. Ohtsu, *Nonlinear Opt.* **29**, 563 (2002).

¹⁵A. Shojiguchi, K. Kobayashi, S. Sangu, K. Kitahara, and M. Ohtsu, *J. Phys. Soc. Jpn.* **72**, 2984 (2003).

¹⁶T. Kawazoe, K. Kobayashi, S. Sangu, and M. Ohtsu, *Appl. Phys. Lett.* **82**, 2957 (2003).

¹⁷S. Sangu, K. Kobayashi, T. Kawazoe, A. Shojiguchi, and M. Ohtsu, *J. Appl. Phys.* **93**, 2937 (2003).

¹⁸K. Kobayashi, S. Sangu, A. Shojiguchi, T. Kawazoe, K. Kitahara, and M. Ohtsu, *J. Microsc.* **210**, 247 (2003).

¹⁹H. Hori, in *Optical and Electronic Process of Nano-Matters*, edited by M. Ohtsu (KTK Scientific, Tokyo/Kluwer Academic, Dordrecht, 2001), pp. 1–55.

²⁰S.D. Rinaldis, I. D'Amico, and F. Rossi, *Appl. Phys. Lett.* **81**, 4236 (2002).

²¹F. Troiani, U. Hohenester, and E. Molinari, *Phys. Rev. B* **65**, 161301 (2002).

²²E. Biolatti, R.C. Iotti, P. Zanardi, and F. Rossi, *Phys. Rev. Lett.* **85**, 5647 (2000).

²³L. Quiroga and N.F. Johnson, *Phys. Rev. Lett.* **83**, 2270 (1999).

²⁴T. Förster, in *Modern Quantum Chemistry*, edited by O. Sinanoğlu (Academic Press, London, 1965), pp. 93–137.

²⁵M.O. Scully and M.S. Zubairy, *Quantum Optics* (Cambridge University Press, Cambridge, 1997).

²⁶P. Zanardi and F. Rossi, *Phys. Rev. Lett.* **81**, 4752 (1998).

²⁷M. Thorwart and P. Hänggi, *Phys. Rev. A* **65**, 012309 (2001).

²⁸C. Cohen-Tannoudji, J. Depont-Roc, and G. Grynberg, *Photons and Atoms: Introduction to Quantum Electrodynamics* (Wiley, New York, 1989).

²⁹D.P. Craig and T. Thirunamachandran, *Molecular Quantum Electrodynamics* (Academic Press, London, 1984).

³⁰J. Knoester and S. Mukamel, *Phys. Rev. A* **39**, 1899 (1989).

³¹J.R. Zurita-Sanchez and L. Novotny, *J. Opt. Soc. Am. B* **19**, 1355 (2002).

³²K. Kobayashi, S. Sangu, H. Ito, and M. Ohtsu, *Phys. Rev. A* **63**, 013806 (2001).

³³S. Sangu, K. Kobayashi, and M. Ohtsu, *J. Microsc.* **202**, 279 (2001).

³⁴M. Ohtsu and K. Kobayashi, *Optical Near Fields: Introduction to Classical and Quantum Theories of Electromagnetic Phenomena at the Nanoscale* (Springer-Verlag, Berlin, 2004).

³⁵E. Hanamura, *Phys. Rev. B* **37**, 1273 (1988).

³⁶B. Coffey, *Phys. Rev. A* **17**, 1033 (1978).

³⁷H.J. Carmichael, *Statistical Methods in Quantum Optics I* (Springer-Verlag, Berlin, 1999).



Combinatorial synthesis and luminescent characteristics of RECa₄O(BO₃)₃ epitaxial thin films

H. Kubota^{a,*}, R. Takahashi^a, T.-W. Kim^b, T. Kawazoe^b, M. Ohtsu^c, N. Arai^a,
M. Yoshimura^d, H. Nakao^d, H. Furuya^d, Y. Mori^d, T. Sasaki^d,
Y. Matsumoto^e, H. Koinuma^{a,f}

^aMaterials and Structures Laboratory, Tokyo Institute of Technology, 4259 Nagatsuta, Midori-ku, Yokohama 226-8503, Japan

^bJapan Science and Technology Corporation, 687-1 Tsuruma, Machida, Tokyo 194-0004, Japan

^cInterdisciplinary Graduate School of Science and Engineering, Tokyo Institute of Technology, 4259 Nagatsuta, Midori-ku, Yokohama 226-8503, Japan

^dDepartment of Electrical Engineering, Graduate School of Engineering, Osaka University, 2-1 Yamadaoka, Suita, Osaka 556-0871, Japan

^eFrontier Collaborative Research Center, Tokyo Institute of Technology, 4259 Nagatsuta, Midori-ku, Yokohama 226-8503, Japan

^fNIMS-COMET, 1-2-1Sengen, Tsukuba, Ibaraki 305-0047, Japan

Abstract

A series of RECa₄O(BO₃)₃ (RECOB) thin films (RE = Rare earth elements) was fabricated on ultrasMOOTH GdCOB (0 1 0) substrates by laser molecular beam epitaxy (MBE) method to explore the optimal growth conditions and to evaluate the luminescent properties. The growing surface of the film on a temperature gradient substrate was diagnosed with scanning reflection high energy electron diffraction (S-RHEED) system for quickly specifying optimum growth temperature and its dependence of rare earth element. The lowest temperature for epitaxial film growth was defined by the appearance of streak pattern in RHEED and it reflected the lattice matching with the substrate. TbCOB and EuCOB emitted respectively very bright green (543 nm) and red (611 nm) light, indicating that they are promising new phosphors. It is noteworthy that we could detect a remarkably strong red emitting region in the EuCOB–ScCOB–PrCOB ternary composition spread library.

© 2003 Elsevier B.V. All rights reserved.

Keywords: Combinatorial; NLO thin film; RECOB; Laser MBE; Phosphor

1. Introduction

In the last few years, nonlinear optics (NLO) has attracted a great deal of attention, and many research works have been carried out for the fabrication of NLO thin films [1]. RECa₄O(BO₃)₃ (RECOB,

RE = rare earth) single crystals possess interesting nonlinear optical properties to be applied for noncritical phase-matching second-harmonic generation (SHG) and third harmonic generation (THG) of Nd:YAG laser [2]. The NLO characteristics of RECOB crystals are sensitive to chemical compositions. The refractive index of Gd_xY_{1-x}COB varies continuously depending on *x* to change the phase-matching conditions. In bulk single crystals, rare earth substitution is limited by thermodynamics [3],

* Corresponding author. Tel.: +81-45-924-5314;

fax: +81-45-924-5377.

E-mail address: koinuma1@oxide.msl.titech.ac.jp (H. Kubota).

whereas a wider allowance of elemental substitution can be expected in thin films deposited under non-equilibrium conditions. We already reported that $\text{Gd}_x\text{Y}_{1-x}\text{COB}$ ($x = 0 \sim 1$) thin films could be epitaxially grown on atomically flat GdCOB (0 1 0) substrates to exhibit SHG [4]. Especially $\text{Gd}_{0.28}\text{Y}_{0.72}\text{COB}$ film satisfied the type II phase matching condition along the b axis as in the case of the bulk single crystal.

Recently, a new function of this material was reported [5]. Red laser light of self frequency doubling of the 1332 nm emitted by the ${}^4\text{F}_{3/2} \rightarrow {}^4\text{I}_{13/2}$ transition of Nd^{3+} in $\text{Nd}:\text{YCOB}$ crystal [6]. The $\text{Nd}:\text{RECOB}$ crystal has such a potential application as tricolor laser display. Here, we report on the first successful fabrication of a series of RECOB epitaxial thin films by combinatorial laser MBE method and on the optical properties that laid the foundation of self-frequency doubling toward the RECOB-based laser emitting device.

2. Experimental

Our combinatorial laser MBE system used in this study was equipped with $\text{Nd}:\text{YAG}$ cw laser heating [7] and scanning reflection high energy electron diffraction (S-RHEED) [8]. In order to achieve the high

throughput optimization of the epitaxial growth temperature for each RECOB film, the film was grown on an atomically flat GdCOB (0 1 0) single crystal substrate whose temperature was varied from 750 to 550 °C by the laser heating focused on an one edge of the substrate. The S-RHEED was used for in situ characterization of the lattice structure of growing films at various sites of the substrate. We determined the epitaxial nature of the films by using concurrent X-ray diffraction (CXRD) [9]. $\text{EuCOB}\text{--}\text{ScCOB}\text{--}\text{PrCOB}$ ternary composition spread film was fabricated by using a specially designed mask scheme. The detailed process will be described elsewhere [10]. A pulsed KrF excimer laser ($\lambda = 248$ nm) with a laser fluence of 5 J/cm^2 was focused on sintered RECOB targets in 1.3×10^{-4} Pa oxygen at 5 Hz repetition rate. Photoluminescence (PL) property was investigated by taking a color photograph of the chip under excitation with an ultraviolet (254 nm) lamp. The corresponding PL spectra were also measured by excitation with a frequency doubled Ar laser (488 nm).

3. Results and discussion

Fig. 1 shows a series of RHEED patterns of YbCOB film observed at various sites of the substrate, which

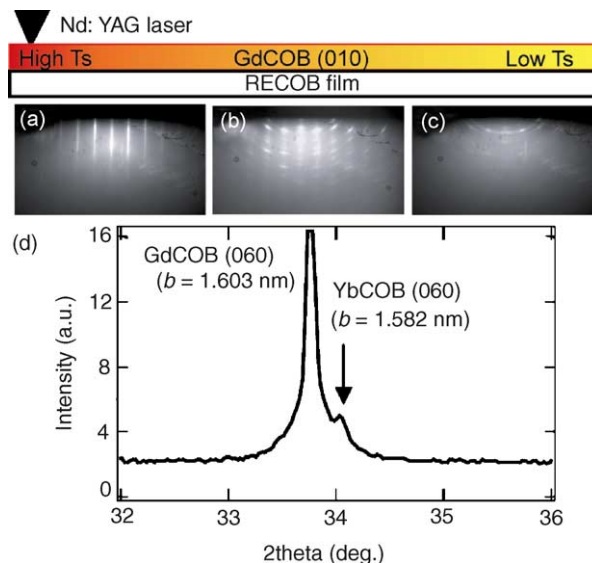


Fig. 1. A series of RHEED patterns of YbCOB film library grown at 750 °C (a), 680 °C (b), 650 °C (c). (d) CXRD pattern of YbCOB epitaxial film grown at 750 °C.

correspond to the growth temperature of (a) 750, (b) 680, (c) 650 °C, respectively. At 750 °C, the RHEED streak pattern was as sharp as the pattern of the GdCOB substrate at the same azimuth angle of the incident electron beam, indicating that the YbCOB film was grown epitaxially on GdCOB at this temperature. Decreasing the substrate temperature to 650 °C changed the RHEED pattern spotty and hallos due to the polycrystalline nature of the film. The YbCOB film grown at 750 °C also showed a clear and strong peak of (0 6 0) in the CXRD pattern (Fig. 1d). The small *b*-axis length of YbCOB ($b = 1.582$ nm) compared to that of GdCOB ($b = 1.603$ nm) could be explained by taking the ion radius of Yb into account. In this way, the optimal growth temperature for YbCOB epitaxial film was determined in a single experiment.

The temperature gradient method was applied to high throughput optimization of other RECOB films (RE = Sc, La ~ Nd, Sm ~ Lu). S-RHEED and CXRD analyses revealed that all the RECOB films were epitaxially grown in specific temperature ranges that varied depending on the RE elements. The lowest temperature for epitaxial growth was plotted against ion radius of the RE element as shown in Fig. 2 to be the lowest for RE = Gd. There is a tendency that the lowest temperature for epitaxial growth increases at the both smaller and larger ion radius sides of Gd. Since GdCOB substrate was used in these experiments, this remarkable trend should reflect a stress effect from the lattice mismatching between the film and substrate.

Among RECOB epitaxial films, TbCOB and EuCOB films were found to emit green (543 nm) and red

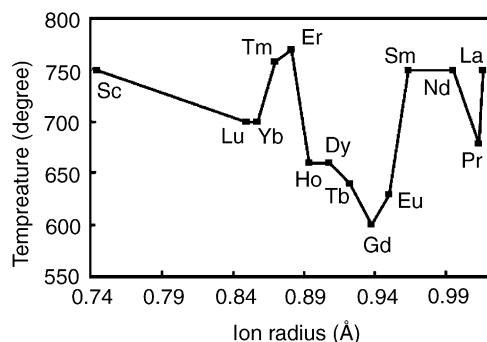


Fig. 2. The lowest temperature estimated for epitaxial growth plotted against the ion radius of RE element.

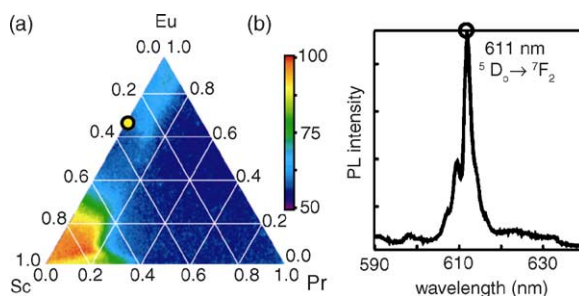


Fig. 3. PL intensity map for $\text{Eu}_{1-x-y}\text{Sc}_x\text{Pr}_z\text{COB}$ ternary composition spread film under ultraviolet (254 nm) excitation (a), and the PL spectrum (b) measured at the point marked \circ in (a).

(611 nm) light, respectively. The effect of RE element substitution on the PL property was investigated by the fabrication of the EuCOB–ScCOB–PrCOB ternary composition spread film library on YCOB (1 0 0) substrate. The variation of ion radius from small Sc to large Pr was presumed to induce a significant stress effect on the PL intensity.

Fig. 3a shows the PL intensity mapping under an excitation with a UV lamp (254 nm). Strong red emission is clearly seen at Sc-rich region and the composition of $\text{Eu}_{0.09}\text{Sc}_{0.85}\text{Pr}_{0.06}\text{COB}$ gives a maximum intensity. Pr substitution drastically decreases its intensity, suggesting that Pr^{3+} ion behaves as inhibitor due to the energy transfer from Eu^{3+} to Pr^{3+} . By Eu substitution from the maximum intensity region, the intensity decreases and then increases to be moderately high Eu-rich region. The intensity decrease should be due to the concentration quenching. Fig. 3b is a typical PL spectrum under an excitation with frequency doubled Ar laser (488 nm) taken at a composition of $\text{Eu}_{0.65}\text{Sc}_{0.35}\text{COB}$ which is marked in Fig. 3a. The light emission at 611 nm corresponds to the red from the Eu^{3+} ion via $^5\text{D}_0 \rightarrow ^7\text{F}_2$ transition of 4f electron.

4. Conclusion

RECOB (RE = Sc, La ~ Nd, Sm ~ Lu) thin films were grown on a temperature gradient substrate to optimize the film growth conditions. S-RHEED and concurrent X-ray diffraction analyses revealed that each RECOB could be epitaxially grown in a specific temperature range that varied depending on the rare earth element. From the results of PL properties of the

RECOB films, RECOB is a material promising as a host for phosphors.

Acknowledgements

Y. Matsumoto acknowledges The Murata Science Foundation for the financial support of this work.

References

- [1] E. Wright, G.L. Stegeman, in: C.G. Someda, G.I. Stegeman (Eds.), *Anisotropy and Nonlinear Optical Waveguides*, Elsevier, North-Holland, 1992.
- [2] M. Yoshimura, H. Furuya, T. Kobayashi, K. Murase, Y. Mori, T. Sasaki, *Optics Lett.* 24 (1999) 193.
- [3] Q. Ye, B.H.T. Chai, *J. Cryst. Growth* 197 (1999) 228–235.
- [4] T.-W. Kim, N. Arai, Y. Matsumoto, M. Yoshimura, H. Furuya, Y. Mori, T. Sasaki, H. Koinuma, *Appl. Phys. Lett.* 799 (2001) 1783.
- [5] A. Aron, P.Y. Tigreat, A. Caramanian, E. Antic-Fidancev, B. Viana, G. Aka, D. Vivien, *J. Lumin.* 87–89 (2000) 611.
- [6] Q. Ye, L. Shah, J. Eichenholz, D. Hammons, R. Peale, M. Richardson, A. Chin, B.H.T. Chai, *Opt. Commun.* 164 (1999) 33–37.
- [7] T. Koida, D. Komiyama, H. Koinuma, M. Ohtani, M. Lippmaa, M. Kawasaki, *Appl. Phys. Lett.* 80 (2002) 565–567.
- [8] T. Ohnishi, D. Komiyama, T. Koida, S. Ohashi, C. Stauter, A. Ohtomo, M. Lippmaa, N. Nakagawa, M. Kawasaki, T. Kikuchi, K. Omote, H. Koinuma, *Appl. Phys. Lett.* 79 (2001) 536.
- [9] M. Ohtani, T. Fukumura, M. Kawasaki, K. Omote, T. Kikuchi, J. Harada, A. Ohtomo, M. Lippmaa, T. Ohmishi, D. Komiyama, R. Takahashi, Y. Matsumoto, H. Koinuma, *Appl. Phys. Lett.* 79 (2001) 3594.
- [10] R. Takahashi, H. Kubota, M. Murakami, Y. Yamamoto, Y. Matsumoto, H. Koinuma, *J. Combi. Chem.*, in press.

Superradiance and Dipole Ordering of an N Two-Level System Interacting with Optical Near Fields

Akira SHOJIGUCHI*, Kiyoshi KOBAYASHI, Suguru SANGU, Kazuo KITAHARA¹ and Motoichi OHTSU²

ERATO Localized Photon Project, Japan Science and Technology, Tokyo 194-0004

¹*Division of Natural Sciences, International Christian University, Tokyo 181-8585*

²*Interdisciplinary Graduate School of Science and Engineering, Tokyo Institute of Technology, Yokohama 226-8502*

(Received January 14, 2003)

A model is presented for a system of N two-level excitons interacting with each other via optical near fields represented as localized photons. In a low exciton density limit, quantum dynamics of the dipole moments or quantum coherence between any two energy levels is linear. As the exciton density becomes higher, the dynamics becomes nonlinear, and the system has several kinds of quasi-steady states of the dipole distribution depending on the system parameters. These quasi-steady states are classified with the help of the effective Hamiltonian that is derived from the renormalization of degrees of freedom of localized photons with a unitary transformation. Among them there exist a “ferromagnetic” state (dipole-ordered state), in which all electric dipoles are aligned in the same direction, and an “anti-ferromagnetic” state, where all dipoles alternately change the direction. In addition, we show that an arbitrary state can be transformed into a dipole-ordered state by manipulating initial values of the population differences appropriately. For example, if we initially prepare a dipole-forbidden state, which is similar to the “anti-ferromagnetic” state and cannot be coupled with propagating far fields, and if we manipulate the distribution of the population differences properly, the initial state evolves into a dipole-ordered state. The radiation property of such dipole-ordered states is examined in detail. Neglecting energy dissipation by radiation, we find that some of the ordered states show strong radiation equivalent to Dicke’s superradiance. Then by introducing a radiation reservoir, the dissipative master equation is derived. Solving the equation with and without quantum correlations, we numerically show that multiple peaks in the radiation profile can survive in both cases. The mechanism of this phenomenon is discussed, and a brief comment on an application to photonic devices on a nanometer scale is given.

KEYWORDS: optical near field, localized photon, local coupling, global coupling, quantum dot, exciton, electric dipole, superradiance, Dicke model

DOI: 10.1143/JPSJ.72.2984

1. Introduction

1.1 Background and optical near fields

Recent progress in nano-fabrication and nano-manipulation has enabled us to explore the excitonic processes and to control quantum states in an electronically isolated semiconductor quantum dot (QD) or several coupled quantum dots (QDs) that are also electronically isolated from other QDs.¹⁾ Near-field optical approaches have achieved a breakthrough in nano-optics, in nano-science, and in nano-technology, utilizing the spatial localization and ultra-high speed originating from the strong coupling of matter and light on a nanometer scale. For example, scanning near-field optical microscopes (SNOM) have been developed as optical microscopes with resolution far beyond the diffraction limit of light.²⁾ A variety of experiments have been carried out in order to control and to manipulate a single atom, molecule, or QD with accuracy beyond the diffraction limit.³⁾ In the near future, the exciton dynamics will be experimentally investigated with the help of the near-field optical techniques⁴⁾ by the local excitation of arbitrarily selected QDs. Therefore, optical near fields are essential for the exploration of excitation processes in a confined space. Optical near fields are localized around a material system, *e.g.*, around a near-field probe tip or a QD system, depending on the size of them, and thus their noticeable effects manifest themselves when the two systems are close within a distance of the order

of the size. The interaction between two material systems is even more dominated by optical near fields, not by propagating light or far fields, if the size of the two systems is smaller than the wavelength of light, and optical near fields and material polarization are mutually related. Therefore in nano-optics, one has to consistently describe both material systems and optical near fields, and needs to know the dynamical properties of the material systems interacting with optical near fields.

We give a few examples to understand the spatial localization of optical near fields. The evanescent field generated on a planar dielectric surface can be obtained by analytical continuation of the wave vector k_{\perp} normal to the surface as $\exp(i\mathbf{k}_{\parallel} \cdot \mathbf{r} - \gamma z)$ with $k_{\perp} = i\gamma$ (γ : real), whose localization range is about that of the wavelength of incident light. Similarly, optical near fields around a tiny dielectric sphere whose size is much smaller than the wavelength is described by the spherical Hankel function with analytic continuation of the radial component of the wave vector k_{\perp} to the pure imaginary $k_{\perp} = i\gamma$; the first kind Hankel function of order 0 gives a typical form of optical near field around a sphere as

$$\phi = \frac{e^{-\gamma r}}{\gamma r}. \quad (1.1)$$

The fields satisfying the spherical boundary condition can be expanded in terms of plane waves, or can be expressed in the angular spectrum representation, and it follows from a numerical analysis that the distribution of the angular

*E-mail: akirasho@ohtsu.jst.go.jp

spectrum has a peak at $\gamma = 1/a$.²⁾ Applying the result to eq. (1.1), we see that the localization range of optical near fields around a sphere is of the order of the radius a , i.e., the size of the material system. Here note that optical near fields should be derived from microscopic polarization of matter by using, for example, a nonlocal theory in a semi-classical way proposed by Cho,⁵⁾ though we can formally obtain an optical near field from a solution of the Helmholtz' equation by analytical continuation of the normal component of the wave vector to the pure imaginary.

We are interested in the dynamics of nanometric material systems interacting with optical near fields as well as quantum behaviors. However, it is very difficult to employ the nonlocal approach for the quantization of the electromagnetic fields and for treating the dynamics of the material systems and the optical fields because of the complexities of the self-consistent procedure in practice. Moreover, we have no formal or phenomenological theory to resolve the above problems. Therefore a new approach is required, which enables us to easily deal with the quantum dynamics of material systems interacting with optical near fields. In this paper, we address the issues and present a simple phenomenological model of optical near fields in order to discuss dynamical properties of a nanometric material system interacting with optical near fields.

1.2 Optical near fields and propagating fields

The main difference between a material system coupled with optical near fields and a material system coupled with propagating far fields, is that one is locally coupled and the other is globally coupled as schematically depicted in Fig. 1. Since the propagating field is usually expanded in terms of a plane wave basis, emitted photons as plane waves propagates from one site to far sites of the material system and can excite the far sites, as shown in Fig. 1(a). On the other hand, as shown in Fig. 1(b), "near field photons" or "localized photons" can only move to near sites and excite them. Generally speaking, the dynamics of a locally coupled system is different from that of a globally coupled system in respect to the relaxation speed towards equilibrium.⁶⁾ Therefore we can expect that the dynamics and equilibrium states for a locally coupled system are different from those for an ordinary globally coupled system such as a propagating field-matter system.⁷⁾ From this point of view, it is significant to investigate a nanometric material system interacting with optical near fields.

In this paper we present a model for a material system, in particular, for a quantum dot system interacting with optical

near fields, and discuss the dynamics of the electric dipole moment and the radiation property of the system in detail. For comparison a material system interacting with radiation field is also examined. We study the propagation of an initial excitation signal in a quantum dot which is locally prepared by optical near fields, and is described in terms of excitons in an N two-level system. In a dilute limit, excitons are approximately treated as bosons, and a rigorous solution of the Heisenberg equation shows that the dipole moment representing quantum coherence between any two levels follows linear dynamics. In a non-dilute case, excitons at a site obey the fermion commutation relations while excitons at different sites satisfy the bose commutation relations, which results in nonlinear equations of motion. We predict a coherent oscillation of all the dipoles of the system (dipole ordering), and strong radiation from some of the dipole-ordered states, which are close to the Dicke's superradiance.⁸⁾

1.3 Two-level system with propagating fields: Dicke's superradiance

Superradiance, the cooperative emission of radiation from a collection of excited two-level systems was originally discussed by Dicke in 1954. He found that under a certain condition the radiation rate is proportional to the square of the number of two-level systems involved, and that an intense pulse is emitted.⁸⁾ Superradiant phenomena have occupied considerable attention of a large number of authors in 1970's.⁹⁻²³⁾ In a small system whose size is much smaller than the wavelength of radiation, the equations of motion for the two-level system coupled to the radiation field (Dicke model) is given as follows:

$$\frac{\partial \rho_A}{\partial t} = -\gamma_0(R_+R_- \rho_A - 2R_- \rho_A R_+ + \rho_A R_+ R_-), \quad (1.2)$$

where ρ_A is the density operator after eliminating radiation field's degrees of freedom from total density operator of the system, R_{\pm} is the collective raising and lowering operators of a two-level system,⁸⁾ and $2\gamma_0$ is the inverse of the spontaneous emission lifetime of each two-level system (Einstein's A-coefficient). From eq. (1.2) one obtains differential equations of the observables of the two-level system and a radiation pulse emitted under a certain initial condition whose height and width are proportional to N^2 and $1/N$, respectively. By using a semi-classical approximation of neglecting quantum correlations in the two-level system, an analytical solution^{10,13)} for radiation intensity I is written as

$$I \propto N^2 \operatorname{sech}^2[\gamma_0 N(t - t_0)], \quad (1.3)$$

which shows a radiation profile of the cowbell shape. It should be noted that the semi-classical approximation does not correctly predict the dynamics starting from the completely inverted states^{13,14)} with no dipole moments because the quantum fluctuations of the dipole moments are essential in the radiation process.

In a large system the superradiant state is affected by both inhomogeneity of the two-level system in a sample and reabsorption of emitted photons,¹⁶⁾ which results in the decoherence; namely, some part of the coherence in the system is destroyed by the induced dipole-dipole interaction. It leads to reduction of the peak height and an extension

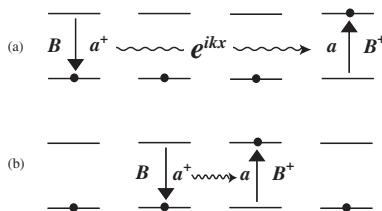


Fig. 1. Schematic drawing for (a) a global coupling system and (b) a local coupling system. Each element of the system in (a) can directly interact with arbitrary elements at far site while elements at near site can only interact with each other in (b).

of the tail of the radiation profile.^{16,17)} For a two-level system confined in a long cylindrical shape of sample, Bonifacio *et al.* predicted multiple peaks in the radiation profile that stem from the stimulated absorptions and emissions in the long active region.^{15,20)} Experimental observation using a cylindrical sample was done by Skribanowitz *et al.*¹⁸⁾ and the experimental results were analysed by Bonifacio *et al.*¹⁹⁾ For a small two-level system emission spectra of CuCl quantum dots were measured, and a single peak of pulse emission was reported by Nakamura *et al.*²³⁾ Tokihiro *et al.* examined a linear excitonic system, where excitons can hop from one site to its nearest neighbors due to the dipole–dipole interaction, and showed that radiation from a totally inverted state as an initial condition exhibits a reduction of the peak intensity and the extension of the tail,²¹⁾ as discussed by Coffey *et al.*¹⁷⁾ They also claimed that radiation from a partially excited state shows an oscillatory behavior of the radiation profile as indicated by Bonifacio *et al.*²⁰⁾ It is clear that the peak intensity reduction of radiation in both cases comes from the dipole–dipole decoherence, but it is not obvious whether the origin of the multiple pulse generation is the same or not. We also show multiple pulse emission in our model, and discuss the mechanism.

1.4 Outline

The paper is organized as follows. In §2 we present a model of an N two-level quantum dot system interacting with optical near fields represented in terms of localized photons, and the model Hamiltonian. In §3 a rigorous solution of the equations of motion for the system is obtained within a boson approximation. With the help of the solution we investigate the propagation of the dipole moments of the system. In §4 without using the boson approximation we obtain the second-order perturbative solution to show the dynamics of the system. In §5 an effective Hamiltonian is introduced by renormalizing degrees of freedom of localized photons. With the help of the effective Hamiltonian we classify the quasi-steady states of the dipole distribution in order to discuss the origin of the dipole ordering. In §6 we examine the radiation property of the system in a weak limit, where the radiation field does not affect the dynamics of the system. In order to discuss the radiation property of the dissipative system, in §7, the master equation is derived after introducing a radiation reservoir, and is solved with and without including quantum correlations between excitons and localized photons. Finally in §8 concluding remarks are provided.

2. Model Hamiltonian

One of the most important features of optical near fields is the localization property, where it is not suitable to use a broad spreading wave as a basis function of quantization of the fields. Therefore, it is significant to find a good normal mode of the electromagnetic fields to satisfy a peculiar boundary condition, by which the optical near fields are produced and quantized.^{24–26)} It is difficult, however, to find a general and appropriate normal mode satisfying any arbitrary boundary conditions. As an alternative approach, it is possible to model optical near fields and their important characters phenomenologically. Such an approach is adopted in this paper to formulate the problem and to discuss the

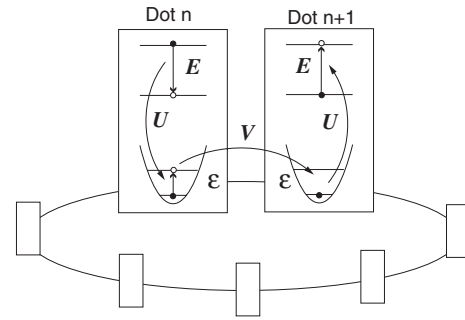


Fig. 2. Schematic diagram of a model system: N two-level QDs labelled by the site number are closely located in a ring, and are interacting with localized photons.

dynamics of a nanoscale material system.

To describe the localizability of the optical near fields it is very effective to use a localized basis function such as a Wannier function or a delta function instead of a plane wave. However, at the same time we need to describe the property of a short range interaction, or a steep gradient of optical near fields. Taking into account such circumstances we model optical near fields phenomenologically in terms of localized photons which are described as a harmonic oscillator localized in each quantum dot site, and are only allowed to hop from one site to the nearest neighbors.²⁸⁾ Figure 2 schematically describes our model system. We suppose a closely located quantum dot chain as a nano-scale material system that is expressed as a one-dimensional N two-level system, or an excitonic system with a periodic boundary condition. Since each exciton can only interact with localized photons in the same QD, each quantum dot indirectly interacts with one another via localized photons, as illustrated in Fig. 2. This model is based on the unique property of localization or non-propagation of optical near fields mentioned above,²⁵⁾ and is preferable for an intuitive understanding of coherent excitation transfer between the QDs and its manipulation by the localized photons. The model Hamiltonian of the system can be written as

$$H = H_a + H_b + H_{\text{int}}, \quad (2.1)$$

where H_a describes localized photons, H_b describes excitons, and H_{int} represents the localized photon–exciton interaction. Each Hamiltonian can be expressed as

$$H_a = \sum_{n=1}^N \{ \epsilon a_n^\dagger a_n + V (a_{n+1}^\dagger a_n + a_n^\dagger a_{n+1}) \}, \quad (2.2a)$$

$$H_b = E \sum_{n=1}^N b_n^\dagger b_n, \quad (2.2b)$$

$$H_{\text{int}} = U \sum_{n=1}^N (a_n^\dagger b_n + b_n^\dagger a_n), \quad (2.2c)$$

where n indicates the site number, and a_n (a_n^\dagger) and b_n (b_n^\dagger) represent annihilation (creation) operators of a localized photon and an exciton, respectively. The periodic boundary condition requires that the $(N + 1)$ -th site corresponds to the first site. The constant energies of the localized photons and excitons are represented $\epsilon = \hbar\omega$ and $E = \hbar\Omega$, respectively. The hopping energy of the localized photons is represented

as $V = \hbar v$, and $U = \hbar g$ gives the strength of the conventional dipolar coupling between the localized photons and the excitons in the rotating wave approximation.

We apply the boson commutation relations to the localized photons as

$$[a_n, a_{n'}^\dagger] = \delta_{nn'}, \quad [a_n, a_{n'}] = [a_n^\dagger, a_{n'}^\dagger] = 0. \quad (2.3)$$

The creation operator of an exciton, b_n^\dagger , can be written in terms of the annihilation operator of a valence electron of n th site, c_{n0} , and the creation operator of a conducting electron of n th site, c_{nf}^\dagger , as $b_n^\dagger = c_{nf}^\dagger c_{n0}$. In the same way, the annihilation operator of an exciton, b_n , can be written as $b_n = c_{n0}^\dagger c_{nf}$. Assuming that only one exciton is generated in a quantum dot site, we obtain the relation as $N_f + N_0 = c_{nf}^\dagger c_{nf} + c_{n0}^\dagger c_{n0} = 1$. With the help of these expressions and the fermi commutation relations for electrons, the commutation relations for excitons are derived as^{27,29)}

$$[b_{n'}, b_n^\dagger] = \delta_{nn'}(1 - 2b_n^\dagger b_n), \quad (2.4)$$

which shows that excitons behave as fermions at intra-site and as bosons at inter-site. It follows from eq. (2.4) that excitons are approximated as bosons in a dilute limit of the exciton density, $\langle b_n^\dagger b_n \rangle \equiv \langle N_n \rangle \ll 1$.

With the boson approximation, the Heisenberg equations of motion can be rigorously solved. First, we obtain a rigorous solution of the Heisenberg equations for bosonic excitons to investigate the dynamical properties. Then we investigate the dynamics of fermionic excitons, solving the Heisenberg equations both perturbatively and numerically.

3. Dynamics of Bosonic Excitons

3.1 Boson approximation and diagonalization of the Hamiltonian

To solve the Heisenberg equation we introduce the spatial Fourier transformation for a_n and b_n as

$$A_k = \frac{1}{\sqrt{N}} \sum_{n=1}^N e^{ikn} a_n, \quad (3.1a)$$

$$B_k = \frac{1}{\sqrt{N}} \sum_{n=1}^N e^{ikn} b_n, \quad (3.1b)$$

where we set $k = 2\pi l/N$ for $l = 1, \dots, N$ and the lattice constant as 1. Fourier transforms A_k satisfy the following commutation relations

$$[A_k, A_{k'}^\dagger] = \delta_{kk'}, \quad [A_k, A_{k'}] = [A_k^\dagger, A_{k'}^\dagger] = 0, \quad (3.2)$$

and the commutation relations of Fourier transforms B_k are similarly obtained as

$$\begin{aligned} [B_k, B_{k'}^\dagger] &= \frac{1}{N} \sum_{n,n'} e^{i(kn-k'n')} [b_n, b_{n'}^\dagger] \\ &= \frac{1}{N} \sum_n e^{i(k-k')n} (1 - 2b_n^\dagger b_n). \end{aligned} \quad (3.3)$$

It follows from this expression that when the expectation value of the number of excitons is small as $\langle b_n^\dagger b_n \rangle \ll N$, the second term of the right hand side of eq. (3.3) can be neglected, and excitons are approximated as bosons as

$$[B_k, B_{k'}^\dagger] = \delta_{kk'}, \quad [B_k, B_{k'}] = [B_k^\dagger, B_{k'}^\dagger] = 0, \quad (3.4)$$

where the following relation

$$\frac{1}{N} \sum_n e^{i(k-k')n} = \delta_{kk'} \quad (3.5)$$

is used. Fourier inverse transforms are also given as

$$a_n = \frac{1}{\sqrt{N}} \sum_{k \in 1BZ} e^{-ikn} A_k, \quad (3.6a)$$

$$b_n = \frac{1}{\sqrt{N}} \sum_{k \in 1BZ} e^{-ikn} B_k, \quad (3.6b)$$

where the summation of k runs over the first Brillouin zone (1BZ). Using eqs. (3.1a), (3.1b), and the following relation

$$\frac{1}{N} \sum_{k \in 1BZ} e^{ik(n-n')} = \delta_{nn'}, \quad (3.7)$$

we can transform the Hamiltonian (2.1) into a Fourier transform representation

$$\begin{aligned} H &= \sum_k \{(\varepsilon + 2V \cos k) A_k^\dagger A_k + E B_k^\dagger B_k \\ &\quad + U(A_k B_k^\dagger + A_k^\dagger B_k)\} \equiv \sum_k H_k. \end{aligned} \quad (3.8)$$

Note that the dispersion relation of localized photons is changed from ε to $(\varepsilon + 2V \cos k)$. The transformed Hamiltonian H_k can be diagonalized into a simple quadratic form

$$\begin{aligned} H_k &= (A_k^\dagger, B_k^\dagger) \begin{pmatrix} \varepsilon + 2V \cos k & U \\ U & E \end{pmatrix} \begin{pmatrix} A_k \\ B_k \end{pmatrix}, \\ &\equiv (A_k^\dagger, B_k^\dagger) \begin{pmatrix} e & U \\ U & E \end{pmatrix} \begin{pmatrix} A_k \\ B_k \end{pmatrix} \\ &\equiv \sum_{i,j=1}^2 M_{ij} X_i^\dagger(k) X_j(k), \end{aligned} \quad (3.9)$$

where the abbreviations $e = \varepsilon + 2V \cos k$ and $X^\dagger(k) = (A_k^\dagger, B_k^\dagger)$ are used. The matrix kernel of the Hamiltonian, M , is diagonalized as

$$S^T M S = \begin{pmatrix} \lambda_+ & 0 \\ 0 & \lambda_- \end{pmatrix}, \quad (3.10)$$

by an orthogonal matrix S

$$S = \begin{pmatrix} \sqrt{\frac{L+K}{2L}} & \sqrt{\frac{L-K}{2L}} \\ \sqrt{\frac{L-K}{2L}} & -\sqrt{\frac{L+K}{2L}} \end{pmatrix}. \quad (3.11)$$

Here eigenvalues λ_\pm are written as

$$\begin{aligned} \lambda_\pm &= \frac{e+E}{2} \pm \frac{1}{2} \sqrt{(e-E)^2 + 4U^2} \\ &\equiv K + E \pm L \end{aligned} \quad (3.12)$$

with $K = (e-E)/2$ and $L = \sqrt{K^2 + U^2}$. Using the polariton transformation as

$$\begin{pmatrix} \alpha_k \\ \beta_k \end{pmatrix} \equiv S^T \begin{pmatrix} A_k \\ B_k \end{pmatrix}, \quad (3.13)$$

we can finally diagonalize the Hamiltonian (3.8) as follows:

$$H = \sum_k H_k = \sum_k (\lambda_+ \alpha_k^\dagger \alpha_k + \lambda_- \beta_k^\dagger \beta_k). \quad (3.14)$$

3.2 Dipole dynamics driven by local excitation

With the help of the diagonalized Hamiltonian eq. (3.14), we can immediately solve the Heisenberg equation and can express the time evolution of exciton–polariton operators (α_k and β_k) as

$$\begin{pmatrix} \alpha_k(t) \\ \beta_k(t) \end{pmatrix} = \begin{pmatrix} e^{-i\lambda_+ t/\hbar} \alpha_k \\ e^{-i\lambda_- t/\hbar} \beta_k \end{pmatrix}, \quad (3.15)$$

where α_k and β_k denote the operators in the Schrödinger representation. It is assumed in this paper that an operator with no indication of the time dependence is expressed in the Schrödinger picture as a time-independent operator. From the inverse transformation of eq. (3.13), we obtain a time-dependent solution of the Fourier transforms [$A_k(t)$ and $B_k(t)$] as

$$\begin{pmatrix} A_k(t) \\ B_k(t) \end{pmatrix} = S \begin{pmatrix} \alpha_k(t) \\ \beta_k(t) \end{pmatrix} = S \begin{pmatrix} e^{-i\lambda_+ t/\hbar} \alpha_k \\ e^{-i\lambda_- t/\hbar} \beta_k \end{pmatrix}. \quad (3.16)$$

By transforming the exciton–polariton operators (α_k and β_k) into (A_k and B_k) again, explicit time-dependent solutions $A_k(t)$ and $B_k(t)$ of the Heisenberg equations are written as

$$\begin{aligned} A_k(t) &= e^{-i(e+E)t/2\hbar} \left(\cos \frac{L}{\hbar} t - i \frac{K}{L} \sin \frac{L}{\hbar} t \right) A_k \\ &\quad - i \frac{U}{L} e^{-i(e+E)t/2\hbar} \left(\sin \frac{L}{\hbar} t \right) B_k, \end{aligned} \quad (3.17a)$$

$$\begin{aligned} B_k(t) &= -i \frac{U}{L} e^{-i(e+E)t/2\hbar} \left(\sin \frac{L}{\hbar} t \right) A_k \\ &\quad + e^{-i(e+E)t/2\hbar} \left(\cos \frac{L}{\hbar} t + i \frac{K}{L} \sin \frac{L}{\hbar} t \right) B_k. \end{aligned} \quad (3.17b)$$

Using the Fourier inverse transformation, we obtain a final expression of the time evolution of the exciton operator $b_n(t)$ as follows:

$$\begin{aligned} b_n(t) &= \frac{1}{N} \sum_{k,m} e^{ik(m-n) - i(e+E)t/2\hbar} \\ &\quad \times \left\{ -i a_m \frac{U}{L} \sin \frac{L}{\hbar} t + b_m \left(\cos \frac{L}{\hbar} t + i \frac{K}{L} \sin \frac{L}{\hbar} t \right) \right\}. \end{aligned} \quad (3.18)$$

Here we introduce a physical quantity of the electric dipole moment for our two-level system defined as

$$\boldsymbol{\mu}_n(t) = \boldsymbol{\mu}(b_n(t) + b_n^\dagger(t)) = \boldsymbol{\mu} P_n(t), \quad (3.19)$$

where $P_n(t) = b_n(t) + b_n^\dagger(t)$ denotes the dipole operator that describes the electric dipole moment of each quantum dot. Moreover, two other independent operators are defined as

$$\begin{aligned} V_n(t) &= i(b_n(t) - b_n^\dagger(t)), \\ W_n(t) &= b_n^\dagger(t)b_n(t) - b_n(t)b_n^\dagger(t), \end{aligned} \quad (3.20)$$

where the latter represents the population difference of the system. The unit operator and these three operators form a basis for any two-level system, and the set (P_n, V_n, W_n) corresponds to the Bloch vector in a collection of two-level

atom system. However, it should be noted that the population difference W_n is always -1 for bosonic excitons, and the number operators of excitons $b_n^\dagger b_n$ are the independent operators in this case.

In order to investigate the coherent excitation dynamics of the system, we examine the time evolution of the expectation value of the dipole moment at an arbitrary QD n , $\langle P_n(t) \rangle$, under a variety of initial conditions. The expression given by eq. (3.18) and its Hermitian conjugate provide a useful result as

$$\begin{aligned} \langle P_n(t) \rangle &= \frac{1}{N} \sum_{k \in 1BZ} \sum_{m=1}^N \left\{ (\langle P_m \rangle \cos \xi_{mn} + \langle V_m \rangle \sin \xi_{mn}) \cos \frac{L}{\hbar} t \right. \\ &\quad \left. + \frac{K}{L} (\langle V_m \rangle \cos \xi_{mn} - \langle P_m \rangle \sin \xi_{mn}) \sin \frac{L}{\hbar} t \right\}, \end{aligned} \quad (3.21)$$

where the operation $\langle \dots \rangle = \text{Tr} \rho \dots$ means the expectation value of an arbitrary operator. The notation $\xi_{mn} \equiv k(m-n) - t(e+E)/2\hbar$ is used. Localized photons are assumed to be initially in the vacuum state. In particular, it is intriguing to investigate the dynamics with the initial condition of a locally excited state, i.e., how the initial excitation prepared only at one site propagates in the system. Setting $\langle P_n(0) \rangle = \delta_{n1} \langle P_1 \rangle$ and $\langle V_n(0) \rangle = 0$ for all n , we obtain from eq. (3.21) an explicit solution as

$$\langle P_n(t) \rangle = \frac{1}{N} \sum_k \left\{ \cos \xi_{1n} \cos \frac{L}{\hbar} t - \frac{K}{L} \sin \xi_{1n} \sin \frac{L}{\hbar} t \right\} \langle P_1 \rangle. \quad (3.22)$$

In Fig. 3 we present one of numerical results of the time evolution of the dipole moment distribution calculated from eq. (3.22), where the total number of sites is eight, and the parameter values $E = 2$, $\varepsilon = 1$, and $V = 1$ are used in a unit of a typical exciton energy in QD. Although the dynamics seems complicated at first sight, we can find a characteristic behavior that the dipole of the first site moves to the fifth site (the opposite site) and returns to the first site again. To see the behavior more precisely we show plots of the time evolution of the dipole moments of the first site and the fifth site in Figs. 4(a) and 4(b), respectively. The result clearly shows as a dominant behavior that when the dipole of the first site is active, that of the fifth site is inactive and *vice versa*, or the dipole moves like a seesaw between the first site and the fifth site. The recurrence behavior is reasonable from the fact that the Heisenberg equation of the system is linear in the boson approximation. Since the dipole moment P_n is quantum coherence between the ground and excited states of a two-level system, quantum coherence is transported to the farthest site of the chain and then comes back to the original site. When the total number of sites is odd, the seesaw motion arises between an initially excited site and its farthest pair of sites of the chain. An interesting point in this case is that we can obtain two copies of coherence at the farthest pair of sites as illustrated in Fig. 5(b). Moreover, it might be possible to use the system as a nanophotonic device of transporting or splitting quantum coherence.

4. Dynamics of Fermionic Excitons

If we rigorously adopt the commutation relation for excitons given by eq. (2.4), the Heisenberg equations for the

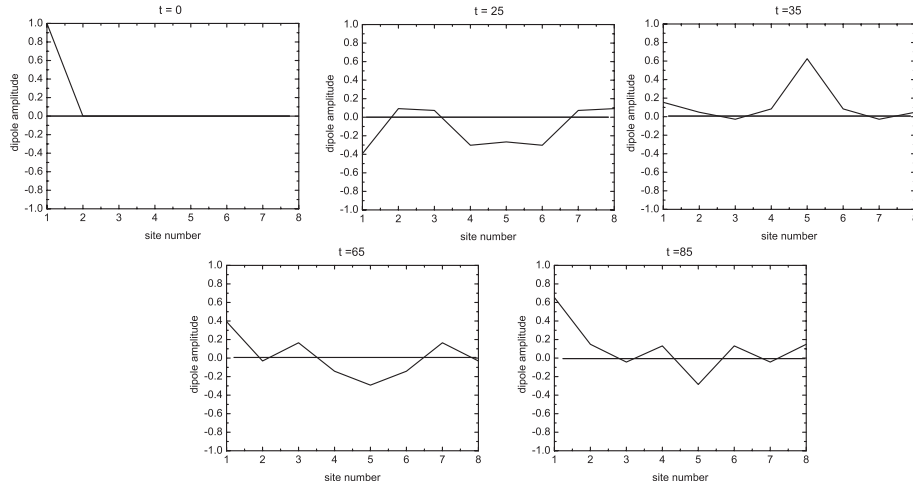


Fig. 3. Time evolution of the dipole-moment distribution when the total number of sites is eight. The parameter $E = 2$, $\varepsilon = 1$, and $V = 1$ are used in the calculation. The vertical and horizontal axes represent the dipole amplitude and the site number, respectively. The dipole moment is initially set only at the first site.

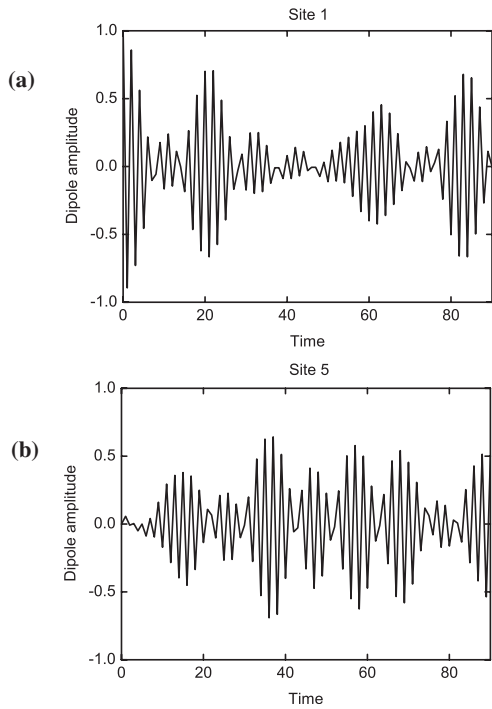


Fig. 4. Time evolution of the dipole moment of (a) the first site and (b) the fifth site. When the dipoles are large in (a), corresponding dipoles in (b) are small, and *vice versa*.

system read

$$\dot{b}_n(t) = \frac{i}{\hbar} [H, b_n(t)] = -\frac{i}{\hbar} E b_n(t) + \frac{i}{\hbar} U a_n(t) W_n(t), \quad (4.1a)$$

$$\begin{aligned} \dot{a}_n(t) = \frac{i}{\hbar} [H, a_n(t)] = & -\frac{i}{\hbar} \varepsilon a_n(t) - \frac{i}{\hbar} V (a_{n+1}(t) \\ & + a_{n-1}(t)) - \frac{i}{\hbar} U b_n(t). \end{aligned} \quad (4.1b)$$

Since the higher-order terms are produced by a mode-mode coupling such as $a_n W_n = a_n (b_n^\dagger b_n - b_n b_n^\dagger)$, the equations become nonlinear and are hardly solved analytically. Thus we first solve the equations perturbatively in order to investigate the dynamics discussed in the preceding section.

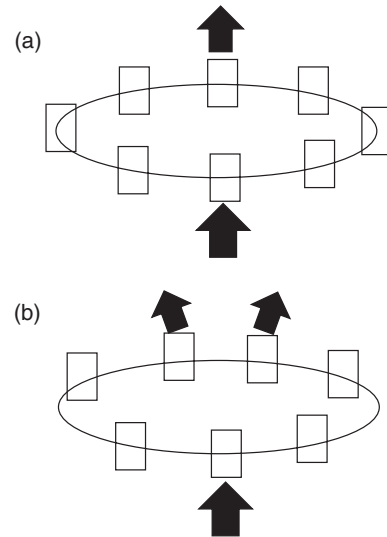


Fig. 5. Transportation of quantum coherence in (a) an even site number system and (b) an odd site number system. In the even site system (a), output signals are obtained from the opposite site to the input site. In the odd site system (b), output signals are split into the two-pair site opposite to the input site.

4.1 Perturbative expansion of time evolution operator

Noticing that the Hamiltonian for localized photons H_a given by eq. (2.2a) can be written in a quadratic form as

$$H_a = (a_1^\dagger, \dots, a_N^\dagger) \begin{pmatrix} \varepsilon & V & & V \\ V & \varepsilon & V & \\ & \dots & \dots & \\ & & V & \varepsilon & V \\ V & & & V & \varepsilon \end{pmatrix} \begin{pmatrix} a_1 \\ \vdots \\ \vdots \\ a_N \end{pmatrix} \quad (4.2)$$

$$\equiv \sum_{n,m} a_n^\dagger R_{nm} a_m, \quad (4.3)$$

we obtain an orthogonal matrix P to diagonalize the matrix

kernel R of the Hamiltonian as

$$(P^{-1}RP)_{ij} = \hbar\lambda_i\delta_{ij}. \quad (4.4)$$

Then new annihilation operators $v_j = \sum_n P_{nj}a_n$ and creation operator $v_j^\dagger = \sum_n P_{nj}a_n^\dagger$ of new modes of localized photons are introduced. Since all the elements of the diagonalization matrix P are not zero, note that the new modes are extended over a whole system. The commutation relation of the new modes can be given as

$$[v_i, v_j^\dagger] = \delta_{ij}.$$

With the help of eq. (4.4) and the modes v_i , the Hamiltonian in eq. (4.3), or eq. (2.2a) is diagonalized as

$$H_a = \sum_j \hbar\lambda_j v_j^\dagger v_j, \quad (4.5)$$

and the localized photon–exciton interaction H_{int} in eq. (2.2c) is written in terms of v_i as

$$H_{\text{int}} = \hbar g \sum_{nj} P_{nj} (v_j^\dagger b_n + v_j b_n^\dagger). \quad (4.6)$$

In order to derive a perturbative expansion of the time evolution of an arbitrary operator, we define the Liouvillians as

$$\begin{aligned} L \cdots &= \frac{1}{\hbar} [H, \cdots], & L_0 \cdots &= \frac{1}{\hbar} [H_0, \cdots], \\ L_{\text{int}} \cdots &= \frac{1}{\hbar} [H_{\text{int}}, \cdots]. \end{aligned} \quad (4.7)$$

Then the Heisenberg equation of an arbitrary operator O is written as

$$\dot{O} = \frac{i}{\hbar} [H, O] = iLO, \quad (4.8)$$

and we can obtain a formal solution as

$$O(t) = G(t)O(0), \quad (4.9)$$

with the time evolution operator $G(t) = e^{iLt}$ that satisfies the following equation

$$\dot{G}(t) = iLG(t) = iL_0G(t) + iL_{\text{int}}G(t). \quad (4.10)$$

Treating the interaction term H_{int} as a perturbation, we solve the eq. (4.10) perturbatively up to the second order of the perturbation as²⁹⁾

$$\begin{aligned} G^{(2)}(t) &= G_0(t) + i \int_0^t G_0(t-s)L_{\text{int}}G_0(s)ds - \int_0^t ds \\ &\quad \times \int_0^s du G_0(t-s)L_{\text{int}}G_0(s-u)L_{\text{int}}G_0(u), \end{aligned} \quad (4.11)$$

where the notation $G_0(t) = e^{iL_0 t}$ is used. Substituting eq. (4.11) into eq. (4.9) and using eq. (4.7), we can obtain the time evolution of the exciton operator $b_n(t) = G^{(2)}(t)b_n$. Suppose that localized photons are initially in the vacuum and $\langle V_n \rangle = 0$, then the expectation value of $b_n(t)$ is expressed

$$\begin{aligned} \langle b_n(t) \rangle &= e^{-i\Omega t} \langle b_n \rangle + g^2 \sum_{j=1}^N \Gamma_j(t) \left(\sum_{m=1}^N P_{nj} P_{mj} \right. \\ &\quad \left. \times (1 - \delta_{nm}) \langle W_n \rangle \langle b_m \rangle - P_{nj}^2 \langle b_n \rangle \right), \end{aligned} \quad (4.12)$$

where the notation

$$\begin{aligned} \Gamma_j(t) &= e^{-i\Omega t} \int_0^t ds e^{is(\Omega-\lambda_j)} \int_0^s du e^{-iu(\Omega-\lambda_j)} \\ &= \frac{e^{-i\Omega t} - e^{-i\lambda_j t}}{(\Omega - \lambda_j)^2} + \frac{ite^{-i\Omega t}}{\Omega - \lambda_j} \equiv c_j(t) + id_j(t) \end{aligned} \quad (4.13)$$

is used, and $c_j(t)$ and $d_j(t)$ represent the real part and the imaginary part of $\Gamma_j(t)$, respectively. The expression given by eq. (4.12) and its Hermitian conjugate provide the time evolution of the expectation value of the dipole at an arbitrary QD site n as

$$\begin{aligned} \langle P_n(t) \rangle &= \langle P_n \rangle \left(\cos \Omega t - g^2 \sum_j c_j(t) P_{nj}^2 \right) \\ &\quad + g^2 \sum_j \sum_{m \neq n} c_j(t) P_{nj} P_{mj} \langle P_m \rangle \langle W_n \rangle. \end{aligned} \quad (4.14)$$

Corresponding to the discussion developed in §3.2, we set initially $\langle P_n \rangle = \delta_{n1}$ and obtain the perturbative solution that describes the dipole dynamics driven by a local excitation as follows:

$$\begin{aligned} \langle P_n(t) \rangle &= \delta_{n1} \left(\cos \Omega t - g^2 \sum_j c_j(t) P_{nj}^2 \right) \langle P_1 \rangle \\ &\quad + (1 - \delta_{n1}) g^2 \sum_j c_j(t) P_{nj} P_{1j} \langle P_1 \rangle \langle W_n \rangle. \end{aligned} \quad (4.15)$$

In the next section we discuss the dynamical properties of the system, on the basis of the solution given by eq. (4.15).

4.2 Numerical results and dynamical properties

As discussed in §3.2, we numerically investigate the dynamics of the dipole of the system depending on the initial conditions. Suppose that localized photons are initially in the vacuum, $\langle V_n \rangle = 0$ for all n , the dipole is initially set only at the first site as $\langle P_n \rangle = \delta_{n1}$, and all the populations are in the ground states except for the first site as $\langle W_n \rangle = -(1 - \delta_{n1})$. As mentioned before, all the population differences are automatically -1 for bosonic excitons. In addition, we impose that the length of the Bloch vector (P_n, V_n, W_n) is normalized as

$$\langle P_n(t) \rangle^2 + \langle V_n(t) \rangle^2 + \langle W_n(t) \rangle^2 = 1. \quad (4.16)$$

In Fig. 6 the time evolution of the dipole distribution is plotted. The parameter values used are the same as in §3.2 ($E = 2$, $\varepsilon = 1$, and $V = 1$). It follows from the figure that the dipole excitation of the first site moves to the opposite site as shown in the boson case (see Fig. 3). The reason is that the initial exciton density is so dilute as to validate the boson approximation. As time advances, the amplitude of each dipole increases because the perturbative solution violates the unitarity.

To find a new feature of fermionic excitons, we vary the initial conditions for the population differences from $\langle W_n \rangle = -(1 - \delta_{n1})$. Since the initial population differences at site n contributes to the perturbative solution of the dipole at the same site, eq. (4.15), in a product of $\langle W_n \rangle \langle P_1 \rangle$, the following hypothesis is proposed.

Proposition 4.1 (Flip hypothesis). *If the sign of the initial population difference of the n -th site, $\langle W_n(0) \rangle$, is inverted,*

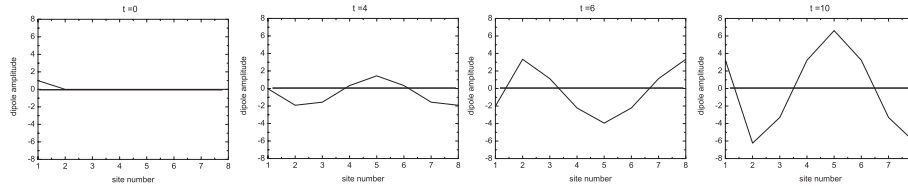


Fig. 6. Time evolution of the dipole distributions ($E = 2, \varepsilon = 1, V = 1$). Initially all of the sites without the first site are in the ground state, while the dipole moment is initially set only at the first site.

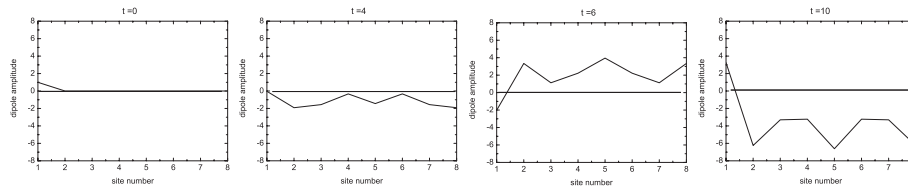


Fig. 7. Time evolution of the dipole distribution ($E = 2, \varepsilon = 1, V = 1$): the initial population differences of site 4, 5 and 6 are inverted from $\langle W_n \rangle = -(1 - \delta_{n1})$.

then the direction of the dipole moment of the n -th site at arbitrary time, $\langle P_n(t) \rangle$, is flipped.

Since the dipoles at site 4, 5 and 6 in Fig. 6 are directed opposite to the others, we invert the sign of $\langle W_n \rangle$ for $n = 4, 5, 6$. Figure 7 shows the result that the direction of the dipoles at site 4, 5, and 6 are flipped, and that all the dipoles oscillate with a same phase but with a different amplitude. Thus we observe that the system is transferred from a locally excited state to a coherently oscillating state of the dipoles, in other words, to a dipole-ordered state. In the ordered state the total dipole is N times larger than each single dipole. Moreover, since radiation from an oscillating dipole is proportional to the square of the dipole moment, we can expect a high intensity of radiation from the dipole-ordered state. The radiation property of the system will be discussed in §6.2.

4.3 Dynamics of dipole-forbidden states via optical near-field interaction

It is well known that the electric interaction between molecules with no dipole moments is weak when they are separated in a macroscopic distance, and that the interaction becomes strong when they are very close to each other. Taking it into account, we investigate the dynamics of the system driven by localized photons, where it is interesting to consider an initial state that alternating dipoles are set and thus the total dipole of the system vanishes for an even number of sites. Such a dipole-forbidden state can be manipulated by localized photons, not by propagating far

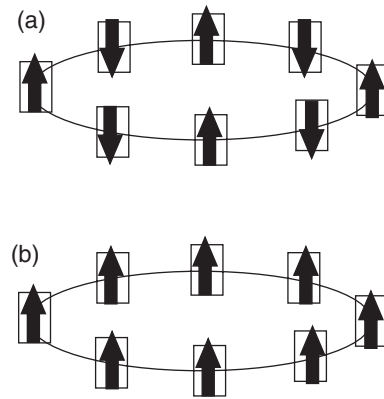


Fig. 8. Schematic illustration of (a) an alternating dipole distribution (a dipole-forbidden state) and (b) a dipole-ordered state. The state with alternating dipoles that result in the total dipole of zero cannot be coupled by the radiation field with the dipole interaction.

fields.

As an initial condition we set $\langle P_n \rangle = (-1)^n$, and for simplicity, localized photons are in the vacuum, $\langle V_n \rangle = 0$, and $\langle W_n \rangle = 0$. The system parameters $E = 2, \varepsilon = 1$, and $V = 1$ are used as before. Figure 9 shows the time evolution of such a dipole-forbidden state. From Fig. 9 it follows that the system oscillates as schematically shown in Fig. 8(a), and that it remains in the initial dipole-forbidden state. This kind of dynamics is achieved in the system whose initial distribution of the population differences are uniform. For example, if we set $\langle P_n \rangle = (-1)^n/\sqrt{2}$ and $\langle W_n \rangle = 1/\sqrt{2}$ for

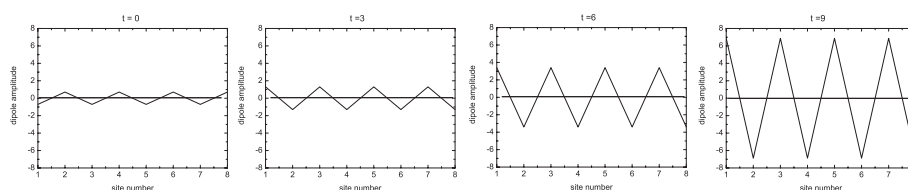


Fig. 9. Time evolution of a dipole-forbidden state (alternating dipole distribution). All the population differences are initially set as 0. We observe an oscillation of the alternating dipoles. The system remains in the dipole-forbidden state.

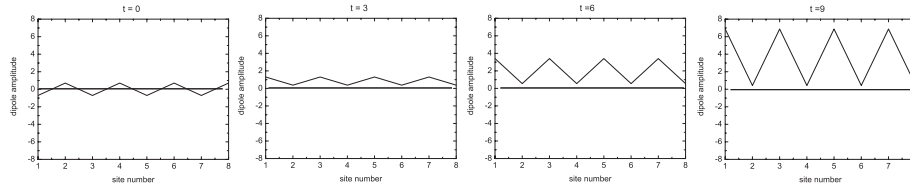


Fig. 10. Time evolution of a dipole-forbidden state ($E = 2$, $\varepsilon = 1$, $V = 1$). The population differences are initially set as $\langle W_n \rangle = -\langle P_n \rangle$. The system is converted from a dipole-forbidden state to a dipole-ordered state.

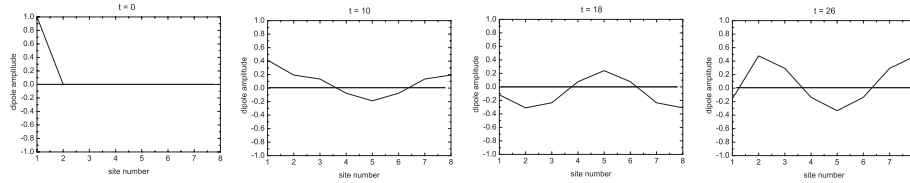


Fig. 11. Time evolution of the dipole distribution for the system ($E = 2$, $\varepsilon = 1$, $V = 1$) obtained from the Heisenberg equation with semi-classical approximation. Initially all of the sites without the first site are in the ground state.

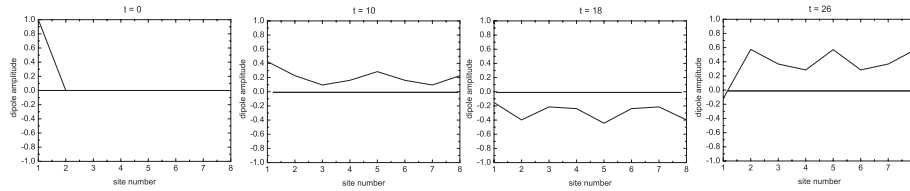


Fig. 12. Time evolution of the dipole distribution for the system ($E = 2$, $\varepsilon = 1$, $V = 1$) obtained from the Heisenberg equation with semi-classical approximation. The initial population differences of site 4, 5, and 6 are inverted.

all n , the result is the same as shown in Fig. 9 except for its amplitude of the oscillation.

Next, we manipulate the distribution of the population difference non-uniformly, so that the signs are set as opposite to those of the corresponding dipoles:

$$\langle P_n \rangle = (-, +, -, +, -, +, -, +) / \sqrt{2},$$

$$\langle W_n \rangle = (-, -, +, -, +, -, +, -) / \sqrt{2}.$$

Figure 10 presents the result that a dipole-forbidden state as shown in Fig. 8(a) is converted to a dipole-ordered state as illustrated in Fig. 8(b). Since the dipole ordering has occurred by manipulating the initial distribution of the population differences, the result can be interpreted by the “*Flip hypothesis*” proposed in §4.2. As a collective oscillation of the dipoles occurred, the system evolved from a non-radiative state to a radiative state through the localized photon–exciton interaction.

4.4 Semi-classical approximation

Here we should note that the second-order perturbative solutions break the unitarity, and that the long-time behaviors of the dynamics given by the solutions are not necessarily same as the exact ones. Thus we have to return to the Heisenberg equations, eqs. (4.1a) and (4.1b), to evaluate the time evolution of physical observables. The Heisenberg equations are first solved by neglecting the quantum correlations between excitons and localized photons such as $\langle W_n y_n \rangle = \langle W_n \rangle \langle y_n \rangle$, and later the quantum correlations are estimated in §7.2. In this semi-classical approximation, eqs.

(4.1a) and (4.1b) can be converted to the following coupled differential equations

$$\begin{cases} \langle \dot{P}_n \rangle = -\Omega \langle V_n \rangle + g \langle W_n \rangle \langle y_n \rangle, \\ \langle \dot{V}_n \rangle = \Omega \langle P_n \rangle - g \langle W_n \rangle \langle x_n \rangle, \\ \langle \dot{W}_n \rangle = g (\langle V_n \rangle \langle x_n \rangle - \langle P_n \rangle \langle y_n \rangle), \end{cases} \quad (4.17)$$

$$\begin{cases} \langle \dot{x}_n \rangle = -\omega \langle y_n \rangle - v (\langle y_{n-1} \rangle + \langle y_{n+1} \rangle) - g \langle V_n \rangle, \\ \langle \dot{y}_n \rangle = \omega \langle x_n \rangle + v (\langle x_{n-1} \rangle + \langle x_{n+1} \rangle) + g \langle P_n \rangle, \end{cases} \quad (4.18)$$

where the notations $x_n = a_n + a_n^\dagger$, $y_n = i(a_n - a_n^\dagger)$, and $v = V/\hbar$ are used.

To check the reliability of the semi-classical approximation, we again investigate the system examined in §4.2. Figure 11 shows the time evolution of the dipole distribution obtained from the semi-classical approach for the system corresponding to Fig. 6. Comparing Fig. 11 with Fig. 6, we find that both profiles are same, and that the amplitude of each dipole obtained from the Heisenberg equations is less than 1, which means that the unitarity of the time evolution is conserved.

In Fig. 12, we show the time evolution of the dipole distribution obtained from the semi-classical approach when the initial population differences of site 4, 5, and 6 are inverted. It follows from the figure that each dipole is ordered as the flip hypothesis predicts, and that the flip hypothesis is still valid in the numerical solution of the semi-classical Heisenberg equation.

Numerical results obtained from eqs. (4.17) and (4.18) with a semi-classical approximation predict the dipole

dynamics with qualitative similarities as shown from the perturbative solution eq. (4.15). The flip hypothesis proposed in §4.2 is also verified by using the numerical solutions of eqs. (4.17) and (4.18), or of the Heisenberg equations without quantum correlations. These results show that the approach discussed in this section, maintaining an advantage to conserve the unitarity, qualitatively describe the dipole dynamics of the system in a similar way as the other two approaches. The validity of the approximation employed here, which we will examine in §7.2, is reported in the Dicke model that superradiant phenomena can be described with a semi-classical approximation which neglects quantum correlations among the atoms,¹²⁾ and that the contribution from the quantum correlations is of the order of $1/N$ for large N .¹³⁾

5. Effective Hamiltonian and the Dipole Ordering

In order to investigate the origin of the dipole ordering discussed above, we first introduce an effective Hamiltonian to renormalize degrees of freedom of localized photons. Using the effective Hamiltonian, we then classify quasi-steady states with respect to the dipole distribution.

5.1 Effective Hamiltonian

An unitary transformation with an anti-Hermitian operator S is applied to the Hamiltonian eq. (2.1) as³²⁾

$$\tilde{H} = e^{-S} H e^S = H + [H, S] + \frac{1}{2} [[H, S], S] + \dots \quad (5.1)$$

If the Hamiltonian eq. (2.1) is divided into the unperturbed part $H_0 = H_a + H_b$ and perturbed part H_{int} , and if S is chosen to make

$$H_{\text{int}} + [H_0, S] = 0, \quad (5.2)$$

the terms linear in the coupling constant $g = U/\hbar$ vanish as

$$\tilde{H} = H_0 + \frac{1}{2} [H_{\text{int}}, S] + O(g^3). \quad (5.3)$$

The transformed Hamiltonian \tilde{H} contains the terms in the second order of the exciton-localized photon interaction that describe exciton-exciton interactions via localized photons. Taking the expectation value of \tilde{H} in terms of the vacuum of localized photons $|vac\rangle$, we obtain the effective Hamiltonian H_{eff} as

$$\begin{aligned} H_{\text{eff}} &= \langle vac | \tilde{H} | vac \rangle = H_b + H_{b-b}, \\ H_b &= \sum_n \hbar \Omega b_n^\dagger b_n, \\ H_{b-b} &= \sum_{n,m} \left(\frac{\hbar g^2}{\Omega I - R/\hbar} \right)_{nm} b_n^\dagger b_m, \end{aligned} \quad (5.4)$$

where the exciton energy E is denoted as $\hbar \Omega$. With the help of the components of the Bloch vector (P_n, V_n, W_n) the effective Hamiltonian eq. (5.4) can be rewritten as

$$\begin{aligned} H_{\text{eff}} &= \hbar \sum_n (\Omega + \Delta \Omega_n) \frac{1 + W_n}{2} \\ &+ \frac{\hbar}{4} \sum_n \sum_{m \neq n} \Delta \Omega_{nm} (P_n P_m + V_n V_m), \end{aligned} \quad (5.5)$$

where the interaction energy or coupling strength between

excitons $\Delta \Omega_{nm}$ are given as

$$\Delta \Omega_{nm} = \left(\frac{g^2}{\Omega I - R/\hbar} \right)_{nm} = \sum_j \frac{g^2}{\Omega - \lambda_j} P_{nj} P_{mj}, \quad (5.6)$$

and the abbreviation $\Delta \Omega_n \equiv \Delta \Omega_{nn}$ is used for a special case.

5.2 Classification of quasi-steady states

Using the effective Hamiltonian H_{eff} , we can obtain the time evolution of the dipole moment at site n in a similar way as discussed in §4.1:

$$\begin{aligned} \langle P_n(t) \rangle &= \langle P_n \rangle \cos[(\Omega + \Delta \Omega_n)t] \\ &+ \sum_{m \neq n} \Delta \Omega_{nm} t \langle W_n \rangle \langle P_m \rangle \sin(\Omega t). \end{aligned} \quad (5.7)$$

If the dipole at site 1, in particular, is only excited at $t = 0$, eq. (5.7) reads

$$\begin{aligned} \langle P_n(t) \rangle &= \delta_{n1} \langle P_1 \rangle \cos[(\Omega + \Delta \Omega_n)t] \\ &+ (1 - \delta_{n1}) \Delta \Omega_{n1} t \langle W_n \rangle \langle P_1 \rangle \sin(\Omega t). \end{aligned} \quad (5.8)$$

It follows from this expression that the sign of the dipole at site n depends on the coefficient $\Delta \Omega_{n1}$ as well as the initial values of $\langle P_1(0) \rangle$ and $\langle W_n(0) \rangle$, and that the coefficient $\Delta \Omega_{n1}$ determines what kind of quasi-steady states of the dipole distribution the system reaches when the initial values are fixed. Therefore we examine the matrix $\Delta \Omega$ to classify the quasi-steady states of the dipole distribution of the system. First, as an example, we show the matrix elements of $\Delta \Omega$ for the system examined in §3 and §4 whose material parameters are $E = 2$, $\varepsilon = 1$, and $V = 1$ as follows:

$$\Delta \Omega = \begin{pmatrix} \frac{1}{3} & \frac{2}{3} & \frac{1}{3} & -\frac{1}{3} & -\frac{2}{3} & -\frac{1}{3} & \frac{1}{3} & \frac{2}{3} \\ \frac{2}{3} & \frac{1}{3} & \frac{2}{3} & \frac{1}{3} & -\frac{1}{3} & -\frac{2}{3} & -\frac{1}{3} & \frac{1}{3} \\ \frac{1}{3} & \frac{2}{3} & \frac{1}{3} & \frac{2}{3} & \frac{1}{3} & -\frac{1}{3} & -\frac{2}{3} & -\frac{1}{3} \\ -\frac{1}{3} & \frac{1}{3} & \frac{2}{3} & \frac{1}{3} & \frac{2}{3} & \frac{1}{3} & -\frac{1}{3} & -\frac{2}{3} \\ -\frac{2}{3} & -\frac{1}{3} & \frac{1}{3} & \frac{2}{3} & \frac{1}{3} & \frac{2}{3} & \frac{1}{3} & -\frac{1}{3} \\ -\frac{1}{3} & -\frac{2}{3} & -\frac{1}{3} & \frac{1}{3} & \frac{2}{3} & \frac{1}{3} & \frac{2}{3} & \frac{1}{3} \\ \frac{1}{3} & -\frac{1}{3} & -\frac{2}{3} & -\frac{1}{3} & \frac{1}{3} & \frac{2}{3} & \frac{1}{3} & \frac{2}{3} \\ \frac{2}{3} & \frac{1}{3} & -\frac{1}{3} & -\frac{2}{3} & -\frac{1}{3} & \frac{1}{3} & \frac{2}{3} & \frac{1}{3} \end{pmatrix}.$$

The matrix is symmetric and has a cyclic structure as

$$\Delta \Omega_{n+1, m+1} = \Delta \Omega_{n, m}.$$

This is due to the fact that the periodic boundary condition is imposed on the system, and that the Hamiltonian given in eq. (2.1) has translational invariance. Owing to the symmetric structure as

$$(\Delta \Omega_{22}, \Delta \Omega_{23}, \Delta \Omega_{24}, \dots) = (\Delta \Omega_{11}, \Delta \Omega_{12}, \Delta \Omega_{13}, \dots),$$

the dipole distribution of the system initiated by the dipole excitation at site 2 can be discussed in terms of $\Delta \Omega_{1n}$ that governs the problem driven by the site-one excitation. In general the problem is reduced to examine the structure of the coefficients $\Delta \Omega_{1n}$ that depend on the material parameters Ω and λ_j , or E , ε , and V . Since the parameter sets crossing the resonant points ($\Omega = \lambda_j$) change the pattern of the dipole distribution in the system, we can classify quasi-steady states of the dipole distribution into four groups in Table I. The system with $E = 2$, $\varepsilon = 1$, and $V = 1$, which has been

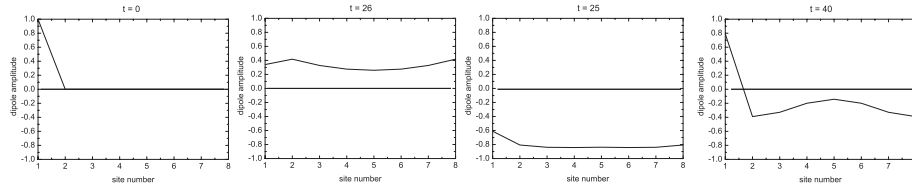


Fig. 13. Time evolution of the dipole distribution of the system belonging to the third group. The initial conditions are set as $\langle P_n \rangle = \delta_{n1}$ and $\langle W_n \rangle = 1 - \delta_{n1}$. All the electric dipole moments are aligned to the same direction, and a dipole-ordered state appears.

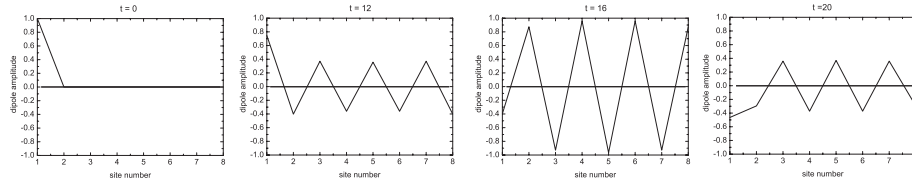


Fig. 14. Time evolution of the dipole distribution of the system belonging to the fourth group. The initial conditions are set as $\langle P_n \rangle = \delta_{n1}$ and $\langle W_n \rangle = 1 - \delta_{n1}$. The dipole distribution similar to the “anti-ferromagnetic” state is shown, where the dipoles alternately change the directions.

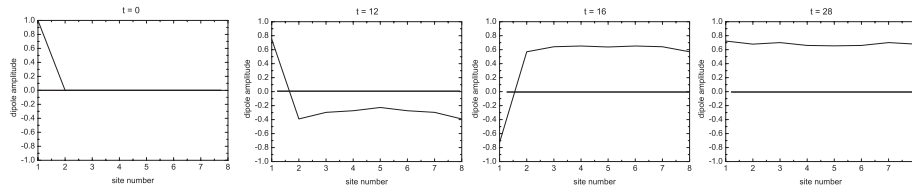


Fig. 15. Time evolution of the dipole distribution of the system belonging to the fourth group. The initial population differences are set as $W_n = (0, -, +, -, +, -, +, -)$. According to the flip hypothesis, the alternating dipoles change their directions and are aligned to form a dipole-ordered state.

Table I. Classification of quasi-steady states.

Group	Signs of $\Delta\Omega_{1n}$ for $n = 1, 2, 3, \dots, 8$
1st	$(-, -, -, +, +, +, -, -)$, $(+, +, +, -, -, -, +, +)$
2nd	$(-, +, -, -, +, -, -, +)$, $(+, -, +, +, -, +, +, -)$
3rd	$(-, -, -, -, -, -, -, -)$, $(+, +, +, +, +, +, +, +)$
4th	$(-, +, -, +, -, +, -, +)$, $(+, -, +, -, +, -, +, -)$

investigated in §4, belongs to the first group. Since the coefficients $\Delta\Omega_{1n}$ in the first group have different signs at site 4, 5, and 6 from others, the quasi-steady state of the dipole distribution that is predicted by the effective Hamiltonian is the one described by the second-order perturbation solution [see eq. (4.15) and Fig. 6]. The third and fourth groups are, in particular, interesting among the four groups of the quasi-steady states. The third group corresponds to a “ferromagnetic” system, in which all the electric dipole moments are aligned to the same direction, while the fourth group corresponds to an “anti-ferromagnetic” system, where the dipoles are aligned to have alternating signs.

Using numerical results of eqs. (4.17) and (4.18), we examine the dynamics of the third and fourth groups whether they behave as predicted by the effective Hamiltonian: “ferromagnetic,” or “anti-ferromagnetic.” The parameter set of $E = 3.01$, $\varepsilon = 1$, and $V = 1$ gives

$$\Delta\Omega_{1n} = (-13.1, -12.7, -12.4, -12.2, \\ -12.2, -12.2, -12.4, -12.7),$$

and thus the system belongs to the third group. The results is shown in Fig. 13, which predicts the “ferromagnetic” behavior as expected. When the parameter set of $E = 1$, $\varepsilon = 3.01$, and $V = 1$ is chosen, the system corresponds to the fourth group. Figure 14 presents the time evolution of the dipole distribution of the system that shows alternating changes in signs, as expected to be similar to anti-ferromagnetics.

With the help of the flip hypothesis proposed in §4.2, we infer that the distribution of the dipoles can be changed by locally manipulating the initial population differences, and that an “anti-ferromagnetic” state can be transformed into a dipole-ordered state. To verify it, the initial population differences are set in the zigzag form as $W_n = (0, -, +, -, +, -, +, -)$ for the “anti-ferromagnetic” system ($E = 1$, $\varepsilon = 3.01$, and $V = 1$), and the time evolution of the dipole distribution is examined. The result, as shown in Fig. 15, clearly indicates that a dipole-ordered state manifests itself owing to the local manipulation of the initial population differences. It is noteworthy that the amplitude of each dipole is close to one, and that the total dipole of the system is of the order of N , whose radiation property is investigated in the following section.

6. Radiation from the Dipole-Ordered States

In this section we examine the radiation property of the dipole-ordered states discussed in §4.2 and §5.2. Our model has excluded radiation fields or free photons from the preceding discussions about the dynamics because the interaction energies of excitons with optical near fields are

much larger in our system than those with radiation fields. This means that radiation fields are so weakly coupled with our system as not to disturb the dynamics of it. On the basis of such an understanding, we investigate radiation from a quantum dot system whose dynamics is driven by optical near fields.

6.1 Dicke states and superradiance^{8,31)}

The components of the Bloch vector of a two-level system as a representative of a collection of atoms or quantum dots, (P_n, V_n, W_n) , are defined by Pauli's spin operators as

$$\begin{aligned} R_1^{(n)} &= \frac{1}{2} (b_n + b_n^\dagger) = \frac{1}{2} P_n, \\ R_2^{(n)} &= \frac{i}{2} (b_n - b_n^\dagger) = \frac{1}{2} V_n, \\ R_3^{(n)} &= \frac{1}{2} (b_n^\dagger b_n - b_n b_n^\dagger) = \frac{1}{2} W_n, \end{aligned} \quad (6.1)$$

where the spin operators $R_i^{(n)}$ satisfy the commutation relations

$$[R_i^{(n)}, R_j^{(n')}] = \delta_{nn'} i \epsilon_{ijk} R_k^{(n)}, \quad (6.2)$$

with Levi-Civita's symbol ϵ_{ijk} . For an N two-level system we introduce the total spin operators as

$$R_1 = \sum_{n=1}^N R_1^{(n)}, \quad R_2 = \sum_{n=1}^N R_2^{(n)}, \quad R_3 = \sum_{n=1}^N R_3^{(n)}, \quad (6.3)$$

which obey the commutation relations

$$[R_i, R_j] = i \epsilon_{ijk} R_k. \quad (6.4)$$

Let us consider a state in which N_1 of the N two-level system are in the lower state $|1\rangle$ and N_2 are in the excited state $|2\rangle$, where

$$N = N_1 + N_2, \quad m = \frac{1}{2} (N_2 - N_1). \quad (6.5)$$

Evidently m is a measure of the total population inversion, and it is an eigenvalue of the spin operator R_3 . Introducing the operator $R^2 = R_1^2 + R_2^2 + R_3^2$ and using eq. (6.4), we obtain the commutation relation

$$[R_i, R^2] = 0, \quad i = 1, 2, 3, \quad (6.6)$$

so that the collective operators R_i obey the same algebra as the angular momentum. Thus there exist the states $|l, m\rangle$ which are simultaneous eigenstates of both R_3 and R^2 as

$$R_3 |l, m\rangle = m |l, m\rangle, \quad \text{for } -\frac{1}{2}N \leq m \leq \frac{1}{2}N, \quad (6.7a)$$

$$R^2 |l, m\rangle = l(l+1) |l, m\rangle, \quad \text{for } |m| \leq l \leq \frac{1}{2}N. \quad (6.7b)$$

The quantum number l is called the cooperation number⁸⁾ and determines the collectivity of cooperative phenomena. For the raising and lowering operators as

$$R_+ = \sum_{n=1}^N b_n^\dagger = R_1 + iR_2, \quad R_- = \sum_{n=1}^N b_n = R_1 - iR_2, \quad (6.8)$$

it follows from the well-known properties of angular momentum operators that

$$R_\pm |l, m\rangle = \sqrt{l(l \mp m)(l \pm m + 1)} |l, m \pm 1\rangle, \quad (6.9)$$

where the collective states $|l, m\rangle$ are called Dicke states.

Here we suppose a transition from an initial state $|l, m\rangle |vac\rangle$ to a final state $|\psi\rangle$, where $|l, m\rangle$ and $|vac\rangle$ represent a Dicke state and the vacuum of the radiation field, respectively. Adopting the dipole interaction between the two-level system and radiation field as

$$H_I(t) = -\boldsymbol{\mu}_{\text{tot}}(t) \cdot \mathbf{E}(t) \quad (6.10)$$

with the total electric dipole of the system

$$\boldsymbol{\mu}_{\text{tot}} = \boldsymbol{\mu} \sum_{n=1}^N (b_n + b_n^\dagger) = \boldsymbol{\mu} (R_+ + R_-), \quad (6.11)$$

we can write the transition probability as

$$-\langle \psi | \boldsymbol{\mu} \cdot \mathbf{E}_-(t) R_-(t) |l, m\rangle |vac\rangle,$$

where $\mathbf{E}_-(t)$ is the $e^{-i\omega t}$ dependent part of the electric field $\mathbf{E}(t)$. By squaring the absolute value of the transition probability and summing over all possible final states, the probability of emission of radiation photons w_{emit} is given as

$$\begin{aligned} w_{\text{emit}} &= \sum_{\psi} |\langle \psi | \boldsymbol{\mu} \cdot \mathbf{E}(t) R_-(t) |l, m\rangle |vac\rangle|^2 \\ &= \langle l, m | R_+(t) R_-(t) |l, m\rangle \langle vac | \boldsymbol{\mu} \cdot \mathbf{E}_+(t) \boldsymbol{\mu} \cdot \mathbf{E}_-(t) |vac\rangle \\ &= \langle R_+(t) R_-(t) \rangle A = (l+m)(l-m+1)A, \end{aligned} \quad (6.12)$$

where eq. (6.9) is used for the final expression, and $A = \langle vac | \boldsymbol{\mu} \cdot \mathbf{E}_+(t) \boldsymbol{\mu} \cdot \mathbf{E}_-(t) |vac\rangle$ is identified as the Einstein A-coefficient for each two-level system like an atom or a quantum dot.

If all quantum dots are in the ground state $|1\rangle$, then $m = -N/2$, and from eq. (6.7b) we must have $l = N/2$. Hence, from eq. (6.12) the radiation rate w_{emit} is zero as expected. If all quantum dots are in the excited states $|2\rangle$, then $m = N/2$ and we again have $l = N/2$. Hence $w_{\text{emit}} = NA$, which is just what one would expect from a group of N independently radiating quantum dots. However, the situation is quite different if the initial state is not the completely excited state. Let us consider a state in which half of the quantum dots are excited and half are not, so that $m = 0$. Then we have

$$w_{\text{emit}} = l(l+1)A, \quad (6.13)$$

and l can have any value between 0 and $N/2$. The larger the value of l , the larger is collective rate of radiation of the system. In particular, if $l = N/2$, then

$$w_{\text{emit}} = \frac{1}{4} N(N+2)A, \quad (6.14)$$

which maximizes the value of cooperative spontaneous radiation. Since the maximum radiation probability is proportional to the square of the site number N , it becomes very large for large N . This phenomenon is called superradiance, and the state $|l = N/2, m = 0\rangle$ is called a superradiant Dicke state. From the definition of the total Bloch vector (P, V, W) as $P = \sum_n \langle P_n \rangle$, $V = \sum_n \langle V_n \rangle$, $W = \sum_n \langle W_n \rangle$, it follows that the Bloch vector for the superradiant state is on the P - V plane and its length reaches a maximum, as shown in Fig. 16.

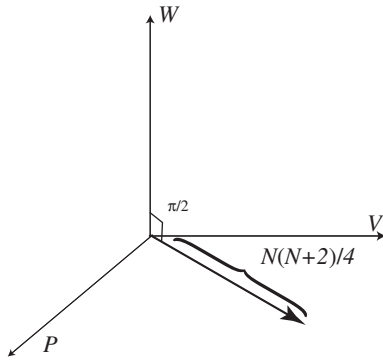


Fig. 16. Total Bloch vector in a superradiant state. It is on the P - V plane, and its length has a maximal value.

6.2 Radiation property of the dipole-ordered states

According to the formulation developed in §6.1, we now investigate the radiation property of the dipole-ordered states discussed in §4.2 and §5.2. From the expression eq. (6.12) the radiation intensity at time t is determined by the radiation factor, $\langle R_+R_- \rangle = (l+m)(l-m+1)$, i.e., the expectation value of the operator

$$R_+R_- = R_1^2 + R_2^2 + R_3 = \left(\frac{P}{2}\right)^2 + \left(\frac{V}{2}\right)^2 + \frac{W}{2}, \quad (6.15)$$

which indicates that there are two elements mainly contributing to the radiation factor; one is the collectiveness of the system measured by the cooperation number l , and the other is the total energy of the quantum dot system given by $\langle R_3 \rangle = m$. Since the dynamics of the system is driven in our system by localized photons, the evolution of the radiation factor is also described in terms of $l(t)$ and $m(t)$ that are developed according to the localized photon–exciton interaction.

Numerical results of eqs. (4.17) and (4.18) are shown in Figs. 17 and 18. The upper parts in Fig. 17 show the time evolution of the radiation factors, while the lower parts illustrate the dipole distribution when each radiation factor has a maximal value. The total dipole in Fig. 17(a) is smaller

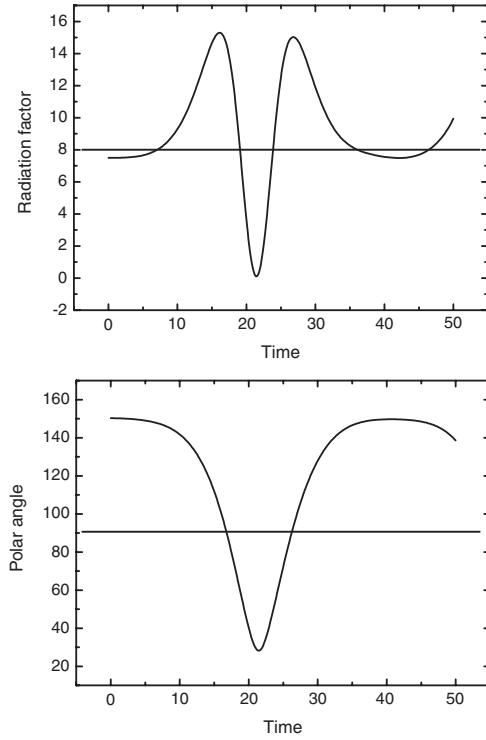


Fig. 18. Time evolution of the radiation factor (upper) and the polar angle of the total Bloch vector (lower) for a system belonging to the third group. The polar angle is measured from the $-W$ axis.

than those in Figs. 17(b) and 17(c), and the peak value of the radiation factor is also smaller. It follows from the figure that the radiation factor increases as the total dipole becomes larger. The peak values of the radiation factor in Figs. 17(b) and 17(c), 15 and 14, correspond to the value for the Dicke’s superradiance, which is obtained as 20 for $N = 8$ from eq. (6.14). We thus expect that quasi-steady states shown in Figs. 17(b) and 17(c) are close to the superradiant states, and that the total Bloch vectors for such states are on the P - V plane. In order to check whether the total Bloch vectors for the states belonging to the third group in Table I [see Fig.

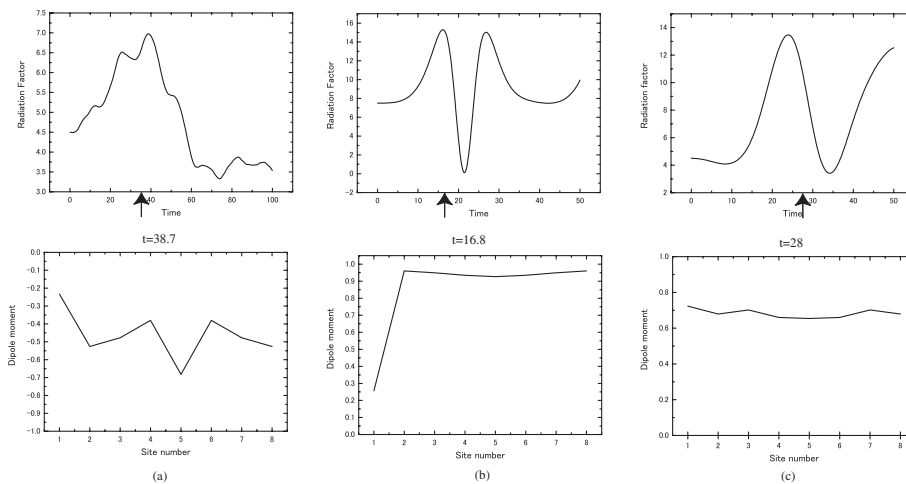


Fig. 17. Time evolution of the radiation factor $\langle R_+R_- \rangle$ (upper) and the dipole distribution at time indicated by the arrows when the radiation factors take maximal values (lower) for (a) a system belonging to the first group with an initial population difference $W_n = (0+ + - - - + +)$, (b) a system belonging to the third group with an initial population difference $W_n = (0+ + + + + + + +)$, and (c) a system belonging to the fourth group with an initial population difference $W_n = (0- + - + - + -)$.

17(b)] are on the P - V plane or not, we examine the time evolution of the polar angles of the Bloch vectors as well as the radiation factors. As shown in Fig. 18, the polar angle of the Bloch vector takes 90° , that is, are on the P - V plane when the radiation factor has a maximal value. Therefore we conclude that the system belonging to the third group in Table I are in transition to a quasi-steady state close to the superradiant Dicke state, judging from its large radiation factor and the polar angle of the total Bloch vector. Figures 17(b) and 17(c) indicate that multiple peaks appear in the radiation, or that multiple pulses are emitted from the system. One may think, as a possible origin, that such a phenomenon stems from the recurrence inherent in an isolated system. However, such multiple pulses may survive even if the system becomes dissipative, which will be examined in detail in the next section.

7. Radiation from a Dissipative System

We have assumed in the previous section that the radiation field is so weak as not to disturb the exciton dynamics of a quantum dot system. When radiation pulses are emitted from the system, however, energy has to be dissipated, and it is interesting but not clear whether multiple pulses shown in Figs. 17(b) and 17(c) are emitted from the system or not. In this section we thus study the radiation profile, adding a radiation field to the system as a reservoir that does not affect the dynamics but makes the system a dissipative one.

Suppose the Hamiltonian

$$H_2 = H_{\text{QDef}} + H_{\text{F}} + H_{\text{Fint}}, \quad (7.1)$$

where H_{QDef} is the effective Hamiltonian given by eq. (5.4) that describes the N two-level quantum dot system interacting with localized photons. The Hamiltonians H_{F} and H_{Fint} describe the free radiation field and the exciton-free photon interaction, respectively. Explicit Hamiltonians in the interaction representation are written as

$$H_{\text{F}} = \sum_{\mathbf{k}, \lambda} \hbar \omega_{\mathbf{k}} a_{\mathbf{k}\lambda}^\dagger a_{\mathbf{k}\lambda}, \quad (7.2)$$

$$H_{\text{Fint}}(t) = \sum_{\mathbf{k}, \lambda} \hbar g_{\mathbf{k}\lambda} a_{\mathbf{k}\lambda}^\dagger R_- e^{i(\omega_{\mathbf{k}} - \Omega)t} + \text{h.c.} \quad (7.3)$$

where creation and annihilation operators of a free photon with wave vector \mathbf{k} , polarization λ , and frequency $\omega_{\mathbf{k}}$ are denoted as $a_{\mathbf{k}\lambda}^\dagger$ and $a_{\mathbf{k}\lambda}$, respectively. The coupling constant between the free photon and exciton is given as

$$g_{\mathbf{k}\lambda} = \frac{i\Omega}{\hbar\sqrt{V}} \sqrt{\frac{\hbar}{2\omega_{\mathbf{k}}\epsilon_0}} \boldsymbol{\mu} \cdot \boldsymbol{\epsilon}_{\mathbf{k}\lambda}^*, \quad (7.4)$$

where V , $\boldsymbol{\epsilon}_{\mathbf{k}\lambda}^*$, and ϵ_0 represent the quantization volume of the radiation field, the unit polarization vector, and the dielectric constant in vacuum, respectively. Using the Hamiltonian H_2 and the density operator $\tilde{\rho}(t)$, we write the Liouville equation as

$$\frac{\partial \tilde{\rho}(t)}{\partial t} = \frac{1}{i\hbar} [H_2, \tilde{\rho}(t)] = -iL_2 \tilde{\rho}(t), \quad (7.5)$$

and eliminate degrees of freedom of the radiation field with the help of a projection operator defined as³¹⁾

$$\mathcal{P} \dots = |0\rangle\langle 0| \text{Tr}_{\text{F}} \dots \quad (7.6)$$

with the vacuum of the radiation field $|0\rangle$. Then, we obtain equations of motion for the density operator $\tilde{\rho}(t)$ as follows:

$$\begin{aligned} \mathcal{P} \frac{\partial \tilde{\rho}(t)}{\partial t} &= -i\mathcal{P}L_2(t)\mathcal{P}\tilde{\rho}(t) - i\mathcal{P}L_2(t)U(t, 0)(1 - \mathcal{P})\tilde{\rho}(0) \\ &\quad - \mathcal{P}L_2(t) \int_0^t d\tau U(t, \tau)(1 - \mathcal{P})L_2(\tau)\mathcal{P}\tilde{\rho}(\tau), \end{aligned} \quad (7.7)$$

where $L_2(t)$ is the Liouville operator associated with $H_2(t)$, and the operator $U(t, \tau)$ is defined as

$$U(t, \tau) = \exp\left(-i(1 - \mathcal{P}) \int_\tau^t L_2(t') dt'\right). \quad (7.8)$$

With the Born–Markov approximation applied to the third term of eq. (7.7), we obtain the following equation for $\tilde{\rho}_{\text{A}} = \mathcal{P}\tilde{\rho}$ as

$$\begin{aligned} \frac{\partial \tilde{\rho}_{\text{A}}}{\partial t} &= -iL_{\text{QDef}}(t)\tilde{\rho}_{\text{A}}(t) - \text{Tr}_{\text{F}} L_{\text{Fint}}(t) \\ &\quad \times \int_0^t d\tau U_{\text{QDef}}(t - \tau)L_{\text{Fint}}(t - \tau)|0\rangle\langle 0|\tilde{\rho}_{\text{A}}(t) \end{aligned} \quad (7.9)$$

with

$$U_{\text{QDef}}(t) = \exp(-iL_{\text{QDef}}t), \quad (7.10)$$

where L_{QDef} and L_{Fint} are the Liouville operators associated with the Hamiltonian H_{QDef} and H_{Fint} , respectively. Moreover, using the Born approximation that neglects the exciton operators of higher than the second order,³¹⁾ we approximate

$$U_{\text{QDef}}(t) \sim 1 \quad (7.11)$$

to obtain a compact equation as

$$\begin{aligned} \frac{\partial \tilde{\rho}_{\text{A}}}{\partial t} &= -iL_{\text{QDef}}(t)\tilde{\rho}_{\text{A}}(t) + \beta\{[R_- \tilde{\rho}_{\text{A}}(t), R_+] \\ &\quad + [R_-, \tilde{\rho}_{\text{A}}(t)R_+]\} - i\gamma[R_+R_-, \tilde{\rho}_{\text{A}}(t)] \end{aligned} \quad (7.12)$$

with

$$\beta + i\gamma \equiv \int_0^t \sum_{\mathbf{k}, \lambda} |g_{\mathbf{k}\lambda}|^2 e^{i(\Omega - \omega_{\mathbf{k}})\tau} d\tau, \quad (7.13)$$

which is exactly the same form as the Lindblad’s master equation³³⁾ describing a general Markovian dynamics for a dissipative quantum system. Here the real and imaginary parts of the right hand side of eq. (7.13) are designated as β and γ , respectively. In the following we neglect the energy shift as $\gamma = 0$, for simplicity. Note that the second and the third terms of the right hand side of eq. (7.12) are known as the Dicke’s master equation.^{12,15,17)}

7.1 Semi-classical description with the effective Hamiltonian

Neglecting quantum correlation between excitons,¹³⁾ we approximate the total density operator ρ_{A} as a direct product of the density operator ρ_n at each site n

$$\rho_{\text{A}} = \prod_n \rho_n, \quad (7.14)$$

and then solve eq. (7.12). Noticing that the dynamics governed by the original Hamiltonian eq. (2.1) is not rigorously identical to the one described by the effective

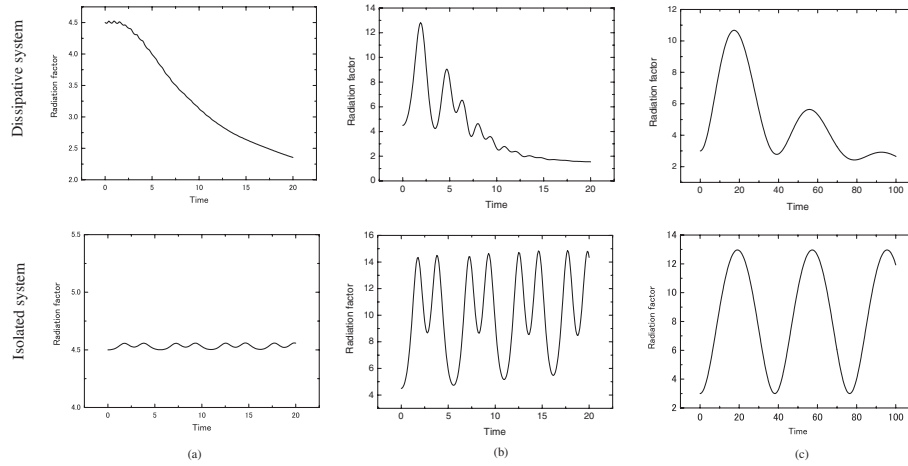


Fig. 19. Time evolution of the radiation factor for dissipative systems (upper) and isolated systems (lower). We consider the following three cases for both systems: (a) a “ferromagnetic” case, (b) an “anti-ferromagnetic” case which is turned to a dipole-ordered state after manipulating the initial population differences, and (c) a “dipole-forbidden” case discussed in §4.3. The parameters $\beta = 0.05$ and $\gamma = 0$ are used.

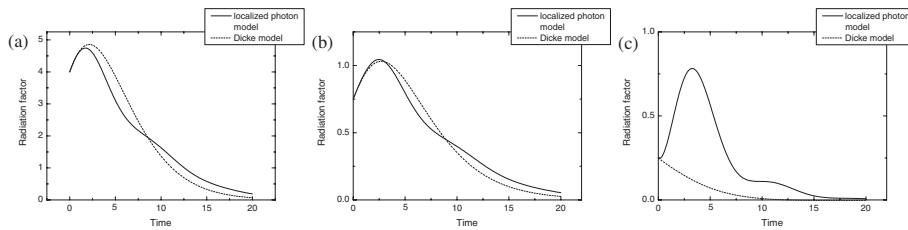


Fig. 20. Time evolution of the radiation factor obtained with quantum correlations. The solid curves are the results for our model while the dashed curves represent the results for the Dicke model. The dissipative system is assumed, and the parameters $N = 4$, $\beta = 0.05$, and $\gamma = 0$ are used. In addition, the following initial conditions are used: (a) $\langle P_n \rangle = 1$ and $\langle W_n \rangle = 1$, (b) $\langle P_n \rangle = (-1)^n / \sqrt{2}$ and $\langle W_n \rangle = 1 / \sqrt{2}$ which correspond to a dipole-forbidden state as shown in Fig. 9, and (c) $\langle P_n \rangle = (-1)^n / \sqrt{2} = -\langle W_n \rangle$ which corresponds to a dipole-ordered state as shown in Fig. 10.

Hamiltonian eq. (5.4), we use an isolated system described by the effective Hamiltonian eq. (5.4) in order to clarify the dynamics governed by eq. (7.12) for a dissipative system whose relevant system is described by the same Hamiltonian eq. (5.4). By comparing the radiation factors for the isolated system and the dissipative system, the similarity and the difference are discussed.

Figure 19 shows the time evolution of the radiation factor for (a) a “ferromagnetic” system belonging to the third group in Table I, (b) an “anti-ferromagnetic” system that belongs to the fourth group in Table I and is turned to a dipole-ordered state after manipulating the initial population differences, and (c) a “dipole-forbidden” system that is converted to a dipole-ordered state by the local manipulation discussed in §4.3 as $\langle W_n(0) \rangle = -\langle P_n(0) \rangle$. It follows from the lower part of Fig. 19(a) that superradiance is suppressed and does not manifest itself due to the difference between the original Hamiltonian eq. (2.1) and the effective Hamiltonian eq. (5.4). On the other hand, superradiant multiple pulses are generated in the isolated system and survive in the dissipative system for both cases shown in Figs. 19(b) and 19(c). Therefore we find with a semi-classical approach that multiple pulses, as predicted for an isolated system, can be emitted superradiantly from dipole-ordered states even in a dissipative system coupled to a radiation reservoir.

7.2 Quantum correlations

It is well known that superradiance in the Dicke model⁸⁾

occurs from a state where all excited states of all sites are occupied. On the other hand, the semi-classical approach discussed above cannot predict the occurrence of superradiance of the system when the total dipole of the system is zero as an initial condition.¹³⁾ This means that quantum fluctuations and correlations should be properly included so as to correctly describe the radiation properties of a system with no initial dipoles, and that the semi-classical approximation is not appropriate in this case. Thus we numerically solve the master equation (7.12), taking quantum correlations into account, and we investigate the radiation properties of the dissipative system. In particular, we compare the results obtained from our model, i.e., the localized photon model with those obtained from the Dicke model, for which the first term of the right hand side is dropped from eq. (7.12). Some of such results are shown in Figs. 20 and 21.

Figure 20(a) shows the time evolution of the radiation factor for the case that all the populations are completely in the excited states and there are no dipoles as an initial condition. The solid curves are the results for our model while the dashed curves represent the results for the Dicke model. It follows from the figure that a single superradiant pulse is emitted in both models, but that the peak value of the superradiant pulse is reduced while the tail is extended in our model. In Fig. 20(b), we present the result obtained from the initial condition as a zigzag profile of the dipole distribution of $\langle P_n \rangle = (-1)^n / \sqrt{2}$ and flat population differences of $\langle W_n \rangle = 1 / \sqrt{2}$. The system corresponds to a dipole-

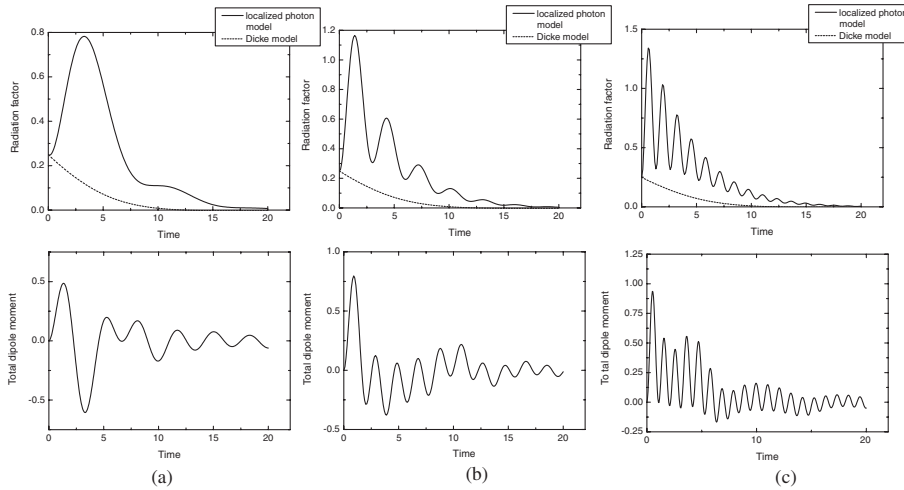


Fig. 21. Time evolution of the radiation factor (upper) and the total dipole moment (lower) obtained with quantum correlations. The solid curves are the results for our model while the dashed curves represent the results for the Dicke model. The system is assumed to be dissipative and in a dipole-ordered state evolved from a dipole-forbidden state, i.e., the same as in Fig. 20(c). The initial conditions are also the same as in Fig. 20(c), except for the exciton-localized photon coupling $g = 0.5$, (b) $g = 0.8$, and (c) $g = 1.2$.

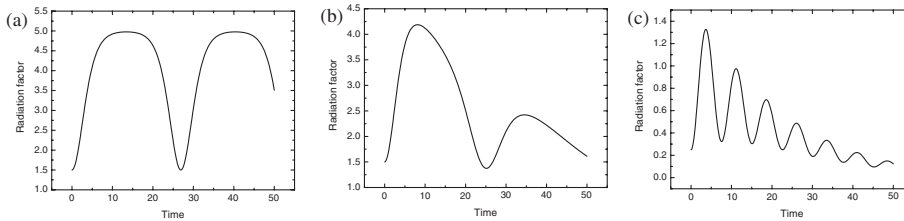


Fig. 22. Radiation profile obtained from three different methods. The system and the initial conditions to be considered are the same as in Fig. 21. The result is obtained (a) for the isolated system by the Liouvillian dynamics of the effective Hamiltonian with the semi-classical approximation, (b) for the dissipative system by the master equation (7.12) with the semi-classical approximation, and (c) for the dissipative system by the master equation (7.12) with quantum correlations. The parameters $N = 4$, $\beta = 0.05$, and $\gamma = 0$ are used.

forbidden state as shown in Fig. 9, where the total dipole is always zero. The radiation profiles obtained for both models are qualitatively same as found as in Fig. 20(a). The time evolution of the radiation factor is illustrated in Fig. 20(c) for the case that initially the alternating dipole is set as $\langle P_n \rangle = (-1)^n / \sqrt{2}$ and the sign of the population difference in each QD is set opposite to that of the corresponding dipole as $\langle W_n \rangle = -\langle P_n \rangle$. Owing to the flip hypothesis, a dipole-ordered state emerges in this case, and a distinct difference between the two models is observed: our model (solid curve) shows superradiance while the Dicke model (dashed curve) does not. Since we can infer that the difference stems from the dipole-ordering phenomenon, we further examine this case in order to clarify the relation between the radiation factor and the total dipole of the system.

Figure 21 presents the time evolution of the radiation factor (upper) and the total dipole (lower) by changing the exciton-localized photon coupling constant g as (a) $g = 0.5$, (b) $g = 0.8$, and (c) $g = 1.2$. It is found that the frequency of the total dipole increases as the coupling constant becomes strong. As a result, the oscillation frequency of the radiation factor increases, and thus multiple pulses are emitted superradiantly from the dissipative system. Therefore the difference between the two models, as we expected, originates from the occurrence of a dipole-ordered state or a collective dipole oscillation via localized photon–exciton

interactions.

At the end of this section, we examine the applicability of the semi-classical approach which has an advantage over the quantum approach that one can easily handle a relatively large number N system. In Fig. 22 we show the radiation profile obtained from three different methods. The system and the initial conditions to be considered are the same as in Fig. 21. The result is obtained (a) for the isolated system by the Liouvillian dynamics of the effective Hamiltonian with the semi-classical approximation, (b) for the dissipative system by the master equation (7.12) with the semi-classical approximation, and (c) for the dissipative system by the master equation (7.12) with quantum correlations. We find from Fig. 22 that multiple pulses are generated for all the cases though each frequency of the oscillation is different. It indicates that the semi-classical approach can describe qualitatively the radiation properties of both isolated and dissipative systems when the total dipole of the system is not zero. The strong radiation coming from the dipole-ordering phenomenon, or the non-linearity and the collective phenomena of the dynamics of the system considered in this paper can be qualitatively predicted by the semi-classical approach.

8. Conclusions

In order to investigate the dynamics of the system, we

presented a model of an N two-level quantum dot system interacting with optical near fields, explicitly expressing localized photonic degrees of freedom that characterize the unique property of localization of optical near fields. In the low density limit of excitons (N two-level system) are approximately treated as bosons, and a rigorous solution of the Heisenberg equation is obtained. Using the solution, we have examined the dynamics of the excitonic system to show that the dipole moments linearly propagate in the system. Since the dipole moments in the system represent the quantum coherence between any two levels, this phenomenon might be applied to a photonic device on a nanometer scale, or transportation of quantum information.

For fermionic excitons, the Heisenberg equation becomes nonlinear, and the dynamics is more complicated. We obtained a perturbative solution given by eq. (4.14) within the second order with respect to the localized photon–exciton interaction, to investigate the dipole dynamics. The study revealed that there exist several oscillating quasi-steady states depending on the material parameters. Using the effective Hamiltonian obtained from renormalization of localized photonic degrees of freedom, we classified such quasi-steady states into several groups, some of which are a “ferromagnetic” state with all the dipoles aligned to the same direction, and an “anti-ferromagnetic” state with the alternating dipoles, as shown in Table I.

Here it should be noted that if the sign of the population difference $\langle W_n(0) \rangle$ at arbitrary site n and at time $t = 0$ is inverted, then the dipole of the same site at arbitrary time t , $\langle P_n(t) \rangle$, also changes the sign [see eq. (4.15)]. Using this flip hypothesis, we can transform an arbitrary dipole distribution of the system into a dipole-ordered state after manipulating the initial distribution of the population differences. This hypothesis is based on the perturbative solution eq. (4.15) that determines the sign of $\langle P_n(t) \rangle$ according to the sign of the product of $\langle P_1(0) \rangle \langle W_n(0) \rangle$. It also originates from the fermionic property of excitons, which gives Heisenberg equations of motion for b_n ($\propto P_n$) as

$$[H_{b-b}, b_n] = \sum_{m \neq n} \Delta \Omega_{nm} W_n b_m. \quad (8.1)$$

The right hand side of eq. (8.1) is proportional to $\langle P_m \rangle \langle W_n \rangle$ for fermions while it is proportional to $\langle P_m \rangle$ for bosons. Therefore the occurrence of this kind of nonlinearity for fermionic excitons is a possible origin of the flip hypothesis.

Solving the Heisenberg equations (4.17) and (4.18) with the semi-classical approximation, we examined the radiation property of our system as an isolated system. It was found from numerical analysis that dipole-ordered states, which have large total dipole moments, show a large radiation probability comparable to Dicke’s superradiance. In particular, it predicted that multiple pulses are superradiantly emitted from the system. In order to verify whether such a phenomenon is inherent in an isolated system or not, we solved master equations (7.12) for a dissipative system with the semi-classical approximation, and found that such multiple pulses in the radiation profile can survive even in a dissipative system coupled to a radiation reservoir. Multiple superradiant peaks have been experimentally observed in an atomic gas system,¹⁸⁾ and the origin has been reported as the dipole–dipole interaction between a

two-level system within the framework of the Dicke model.¹⁹⁾ Since excitons in our model are indirectly coupled with one another through the interactions with localized photons, it may be concluded that the pulse oscillation in the radiation profile occurs in a similar mechanism as that of the Dicke model.

Finally we solved master equation (7.12), taking quantum correlations into account, and compared the results with those obtained from the Dicke model. When all the populations are initially in the excited states, similar radiation profiles for both models are obtained. The qualitative difference is that the peak value of the radiation pulse in our model is reduced and the tail is extended. This tendency has been examined from comparison between the atomic system and the Frenkel exciton system, where excitons can propagate via the dipole–dipole interaction, and the same qualitative difference as ours has been reported.²¹⁾ Regarding to the multiple-pulse generation which we have obtained, the Frenkel exciton model has also predicted a possibility that the superradiance profile oscillates if the system is initially prepared with a partial population inversion.²²⁾ We concluded from our modeling that the superradiant peaks of multiple pulses correspond to the occurrence of a collective dipole oscillation, or a dipole-ordered state.

It is an open question why the dipole distribution of our system has several quasi-steady states, which was predicted in this paper by using the perturbative expressions, numerical solutions of the Heisenberg equations, and the effective Hamiltonian. Since our system considered here has several kinds of symmetry, we expect that the stability of such quasi-steady states is clarified from the viewpoint of symmetry. The size dependence of the radiation profile has been investigated in the Dicke model.⁹⁾ In order to clarify the differences between optical near fields and propagating fields, it is interesting to examine such size dependence in our model. The semi-classical approach may be useful for such a qualitative study because it has an advantage over the quantum approach with respect to the computational time. One of our main goals was to clarify the inherent characteristics in optical near fields from the viewpoint of the coupling scheme: a local coupling system and a global coupling system. We have shown several differences between our model (local coupling system) and the Dicke model (global coupling system), but we require further efforts to answer the question more directly.

Acknowledgments

The authors are grateful to H. Hori, I. Banno, N. Ohnishi, and C. Uchiyama of Yamanashi University for fruitful discussions. They also gratefully acknowledge valuable suggestion from F. Shibata of Ochanomizu University on the topics in §5.1.

- 1) T. H. Stievater, Xiaoqin Li, D. G. Steel, D. Gammon, D. S. Katzer, D. Park, C. Piermarocchi and L. J. Sham: *Phys. Rev. Lett.* **87** (2001) 133603; H. Kamada, H. Gotoh, J. Temmyo, T. Takagahara and H. Ando: *ibid.* **87** (2001) 246401; T. Kawazoe, K. Kobayashi, J. Lim, Y. Narita and M. Ohtsu: *ibid.* **88** (2002) 067404; H. Htoon, T. Takagahara, D. Kulik, O. Baklenov, A. L. Holmes, Jr. and C. K. Shih: *ibid.* **88** (2002) 087401.

- 2) M. Ohtsu and H. Hori: *Near-Field Nano-Optics* (Kluwer Academic/Plenum, New York, 1999).
- 3) *Near-Field Nano/Atom Optics and Technology*, ed. M. Ohtsu (Springer-Verlag, Tokyo, 1998).
- 4) M. Ohtsu, K. Kobayashi, T. Kawazoe, S. Sangu and T. Yatsui: *IEEE J. Sel. Top. Quantum Electron.* **8** (2002) 839.
- 5) K. Cho: *Prog. Theor. Phys. Suppl. No. 106* (1991) 225.
- 6) H. A. Posch, W. G. Hoover and F. J. Vesely: *Phys. Rev. A* **33** (1986) 4253.
- 7) W. G. Hoover and H. A. Posch: *Phys. Rev. E* **49** (1994) 1913.
- 8) R. H. Dicke: *Phys. Rev.* **93** (1954) 99.
- 9) M. Gross and S. Haroche: *Phys. Rep.* **93** (1982) 301.
- 10) N. Rehler and J. Eberly: *Phys. Rev. A* **3** (1971) 1735.
- 11) R. H. Lehnberg: *Phys. Rev. A* **2** (1970) 883.
- 12) G. S. Agarwal: *Phys. Rev. A* **2** (1970) 2038.
- 13) G. S. Agarwal: *Phys. Rev. A* **4** (1971) 1791.
- 14) L. M. Narducci, C. A. Coulter and C. M. Bowden: *Phys. Rev. A* **9** (1974) 829.
- 15) R. Bonifacio, P. Schwendimann and F. Haake: *Phys. Rev. A* **4** (1971) 302; *ibid.* **4** (1971) 854.
- 16) R. Friedberg and S. R. Hartmann: *Phys. Rev. A* **10** (1974) 1728.
- 17) B. Coffey and R. Friedberg: *Phys. Rev. A* **17** (1978) 1033.
- 18) N. Skribanowitz, I. P. Herman, J. C. MacGillivray and M. S. Feld: *Phys. Rev. Lett.* **30** (1973) 309.
- 19) R. Bonifacio, L. A. Lugiato and A. A. Crescentini: *Phys. Rev. A* **13** (1976) 1648.
- 20) R. Bonifacio and L. A. Lugiato: *Phys. Rev. A* **11** (1975) 1507.
- 21) T. Tokihiro, Y. Manabe and E. Hanamura: *Phys. Rev. B* **47** (1993) 2019.
- 22) T. Tokihiro, Y. Manabe and E. Hanamura: *Phys. Rev. B* **51** (1995) 7655.
- 23) A. Nakamura, H. Yamada and T. Tokizaki: *Phys. Rev. B* **40** (1989) 8585.
- 24) K. Kobayashi and M. Ohtsu: *J. Microsc.* **194** (1999) 249.
- 25) K. Kobayashi, S. Sangu, H. Ito and M. Ohtsu: *Phys. Rev. A* **63** (2001) 013806.
- 26) C. Carniglia and L. Mandel: *Phys. Rev. D* **3** (1971) 280.
- 27) V. M. Agranovich and M. D. Galanin: *Electric excitation energy transfer in condensed matter* (North-Holland, Amsterdam, 1982) Chap. 4.1.
- 28) T. Saso, Y. Suzumura and H. Fukuyama: *Prog. Theor. Phys. Suppl. No. 84* (1985) 269.
- 29) J. Knoester and S. Mukamel: *Phys. Rev. A* **39** (1989) 1899.
- 30) J. Schwinger: *Phys. Rev.* **74** (1948) 958; H. Bethe: *ibid.* **66** (1944) 163; J. Bouwkamp: *Rep. Prog. Phys.* **17** (1954) 35.
- 31) L. Mandel and E. Wolf: *Optical coherence and quantum optics* (Cambridge University Press, Cambridge, 1995) Chap. 16.
- 32) C. Kittel: *Quantum theory of solids* (John Wiley & Sons, New York, 1987) 2nd revised printing, p. 148.
- 33) G. Lindblad: *Commun. Math. Phys.* **48** (1976) 119.

Evaluation of the discrete energy levels of individual ZnO nanorod single-quantum-well structures using near-field ultraviolet photoluminescence spectroscopy

T. Yatsui^{a)}

Solution-Oriented Research for Science and Technology (SORST), Japan Science and Technology Agency, Machida, Tokyo 194-0004, Japan

J. Lim and M. Ohtsu^{b)}

Interdisciplinary Graduate School of Science and Engineering, Tokyo Institute of Technology, Yokohama, Kanagawa 226-8502, Japan

S. J. An and G.-C. Yi

National CRI Center for Semiconductor Nanorods and Department of Materials Science and Engineering, Pohang University of Science and Technology (POSTECH), San 31 Hyoja-dong, Pohang, Gyeongbuk 790-784, Korea

(Received 13 February 2004; accepted 2 June 2004)

Spatially and spectrally resolved photoluminescence imaging of individual ZnO/ZnMgO nanorod single-quantum-well structures (SQWs) with a spatial resolution of 55 nm was performed using the optical near-field technique with a metallized UV fiber probe. Using excitation power density-dependent photoluminescence spectra of a ZnO/ZnMgO SQW nanorod, we observed the discrete energy levels in a ZnO quantum-well layer. © 2004 American Institute of Physics.

[DOI: 10.1063/1.1776338]

For future optical transmission systems with high data transmission rates and capacity, we have proposed nanometer-scale photonic devices (i.e., nanophotonic devices) and a method of integrating them.¹ These devices consist of nanometer-scale dots, and an optical near field is used as the signal carrier. As a representative device, a nanophotonic switch can be realized by controlling the dipole forbidden optical energy transfer among resonant energy level in nanometer-scale quantum dots via an optical near field.² It is made of sub-100-nm scale dots and wires, and their size and position on the substrate must be controlled with nanometer-scale accuracy. A nanometer-scale ZnO dot is a promising material for realizing these devices at room temperature, due to its large excitation binding energy (60 meV).^{3,4} Furthermore, the recent demonstration of semiconductor nanorod quantum-well structure enables us to fabricate nanometer-scale electronic and photonic devices on single nanorods.⁵⁻⁸ Recently, ZnO/ZnMgO nanorod multiple-quantum-well structures (MQWs) were fabricated and the quantum confinement effect of the MQWs was successfully observed.⁸ In addition, further improvement in the fabrication of nanorod heterostructures has resulted in the observation of significant photoluminescence (PL) intensity, even from nanorod single-quantum-well structures (SQWs).⁹

To confirm the promising optical properties of individual ZnO/ZnMgO SQWs for realizing nanophotonic devices, we measured the PL spectra using a low temperature near-field optical microscope (NOM). Using a metallized UV fiber probe, the spatial distribution of PL intensity and sharp PL spectra of individual ZnO well layers were observed.

ZnO/Zn_{1-x}Mg_xO SQWs were fabricated on the ends of ZnO nanorods with a mean diameter of 40 nm using

catalyst-free metalorganic vapor phase epitaxy.^{8,10} The nanorods were grown on Al₂O₃(0001) substrate. The average concentration of Mg (x) in the Zn_{1-x}Mg_xO layers used in this study was determined to be $x=0.2$ using energy dispersive x-ray spectroscopy in a transmission electron microscopy chamber. The ZnO well layer thickness (L_w) investigated in this study was 2.5 nm, while the thicknesses of the Zn_{0.8}Mg_{0.2}O bottom and top barrier layers in the SQWs were fixed at 60 and 18 nm, respectively (Fig. 1 shows a schematic diagram of the SQWs).

Figure 2(a) shows far-field PL spectra taken at 15 K at various excitation power densities. A strong, sharp peak (I_2)

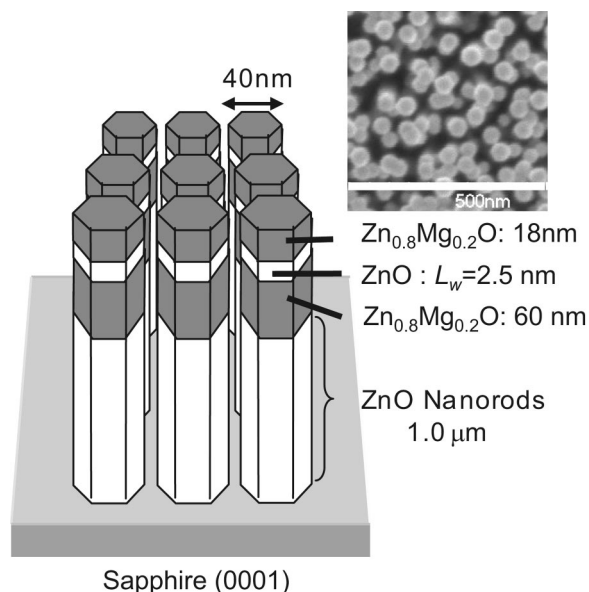


FIG. 1. Schematic of ZnO/ZnMgO SQWs on the ends of ZnO nanorods. The inset shows an overview of the ZnMgO/ZnO nanorod SQWs.

^{a)}Electronic mail: yatsui@ohtsu.jst.go.jp

^{b)}Also with: SORST, Japan Science and Technology Agency, 687-1 Tsuruma, Machida, Tokyo 194-0004, Japan.

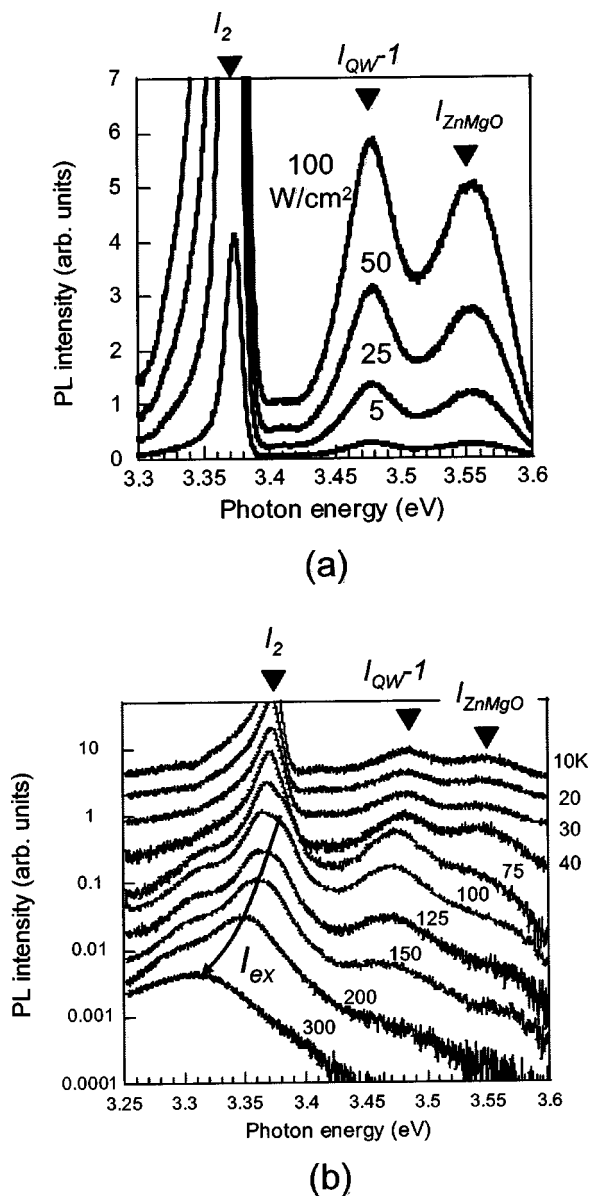


FIG. 2. (a) Power- (at 15 K) and (b) temperature-dependence of the far-field PL spectra of ZnO/ZnMgO nanorod SQWs.

was observed at 3.371 eV, while broad peaks (I_{QW-1} and I_{ZnMgO}) appeared at 3.480 and 3.555 eV. The number of peaks and their positions did not change up to 100 W/cm². Further experiments on the temperature-dependent evolution of the PL spectra in ZnO/Zn_{0.8}Mg_{0.2}O nanorod SQWs confirmed the origin of the PL peaks. Figure 2(b) shows typical PL spectra of ZnO/Zn_{0.8}Mg_{0.2}O nanorod SQWs measured over a temperature range from 10 to 293 K. At 10 K, a strong, sharp peak (I_2) was observed at 3.371 eV, while broad peaks appeared at 3.485 eV (I_{QW-1}) and 3.555 eV (I_{ZnMgO}). As the temperature increased, the intensities of the I_2 and I_{ZnMgO} peaks decreased drastically, and they almost disappeared at temperatures above 100 K, while the I_{ex} and I_{QW-1} peaks increased relative to I_2 and I_{ZnMgO} . This behavior presumably results from the decomposition of bound excitons to free excitons owing to the increased thermal energy, and supports the argument described above, that PL I_{ex} and I_{QW-1} peaks correspond to a free exciton peaks, and I_2 and I_{ZnMgO} are the well-known neutral-donor bound exciton peak emitted from ZnO nanorod stems and

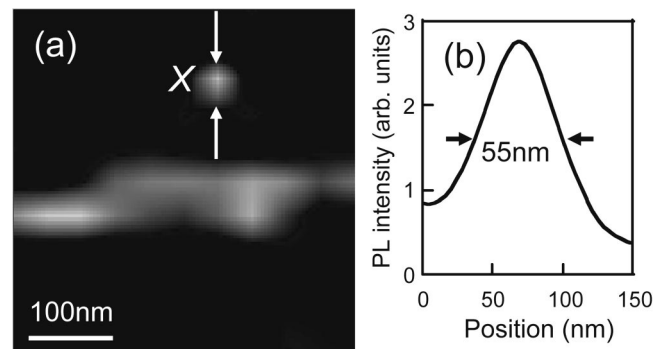


FIG. 3. Monochromatic PL image of ZnO/ZnMgO nanorod SQWs obtained at a photon energy of 3.483 eV. (b) Cross-sectional PL profile through spot X.

Zn_{0.8}Mg_{0.2}O barrier layers, respectively. Furthermore, the I_{QW-1} peak quenched rather slowly in comparison with the rapid quenching behavior of I_2 . Slow thermal quenching is characteristic of quantum structures, supporting our postulate that I_{QW-1} results from the quantum confinement effect. The experimental I_{QW-1} peak energy was consistent with the theoretical value in a one-dimensional square potential well, in which $0.28m_0$ and $1.8m_0$ are the effective masses of electron and hole in ZnO, respectively, at a ratio of conduction and valance band offsets ($\Delta E_c/\Delta E_v$) of 9, and a band gap offset (ΔE_g) of 250 meV.

To examine the optical properties of individual ZnO/ZnMgO nanorod SQWs, we performed spatially and spectrally resolved PL spectroscopy using a low-temperature NOM system in illumination-collection mode.¹¹ A sharpened UV fiber probe with a 50-nm-thick aluminum film was used for the scanning. He-CD laser light ($\lambda=325$ nm) was used to excite the ZnO/ZnMgO SQW through the UV fiber probe. The PL signal was collected with the same fiber probe as used for excitation, and detected using a cooled charge coupled device through a monochromator. The fiber probe was kept in close proximity to the sample surface (~ 10 nm) using the shear-force feedback technique.

Figure 3(a) shows the spatially and spectrally resolved PL image at 3.483 eV. Considering the rod diameter (40 nm), the bright spot labeled X [see Fig. 3(a)], the full width at half maximum of which was as small as 55 nm [see Fig. 3(b)], originated from one SQW nanorod. The spatial resolution, which almost equals the ZnO nanorod diameter, indicates that carrier tunneling between the nanorods can be neglected. Since the deep potential depth between the vacuum and the barrier layer is as much as 4 eV,¹² the carriers generated in the barrier layer in one nanorod are confined to the same nanorod through which the PL signal is collected. Furthermore, high spatial resolution imaging can be realized by enhancing the spatial resolution due to the plasmon resonance at the metallized sharpened tip.¹³ Since the sharpened UV probe is entirely coated with a thin metal film, light propagates inside the fiber core and is efficiently converted into the surface plasmon mode at the metallic tip, just as with a Kretschmann configuration.¹⁴ Such plasmon excitation effectively excites the carriers in the barrier layer and scatters the evanescent field of the ZnO quantum-well layer.

The five solid curves in Fig. 4(a) show the near-field PL spectra and their power dependence as determined by fixing the fiber probe at position X in Fig. 3(a). In the weak exci-

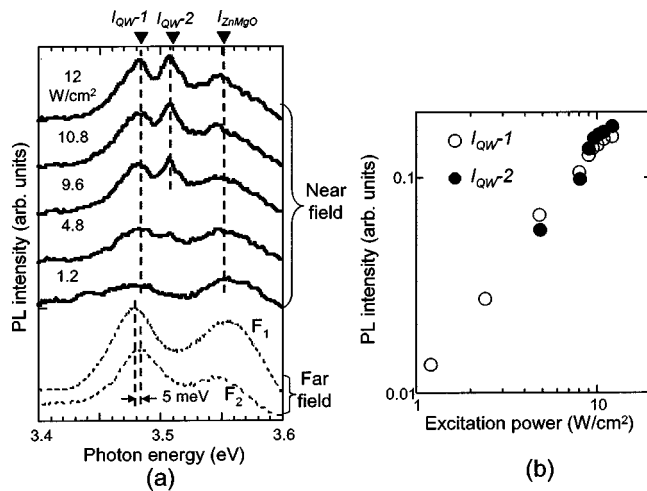


FIG. 4. (a) Solid curves show the near-field PL spectra of ZnO/ZnMgO nanorod SQWs at excitation densities ranging from 1.2 to 12 W/cm². The dashed curves (F_1 and F_2) show the far-field PL spectra. All the spectra were obtained at 15 K. (b) The excitation power dependence of the PL intensity at 3.483 (open circles) and 3.508 (closed circles) eV.

tation condition, a single PL peak is observed at 3.483 eV (I_{QW-1}). At excitation power densities exceeding 5 W/cm², another peak appears and grows at an energy of 3.508 eV (I_{QW-2}), which is 25 meV higher than I_{QW-1} . To confirm the origin of these emission lines, we plot the integrated PL intensity for the emission lines of both I_{QW-1} and I_{QW-2} in Fig. 4(b). The PL intensity of I_{QW-1} , indicated by the open circles, increases almost linearly up to 9 W/cm² and gradually saturates. This strongly implies that the I_{QW-1} emission line originates from the recombination of the ground state, and the saturation suggests band-filling. As shown in the far-field spectra in Fig. 4(a) [see dashed curves F_1 and F_2], the energy difference at different positions was as small as 5 meV. Therefore, the large difference (25 meV) between I_{QW-1} and I_{QW-2} is not due to fluctuations in the ZnO well width. Furthermore, changing the temperature drastically alters the emission energy, as shown in Fig. 2(b); thermal heating due to the illumination light is absent. At a power density of around 6 W/cm², the PL line of I_{QW-2} indicated by the closed circles appears. From this threshold-like PL behavior as a function of excitation power density, the PL line of I_{QW-2} is associated with the emission of the first excited state. Considering the composition and size of the SQWs, the energy separation between I_{QW-1} and I_{QW-2} (25 meV) is in agreement with the prediction of the the-

oretical value of the energy difference ($\Delta E = E_{h2} - E_{h1} = 21$ meV) between the first excited state of the hole (E_{h2}) and the ground state of the hole (E_{h1}). In this calculation, we used the following parameters: 0.28 m_0 and 1.8 m_0 for the effective masses of the electron and hole, respectively, and a band gap offset (ΔE_g) of 250 meV. This is the first detection of the excited state in ZnO quantum structures, although it has previously been observed in high-quality ZnO bulk crystals.¹⁵

In conclusion, we investigated the power-dependent features of individual ZnO/ZnMgO nanorod SQWs. Using a thin aluminum-coated UV fiber probe, we observed band-filling in the ground state and the resultant first excited state of a hole in ZnO/ZnMgO SQWs. This successful detection is attributed to the high spatial resolution (55 nm) of NOM and the high detection sensitivity utilizing plasmon resonance at the tip of the metallized UV fiber probe. The results shown here provide one criterion for realizing nanophotonic devices, such as the switching devices confirmed by the authors in CuCl quantum cubes.²

Research by S.J.A. and G.C.Y. was supported by Korea Research Foundation Grant No. KRF-2002-041-C00098.

- ¹M. Ohtsu, K. Kobayashi, T. Kawazoe, S. Sangu, and T. Yatsui, *IEEE J. Sel. Top. Quantum Electron.* **8**, 839 (2002).
- ²T. Kawazoe, K. Kobayashi, S. Sangu, and M. Ohtsu, *Appl. Phys. Lett.* **82**, 2957 (2003).
- ³A. Ohtomo, K. Tamura, M. Kawasaki, T. Makino, Y. Segawa, Z. K. Tang, G. K. L. Wong, Y. Matsumoto, and H. Koinuma, *Appl. Phys. Lett.* **77**, 2204 (2000).
- ⁴M. H. Huang, S. Mao, H. Feick, H. Yan, Y. Wu, H. Kind, E. Weber, R. Russo, and P. Yang, *Science* **292**, 1897 (2001).
- ⁵Y. Wu, R. Fan, and P. Yang, *Nano Lett.* **2**, 83 (2002).
- ⁶M. T. Björk, B. J. Ohlsson, C. Thelander, A. I. Persson, K. Deppert, L. R. Wallenberg, and L. Samuelson, *Appl. Phys. Lett.* **81**, 4458 (2002).
- ⁷M. S. Gudiksen, L. J. Lauhon, J. Wang, D. C. Smith, and C. M. Lieber, *Nature (London)* **415**, 617 (2002).
- ⁸W. I. Park, G.-C. Yi, M. Kim, and S. J. Pennycook, *Adv. Mater. (Weinheim, Ger.)* **15**, 526 (2003).
- ⁹W. I. Park, S. J. An, G.-C. Yi, S. Hong, T. Joo, and H. M. Cheong, *Appl. Phys. Lett.* (in press).
- ¹⁰W. I. Park, D. H. Kim, S.-W. Jung, and G.-C. Yi, *Appl. Phys. Lett.* **80**, 4232 (2002).
- ¹¹T. Saiki and K. Matsuda, *Appl. Phys. Lett.* **74**, 2773 (1999).
- ¹²M. W. Wang, J. O. McCaldin, J. F. Swenberg, T. C. McGill, and R. J. Hauenstein, *Appl. Phys. Lett.* **66**, 1974 (1995).
- ¹³T. Yatsui, K. Itsumi, M. Kourogi, and M. Ohtsu, *Appl. Phys. Lett.* **80**, 2257 (2002).
- ¹⁴*Surface Plasmons*, edited by H. Raether (Springer, Berlin, 1988).
- ¹⁵D. C. Reynolds, D. C. Look, B. Jogai, C. W. Litton, G. Cantwell, and W. C. Harsch, *Phys. Rev. B* **60**, 2340 (1999).

Quantum-Coherence Effect in a Quantum Dot System Coupled by Optical Near Fields

Suguru Sangu*, Kiyoshi Kobayashi*, Tadashi Kawazoe*, Akira Shojiguchi*, and Motoichi Ohtsu***

*ERATO Localized Photon Project, Japan Science and Technology Corporation
687-1 Tsuruma, Machida, Tokyo 194-0004, Japan
Fax: 81-42-788-6031, e-mail: sangu@ohtsu.jst.go.jp

**Interdisciplinary Graduate School of Science and Engineering, Tokyo Institute of Technology
4259 Nagatsuta-cho, Midori-ku, Yokohama, Kanagawa 226-8502, Japan

Dynamics of the exciton population in a quantum dot system coupled via optical near fields is theoretically investigated. We derive analytical solutions of the density matrix elements for one-exciton and two-exciton states. Based on the results, the transient response from a steady state induced by an applied light pulse is obtained as approximated solutions. The results show fast increase of the population due to the state filling of a sub-level and the oscillation behavior, which originate from coherence effects inherent in such a system. Moreover, slow population decay appears in the nanosecond regime, which is related to the effect of state filling and radiative relaxation. These characteristics well explain recent experimental data of time-resolved near-field spectroscopy, and clarify physics behind the phenomenon.

Key words: coupled quantum dot, optical near fields, coherence, population dynamics, relaxation

1. INTRODUCTION

Optical near fields provide a powerful tool to control the states of nanometric matter as well as to observe nanometric structures. The localization property of the optical near fields, which is free from the diffraction limit of light, allows selective access to nanometric objects. This induces interesting and inherent effects, such as non-radiative energy transfer between optically (dipolar) forbidden levels [1]. We previously estimated energy transfer time via optical near-field interaction, which is less than 100 ps [2]. Such characteristic features inherent in the optical near fields open up a way to realize a novel type of nanophotonic functional devices.

Since unidirectional energy transfer is an indispensable character for functional devices, we have considered a quantum dot system with intra-sublevel relaxation due to exciton-phonon interaction, where a few quantum dots are coupled via optical near-field interaction. In this paper, we assume a two-quantum dot system; one is two-level and the other is three-level. We theoretically derive the dynamics of exciton population in this system, and compare our results to data obtained in a recent time-resolved experiment [3]. Here, the key point is to control the exciton-population dynamics by applying a light pulse. In other word, transient dynamics from one-exciton states to two-exciton states determines the characteristics of device control.

In the case of resonant two-level quantum dots, the optical near-field interaction induces nutation of the population, or coherent oscillation, which is analogous to the Förster process describing molecular excitation [4]. We theoretically show that fluctuations of luminescence intensity in the experimental results are related to the coherent oscillation between resonant

energy levels. Moreover the quantum coherence can realize fast energy transfer in the system. As another aspect, we demonstrate slower population decay that is a characteristic effect in two-exciton states.

This paper is organized as follows. Section 2 is devoted to describing a theoretical model and equations of motion of the population in a coupled quantum dot system with analytical solutions for typical initial conditions. In Sec. 3, transient variation from one-exciton states to two-exciton states is investigated analytically, by comparing to the experimental results. Finally, concluding remarks are given in Sec. 4.

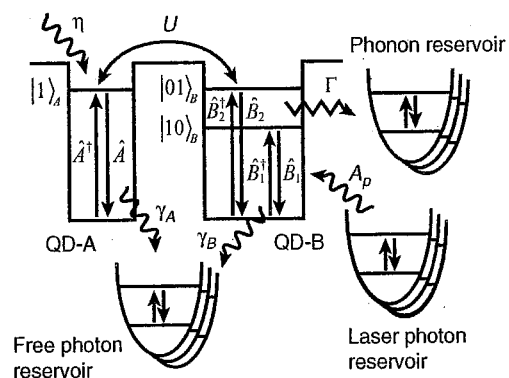


Fig. 1: A model of coupled quantum dot system. The reservoirs for phonons and free photons are introduced in order to represent the dissipation processes.

2. MODEL OF COUPLED QUANTUM DOT SYSTEM

2.1 Equations of motion

In order to evaluate luminescence intensity, we incorporate some reservoir systems as illustrated in Fig. 1. The energy levels $|1\rangle_A$ and $|10\rangle_B$ are coupled to a free photon reservoir, while the level $|01\rangle_B$ is not because the transition with even total quantum number is dipole forbidden by assuming cubic quantum dots. Temporal evolution of the density operator in this system can be described on the basis of the Born-Markov approximation [5] as

$$\begin{aligned} \dot{\hat{\rho}}(t) = & -\frac{i}{\hbar}[H_0 + H_{NF}, \hat{\rho}(t)] \\ & -\frac{\Gamma}{2}[\hat{B}_2^\dagger \hat{B}_1 \hat{B}_1^\dagger \hat{B}_2 \hat{\rho}(t) + \hat{\rho}(t) \hat{B}_2^\dagger \hat{B}_1 \hat{B}_1^\dagger \hat{B}_2 \\ & \quad - 2\hat{B}_1^\dagger \hat{B}_2 \hat{\rho}(t) \hat{B}_1^\dagger \hat{B}_1] \\ & -\frac{\gamma_A}{2}[\hat{A}^\dagger \hat{A} \hat{\rho}(t) + \hat{\rho}(t) \hat{A}^\dagger \hat{A} - 2\hat{A} \hat{\rho}(t) \hat{A}^\dagger] \\ & -\frac{\gamma_B}{2}[\hat{B}_1^\dagger \hat{B}_1 \hat{\rho}(t) + \hat{\rho}(t) \hat{B}_1^\dagger \hat{B}_1 - 2\hat{B}_1 \hat{\rho}(t) \hat{B}_1^\dagger], \end{aligned} \quad (1)$$

where

$$\begin{aligned} \hat{H}_0 = & E_1 \hat{A}^\dagger \hat{A} + E_1 \hat{B}_2^\dagger \hat{B}_2 + E_0 \hat{B}_1^\dagger \hat{B}_1, \\ \hat{H}_{NF} = & \hbar U (\hat{A}^\dagger \hat{B}_2 + \hat{B}_2^\dagger \hat{A}), \end{aligned} \quad (2)$$

where Γ , γ_A , and γ_B represent the relaxation constants of intra-sublevel transition via exciton-phonon coupling, and radiative transition in QD-A and B, respectively, which appear after tracing over both phonon and photon degrees of freedom. The strength of the optical near-field interaction is denoted as U . We have already derived the optical near-field interaction between two nanometric objects in our previous study [6] in which exciton-polariton degrees of freedom are eliminated. In this stage, we assume that phonon and photon reservoirs are in vacuum states, *i.e.*, zero temperature. Therefore, a process of stimulated absorption and emission for phonons and photons is not considered. What we focus on in this paper is the transition dynamics from one-exciton state to two-exciton state, and vice versa, and thus, we introduce six bases to present the state of the system as depicted in Fig. 2. Taking the expectation values by using these bases, we can evaluate the population dynamics in this system.

2.2 Dynamics driven from definite initial conditions

Before discussing the transient dynamics, we examine the dynamics driven from definite initial conditions. First, we pay attentions to the dynamics for one-exciton states where the initial conditions are set as $\rho_{A'A'B} (0) = 1$ and otherwise zero, where the subscripts are labeled as follows: $|0\rangle_A$ and $|1\rangle_A$ are abbreviated as A and A' , and $|00\rangle_B$, $|10\rangle_B$, and $|01\rangle_B$ as B , B' , and B'' . In this case, two-exciton states are not excited, and the equations of motion are closed within one-exciton states. Analytical solutions in this problem

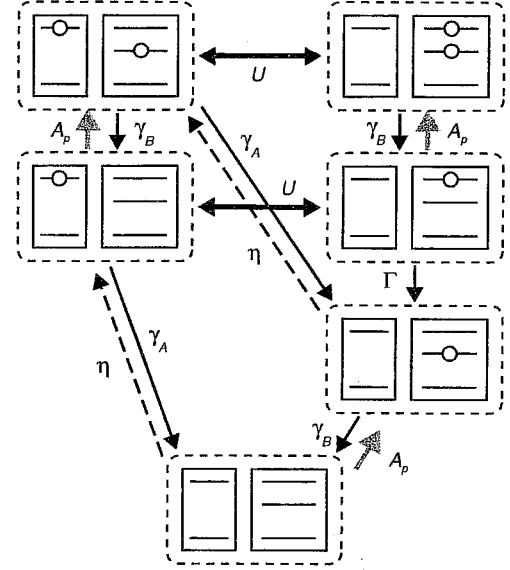


Fig. 2: Bases of the coupled quantum dot system with an exciton and two excitons.

can be obtained rigorously, and the population of the level $|1\rangle_A$ is given as

$$\begin{aligned} \rho_{A'B,A'B} (t) = & \exp\left[-\frac{\Gamma + \gamma_A}{2} t\right] \\ & \times \left[\cosh(Zt) + \frac{\Gamma - \gamma_A}{Z} \sinh(Zt) \right], \end{aligned} \quad (3)$$

where $Z = [(\Gamma - \gamma_A)^2 / 4 - U^2]^{1/2}$. We theoretically estimate that the optical near-field interaction U is much stronger than the radiative relaxation constant γ_A . When we assume the condition $\gamma_A \ll U < \Gamma$, Eq. (3) is reduced to a simple form as

$$\rho_{A'B,A'B} (t) = \exp\left[-2U \left(\frac{2U}{\Gamma}\right) t\right], \quad (4)$$

Apparently, the decay time on the level $|1\rangle_A$ is determined by $\Gamma/(4U^2)$, and the ratio in the round brackets in Eq. (4) represents a balance of the optical near-field interaction and intra-sublevel transition. Figure 3(a) shows a plot of Eqs. (3) and (4) as a function of time. In this figure, we can observe fast energy transfer from $|1\rangle_A$ to $|10\rangle_B$ in the order of 200 ps.

On the other hand, when a two-exciton state is prepared in which the level $|10\rangle_B$ is initially filled, it follows from Eq. (1) that intra-sublevel transition is prohibited because of the Fermion-like feature of excitons. In this case, the excitation remains in the resonant level of either QD-A or B, leading to long decay time. The equations of motion for two-exciton states are completely decoupled from one-exciton states,

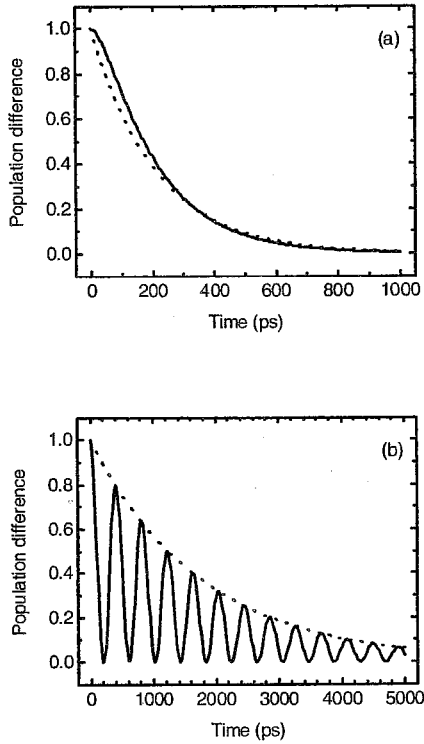


Fig. 3: Time evolution of the populations in QD-A. Initial conditions are set as follows: (a) completely excited on the level $|1\rangle_A$ in QD-A and (b) simultaneously excited on the levels $|1\rangle_A$ and $|10\rangle_B$. The fixed parameters are set as $U^{-1}=130$ ps, $\Gamma^{-1}=20$ ps, $\gamma_A^{-1}=5.9$ ns, and $\gamma_B^{-1}=2.1$ ns. The dotted curves in (a) and (b) represent exponential decay functions with decay constants of $2U/(2U/\Gamma)$ and $\gamma=\gamma_A/2+\gamma_B$, respectively.

and the analytic solutions are obtained by replacing the phonon relaxation constant Γ in Eq. (3) with zero and by multiplying the factor $e^{-\gamma t}$. Although two-exciton states are connected to one-exciton states with the radiative transition, the lifetime of population in the level $|1\rangle_A$ is in the order of 200 ps for one-exciton states as mentioned above. The population in two-exciton states has long decay time in the order of a few nanoseconds, while the population in one-exciton state is much smaller than that in two-exciton state. Therefore, the population of two-exciton state $\rho_{A'B',AB'}(t)$ is dominant in the luminescence-intensity measurement. The result is shown in Fig. 3(b). Sinusoidal oscillation appears with an exponential decay whose decay constant is given by $\gamma=\gamma_A/2+\gamma_B$. Our further interests are transient transitions between above two situations in order to investigate excitation or

signal control toward to nanophotonic devices.

3. TRANSIENT RESPONSE BY A LIGHT PULSE

Suppose to apply a light pulse to excite the level $|10\rangle_B$ in QD-B in order to demonstrate a change from a steady state. For the purpose, we introduce a coupling to a laser photon reservoir. Then, the following terms

$$\eta \left\{ \left[\hat{A} \hat{\rho}(t), \hat{A}^\dagger \right] + \left[\hat{A}^\dagger, \hat{\rho}(t) \hat{A} \right] \right\} + A_p(t) \left\{ \left[\hat{B}_i, \hat{\rho}(t), \hat{B}_i^\dagger \right] + \left[\hat{B}_i^\dagger, \hat{\rho}(t) \hat{B}_i \right] \right\} \quad (5)$$

are added to Eq. (1), where η and $A_p(t)$ are the rate of weak continuous excitation of QD-A to achieve a steady state, and that of strong pulse excitation for state filling in QD-B, respectively. These rates are proportional to the number of photons, and thus, the stimulated absorption and emission processes are involved. Here we assume incoherent excitations for simplicity. It would be valid if the period of the Rabi oscillation due to the laser pulse is longer than the applied pulse width. The light pulse couples one-exciton states to two-exciton states, and rigorous analytic solutions are hardly obtained. In the following, we show approximated solutions for the transient dynamics, separating the dynamics into two stages, an early stage and a later stage.

The steady state before applying the light pulse can be obtained from Eqs. (1) and (5) by setting the left hand side as zero. The populations in the steady state under the condition of $\gamma_A, \gamma_B \ll U < \Gamma$ are expressed as

$$\rho_{A'B,AB}(0_-) = \frac{\eta}{2U} \frac{\Gamma}{2U}, \quad \rho_{AB',AB'}(0_-) = \frac{\eta}{\Gamma} (\sim 0), \quad (6)$$

$$\rho_{AB',AB'}(0_-) = \frac{\eta}{\gamma_B}.$$

After the pulse excitation, each population is divided into two components. For example, the populations on the level $|1\rangle_A$ are given by $\rho_{A'B,AB}(0_+) = R\rho_{A'B,AB}(0_-)$ and $\rho_{AB,AB}(0_+) = (1-R)\rho_{A'B,AB}(0_-)$, where R denotes the changing rate from one-exciton states to two-exciton states. The other populations in Eq. (6) change in a similar way.

In the early stage, two-exciton states have long decay time as mentioned in Sec.2, and thus, it is reasonable to be $\rho_{AB',AB'}(t) \approx \rho_{AB',AB'}(0_+)$. From this approximation, equations of motion for one-exciton and two-exciton states are decoupled, and an approximated solution is obtained as

$$\rho_{A'B',AB'}^{\text{early}}(t) = \frac{R}{2} \left\{ \rho_{A'B,AB}(0_-) e^{-\gamma t} + \rho_{AB',AB'}(0_-) (1 - e^{-\gamma t}) + [\rho_{A'B,AB}(0_-) \cos(2Ut) + i \frac{\Delta \rho_{A'B,AB}(0_-)}{2} \sin(2Ut)] e^{-\gamma t} \right\}. \quad (7)$$

The second term in Eq. (7) represents an

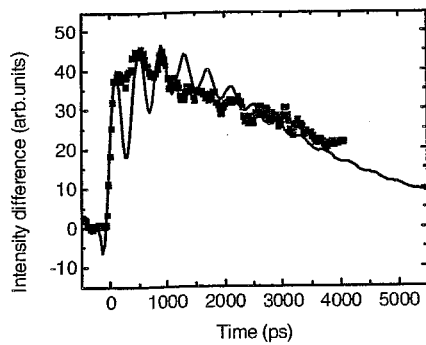


Fig. 4: Transient population dynamics from a steady state by applying a light pulse. The square dots represent the data of time-resolved experiment with CuCl quantum cubes embedded in a NaCl matrix. Analytical solution is depicted as the solid curve. The appropriate constant is multiplied by the analytical solution in order to compare the experimental data. The parameters are set as $U^{-1}=130$ ps, $\Gamma^{-1}=20$ ps, $\gamma_A^{-1}=5.9$ ns, and $\gamma_B^{-1}=2.1$ ns.

increase of the population that originates from the state filling of the level $|10\rangle_B$, and the terms in the rectangular brackets denote the coherence effect depending on the initial population.

On the other hand, in the later stage, the coherence in the two-exciton states disappears due to the radiative relaxation in both quantum dots. Therefore, the dynamics of the population follows a simple exponential curve as

$$\rho_{A'B',A'B'}^{\text{inter}}(t) = R\rho_{A'B',A'B'}(0_-) - (1 - R\rho_{A'B',A'B'}(0_-))e^{-\gamma t}. \quad (8)$$

An approximated solution in the whole time can be given by multiplying the density matrix elements in the early and later stages as

$$\rho_{A'B',A'B'}(t) = \rho_{A'B',A'B'}^{\text{early}}(t) \rho_{A'B',A'B'}^{\text{inter}}(t). \quad (9)$$

In Fig. 4, the temporal evolution obtained from Eq. (9) is plotted, together with experimental data. In first order approximation of η (weak excitation), the population increases with an exponent of $2\gamma_B$, and oscillates with a frequency of $2U$. The exponent reflects an increment due to continuous excitation and the components flowing into the lowest level $|10\rangle_B$ in the steady state. It follows the result that the fast state-filling time observed in the experiment comes from the effect of nutation or coherent energy transfer. With the radiative relaxation, the coherence effect is lost, and the excitation is occupied on the resonant energy levels, which have long decay time as same as in two-exciton

states. The slow decay observed around $t = 2$ ns originates from the competition of the population increase due to the state filling and decrease due to the radiative relaxation. Hence, our approximated solution well describes the experimental results and clarifies physics behind the phenomenon.

4. CONCLUSIONS

In order to confirm a possibility to control excitation transfer in a coupled quantum dot system, we have investigated transition from a steady state to transient state by applying a light pulse. An approximated analytic solution of the dynamics well explains characteristic features of recent experimental results. Both fast increase of population in the early stage and the oscillation behavior originate from coherent effect between two quantum dots with sub-levels to be filled. This state-filling effect and the radiative relaxation cause the slow decay in the stage of a few nanoseconds. As a result, signal transfer and control in such a quantum dot system can be achieved, and we expect that this is a promising technique for future nanophotonic devices.

REFERENCES

- [1] T. Kawazoe, K. Kobayashi, J. Lim, Y. Narita, and M. Ohtsu, *Phys. Rev. Lett.*, **88**, 067404 (2002).
- [2] M. Ohtsu, K. Kobayashi, T. Kawazoe, S. Sangu, and T. Yatsui, *IEEE J. Sel. Top. Quant. Electron.* **8**, 839-862 (2002).
- [3] T. Kawazoe, private communication.
- [4] Th. Förster, "Modern Quantum Chemistry", Ed. by O. Sinanoğlu, Academic Press, New York (1965) pp.96-137.
- [5] H. J. Carmichael, "Statistical Methods in Quantum Optics 1", Springer-Verlag, Berlin (1999).
- [6] K. Kobayashi, S. Sangu, H. Ito, and M. Ohtsu, *Phys. Rev. A* **63**, 013806 (2001).

(Received December 20, 2002; Accepted April 30, 2003)

Superradiant multiple pulses from excitons interacting with optical near fields

Akira Shojiguchi, Kiyoshi Kobayashi, Suguru Sangu, Kazuo Kitahara* and Motoichi Ohtsu**

ERATO Localized Photon Project, Japan Science and Technology, Tokyo, 194-0004, Japan

Fax: 81-42-788-6045, e-mail: akirasho@ohtsu.jst.go.jp

* Division of Natural Sciences, International Christian University, Tokyo, 181-8585, Japan

** Interdisciplinary Graduate School of Sciences and Engineering, Tokyo Institute of Technology, Kanagawa, 226-8502, Japan

A model of an N two-level system interacting with optical near fields is presented. Varying the initial conditions, we examine the dynamics of the electric dipoles of the system to predict a collective dipole oscillation, *i.e.*, manifestation of a dipole-ordered state. Multiple pulses superradiantly emitted from such a state is also shown, and the origins of the phenomena are discussed, on the basis of a localized photon model using both semi-classical and quantum master equations. Brief comments on an application to a nanometric photonic component are given.

Key words: localized photon, dipole ordering, superradiance, Dicke model

1. INTRODUCTION

Nano-fabrication and its application to nanophotonic devices have been actively investigated, and special attention has been paid to optical near-field approaches because of their potential for ultra-high speed operation and miniaturization[1, 2]. It is now essential to clarify the inherent phenomena of optical near fields that are applicable to nano-fabrication and devices of a nanometer scale. In this context, a localized photon model has been proposed to predict a collective dipole oscillation of an N two-level quantum dots (QD) system after local manipulation of the initial quantum states [3]. However, the origin and features of this dipole-ordered state have not been fully explored. In this paper we report an intriguing phenomenon of multiple pulses superradiantly emitted from the dipole-ordered state on the basis of a localized photon model using both semi-classical and quantum master equations. We discuss its mechanism, features, and a possible nanophotonic application.

2. MODEL HAMILTONIAN

In this section we review the localized photon model which has been introduced in Ref. [3]. The system consists of N two-level QDs closely configured in a ring and localized photons coupled to each QD. The model Hamiltonian H can be written in the following form:

$$H = H_a + H_b + H_{\text{int}}, \quad (1a)$$

$$H_a = \varepsilon \sum_{n=1}^N a_n^\dagger a_n + V \sum_{n=1}^N (a_{n+1}^\dagger a_n + a_n^\dagger a_{n+1}), \quad (1b)$$

$$H_b = E \sum_{n=1}^N b_n^\dagger b_n, \quad (1c)$$

$$H_{\text{int}} = U \sum_{n=1}^N (a_n^\dagger b_n + a_n b_n^\dagger), \quad (1d)$$

where H_a and H_b describe localized photons and excitons in QDs, respectively, and the intradot interaction between the localized photons and the excitons is denoted as H_{int} . Creation and annihilation operators for a localized photon and an exciton in each QD labeled by n are expressed as a_n^\dagger, a_n and b_n^\dagger, b_n respectively. We apply the boson commutation relations to the localized photons as

$$[a_n, a_n^\dagger] = \delta_{nn'}, \quad [a_n, a_{n'}] = [a_n^\dagger, a_{n'}^\dagger] = 0.$$

The excitons on a site obey the fermion commutation relations while excitons at different sites satisfy the boson commutation relations as

$$[b_n, b_n^\dagger] = \delta_{nn'}(1 - 2b_n^\dagger b_n).$$

The constant energies of the localized photons and excitons are assumed to be $\varepsilon = \hbar\omega$ and $E = \hbar\Omega$ respectively. The hopping energy of the localized photons is represented as $V = \hbar v$, and $U = \hbar g$ is for the conventional dipolar coupling between the localized photons and the excitons in the rotating wave approximation. We show an illustration of our system in Fig. 1.

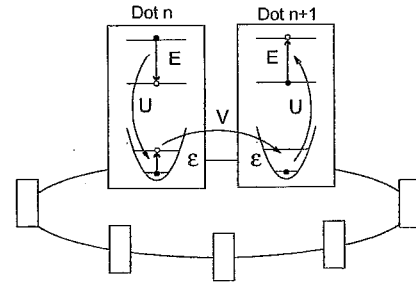


Fig. 1. Model of a quantum dots system interacting with localized photons. Each quantum dot interacts with the adjacent dots via localized photons.

3. DIPOLE-ORDERED STATE

Using the Hamiltonian (1), we can obtain the second-order perturbation solution for temporal evolution of the dipole moment at the n -th site [3]

$$\langle P_n(t) \rangle = \langle b_n(t) + b_n^\dagger(t) \rangle \text{ as}$$

$$\langle P_n(t) \rangle = \langle P_n(0) \rangle \left(\cos \Omega t - g^2 \sum_j c_j(t) P_{nj}^2 \right) + g^2 \sum_j \sum_{m \neq n} c_j(t) P_{nj} P_{mj} \langle P_m(0) \rangle \langle W_n(0) \rangle. \quad (2)$$

Here P_{nj} is the diagonalization matrix element of the Hamiltonian of the localized photons H_a , and $c_j(t)$ is the time dependent coefficient depending on the exciton energy $\hbar\Omega$ and j -th eigenvalue $\hbar\lambda_j$ of the Hamiltonian H_a . The initial dipole moment and the population difference at site n are denoted as $\langle P_n(0) \rangle$

and $\langle W_n(0) \rangle = \langle b_n^\dagger b_n - b_n b_n^\dagger \rangle$, respectively. From Eq. (2) it follows that the dipole distribution of the system at time t can be controlled by the initial population differences, which indicates a possibility of a local manipulation of dipole moment of an arbitrary site which results in a collective behavior of the dipoles, or in a dipole ordered state.

On the basis of Eq. (2), we numerically investigate the dynamics of the dipoles depending on initial conditions. Figure 2 illustrates an intriguing non-radiative case, where the alternating dipoles $\langle P_n(0) \rangle = (-1)^n$ are initially set, *i.e.*, the total dipole of the system is vanishing.

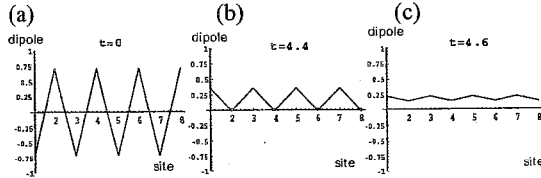


Fig. 2. Temporal evolutions of the dipole moments for the system size $N=8$ at time (a) $t=0$, (b) $t=4.4$ (c) $t=4.6$ with a unit of time \hbar/E . A unit of energy of our system is a typical excitation energy E of a quantum dot which is of the order of 1 eV. The vertical and horizontal axes represent the dipole and the site number, respectively. From (b) and (c), one can see that a collective oscillation is growing, which is originated from a local manipulation of the initial distribution of the population difference as $\langle W_n(0) \rangle = -\langle P_n(0) \rangle$.

Figures 2(b) and 2(c) show that a collective oscillation of the dipoles is growing, *i.e.*, a dipole-ordered state is manifested. The point of the dipole ordering is a local manipulation in which the sign of the population difference in each QD is set opposite to that of the

corresponding diopole as $\langle W_n(0) \rangle = -\langle P_n(0) \rangle$.

4. RADIATION PROPERTY

We examine the radiation properties of the dipole-ordered state discussed above, for which we expect that intense radiation is emitted. For simplicity, we renormalize the localized photonic degrees of freedom into an effective Hamiltonian, $H_{\text{QD-eff}}$, with the help of the unitary transformation [4, 5]:

$$H_{\text{QD-eff}} = \sum_n \hbar\Omega b_n^\dagger b_n + \sum_n \sum_{m \neq n} \hbar J_{nm} b_n^\dagger b_m, \quad (3)$$

where the hopping energy of excitons is expressed as

$$J_{nm} = \sum_j \frac{g^2}{\Omega - \lambda_j} P_{nj} P_{mj}.$$

In addition, a radiation field weakly interacting with the QDs is included in the system as a reservoir that makes the system dissipative. Then, equations of motion for the density operator $\rho_{\text{QD}}(t)$ of the QD system can be written as

$$\frac{\partial \rho_{\text{QD}}(t)}{\partial t} = -iL_{\text{eff}} \rho_{\text{QD}}(t) + \gamma([R_- \rho_{\text{QD}}(t), R_+] + [R_-, \rho_{\text{QD}}(t) R_+]), \quad (4)$$

where L_{eff} is the Liouville operator associated with $H_{\text{QD-eff}}$ and the relaxation constant due to the elimination of the radiation field's degrees of freedom is denoted as γ . The raising and lowering operators R_\pm are defined, respectively in terms of the creation and annihilation operators of excitons in the QDs as

$$R_- = \sum_n b_n, \quad R_+ = \sum_n b_n^\dagger.$$

To study the emission properties of the radiation, we solve Eq. (4) and calculate the radiation intensity

$$I(t) = \langle R_+(t) R_-(t) \rangle A,$$

where A is the Einstein's A coefficient which represents the probability of spontaneous emission of an excited single two-level system. We first solve Eq. (4) semi-classically without taking account of quantum correlations. This method has an advantage over the full quantum method to enable us to easily handle a relatively large number N system. However, it should be noted that the Dicke model shows superradiance from the initial condition of a perfect inversion population, while semi-classical descriptions in the same condition do not predict superradiance because the system has initially no dipoles [6, 7]. We consider the case discussed in Sec. 3 that is initially non-radiative and subsequently dipole-ordered. Figure 3 shows that multiple pulses can be emitted from the system superradiantly (while the Dicke model shows no superradiance under such conditions), and indicates that the ordered total dipole moment of the system plays an important role in the oscillating radiation profile.

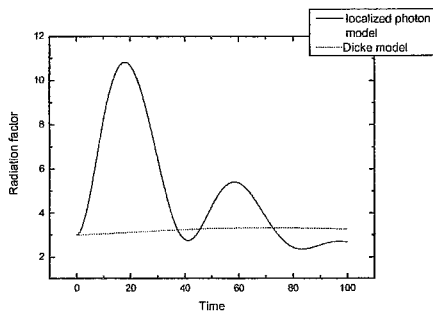


Fig. 3. Temporal evolution of the radiation intensity for the system size $N=8$ obtained semi-classically without a quantum correlation among excitons. The solid curve is the result for the localized photon model while the dotted curve represents the result for the Dicke model. The initial condition is the same with Fig. 2. Three radiation peaks are seen for the dipole-ordered state when $\gamma=0.005$ is used. The coupling strength of exciton-localized photon interaction is assumed to be weak, $g=0.2$.

Considering the quantum correlation, we then solve Eq. (4) with the same initial conditions and system size $N=4$ to further investigate the origin and mechanism of the multiple pulse generation and quantum effects. As shown in Fig. 4, a superradiant pulse is emitted in our case, while the Dicke model shows no superradiance under such conditions.

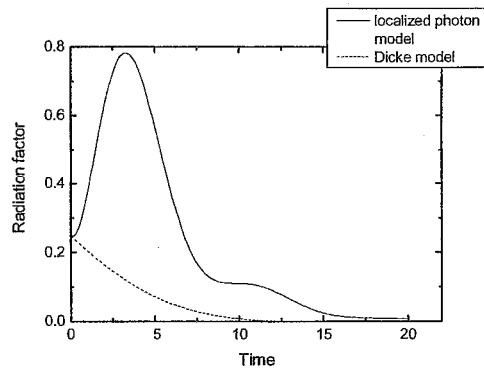


Fig. 4. Temporal evolution of the radiation intensity for the system size $N=4$ obtained with quantum correlations. The solid curve is the result for the localized photon model while the dotted curve represents the result for the Dicke model. The parameters are $\gamma=0.05$ and $g=0.5$.

The difference is due to the following fact: the dipole-ordered state appears in our case while it does not in the Dicke model. This is qualitatively predicted in the semi-classical approach (see Fig 3). This feature is seen more clearly in Figs. 5(a)-(b) when the coupling strength of the exciton-localized photon interaction is changed.

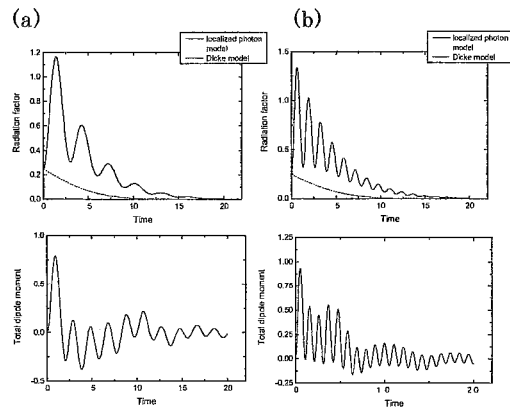


Fig. 5. Temporal evolution of radiation intensity (upper) and the total dipole of the system (lower) obtained with quantum correlations. The solid curves are the result for the localized photon model while the dotted curves represent the result for the Dicke model. The parameters and the system size are the same as in Fig. 4, except (a) $g=0.8$ and (b) $g=1.2$.

As the coupling becomes stronger, the oscillation frequency of the total dipole moment increases because of the nonlinearity of the first term on the right hand side of Eq. (4) (see lower of Fig 5). It results in collective multiple pulse generation (see upper of Fig. 5). This phenomenon can be applied to a nanometric photonic source whose radiation intensity is proportional to the square of the total number of QDs [1].

Comparing the semi-classical results shown in Fig. 3 with the quantum results in Fig. 5, we find a similar behavior of the radiation profiles between them. In Fig. 6 we show the radiation intensities calculated (a) semi-classically and (b) with quantum correlation under the identical conditions.

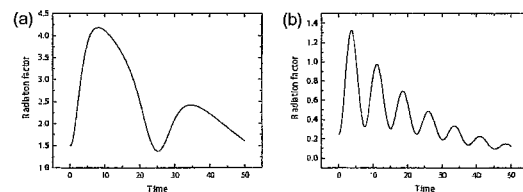


Fig. 6. Temporal evolution of the radiation intensity obtained (a) semi-classically without a quantum correlation among excitons and (b) with quantum correlation. We use the parameters $\gamma=0.05$ and $g=0.5$ for the system $N=4$.

Although the frequencies and the amplitudes are different, both results have qualitatively a similar tendency, that is, occurrence of multiple peaks. One can thus infer that when the total dipole moment is initially not zero the semi-classical treatment can qualitatively describe the radiation property of the system. Note that when there is initially no dipole moment, the quantum

fluctuation is essential as a trigger of radiation. On the other hand, without quantum fluctuation, the initial non zero dipole moments can develop an ordering process due to the non-linear dynamics of the system, and it leads to strong radiation from the system. Since the semi-classical approach does not require a large scale computation, it has an advantage that one can easily examine the system of a relatively large number of sites. Our discussion indicates that the semi-classical approach is powerful for qualitative investigation of radiation properties of a large system. However, for quantitative investigation and for classification of the approximation it is important to have a clear criterion for the applicability of the semi-classical approach.

5. CONCLUSION AND DISCUSSION

We have predicted superradiant multiple pulse emission from the dipole-ordered state prepared by the exciton-localized photon interaction, and discussed the origin of the phenomenon, on the basis of the localized photon model using the dissipative master equation. One expects that this kind of phenomenon can be applied to a component of nanophotonics. The superradiant multiple pulse generation has been discussed in the Dicke model for a large system [8] and a Frenkel exciton system with dipole-dipole interaction [9]. In the former multiple pulses are the results of the stimulated emission and absorption of emitted photons stayed inside the large system. In the latter the oscillation in the radiation originates from the hopping of the excitation due to the dipole-dipole interaction. The origin of the multiple pulse generation in our system is similar to the latter case. However, our system includes a dipole-ordered state, and the mechanism is not completely same as that of Ref. [9]. Moreover, we have clarified that the multiple pulsation is a direct consequence of the ordering of the total dipole.

ACKNOWLEDGEMENTS

Authors are grateful to Prof. H. Hori, Dr. I. Bannno, Prof. N. Ohnishi, and Prof. C. Uchiyama of Yamanashi Univ. for their fruitful discussions. They also acknowledge valuable suggestion from Prof. H. Shibata of Ochanomizu Univ. for the discussion of the effective Hamiltonian.

REFERENCES

- [1] M. Ohtsu, K. Kobayashi, T. Kawazoe, S. Sangu, and T. Yatsui, *IEEE J. Select. Topics in Qunt. Electron.* **8**, 839-862 (2002).
- [2] T. Kawazoe, K. Kobayashi, J. Lim, Y. Narita, and M. Ohtsu, *Phys. Rev. Lett.* **88**, 067404-1-4 (2002).
- [3] A. Shojiguchi, K. Kobayashi, S. Sangu, K. Kitahara, and M. Ohtsu, *Nonlinear Opt.* (2002) in press.
- [4] C. Kittel, "Quantum Theory of Solids", 2nd revised printing, John Wiley & Sons, New York, (1987) pp. 148-149.
- [5] K. Kobayashi, S. Sangu, H. Ito, and M. Ohtsu, *Phys. Rev. A* **63**, 013806-1-9 (2001).
- [6] G. S. Agarwal, *Phys. Rev. A* **4**, 1791-1801 (1971).
- [7] M. Gross and S. Haroche, *Phys. Rep.* **93**, 301-396 (1982).
- [8] R. Bonifacio and P. Schwendimann, *Phys. Rev. A* **4**, 302-313 (1971); R. Bonifacio and L. A. Lugiato, *ibid*, *Phys. Rev. A* **11**, 1507-1521 (1975); R. Bonifacio, L. A. Lugiato and A. A. Crescentini, *ibid*, *A* **13**, 1648-1651 (1976).
- [9] T. Tokihiro, Y. Manabe and E. Hanamura, *Phys. Rev. A* **51**, 7655-7668 (1995).

(Received December 20, 2002; Accepted April 30, 2003)

[II] PRESENTATIONS IN INTERNATIONAL CONFERENCES



EXCITON DYNAMICS AND LOGIC OPERATIONS IN A NEAR-FIELD OPTICALLY COUPLED QUANTUM-DOT SYSTEM

K. Kobayashi,¹⁾ S. Sangu,²⁾ T. Kawazoe,¹⁾ and M. Ohtsu^{1),3)}

- 1) *Japan Science and Technology Agency, 687-1 Tsuruma, Machida, Tokyo, 194-0004, Japan, kkoba@ohtsu.jst.go.jp*
- 2) *Ricoh Company Limited, Yokohama, Kanagawa, 224-0035, Japan*
- 3) *Tokyo Institute of Technology, Yokohama, Kanagawa, 226-8502, Japan*

High spatial localization of an optical near field allows us to access and excite individual nanometric materials that are much smaller than the diffraction limit of light, while propagating or far field light can only excite the system globally. This difference, as an initial condition, provides the new exciton dynamics by effective use of a dark state in a quantum-dot (QD) system coupled by the optical near field. We have previously showed theoretically and experimentally excitation energy transfer between CuCl quantum cubes, using temporally and spatially resolved near-field spectroscopy [1]. In this paper we report another new feature of the exciton dynamics inherent in a similar system, or characteristic functional (AND/XOR-logic) operations, depending on the initial excitation as well as symmetry of the spatial arrangement of the QDs [2].

We consider a QD system divided into two parts, as illustrated in Fig. 1(a): one is a coherent part composed of two identical dots (QD-A and -B). The other is a three-level dot (QD-C) as an output part with a dissipation process. The exciton dynamics is determined by using density-matrix formalism. Figure 1(b) shows temporal evolution of the output populations for two-exciton states, where both QD-A and -B are initially occupied. It follows that selective energy transfer occurs from the coherent part to the output part only if the energy difference $\Delta\Omega$ between the upper level of QD-C and the lowest level of QD-A or -B satisfies the condition $\Delta\Omega = -U$, as shown in the dotted curve. Here U denotes the near-field optical coupling strength. Thus the system behaves as an AND-gate for $\Delta\Omega = -U$, while it provides an XOR-gate for $\Delta\Omega = U$. We also show that an asymmetric arrangement of QDs permits energy transfer from the coherent part to the output part via a certain entangled state, or a dark state in a symmetric system. This is useful for detection of a quantum entangled state.

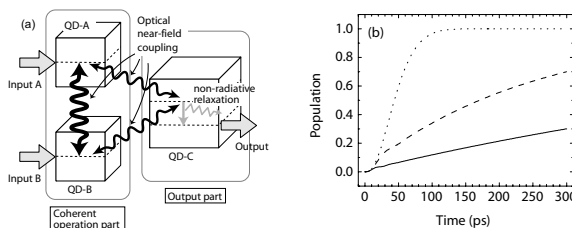


Fig. 1 (a) Considered system
(b) Temporal evolution of the output population

- [1] T. Kawazoe, K. Kobayashi, J. Lim, Y. Narita, and M. Ohtsu, *Phys. Rev. Lett.* 88 (2002) 067404.
- [2] S. Sangu, K. Kobayashi, A. Shojiguchi, and M. Ohtsu, *Phys. Rev. B* 69 (2004) 115334.

Plasmon polariton transfer along nano-dot coupler for optical far/near field conversion

Takashi Yatsui,¹ Wataru Nomura,² and Motoichi Ohtsu^{1,2,3}

¹ "Nanophotonics" team, SORST, Japan Science and Technology Agency
687-1 Tsuruma, Machida Tokyo 194-0004, Japan

Phone: +81-42-788-6030, Fax: +81-42-788-6031, E-mail: yatsui@ohtsu.jst.go.jp

² Faculty of Engineering, University of Tokyo,

7-3-1 Hongo, Bunkyo-ku, Tokyo 113-8656, Japan

³ Interdisciplinary Graduate School of Science and Engineering, Tokyo Institute of Technology
4259, Nagatsuda, Midori-ku, Yokohama 226-8502, Japan

We have successfully fabricated a nano-dot coupler for optical far/near-field conversion. Highly efficient energy transport in the nano-dot coupler via near-field coupling between resonant plasmon-polariton modes of neighboring particles was observed.

1. Introduction

For future optical transmission systems, nanophotonic integrate circuits [1], which are composed of sub-100 nm scale dots, are necessary to increase data transmission rates and capacity. As a representative device, a nanophotonic switch can be realized by controlling the dipole forbidden optical energy transfer among resonant energy states in nanometer-scale quantum dots via an optical near field [2]. To operate this, coupling them with external conventional diffraction-limited photonic devices is required by using a nanometer-scale optical waveguide for far/near -field conversion. To realize this, we have reported plasmon-polariton waveguide using a metallized silicon wedge structure that converts far-field light to optical near field via metallic core waveguide [3]. To obtain higher efficiency of coupling with plasmon-polariton mode, we evaluated the size of Au nanoparticle for plasmon resonance. Furthermore, the efficient energy transport along the nano-dot chain via near-field coupling was observed.

2. Nano-dot coupler

As shown in Fig. 1, we proposed plasmon polariton condenser with nano-dot coupler. The

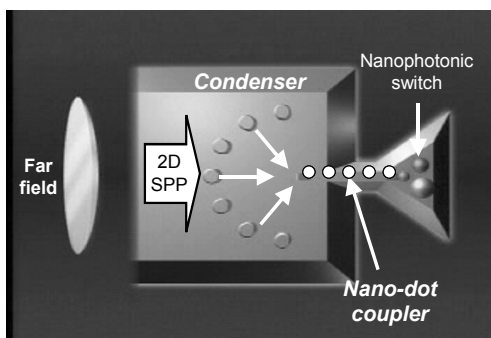


Fig.1 Plasmon-polariton condenser with nano-dot coupler for optical far-/near- field conversion devices.

condenser consists of several hemispheres and they are positioned on an arc, and works as a "phased array". A nano-dot coupler consists of chains of closely spaced metal nanoparticles. Energy transport in the nano-dot coupler relies on near-field coupling between plasmon-polariton modes of neighboring particles [4]. In comparison with metallic waveguide, the use of nano-dot coupler is expected to realize lower energy loss due to the plasmon resonance in the metallic nanoparticles.

3. Experiment

In order to optimize the efficiency in the nano-dot coupler, we checked whether the Au nanoparticles led to efficient scattering. The 50-nm thick Au nanoparticles on the glass substrate were fabricated by the focused ion beam (FIB) milling technique. The spatial distribution of the optical near-field intensity for the Au nanoparticles in diameter D range from 100 to 300 nm were observed by the collection mode near-field optical microscope (NOM) at $\lambda = 785$ nm. Figures 2(a) and 2(b) show the topographical and NOM images of the Au nanoparticles. As shown in the cross sectional profile [see Fig. 2(c)], the optical near-field intensity I takes the maximum for the Au nanoparticle with 200 nm in diameter (labeled w). In order to find the origin of this resonance, a calculation was performed. Mie's theory of scattering by an Au prolate spheroid (see Fig. 2(d)) was employed, and only the first TM mode was considered [5]. The solid curve in Fig. 2(e) represents the calculated polarizability α depending on the diameter D of the Au prolate spheroid whose short axis was fixed as 50 nm. The calculated resonant diameter (230 nm) is in good agreement with the experimentally confirmed particle size ($D = 200$ nm).

Next, we checked whether the plasmon-polariton transfer along the Au nano-dot coupler. As a nano-dot

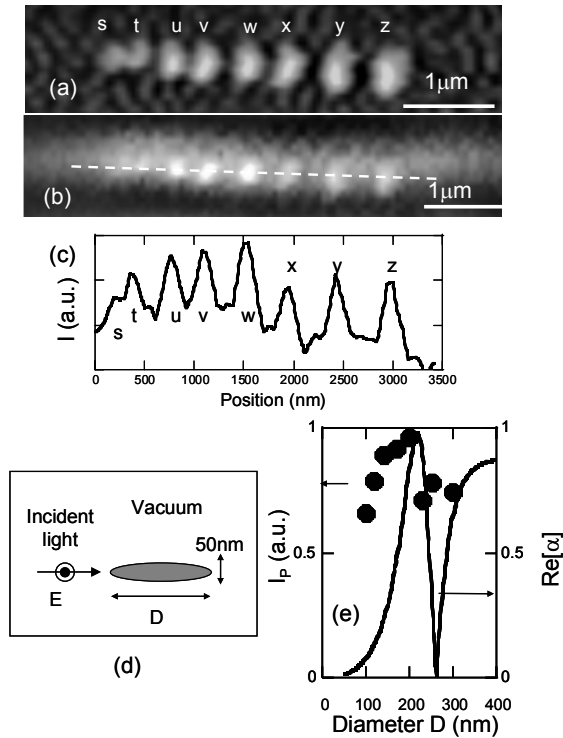


Fig.2 (a) Shear-force image of Au nanoparticles with respective diameter $D=100$ nm (s), 120 nm (t), 140 nm (u), 170 nm (v), 200 nm (w), $D=230$ nm (x), 250 nm (y), 300 nm (z). (b) Intensity I distribution of optical near-field of (a). (c) Cross-sectional profiles along the dashed white line in (b). (d) Calculation model of prolate spheroid. (e) Solid circles show the peak intensity I_p of the respective Au nanoparticles. Solid curve shows the calculated polarizability α of Au prolate spheroid.

coupler, a linear array of Au nanoparticles in diameter D range from 150 to 300 nm with their separations of $2.4 D$ were fabricated using FIB milling technique (see the topographical image of Fig. 3(a)). The spatial distributions of optical near-field energy were observed by the collection mode NOM taken at arrangement for 2D SPP mode excitation. Figure 3(b) shows the NOM image for the nano-dot coupler. Figure 3(c) shows the cross-sectional profile through the outlet of the nano-dot couplers. Note that the output energy was efficiently obtained only for the nano-dot coupler with $D = 200$ nm, which is consistent with the experimental results shown in Fig. 2. These results confirm that such an efficient energy transfer along the Au nanoparticles is due to the near-field coupling between resonant plasmon-polariton modes of neighboring particles.

4. Conclusions

In through our proposal, we fabricated nano-dot coupler as far-field and near-field converter. Highly efficient energy transport in the nano-dot coupler via near-field coupling between plasmon-polariton modes

of neighboring particles was observed. These results confirm that it will be possible to create the optical far-/near-field conversion devices required by future systems.

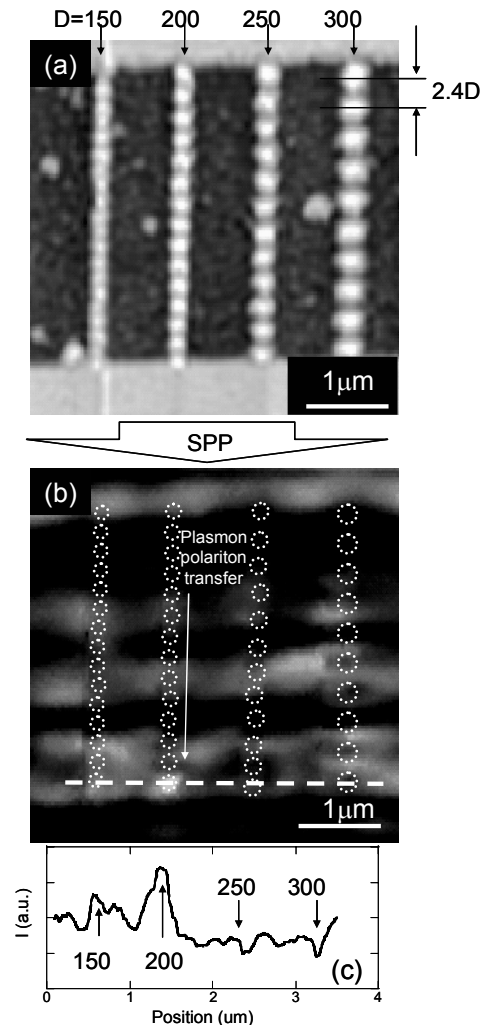


Fig. 3 (a) Shear-force image of Au nano-dot coupler with $D = 150, 200, 250,$ and 250 nm. (b) Spatial distribution of optical-near field intensity of (a). (c) Intensity I distribution of optical near field along the dashed white line in (b).

References

- [1] M. Ohtsu, K. Kobayashi, T. Kawazoe, S. Sangu, and T. Yatsui, IEEE Journal of Selected Topics in Quantum Electronics **8**, 839 (2002).
- [2] T. Kawazoe, K. Kobayashi, S. Sangu, and M. Ohtsu, Appl. Phys. Lett. **82**, 2957 (2003).
- [3] Yatsui, M. Kourogi, and M. Ohtsu, Appl. Phys. Lett. **79**, 4583 (2001).
- [4] M. L. Brongersma, J. W. Hartmanm and Harry A. Atwater, Phys. Rev. B **62**, R16356 (2000).
- [5] H. Kuwata, H. Tamaru, K. Miyano, Appl. Phys. Lett. **83**, 4625 (2003).

Nanophotonics: Devices, fabrications, and systems

M. Ohtsu¹⁻³⁾

- 1) Interdisciplinary Graduate School of Sci. and Technol., Tokyo Institute of Technology
4259 Nagatsuta-cho, Midori-ku, Yokohama, Kanagawa 2265-8502, Japan
Phone: +81-45-924-5455, E-mail: ohtsu@ae.titech.ac.jp, URL: http://uuu.ae.titech.ac.jp
- 2) Faculty of Engineering, University of Tokyo,
7-3-1 Hongo, Bunkyo-ku, Tokyo 113-8656, Japan
- 3) "Nanophotonics" team, SORST, Japan Science and Technology Agency
687-1 Tsuruma, Machida-shi, Tokyo 194-0004, Japan

Definition, principle, and true nature of nanophotonics are presented. Recent progresses in nanophotonic device operation (e.g., switches), size- and position-controlled fabrications (e.g., deposition and lithography), and future systems (e.g., optical fiber communication) are reviewed.

1. Introduction

This talk reviews the definition, true nature, and technical progress of nanophotonics¹⁻⁶⁾. After the word "nanophotonics" was proposed by Ohtsu in 1994, the nanophotonics technical group was organized by OITDA (Optical Industry Technology Development Association, Japan) to discuss future direction of optical science, technology, and industry.

2. Principles

Nanophotonics is defined as "the technology for fabricating and operating nanophotonic devices by using the optical near field as signal carrier and small numbers of nanoparticles as device materials"(Fig.1). However, nanophotonics is not to realize nanometer-sized optical science and technology but to realize "novel functions and phenomena originated from the localized nature of optical near fields". These novel functions and phenomena are possible by noting that the nanometric system (composed of nanometric particles and optical near fields) is buried in a macroscopic heat bath. Energy non-conservation can be observed in

the nanometric system due to energy exchange between the two systems.

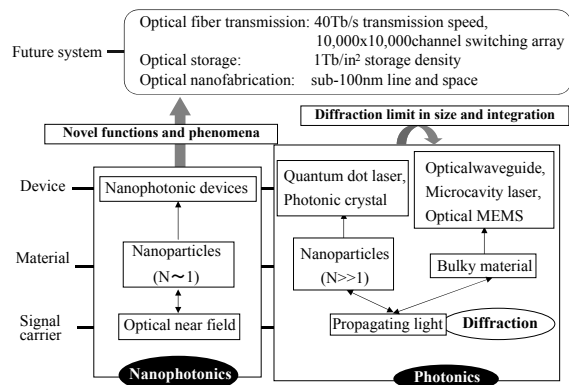


Fig.1

Concepts of nanophotonics.

Further, higher order effects, e.g., magnetic dipole or electric quadrupole transitions are not neglected due to localized nature of optical near fields. True nature of nanophotonics is to utilize these "novel functions and phenomena originated from the localized nature of optical near fields", which is completely impossible by propagating

lights.

The essential features of nanophotonic devices are their novel functions and phenomena. In addition, their sizes are far smaller than the diffraction limit of light. Conventional photonic devices, e.g., quantum dot lasers, photonic crystals, and optical MEMS do not have these features because they use the diffraction-limited propagating light as a signal carrier.

3. Devices, fabrications, and systems

Nanophotonics have been proposed and developed by my research group. Their recent technical progress is reviewed(Fig.2). They are; (1) nanophotonic devices (switches, AND/XOR gates, delay gate, super-radiant-type pulsed generator) and optical input/output terminals, (2) nanophotonic fabrication (size-and position-controlled photochemical vapor deposition and non-adiabatic process, desorption and self-organization based on size-dependent resonance, application of non-radiative process to photo-lithography), and (3) future prospect to realize nanophotonic systems (optical routers in fiber communication systems, optical memory, optical data processing, and so on.).

References

- 1) M. Ohtsu, *Near-Field Nano/Atom Optics and Technology*, Springer-Verlag, Berlin, 1998
- 2) M. Ohtsu and H. Hori, *Near-Field Nano-Optics*, Kluwar Academic/Plenum Publishers, New York, 1999
- 3) M. Ohtsu, et al., "Nanophotonics: Design, Fabrication, and Operation of Nanometric Devices Using Optical Near Fields", IEEE J. Selected Topics in Quantum Electron.,

vol.8, no.4, (2002) , pp.839-862

- 4) M. Ohtsu(ed.), *Progress in Nano-Electro-Optics I*, Springer-Verlag, Berlin, 2002
- 5) M. Ohtsu(ed.), *Progress in Nano-Electro-OpticsII*, Springer-Verlag, Berlin, 2003
- 6) M. Ohtsu and K. Kobayashi, *Optical Near Fields*, Springer-Verlag, Berlin, 2003

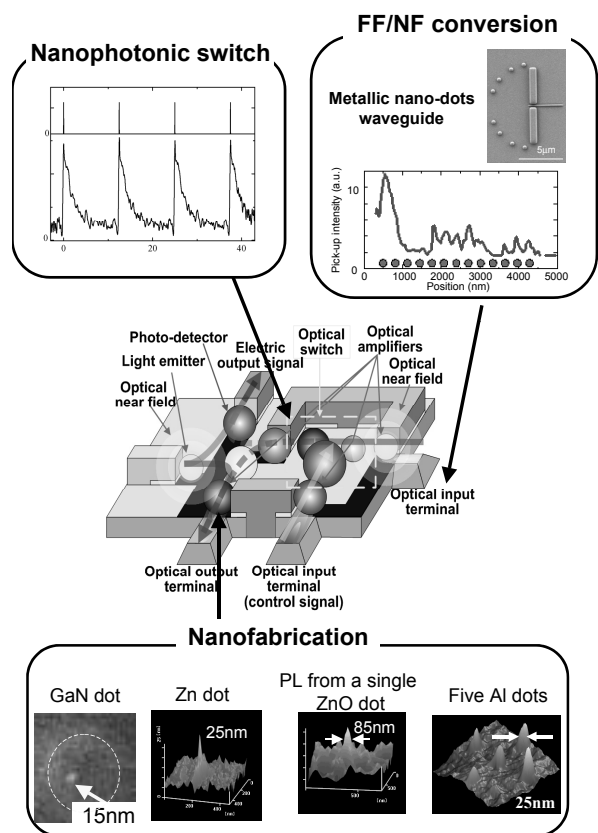


Fig.2

Nanophotonic devices, their integration, and present status of the technical progress.

Nanophotonic functional devices using optical near-field energy transfer

Suguru Sangu¹, Kiyoshi Kobayashi², and Motoichi Ohtsu^{2,3}

¹Ricoh Company, Limited, ²Solution-Oriented Research for Science and Technology, Japan Science and Technology Agency, ³Interdisciplinary Graduate School of Science and Engineering, Tokyo Institute of Technology

Nanophotonic functional devices are proposed, and the operation principles are discussed theoretically. Optical AND- and XOR-logic gates can be realized by matter coherence via optical near-field interaction and spatial symmetry in three- and four-quantum dot systems.

1. Introduction

Optical near-field interaction in a nanometric system has introduced some interesting features that cannot be found in a macroscopic system. Recently, we have proposed nanometric functional devices below the diffraction limit of light,^{1,2)} which we call *nanophotonic devices*. In this paper, we propose another nanophotonic device, and discuss the operations, using optical near field and discrete energy levels in a few quantum dot system.

As is well known, optical near field is localized in the order of material size. Energy transfer between nanometric materials via such local interaction is much faster than radiation by far-field light. Therefore, matter coherence can be maintained in a nanometric system. Noticing this fact, we demonstrate nanophotonic device operations theoretically.

2. Coupled States via an Optical Near Field

First, we consider exciton dynamics in a three-quantum dot system as illustrated in Fig. 1(a). In this system, two identical quantum dots (QD-A and B) are coupled coherently with each other, and the excitation (an exciton) in the coupled states is transferred to the third quantum dot (QD-C) under the resonance condition. Since QD-C is larger than the others, the exciton in QD-A and B is transferred to the higher energy sublevel in QD-C, and then decays in the lower energy sublevel via an exciton-phonon interaction, or energy dissipation. In order to understand the resonant energy transfer, the energy levels in the system are shown in Fig. 1(b). One or two excitons can exist in QD-A and/or B in the input state, while in the output state one exciton always exists on the higher energy sublevel in QD-C. The two split energy levels around the energy $\hbar\Omega$ correspond to symmetric and anti-symmetric states, *i.e.*,

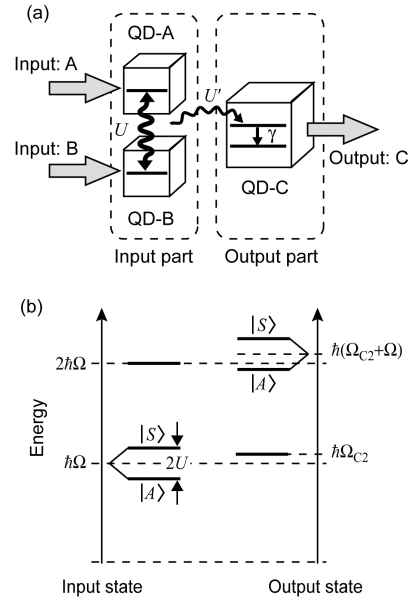


Fig. 1 (a) Schematic illustration of a three-quantum dot system. (b) Energy levels of coupled states, where U denotes the optical near-field interaction, while Coulomb interactions are included in $\hbar\Omega$, $\hbar\Omega_{C1}$, and $\hbar\Omega_{C2}$.

$$\begin{aligned} |S\rangle &= (|1\rangle_A |0\rangle_B + |0\rangle_A |1\rangle_B) / \sqrt{2}, \\ |A\rangle &= (|1\rangle_A |0\rangle_B - |0\rangle_A |1\rangle_B) / \sqrt{2}, \end{aligned} \quad (1)$$

where $|0\rangle_\alpha$ and $|1\rangle_\alpha$ represent crystal and exciton ground states in QD- α , respectively. Note that the anti-symmetric state is a *dipole-inactive state* for far-field light. Using an optical near field, we can manipulate the state as dipole-active and inactive, adjusting spatial arrangement of QD-C relative to QD-A and B. When QD-C is located symmetrically as shown in Fig. 1(a), the $|A\rangle$ -state cannot be coupled with QD-C because total dipole in the input part is zero. Thus, matter coherence and spatial symmetry play important roles in a nanophotonic system, and are useful for optical signal processing on a nanometric

scale.

3. Nanophotonic functional devices

3.1 AND/XOR logic operations

The system shown in Fig. 1(a) operates as two kinds of logic gates depending on the resonant conditions in QD-C. When the higher energy sublevel in QD-C is set as $\hbar\Omega_{C2}=\hbar\Omega+U$, the $|S\rangle$ -state resonantly couples to the sublevel in QD-C in the case that an exciton is created in QD-A. However, the energy transfer cannot occur when two excitons are excited simultaneously in QD-A and B because the resonant $|A\rangle$ -state is dipole-inactive in the case of symmetrically arranged system. This behavior is exactly a XOR-logic operation. The exciton dynamics is plotted as the solid curves in Fig. 2, where the exciton population is calculated on the basis of the density matrix formalism³⁾ and Yukawa interaction⁴⁾ as the optical near-field coupling.

In the opposite case of $\hbar\Omega_{C2}=\hbar\Omega-U$, the above operation is reversed as shown by the dashed curves in Fig. 2; the exciton energy transfer is forbidden unless both of QD-A and B are excited. This is an AND-logic operation. The exciton population reaches a unit value for the AND-logic operation, while does not for the XOR-logic operation. This is caused by the difference of initial conditions, that is, the excitation in a single quantum dot is expressed in terms of a superposition of the $|S\rangle$ - and $|A\rangle$ -states, where the $|A\rangle$ -state is inactive. Therefore, we need to take an ensemble average for an actual XOR-logic operation.

3.2 Controlled logic system

As another type of devices, it is interesting to consider four-quantum-dot system as illustrated in Fig. 3, which consists of three coherently coupled quantum dots and an output quantum dot. Similar to Sec. 3.1, the energy transfer in this system depends on the number of excitons initially prepared. Note that AND- and XOR-logic operations can be realized by using identical system when the energy sublevel in QD-D is set as $\hbar\Omega_{D2} = \hbar\Omega - 2\sqrt{2}U$. (See the energy levels in Fig. 3) When QD-A and B are assigned as input terminals and QD-C is a control terminal, this system operates as an AND-logic gate without control signal, and as an XOR-logic gate with control signal. Since a few different operations can be realized in the same system, this system has the great advantage not only to signal processing all-optically controlled but also to nanofabrication.

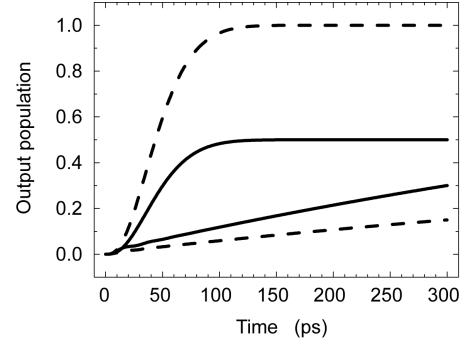


Fig. 2 Time evolution of exciton population at the lower energy sublevel in QD-C. The solid and dashed curves represent XOR- and AND-logic operations in the systems with the energy differences $+U$ and $-U$, respectively.

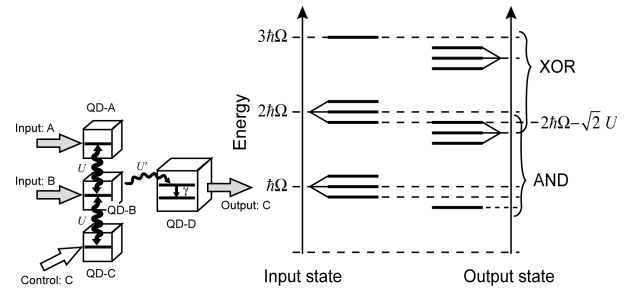


Fig. 3 Energy levels of coupled state in a four-quantum dot system. The higher energy sublevel in QD-D is adjusted by $\hbar\Omega - 2\sqrt{2}U$ to resonantly couple to a state in three identical quantum dots.

4. Conclusions

In nanometric systems, matter coherence and spatial symmetry play important roles for energy transfer dynamics, and are useful for nanophotonic signal processing. We have proposed and evaluated XOR- and AND-logic operations, and controlled-type logic operations theoretically. These devices discussed above always include decoherence (energy dissipation), and one operation is independent of the other connected systems. It is an advantage for connection of conventional optical and electric devices.

References

- 1) M. Ohtsu, K. Kobayashi, T. Kawazoe, S. Sangu, and T. Yatsui: IEEE J. Sel. Top. Quant. Electron. 8 (2002) 839.
- 2) T. Kawazoe, K. Kobayashi, S. Sangu, and M. Ohtsu: Appl. Phys. Lett. 82 (2003) 2957.
- 3) H. J. Carmichael: *Statistical Methods in Quantum Optics I* (1999, Springer-Verlag, Berlin).
- 4) K. Kobayashi, S. Sangu, H. Ito, and M. Ohtsu: Phys. Rev. A 63 (2001) 013806.

Nanoscale matching architecture using optical near-field coupling

Makoto Naruse^{1,2}, Tetsuya Miyazaki¹, Fumito Kubota¹,
Suguru Sangu³, Kiyoshi Kobayashi², Tadashi Kawazoe², and Motoichi Ohtsu^{2,4}

¹Communications Research Laboratory, ²Japan Science and Technology Agency,
³Ricoh Co. Ltd., ⁴Tokyo Institute of Technology

A nanoscale data matching architecture is proposed based on optical near-field interaction between quantum dots. This architecture enables the design of a highly dense content addressable memory, which is a key device in optical networks.

1. Introduction

To meet future bandwidth requirements, a huge amount of computation must be performed at the nodes in optical networks and in data centers. Performing such computations in the optical domain, such as address lookup in optical packet switching applications [1], is expected to enhance overall system performance. However, there are serious technological difficulties to be overcome before such systems can be demonstrated, such as compact integration of a large number of optical waveguides [2]. Essentially, the level of integration cannot be improved beyond that allowed by the diffraction limit of light. Nanophotonics, on the other hand, is not restricted by the diffraction limit since it is based on local electromagnetic interactions between a few nanometric elements via an optical near field [3]. From an architectural perspective, this drastically changes the fundamental design rules of computational systems. Consequently, suitable architectures should be built to exploit this capability of the physical layer. In this paper, we propose an optical data matching or content addressable memory architecture based on nanophotonics [Fig. 1].

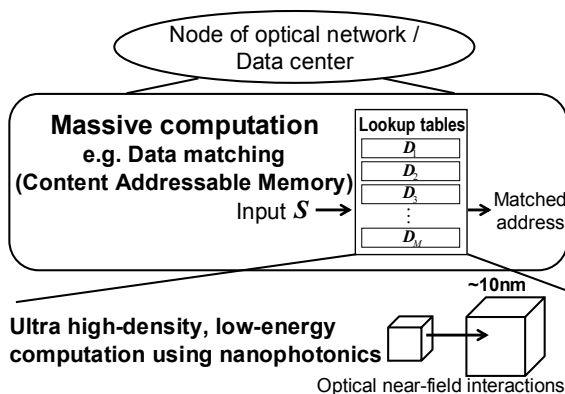


Fig. 1 Highly dense optical data matching architecture based on nanophotonics.

2. Matching architecture using nanophotonics

Data matching can be generalized to the Content Addressable Memory (CAM) architecture, where an input signal is used as a query to a database and the output is the address of the data matching the input. CAM is one of the key functionalities in network applications.

CAM requires an architecture providing a “global”

evaluation scheme; in known methods of realizing such a scheme, such as by focusing lenses, optical waveguide coupling, photodetector arrays, and so forth, yet another integration barrier exists. In nanophotonics, on the other hand, optical energy is attracted to a certain quantum dot by means of optical near-field coupling, as will be explained in section 3. Therefore, we can collect multiple variables, or summation $\sum x_i$, on a nanometric scale. If each variable x_i is the product of two variable s_i and d_i , then the inner product $\sum s_i d_i$, which is used for matching applications [Fig. 2(a) and (b)], is achieved.

Exclusiveness is one of the problems encountered in matching operations: Assuming an N -bit input signal $\mathbf{S}=(s_1, \dots, s_N)$ and reference data $\mathbf{D}=(d_1, \dots, d_N)$, then the inner product $\sum s_i d_i$ is not enough to determine the correct matching of \mathbf{S} and \mathbf{D} ; inner products of the inverted input signal and reference data are also required. (For example, for 4-bit input $\mathbf{S}=(1010)$ and table data $\mathbf{D}_1=(1010)$ and $\mathbf{D}_2=(1110)$, both inner products result in a value of 2, but the correct matching is only for \mathbf{D}_1 .) Inversion is, however, one of the difficult functions to implement optically. One possible option is to properly design the modulation format [4], for instance by representing a logical level by two digits such as by “logic 1=(10)” and “logic 0=(01)”. (Therefore, an N -bit logical input is physically represented by $2N$ bits.) Doing so makes the inner products equivalent to the matching operations. A “don’t care” status could be coded by (11) in this scheme. Suppose that the reference data in the memory $\mathbf{D}_1, \dots, \mathbf{D}_M$, and the input \mathbf{S} are represented in the above format. Then the function of the content addressable memory is to derive j that maximizes $\mathbf{S} \cdot \mathbf{D}_j$ ($j=1, \dots, M$). Each of the inner products is realized on the nanoscale, and therefore, the overall CAM is realized in an extremely compact volume compared to its conventional counterpart. Moreover, conventional CAM VLSI chips consume lots of current and energy, whereas nanophotonic devices can be operated with extremely low energy.

3. Nanometric summation using nanophotonics

The multiplication operation of two bits, namely $x_i = s_i d_i$, has already been demonstrated by combinations of three quantum dots [5]. Therefore, the key function to achieve a nanophotonic CAM is the summation,

which is explained as follows. Here we assume two quantum dots QD_A and QD_B , as shown in Fig. 2(c). The ratio of the sizes of QD_A and QD_B is $1:\sqrt{2}$. There is a resonant energy level between those two dots, which are coupled by an optical near field interaction. Therefore, the exciton population in the (1,1,1)-level in QD_A is transferred to the (2,1,1)-level of QD_B . It should be noted that this interaction is forbidden for far-field light. Since the inter-sublevel relaxation via exciton-phonon coupling is fast, the population is quickly transferred to the lower (1,1,1)-level in QD_B . Similar energy transfers may take place in the dots surrounding QD_B by setting the resonant energy level so that energy flow can occur. One could worry that if the upper energy level of QD_B is occupied, another exciton in QD_A cannot be transferred due to the Pauli exclusion principle. Here, thanks again to the nature of the optical near-field interaction, the exciton population goes back and forth between QD_A and QD_B , which is called nutation [6]. Therefore, we can effectively regard this state as the exciton remaining in QD_A until QD_B becomes empty. Finally, both excitons can be transferred to QD_B .

Numerical calculations were performed based on quantum master equations in a density matrix formalism. First, we considered an initial condition where there are two excitons, one in QD_A and one in QD_B (two-exciton system). The solid and dotted lines in Fig. 3(a) respectively show the time evolution of the exciton population of the lower level of QD_B and the other states where an exciton remains in QD_A . Nutation is observed, as indicated by the dotted line, since QD_B is initially busy due to the initial conditions.

We then compared the population to a one-exciton system. The dotted line in Fig. 3(b) shows the population of the lower level of QD_B with the initial condition of one exciton in QD_A . The solid line in Fig. 3(b) is for the two-exciton system. Physically the “output” signal is related to the integration of the population in the lower level of QD_B . By numerically integrating the population between 0 and 5 ns, we can see that the ratio of the output signals between the two- and one-exciton systems is 1.83:1, which reflects the number of initial excitons, or the summation mechanism.

4. Conclusions

An architecture for high-density data matching, or content addressable memory, is proposed based on near-field coupling between quantum dots. Consideration of both device and system architecture issues will be indispensable [7] to realize effective nanophotonic systems in future.

Acknowledgement: This work is supported in part by a grant for “Ultra high-density optical nodes using nanophotonics” from the Ministry of Public Management, Home Affairs, Posts and

Telecommunications of Japan.

References

1. M. J. O'Mahony, et. al., IEEE Comm. Mag. **39**, 128 (2001).
2. P. C. Teh, et. al., IEEE J. Lightwave Technol. **19**, 1352 (2001).
3. M. Ohtsu, et. al., IEEE J. Select. Topics Quantum Electron. **8**, 839 (2002).
4. M. Naruse, et. al., Opt. Lett. in press.
5. T. Kawazoe, et. al., Appl. Phys. Lett. **82**, 2957 (2003).
6. S. Sangu, et. al., J. Appl. Phys. **93**, 2937 (2003).
7. For example, Proc. IEEE-NANO

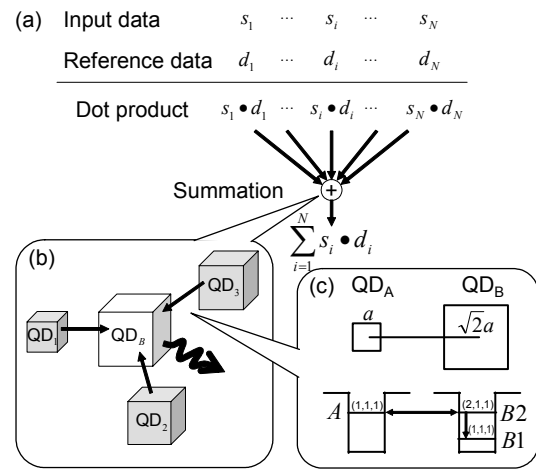


Fig. 2. (a) Inner product operation as a data matching application. (b) Summation mechanism in quantum dots. (c) Inter-dot interaction via optical near-field.

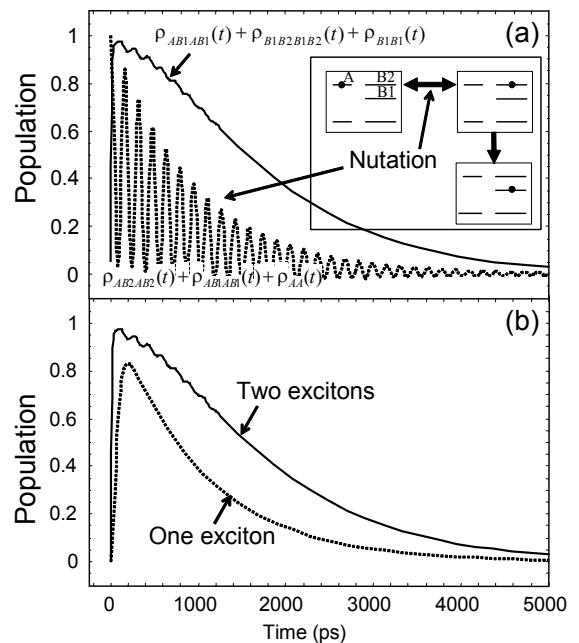


Fig. 3. (a) Population evolution in a two-exciton system. (b) Population comparison between one- and two-exciton systems.

Development of nanophotonic devices and their integration by optical near-field

Takashi Yatsui¹ and Motoichi Ohtsu^{1,2,3}

¹ Nanophotonics Team, Solution-Oriented Research for Science and Technology (SORST), Japan Science and Technology Agency, 687-1 Tsuruma, Machida, Tokyo 194-0004, Japan

² Interdisciplinary Graduate School of Science and Engineering, Tokyo Institute of Technology, 4259 Nagatsuta, Yokohama, Kanagawa, 226-8502, Japan

³ Faculty of Engineering, University of Tokyo, 7-3-1 Hongo, Bunkyo-ku, Tokyo 113-8656, Japan

ABSTRACT

This paper reviews the recent progress of application of interactions between optical near-fields and nanoscale material. For future optical transmission systems with high data transmission rates and capacity, we have proposed nanometer-scale photonic devices (i.e., nanophotonic devices), which is composed of sub-100-nm scale dots and wires. To realize this, we demonstrated the feasibility of nanometer-scale optical chemical vapor deposition using optical near-field techniques. Furthermore, we also demonstrated possibilities of mass-production of nanometric structures without scanning the fiber probe.

Optical transmission systems require increased integration of photonic switching devices. To support this increase, it is estimated that the size of photonic matrix switching devices should be reduced to less than 100 nm by the year 2015. To realize this, we have proposed nanometer-scale photonic devices and their integration [i.e., nanophotonic integrated circuits (ICs), see Fig. 1] [1]. These devices consist of nanometer-scale dots, and an optical near field is used as the signal carrier (see Fig. 2). As a representative device, a nanophotonic switch can be realized by controlling the dipole forbidden optical energy transfer among resonant energy states in nanometer-scale quantum dots via an optical near field [2]. It is composed of sub-100-nm scale dots and wires, and their size and position must be controlled on a nanometer scale to fabricate the device.

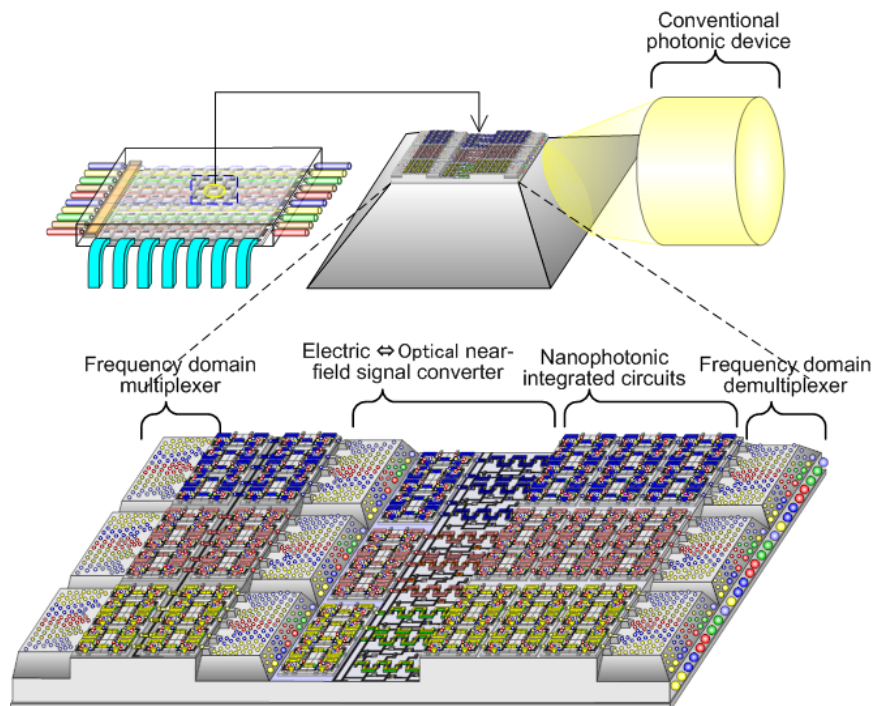


Fig. 1 Nnanophotonic ICs.

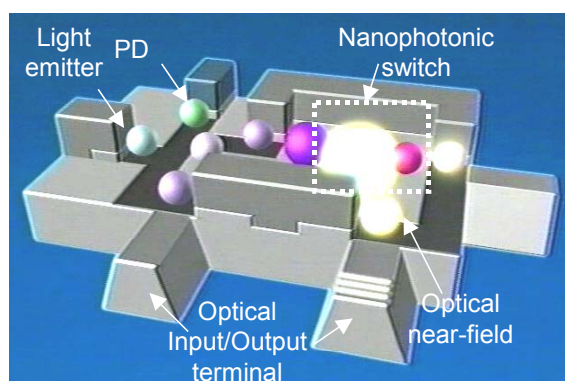


Fig. 2 Single cell of nanophotonic ICs.

In order to realize this level of controllability, we proposed and demonstrated near-field optical chemical vapor deposition (NFO-CVD, see Fig. 3), which enables the fabrication of nanometer-scale structures, while precisely controlling their size and position [3-5]. In this process, resonant photons excite metal-organic (MO) molecules from the ground state to the excited electronic state and the excited molecules relax to the dissociation channel. Then the dissociated metal atoms adsorb to the substrate [6]. For photodissociation, the far-field light must resonate the reacting molecular gasses in order to excite molecules from the ground state to excited electronic state. The Frank-Condon principle claims that this resonance is essential for excitation. The conventional MO gas source for optical CVD has the excited electron state in the ultraviolet region. For NFO-CVD, however, photodissociation can take place under nonresonant conditions, i.e., using visible light, due to the inherent properties of optical near-fields [7]. Since the optical near field has a very large spatial gradient with a nanometric decay length, it can interact with the polarization of molecule. As a result of this interaction, atoms in the molecule can be translated directly. Thus, NFO-CVD is applicable to various materials, including metals, semiconductors, and insulators with various shapes [see Figs. 4(a), (b), and (c)]. By changing the reactant molecules during deposition, nanometric Zn and Al dots were successively deposited on a sapphire substrate with high precision [see Fig. 4(d)] [8].

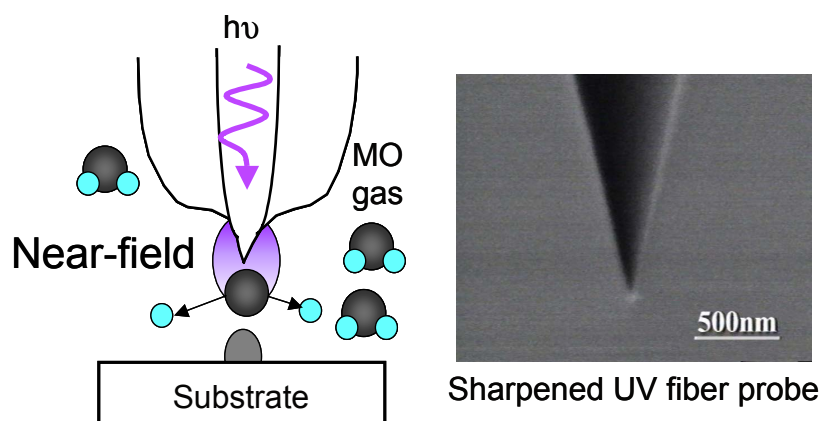


Fig. 3 Schematics of NFO-CVD.

We fabricated UV-emitting ZnO dots by oxidizing Zn immediately after deposition to confirm that the deposited dots are Zn. Laser annealing was employed for this oxidization. The deposited Zn dot was irradiated with a pulse of ArF excimer-laser in a high-pressure oxygen environment. To evaluate the optical properties of the oxidized dot, the photoluminescence (PL) intensity distribution was measured using an illumination and collection mode (IC-mode) near-field optical microscope. Figure 4(e) shows the PL intensity distribution of the oxidized dot integrated for the wavelength region longer than 360 nm. The low collection efficiency due to the IC-mode configuration did not establish the spectrum. However, in the case of a ZnO thin film deposited using the same CVD process, except the optical near-field was replaced by the far-field light, we found that the PL intensity of the spontaneous emission from the free exciton was ten times greater than that of the deep-level green emission. From this result, we concluded that the luminescence in this figure originated from spontaneous emission from the free exciton in ZnO nano-dot. This is the first observation of PL from a single deposited ZnO nanocrystallite [5].

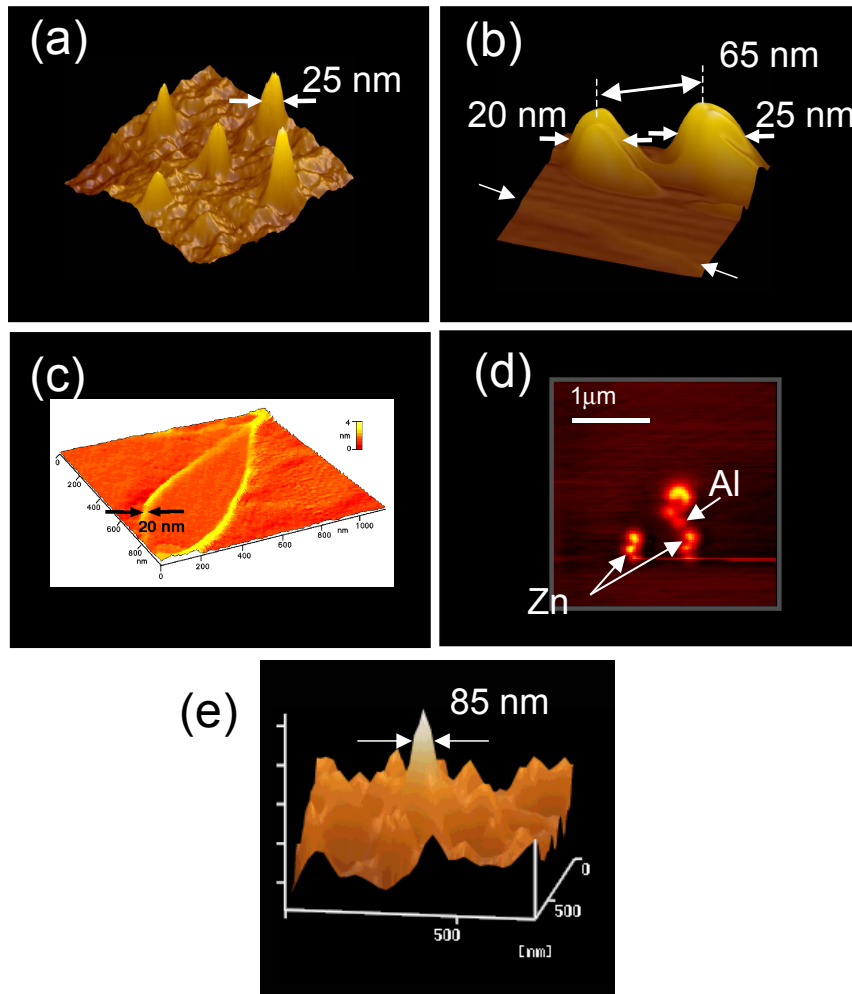


Fig. 4 Shear-force images of deposited Al dots (a), Zn dots (b), Zn looped shape (c), and Zn and Al dots (d). (e) Photoluminescence image of single deposited ZnO dot.

In order to realize further controllability in size, we studied dependence of nanoparticle formation on photon energy used for the NFO-CVD. As the light source for the photodissociation of diethylzinc (DEZn), a He-Cd laser [photon energy $E_p = 3.81$ eV] was used. This is a resonant light because its photon energy exceeds the band edge energy of DEZn. Figure 5(a) shows topographical image of Zn deposited on a (0001) sapphire substrate by NFO-CVD.

To control the size distribution, we introduced Ar^+ ($E_p = 2.54$ eV) or He-Ne ($E_p = 1.96$ eV) lasers, in addition to the He-Cd laser. Their photon energies are lower than the absorption band edge energy of DEZn, i.e., they are nonresonant light sources for the dissociation of DEZn. Figures 5(b) and 5(c) show topographical images of Zn deposited by NFO-CVD with irradiation at $E_p = 3.81$ and 2.54 eV and at $E_p = 3.81$ and 1.96 eV, respectively. The respective FWHMs were 60, 30, and 15 nm [see Fig. 5(d)]; i.e., a lower photon energy gave rise to smaller particles.

The dependency of fabricated size on the photon energy is due to plasmon resonance of optical absorption in a metal nanoparticle [9-11], which strongly depends on particle size. This can induce the desorption of the deposited metal nanoparticles [12]. As the deposition of metal nanoparticles proceeds in the presence of light, the growth of the particles is affected by a trade off between deposition and desorption, which determines their size, and depends on the photon energy.

These results suggest that the additional light controls the size of the dots and reduces the size fluctuation, i.e., size regulation is realized. Furthermore, the position can be controlled accurately by controlling the position of the fiber probe used to generate the optical near field. The experimental results and the suggested mechanisms described above show the potential advantages of this technique in improving the regulation of size and position of deposited nanodots. Furthermore, since our deposition method is based on a photodissociation reaction, it could be widely used for nanofabrication of the other material for example GaN, GaAs, and so on.

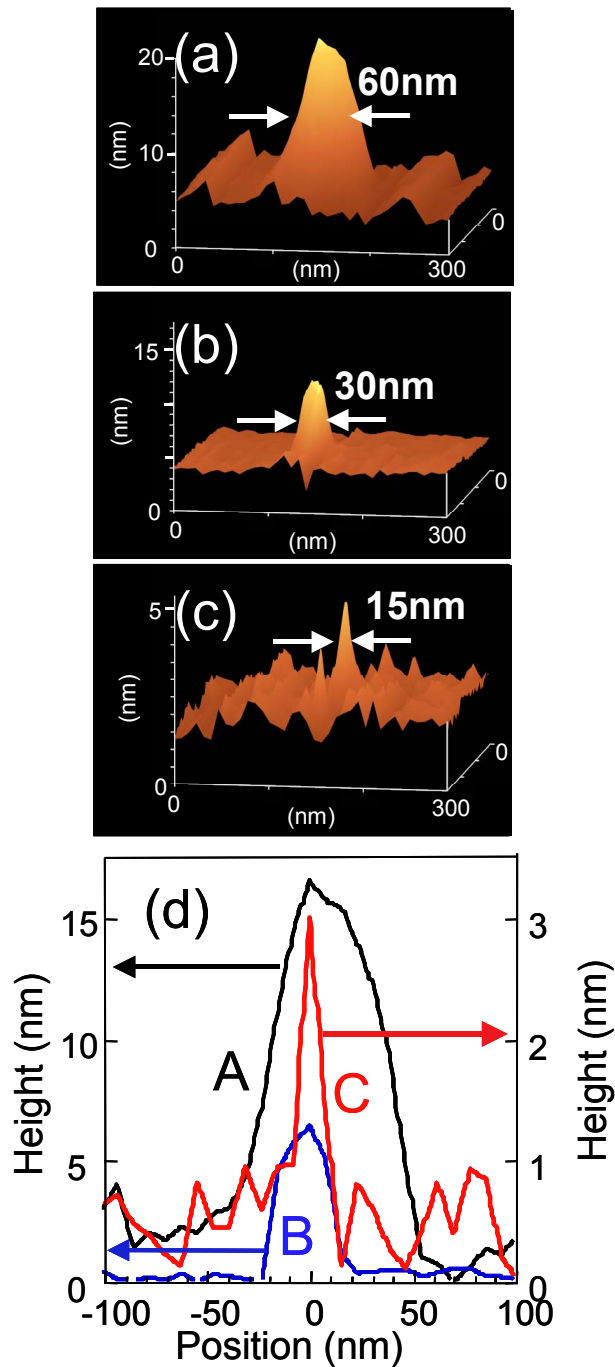


Fig. 5 Bird's-eye views of shear-force topographical images of Zn deposited by NFO-CVD with (a) $E_p = 3.81$ eV, (b) $E_p = 3.81$ and 2.54 eV, and (c) $E_p = 3.81$ and 1.96 eV, respectively. (d) Curves A, B, and C show the cross-sectional profile of the dot in (a), (b), and (c), respectively.

For realization of mass-production of nanometric structures, we also demonstrated possibilities of applying such a near-field desorption to other deposition technique, which does not use fiber probe. We performed metal-nanoparticles deposition over the pre-formed grooves on the glass substrate by the sputtering under the illumination [see Fig. 6(a)]. Since the optical near-field is enhanced at the edge of the groove, it can induce the desorption of the deposited metal nanoparticles when they reach at their resonant size for optical absorption. By illuminating 2.33-eV light during the deposition of Al film, we successfully fabricated 80-nm Al dots chain with 40-nm separation as long as 20 μm [see Fig. 6(c)].

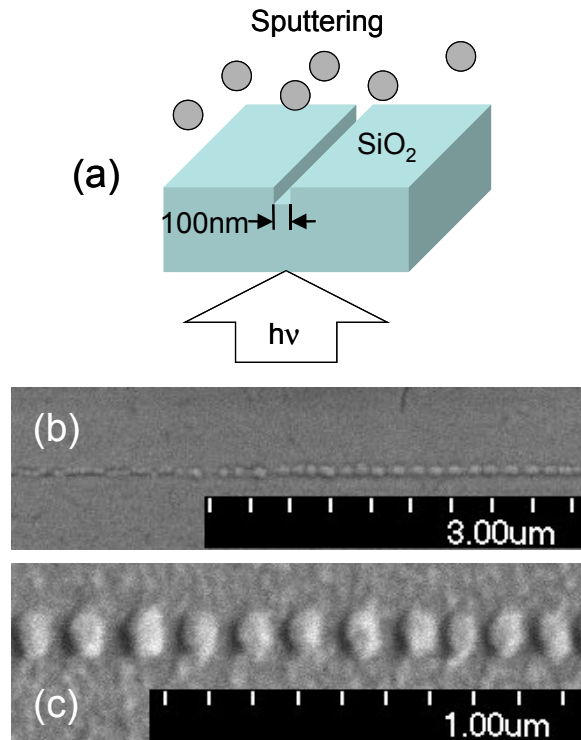


Fig. 6 (a) Fabrication process of metal dots-chain by the sputtering using near-field desorption technique. (b) Au dots-chain with 1.96-eV light illumination. (c) Al dots-chain with 2.33-eV light illumination.

In order to realize a far/near -field conversion device coupling nanophotonic ICs with external conventional diffraction-limited photonic devices, we will also discuss possibilities of applying such a structure to a nano-dot coupler, in which energy transfer relies on near-field coupling between plasmon-polariton modes of neighboring particles [14].

REFERENCES

- [1] M. Ohtsu, K. Kobayashi, T. Kawazoe, S. Sangu, and T. Yatsui, "Nanophotonics: Design, Fabrication, and Operation of Nanometric Devices Using Optical Near Fields," *IEEE J. Sel. Top. Quantum Electron.* IEEE J. Selected Topics in Quantum Electron., Vol.8, No.4, pp.839-862, 2002.
- [2] T. Kawazoe, K. Kobayashi, S. Sangu, and M. Ohtsu, "Demonstration of a nanophotonic switching operation by optical near-field energy transfer," *Appl. Phys. Lett.*, Vol.82, No.18, pp. 2957-2959, 2003.
- [3] V. V. Polonski, Y. Yamamoto, M. Kouroggi, H. Fukuda, and M. Ohtsu, "Nanometric patterning of zinc by optical near-field photochemical vapour deposition," *J. Microscopy*, Vol.194, pt.2/3, pp. 545-551, 1999.
- [4] Y. Yamamoto, M. Kouroggi, M. Ohtsu, V. Polonski, and G. H. Lee, "Fabrication of nanometric zinc pattern with photodissociated gas-phase diethylzinc by optical near field," *Appl. Phys. Lett.*, Vol.76, No.16, pp. 2173-2175, 2000.
- [5] T. Yatsui, T. Kawazoe, M. Ueda, Y. Yamamoto, M. Kouroggi, and M. Ohtsu, "Fabrication of nanometric single zinc and zinc oxide dots by the selective photodissociation of adsorption-phase diethylzinc using a nonresonant optical field," *Appl. Phys. Lett.*, Vol.81, No.19, pp. 3651-3653, 2002.
- [6] R. L. Jackson, "Vibrational energy of monoalkylzinc product formed in the photodissociation of dimethyl zinc, diethyl zinc, and dipropyl zinc," *J. Chem. Phys.*, Vol. 96, pp. 5938-5951, 1992.
- [7] T. Kawazoe, Y. Yamamoto, and M. Ohtsu, "Fabrication of nanometric Zn dots by nonresonant near-field optical chemical-vapor deposition," *Appl. Phys. Lett.*, Vol.79, No.8, pp. 1184-1186, 2001.
- [8] Y. Yamamoto, M. Kouroggi, M. Ohtsu, and T. Kawazoe, "Lateral Integration of Zn and Al Dots with Nanometer-Scale Precision by Near Field Optical Chemical Vapor Deposition Using a Sharpened Optical Fiber Probe," *IEICE Trans. Electron.*, Vol.E85-C, No.12, pp. 2081-2085, 2002.
- [9] G. T. Boyd, Th. Rasing, J. R. R. Leite, and Y. R. Shen, "Local-field enhancement on rough surfaces of metals, semimetals, and semiconductors with the use of optical second-harmonic generation," *Phys. Rev. B*, Vol. 30, No. 2, pp. 519-526, 1984.
- [10] H. Kuwata, H. Tamaru, K. Esumi, and K. Miyano, "Resonant light scattering from metal nanoparticles: Practical analysis beyond Rayleigh approximation," *Appl. Phys. Lett.* Vol. 83, No. 22, pp. 4625-4627 (2003).

- [11] R. G. Yarovaya, I. N. Shklyarevskii, and A. F. A. El-Shazly, "Temperature dependence of the optical properties and the energy spectrum of zinc," *Sov. Phys. JETP*, Vol. 38, No. 2, pp. 331-334, 1974.
- [12] K. F. MacDonald, V. A. Fedotov, S. Pochon, K. J. Ross, G. C. Stevens, N. I. Zheludev, W. S. Brocklesby, and V. I. Emel'yanov, "Optical control of gallium nanoparticle growth," *Appl. Phys. Lett.* Vol. 80, No. 9, pp. 1643-1645, 2002.
- [13] *Near-Field Nano/Atom Optics and Technology*, edited by M. Ohtsu, (Springer, Tokyo, 1999) Chap. 3.
- [14] T. Yatsui, W. Nomura, M. Kourogi, M. Ohtsu, "Plasmon polariton transfer along nano-dot coupler for optical far/near field conversion," International Quantum Electronics Conference, May 21, 2004, San Francisco, CA.

Observation of optical near-field energy transfer in closely spaced ZnO/ZnMgO multiple-quantum-well nanorods for nanophotonic devices

T. Yatsui,* J. Lim,** T. Kawazoe,* K. Kobayashi,* M. Ohtsu,*,** W. I. Park,† and G.-C. Yi†

*SORST, Japan Science and Technology Agency
687-1 Tsuruma, Machida, Tokyo, Japan 194-0004
+81 42-788-6040, +81 42-788-6031, yatsui@ohtsu.jst.go.jp

** Interdisciplinary Graduate School of Science and Engineering, Tokyo Institute of Technology
4259 Nagatsuta, Midori-ku, Yokohama, Japan 226-8502
+81 45-924-5476, +81 45-924-5599

† Department of Materials Science and Engineering, Pohang University of Science and Technology
Kyungbuk, Korea 790-784
+82 54-279-2155, +82 54-279-2399

Abstract: We observed an anti-correlation feature in the photoluminescence intensity distribution of ZnO/ZnMgO multiple-quantum-well nanorods. This is attributed to the optical near-field energy transfer between resonant energy levels in closely spaced pairs of ZnO/ZnMgO multiple-quantum-well nanorods.

©2003 Optical Society of America

OCIS codes: (300.6540) Spectroscopy, ultraviolet, (310.6860) Thin films, optical properties

ZnO nanocrystallite is a promising material for realizing nanometer-scale photonic devices [1] at room temperature, due to its large exciton binding energy. To confirm its promising optical properties, we performed spatially and spectrally resolved photoluminescence (PL) imaging of individual ZnO/ZnMgO multiple-quantum-well (MQW) nanorods.

We used ZnO/ZnMgO MQW nanorods that consisted of ten periods of 3-nm ZnO/6-nm Zn_{0.8}Mg_{0.2}O. They were grown on the ends of ZnO nanorods with a 40-nm mean diameter using metalorganic vapor phase epitaxy [2].

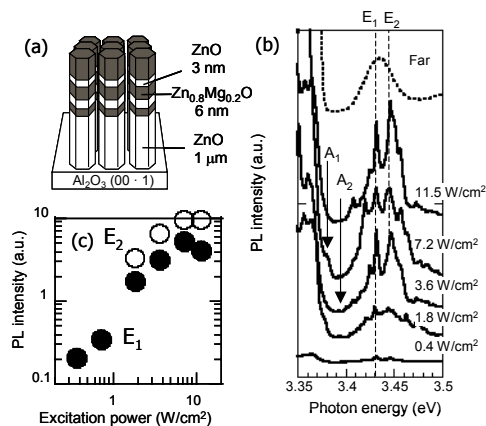


Fig. 1. (a) Schematic of MQW nanorods consisting of 10 periods of ZnMgO/ZnO on the tips of ZnO nanorods. (b) Far-field (dashed line) and near-field (solid lines) PL spectra of the MQW ZnO/ZnMgO nanorods at 15 K. A He-Cd laser light ($\lambda = 325$ nm) was used to excite the ZnO nanocrystallites. (c) The excitation power density dependence of the integrated PL intensity at $E_1 = 3.432$ eV (closed circles) and $E_2 = 3.447$ eV (open circles).

The dashed curve in Fig. 1(b) shows the far-field PL spectrum at 15 K. A blue-shifted PL emission peak was observed around 3.43 eV. The magnitude of the blue shift was consistent with the theoretical value of the quantum confinement effect in the ZnO QW layer. To investigate the optical properties of individual ZnO/ZnMgO MQW, we observed the dependence of near-field PL spectra on the excitation power density at 15 K [Fig. 1(b)]. In the weak

excitation condition, a single PL peak was observed at 3.432 eV (E_1). At excitation power densities exceeding 2 W/cm², another PL peak appeared at the higher energy of 3.447 eV (E_2). To confirm the origin of the emission lines, we plotted the integrated PL intensity for the emission lines of both E_1 and E_2 [Fig. 1(c)]. This showed that the E_1 and E_2 emission lines originated from the recombination of the ground state and first excited state. This estimation is also supported by the fact that the energy difference between E_1 and E_2 is about 15 meV, which is in good agreement with the theoretical calculation [3].

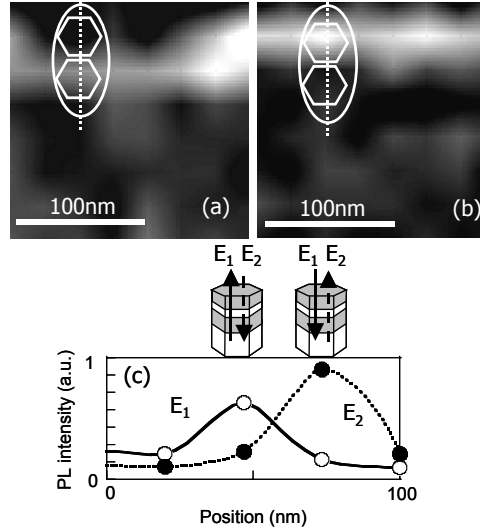


Fig. 2. Monochromatic PL images of ZnO/ZnMgO MQW nanorods obtained at photon energies of (a) E_1 and (b) E_2 , respectively. (c) The open and closed circles represent the cross-sectional profiles along the dashed white lines in (a) and (b).

In order to investigate the optical properties in the coupled quantum structures, we performed monochromatic PL imaging of ZnO/ZnMgO MQW nanorods (Fig. 2). The outstanding feature was the anti-correlation in the PL intensity of E_1 and E_2 ; E_1 was suppressed, while E_2 was enhanced in a closely adjacent nanorod [Fig. 2(c)]. Based on this result, we considered a model of the PL process from closely spaced pairs of ZnO/ZnMgO MQW (Fig. 3). Due to the deep potential depth of 4 eV to the vacuum [4], carrier tunneling between the nanorods can be neglected. Since the inter sub-level transition time (denoted by τ_{sub}) is much shorter than the decay rate of E_1 , the suppression of E_1 is due to the luminescence center. Even in a ZnO MQW with such defects, the emission from the excited state E_2 can be detected by an optical fiber probe due to near-field coupling of the probe and ZnO/ZnMgO MQWs (denoted by γ). Since the degree of the anti-correlation was larger for a more closely spaced pair of nanorods, the anti-correlation feature is attributed to optical near-field coupling between the ZnO/ZnMgO MQW (denoted by NF), *i.e.*, energy transfer phenomena induced by the optical near field between two resonant energy levels in a ZnO/ZnMgO MQW and an adjacent ZnO/ZnMgO MQW.

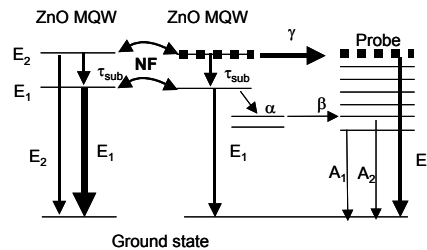


Fig. 3 Model of closely spaced pairs of ZnO/ZnMgO MQW nanorods.

This phenomenon can be used to realize nanometer-scale photonic devices, such as the switching mechanism confirmed by the authors in CuCl quantum cubes [5].

References

1. M. Ohtsu, K. Kobayashi, T. Kawazoe, S. Sangu, and T. Yatsui, "Nanophotonics: design, fabrication, and operation of nanometric devices using optical near fields," *IEEE Journal of Selected Topics in Quantum Electronics* **8**, 839-862 (2002).
2. W. I. Park, G.-C. Yi, M. Kim, and S. J. Pennycook, "Quantum confinement observed in Zn/ZnMgO nanorod heterostructures," *Adv. Mater.* **15**, pp.526–529 (2003).
3. S. L. Chuang, *Physics of Optoelectronic Devices* (Wiley, New York, 1995), Chap. 4.
4. N.W. Wang, J. O. McCaldin, J. F. Swenberg, T. C. McGill, and R. J. Hauenstein, "Schottky-based band lineups for refractory semiconductors," *Appl. Phys. Lett.* **66**, 1974-1976 (1995).
5. T. Kawazoe, K. Kobayashi, S. Sangu, and M. Ohtsu, "Demonstration of a nanophotonic switching operation by optical near-field energy transfer," *Appl. Phys. Lett.* **82**, 2957-2959 (2003).

Nano-photolithography using a visible light based on the nonadiabatic near-field photochemical reaction

Tadashi Kawazoe¹⁾, Ryoichi Haga²⁾, and Motoichi Ohtsu^{1,2)}

¹⁾SORST, Japan Science and Technology Agency, Tenkoh building 17-4F687-1 Tsuruma, Machida, Tokyo 194-0004, Japan.

Telephone: +81-42-788-6039, Fax: +81-42-788-6031, e-mail: kawazoe@ohtsu.jst.go.jp

²⁾ Interdisciplinary Graduate School of Science and Engineering,

Tokyo Institute of Technology, 4259 Nagatsuta, Midori-ku, Yokohama 226-8502, Japan

Abstract: We applied nonadiabatic near-field photochemical reaction to the photolithography. The optical near field with the steep spatial gradient of optical power activates the unique photochemical reaction and enables nanometric patterning even by using visible light.

©2003 Optical Society of America

OCIS codes: (110.5220) Photolithography; (260.5130) Photochemistry; (220.4610) Optical fabrication

The spatial locality of the optical near field leads to novel physical phenomena such as optically forbidden energy transfer [1] and giant second harmonic generation. Previously, we found another novel phenomenon, *i.e.*, the photodissociation of metal organic molecules using a nonresonant optical near field with photon energy lower than the photodissociation energy of the molecule [2]. We succeeded to explain this unique photodissociation by the exciton-phonon polariton model and the nonadiabatic process based on the spatial locality of the optical near field [3]. The photodissociation using optical near field seems to violate the Franck-Condon principle due to the nonadiabatic process. According to our model, the nonadiabatic photochemical reaction is a universal phenomenon and is applicable to many other photochemical processes. In this presentation, we propose the unique nano-photolithography using this reaction.

Figure 1(a) shows the schematic configuration of the used photo-mask and the Si-substrate spin-coated with the photoresist (OFPR-800) at the exposure process in contact mode. We adjusted the gap between the photo-mask and photoresist to become as narrow as possible. Figures 1(c) and (e) show the atomic force microscope images of the photoresist surface after development by g and i lines of Hg lamp and 672-nm laser, respectively. Figures 1(b) and (d) show the cross-sectional distribution of the optical energy and its spatial gradient at the contact plane between the photo-mask and the photoresist calculated by the finite difference time domain (FDTD) Method. By g and i lines, the conventional exposure process forms the corrugation whose size corresponds to the optical intensity distribution generated by the photo-mask pattern, *i.e.*, lines and spaces 1 μm (Fig. 1(b) and (c)), because the used photoresist is active to the g and i lines. The 672-nm laser also developed the corrugation pattern on the photoresist though this photoresist must be inactive to the 672-nm light. The width and depth of the groove in the corrugation pattern were 250nm and 25nm, respectively. The period (lines and spaces) of the corrugation by the 672-nm laser is different from that by g and i lines and is a half that. This result can be explained by the optical near-field effect. The exposure process cannot occur by direct irradiation of 672-nm light. However, the optical near field causes the exposure process due to the nonadiabatic photochemical reaction. This unique photochemical reaction is induced by the steep spatial gradient of the optical energy, which is one of the features of the optical near field. Since the optical near field is strongly generated at around the edges of the Cr-mask, the spatial gradient of the optical energy is large at the edges as shown in Fig. 1(d). The developed pattern by the 672-nm laser agrees well with the distribution of the gradient (Fig. 1(d) and (e)). This agreement confirms the nonadiabatic photochemical process, that we proposed, occurs due to the steep spatial gradient of the optical energy.

This novel process for photolithography is one of the promising techniques for nanofabrication, because it does not require the expensive vacuum UV light source and optics for the nano-photolithography.

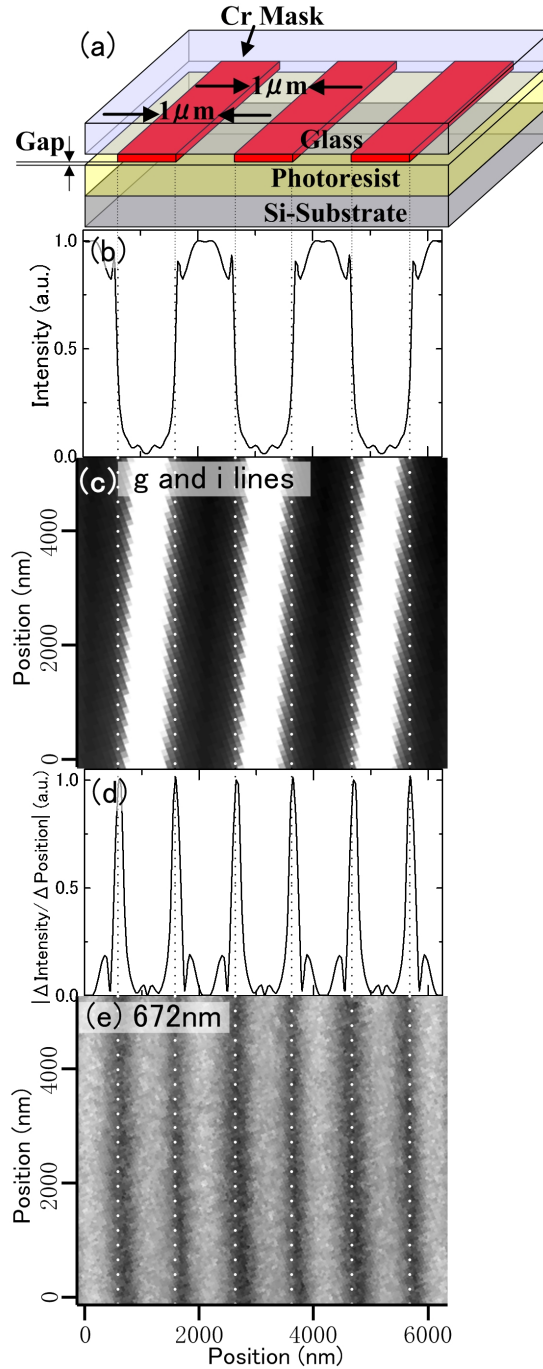


Fig.1. (a) The schematic configuration of the used photo-mask and the Si-substrate spin-coated with the photoresist (OFPR-800) at the exposure process. (b) The cross-sectional distribution of the optical energy at the contact plane between the photo-mask and the photoresist calculated by FDTD. (c) AFM images of photoresist by g and i lines of Hg lamp after development. (d) The spatial gradient of the cross-sectional distribution of the optical energy (Fig.1(b)). (e) AFM images of photoresist by 672-nm laser after development.

- [1] T. Kawazoe, K. Kobayashi, J. Lim, Y. Narita, and M. Ohtsu, Phys. Rev. Lett., 88, pp.067404 (2002).
- [2] T. Kawazoe, Y. Yamamoto, and M. Ohtsu, Appl. Phys. Lett., 79, pp.1184 (2001).
- [3] T. Kawazoe, K. Kobayashi, S. Takubo, and M. Ohtsu, Technical digest of QELS QWA12 (2003).

Fiber optical devices using a gigantic Faraday rotation in nanometric region

Tadashi Kawazoe¹, Shinya Maruyama², and Motoichi Ohtsu^{1,2}

¹⁾SORST, Japan Science and Technology Agency, Tenkoh building 17-4F687-1 Tsuruma, Machida, Tokyo 194-0004, Japan.

Telephone: +81-42-788-6039, Fax: +81-42-788-6031, e-mail: kawazoe@ohtsu.jst.go.jp

²⁾ Interdisciplinary Graduate School of Science and Engineering,

Tokyo Institute of Technology, 4259 Nagatsuta, Midori-ku, Yokohama 226-8502, Japan

Abstract: We demonstrate a novel fiber device using a gigantic Faraday rotation in sharpened optical fiber. The rotation angle of this reaches as much as 105 degrees in spite of the sub-wavelength size of the device.

©2003 Optical Society of America

OCIS codes: (230.3810) Magneto-optical devices; (240.6680) Surface plasmons; (230.3990) Microstructure devices

Optical fiber and guided-wave techniques have been bringing the high efficiency, functions, and downsizing to optical devices. Especially, the demand of the downsizing is strong and several approaches, *e.g.*, photonic crystals and nanophotonics [1], have been reported. The polarization control in such devices is one of the important functions to realize the optical isolator, circulator, and so on. However, current polarization control devices are too large to integrate for downsizing. This presentation reports a novel approach to control the polarization of light and a demonstration of the Faraday rotator based on the gigantic magneto-optical effect of the surface plasmon-polariton.

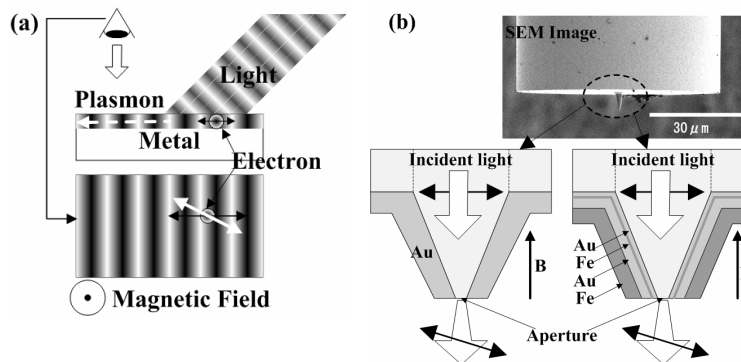


Fig. 1. (a) Schematic explanations of surface plasmon-polariton and its polarization rotation induced by external magnetic field. (b) SEM image of a typical fabricated fiber probe and schematics of its structures.

Figure 1(a) shows the schematic explanations of surface plasmon-polariton and its polarization rotation induced by external magnetic field. The surface plasmon on metal corresponds to the density wave of electrons, *i.e.*, the electron vibration. The external magnetic field normal to the metal surface can incline the vibrational direction of electron due to the Lorentz force. We consider that this inclined electron vibration can rotate the polarization of light reconverted from plasmon wave to light wave. Figure 1(b) shows the typical SEM image of the fabricated Faraday rotator using an optical fiber sharpened by etching and metal coating. First, we fabricated the fiber tip coated only with Au layer of 160-nm thick. When the aperture diameter is much smaller than the diffraction limit of light, the optical power is transferred by the plasmon wave at the boundary between glass composing a fiber and the metal layer. The plasmon wave is reconverted to the optical field at the aperture. Therefore, the polarization of the output light passing through the fiber tip should be controlled, if the polarization of the plasmon wave is controlled by the external magnetic field. In the experiment, we used the linearly polarized incident light of 633-nm wavelength and the external magnetic field B was applied by the permanent magnet whose direction was parallel to the fiber axis. The polarization of the output light was measured by the angle of the polarizer in front of the photodetector.

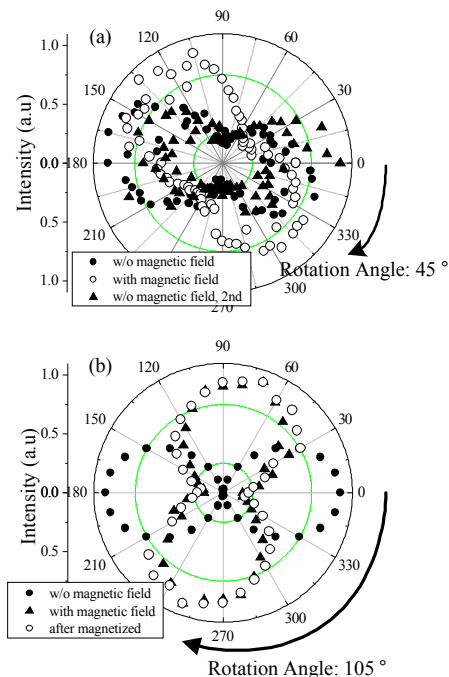


Fig.2. Polarizations of output light. (a) Au coated fiber tip with 100-nm aperture. (b) Au/Fe/Au/Fe coated fiber tip with 80-nm aperture.

Figure 2 shows the experimental results shown. The polar angle and radial axis show the angle of polarizer and detected intensity, respectively. For the fiber tip with aperture larger than 200 nm, the Faraday rotation angle was small. However, we observed gigantic Faraday rotations for the fiber tips with less than 200-nm aperture, *i.e.*, much smaller than the diffraction limit. We obtained a Faraday rotation angle of 45 degrees for the Au coated fiber tip with 100-nm aperture at $B=0.3T$, as shown in Fig. 2(a). Next, we fabricated the fiber tip coated with the Au/Fe/Au/Fe (10nm/ 2nm/ 80nm/ 100nm) layers expecting the increase in the magneto-optical effect, which comes from the large magneto-optical effect of the ferromagnetic material Fe [2] and the quantum size effect of Au/Fe/Au quantum well structures. Finally, we obtained a Faraday rotation angle of 105 degrees for the Au/Fe/Au/Fe coated fiber tip with 80-nm aperture at $B=0.35T$, as shown in Fig. 2(b). This rotation angle is large enough for the optical isolator and circulator. The Au/Fe/Au/Fe coated fiber tip does not require the external magnetic field after magnetization. The Faraday rotation angle was preserved even after removing the external magnetic field due to its Fe magnetized layer (\circ in Fig.2(b)). This becomes the strong advantage for integration, because magnet is not necessary, which is a large and negative effecting to the surroundings.

These experimental results show that our proposed optical fiber tip is promising for the miniature polarization controller that can be integrated in the photonic integrated.

[1] T. Kawazoe, K. Kobayashi, S. Sangu, and M. Ohtsu, Appl. Phys. Lett. 82, 2957 (2003)

[2] J. Lim, T.Kawazoe, T.Yatsui, M.Ohtsu, IEICE TRANS. ELECTRON., Vol.E85-C, No.12, pp.2077-2080, 2002

Near Field Optical Spectroscopy of GaN/AlN Quantum Dots

A. Neogi

Department of Physics, University of North Texas, Denton TX 76203

H. Morkoc

Dept. of Physics, Virginia Commonwealth Univ., Richmond, VA

A. Tackeuchi and T. Kuroda

Dept. of Appl. Physics, Waseda Univ., Tokyo 156-03, Japan

M. Ohtsu, T. Kawazoe

Japan Science and Technology Agency, University of Tokyo, Japan

Quantum dots (QDs) in nitride-based structures are expected to improve characteristics of visible-to-UV optical emitters that are currently developed by employing 2-and 3 dimensional growth processes. The optical property of these nitride quantum dots (QD) is particularly interesting as it depicts the interplay of in-built strain induced electric fields and quantum confinement in the nitride based material system. When the dot size is of the order of the exciton Bohr radius, the quantum confinement and built-in polarization field affects both the exciton binding energy and the optical bandgap and allow tailoring of the optical properties of the system.

GaN dots on AlN layers discussed here were grown on sapphire substrates by rf-Nitrogen plasma Molecular Beam Epitaxy. We have demonstrated size control of QDs by strain modification using various growth techniques to achieve emission energies ranging from 2.5 eV to 3.9 eV [1]. In self-organized GaN QDs, the quantum confinement effect observed in the “classical” GaAs-based QD or QW, is offset by the large piezoelectric fields resulting in a red-shift of the ground state optical transition below the bulk bandgap by about 0.5-1.2 eV. This enormous shift is attributed to the piezoelectric field exceeding 5 MV/cm. The built-in strain field along with size-control of the QDs can therefore be used to tune the emission wavelength of ultraviolet light from GaN-QD based optical emitters.

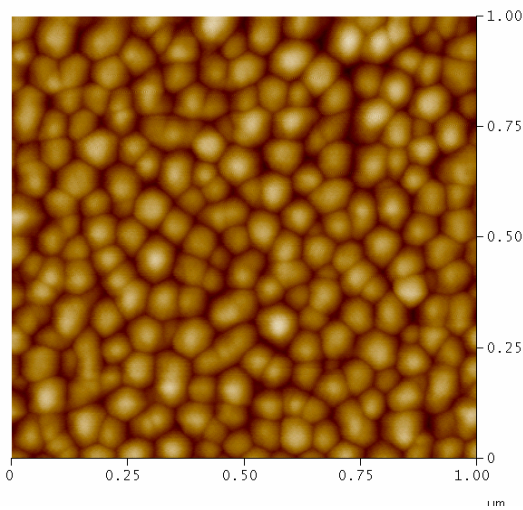


Fig.1. AFM Image of GaN QDs: Dot density $3 \times 10^{10} \text{ cm}^{-2}$

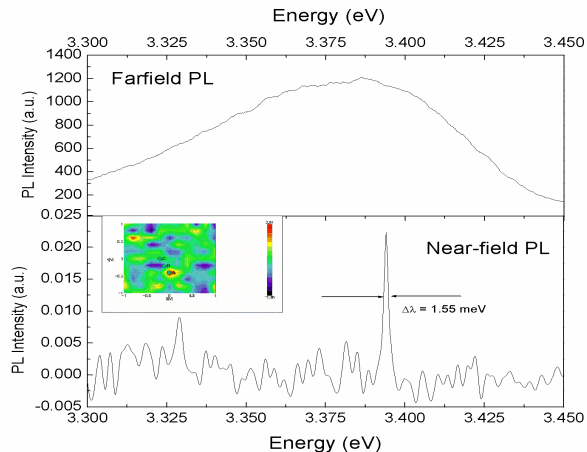


Fig.2. Near field Luminescence spectrum of a single period GaN QDs measured in the illumination collection mode and its comparison to the far field PL spectrum

Figure 1 shows the honeycomb structure of GaN QDs observed from atomic force microscopy measurements. The dot density exceeds $3 \times 10^{10} \text{ cm}^{-2}$ with dot width $\sim 50\text{-}70$ nm and height of $\sim 7\text{-}10$. The near-field luminescence spectrum has also been measured to isolate the optical properties of single quantum dots from the ensemble effect. Using an NSOM measurement setup [2] with a spatial resolution of 50 nm and spectral resolution of 0.001 nm, the PL line-width (FWHM) of a single or an ensemble of few QDs has been observed to be 1.55 meV. Comparatively in the far-field limit the FWHM exceeds 100 meV (Fig.2.).

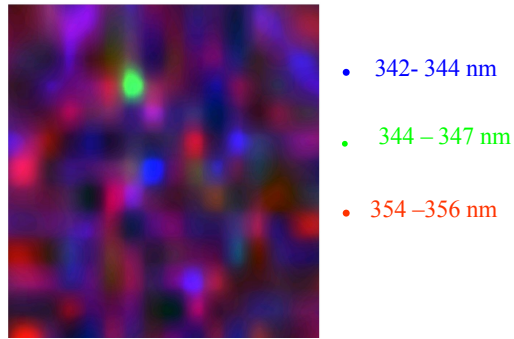


Fig.3. QD Size dependence of near-field luminescence spectrum (Area: 450 nm x 450 nm)

The near field PL spectrum shows the size variation and the dependence of emission energy in 20 period stacked QDs (Fig.3.). A large emission from a single QD structure within 450 nm x 450 nm region is observed at ~ 3.59 eV, which corresponds to monolayer fluctuations. There are larger numbers of dots luminescent at 3.49 eV and 3.61 eV and the emission intensity are relatively weaker than QDs emitting at 3.59 eV. The preferential emission characteristics of these dots at various energies is also related to the strain relaxation in the QD matrix

The emission mechanism in GaN QDs is also investigated by time resolved photoluminescence and differential transmission spectroscopy. A comparison of the temperature dependent spectrally integrated decay characteristics of stacked and single layer QD structures is shown in figure 4. In un-stacked (single layer) QDs non-radiative recombination process dominates the emission at higher temperature. In stacked QDs nonradiative processes are considerably reduced as there is no significant difference in the decay constants due to change in temperature from 10 K to 100 K. Stacking results in higher emission efficiencies at 300 K. We also observed signature of phonon-bottle neck phenomenon in un-stacked single QD layers as evidenced by the large PL decay constant at 10 K.

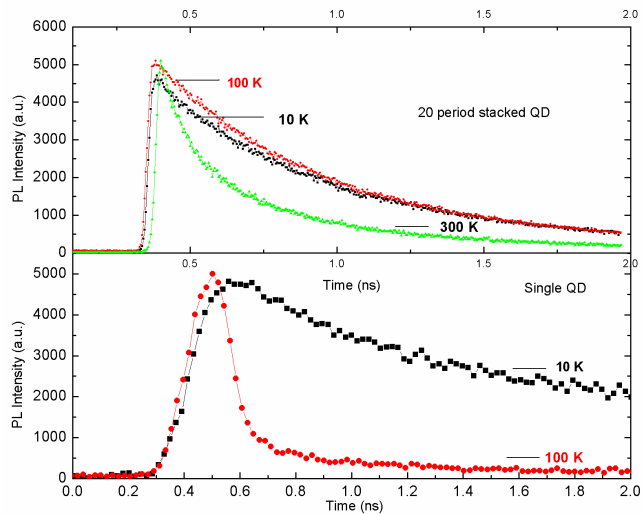


Fig.4. Time-resolved PL decay characteristics of stacked and single layer QD.

[1] A. Neogi, et al., 2003, J.Appl. Phys. {in Press}.

[2] T. Kawazoe, K. Kobayashi, S. Sangu, M. Ohtsu, Appl. Phys. Lett, **82**, 2957, (2003).

The optical nano-fountain for concentrating optical energy to a nanometric region

Tadashi Kawazoe¹⁾, Kiyoshi Kobayashi²⁾, and Motoichi Ohtsu^{1,3)}

¹⁾ SORST, Japan Science and Technology Agency, Tenkoh building 17-4F, 687-1 Tsuruma, Machida, Tokyo 194-0004, Japan.

Telephone: +81-42-788-6039, fax: +81-42-788-6031, e-mail: kawazoe@ohtsu.jst.go.jp

²⁾ Japan Science and Technology Corporation, Tenkoh building 17-4F, 687-1 Tsuruma, Machida, Tokyo 194-0004, Japan.

³⁾ Interdisciplinary Graduate School of Science and Engineering,

Tokyo Institute of Technology, 4259 Nagatsuta, Midori-ku, Yokohama 226-8502, Japan

Abstract: We demonstrate a novel method for concentrating optical energy to a nanometric region using energy transfers among CuCl quantum dots in a NaCl matrix. The optical energy was concentrated to 10nm in diameter.

©2003 Optical Society of America

OCIS codes: (220. 2560) Focus; (230. 3990) Microstructure devices; (999.9999) Optical Near Field

Concentration of optical energy to nanometric region enables a terabits optical memory, a highly integrated photonic device, a nanometric optical microscope, and so on [1]. A convex lens has been used to concentrate optical energy. However, the focused spot size is limited by diffraction. To go beyond the diffraction limit, we propose here a novel nanophotonic device that we call the “optical nano-fountain”, which uses optical near-field energy transfer among quantum dots and demonstrate its operation.

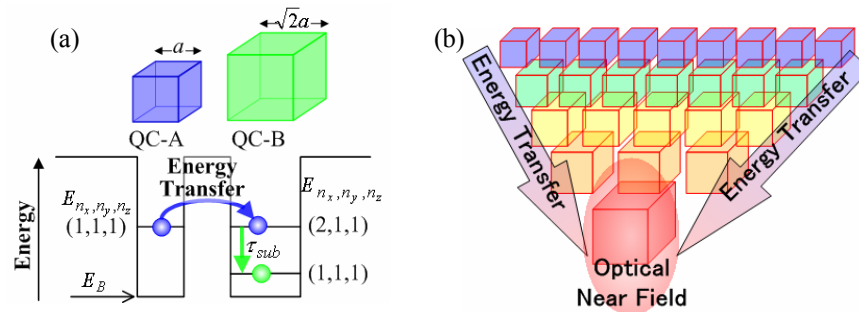


Fig. 1. Schematic explanation of the near-field energy transfer (a) and the optical nano-fountain composing many quantum dots (b).

We have recently reported energy transfer among quantum dots via an optical near field [2]. The energy transfer occurs from a higher energy level to a lower energy level, *i.e.*, from smaller to larger quantum dots, as shown in Fig. 1(a). This unidirectional energy transfer and successive relaxation are applicable to the optical energy concentration. Figure 1 (b) shows a schematic explanation of the optical nano-fountain, which is composed of many different-sized quantum dots. When these quantum dots have resonant energy sublevels of carriers, the energy transfer occurs via the optical near field as illustrated by the arrows in Fig. 1(a). Light incident to the optical nano-fountain is ultimately concentrated at the largest quantum dot whose size corresponds to the focal spot size of this device. We call this device an optical nano-fountain, because its mechanism looks like a fountain, which concentrate and spurt water caught at high potentials. The mechanism is also similar to that of the light trapping system in the photosynthesis bacteria [3], so its operation is biomimetic. From previous experimental tests of nanophotonic switch, it is expected that the concentration efficiency of this device will be close to 100 % [4].

To demonstrate the operation of the optical nano-fountain, we used CuCl cubic quantum dots embedded in a NaCl matrix. This has an inhomogeneous size distribution and a random arrangement of quantum dots. Therefore, in some areas of the sample, the quantum dots are arranged to act as an optical nano-fountain. In the experiment, we maintained the sample temperature at 40 K, as at too low a temperature the resonant condition becomes tight, due to narrowing of the homogeneous linewidth, while at too high a temperature unidirectional energy transfer is obstructed by thermal activation of excitons in the quantum dots. A 325-nm He-Cd laser was used as the excitation light source.

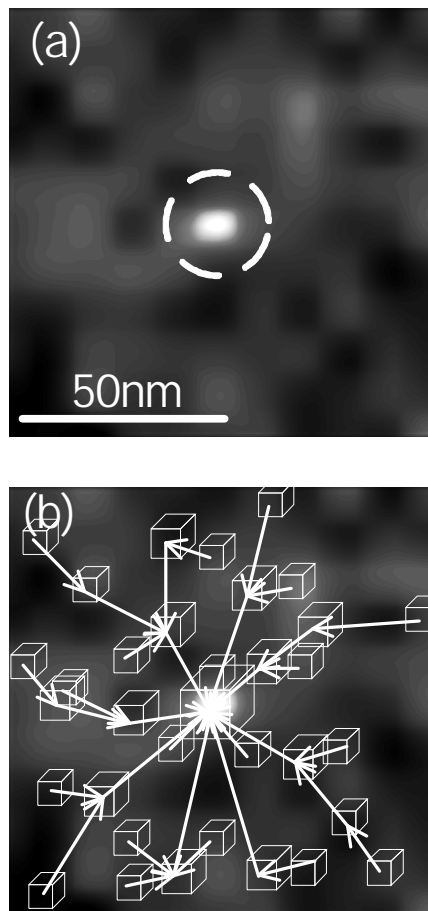


Fig.2. Luminescence intensity distribution of CuCl quantum dots. Schematic quantum dots show their size and positions estimated by size selective measurement.

Figure 2 (a) shows the spatial distribution of the luminescence intensity of the sample observed with an optical near-field microscope. Here, the collected luminescence photon energy was from 3.350 eV to 3.215 eV, which corresponded to the luminescence from 2- to 10-nm quantum dots, respectively. The bright spot in a broken circle corresponds to the spurt from the optical nano-fountain and its full-width half maximum is estimated at 10 nm. To investigate the optical energy transfer from smaller to larger quantum dots, we measured the selective luminescence intensity distribution by size, *i.e.*, by photon energy. Thus, we obtained the size and positions of quantum dots existing in the scanning area, as shown by the schematic drawings of cubic quantum dots in Fig.2 (b). Only one quantum dot of 6-10 nm size exists at the spurt position and many smaller quantum dots exist in the area of 100-nm diameter around the spurt. The luminescence intensity at the bright spot is several times stronger than that from a single isolated 10-nm quantum dot. Conversely, the luminescence intensities of surrounding smaller quantum dots are weaker than those of the isolated quantum dots. This indicates that energy is transferred from smaller to larger quantum dots and is finally concentrated at the largest quantum dot. This is the first demonstration of the novel nanometric optical condensation device, the optical nano-fountain. Its optical energy concentration diameter was more than 100 nm and the focal spot size was 10 nm.

We proposed a new nanophotonic device, the optical nano-fountain, which uses energy transfer among quantum dots, and demonstrated its operation using CuCl quantum dots embedded in a NaCl matrix. The nanophotonic device concentrates optical energy from a 100-nm area and spurts it in a 10-nm region.

[1] M. Ohtsu, K. Kobayashi, T. Kawazoe, S. Sangu, and T. Yatsui, IEEE J. Sel. Top. Quant. Electron, 8 No.4 p 839 (2002).

[2] T. Kawazoe, K. Kobayashi, J. Lim, Y. Narita, and M. Ohtsu, Phys. Rev. Lett., 88 No.6 pp. 067404 (2002).

[3] K. Mukai, S. Abe, and H. Sumi, J. Phys. Chem. B 103, (1999) p.6096.

[4] T. Kawazoe, K. Kobayashi, S. Sangu, and M. Ohtsu, Appl. Phys. Lett., 82 No.18 (2003) p.2957.

Plasmon polariton transfer along a nano-dot coupler for optical far/near field conversion

T. Yatsui^{*}, W. Nomura^{**}, M. Kourogi[†], and M. Ohtsu^{*,**}

^{*}SORST, Japan Science and Technology Agency
687-1 Tsuruma, Machida, Tokyo, Japan 194-0004

+81 42-788-6040, +81 42-788-6031, yatsui@ohtsu.jst.go.jp

^{**}Interdisciplinary Graduate School of Science and Engineering, Tokyo Institute of Technology
4259 Nagatsuta, Midori-ku, Yokohama, Japan 226-8502

+81 45-924-5476, +81 45-924-5599

[†]Optical Comb Institute, Inc.

2-12-1, O-okayama, Meguro-ku, Tokyo, Japan 152-8550

+81 3-5734-2337, +81 3-5734-2327

Abstract: We successfully fabricated a nano-dot coupler with a plasmon-polariton condenser for optical far/near-field conversion. Highly efficient energy transfer in the nano-dot coupler via near-field coupling between the plasmon-polariton modes of neighboring particles was observed.

©2003 Optical Society of America

OCIS codes: (230.3120) Integrated optics devices, (240.6680) Surface plasmons

Future optical transmission systems will require nanophotonic integrated circuits [1] composed of nanometer-scale dots to increase data transmission rates and capacity. As a representative device, we demonstrated a nanophotonic switch that was produced by controlling the dipole forbidden optical energy transfer among resonant energy states in quantum dots [2]. To install the switch in an integrated circuit, a novel device that couples with external conventional diffraction-limited photonic devices is required for far/near-field conversion. To realize this coupler, we propose a nano-dot coupler that consists of a chain array of closely spaced metal nanoparticles (see Fig.1). Energy transfer in the nano-dot coupler relies on near-field coupling between the plasmon-polariton modes of neighboring particles [3]. Compared with a metallic core waveguide, the use of our nano-dot coupler is expected to realize lower propagation loss due to the plasmon resonance in the metal nanoparticles.

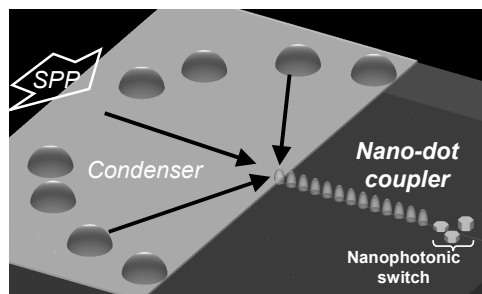


Fig.1. Nano-dot coupler with a plasmon-polariton condenser for optical far/near-field conversion devices.

To further increase the efficiency of our device, we also propose a plasmon-polariton condenser that is inserted between a diffraction-limited photonic device and a nano-dot coupler. It consists of several hemispherical metal nanoparticles that are arranged in an arc and work as a "phased array". After the carbon hemispheres were deposited in an arc using a focused ion beam (FIB), they were coated with a 100-nm-thick gold film to excite the 2-dimensional (2D) surface plasmon-polariton (SPP) mode [see Fig. 2(a)]. The spatial distribution of the optical near-field energy was observed using a collection mode near-field optical microscope (NOM) at $\lambda = 785$ nm with an arrangement for 2D SPP mode excitation using grating coupling. Figure 2(b) shows a NOM image of the plasmon-polariton condenser without a nano-dot coupler. We obtained a focused 2D SPP as small as 400 nm [see broken curve in Fig. 2(d)], which was in good agreement with the calculated result [see Fig. 2(c) and solid curve in Fig. 2(d)] obtained using the finite-difference time domain (FDTD) method.

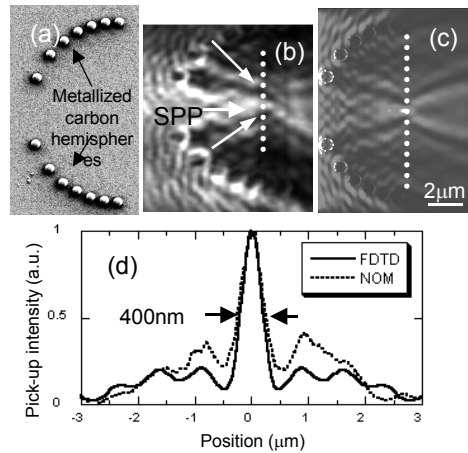


Fig. 2. (a) SEM image of the plasmon condenser. (b) NOM image of (a). (c) Calculated results obtained using FDTD. (d) Cross-sectional profiles along the dashed white lines in (b) and (c).

Next, we compared the spatial distribution of the optical near-field intensity between the linear nano-dot coupler and the metallic core waveguide. Their input terminals were installed at the focal point of the plasmon-polariton condenser. For the nano-dot coupler or metallic core waveguide, carbon hemispheres [see Fig. 3(a)] or wire [see Fig. 3(c)] were deposited using FIB and were coated with a 100-nm-thick gold film. For the nano-dot coupler (a linear array of metal nanoparticles 230-nm in diameter and separated by 70 nm), we found plasmon-polariton transfer as long as 4 μm [see Fig. 3(b) and solid curve in Fig. 3(g)]. Furthermore, the propagation loss was 10 times lower than that of the metallic core waveguide [see Figs. 3(d) and dashed curve in Fig. 3(g)]. A similar energy transfer was also observed with a crenellated-shaped nano-dot coupler [see Figs. 3(e) and 3(f)] with low energy loss at the corners due to the efficient coupling of the TM and TE modes in the nano-dot coupler [see Fig. 3(h)]. Such high flexibility in the arrangement of nanoparticles is an outstanding advantage for optical far/near-field conversion for driving nanophotonic devices.

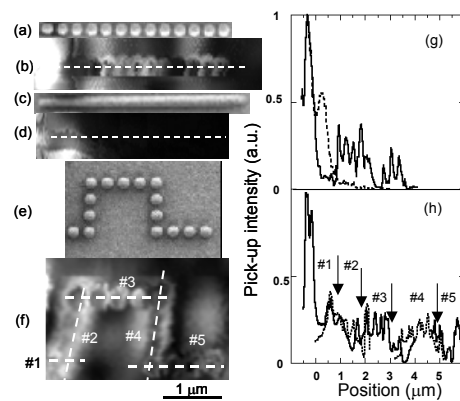


Fig. 3. SEM (a) and NOM (b) images of a linearly chained nano-dot coupler. SEM (c) and NOM (d) images of a metallic core waveguide. SEM (e) and NOM (f) images of a crenellated-shaped nano-dot coupler. (g) The solid and dashed curves show the cross-sectional profiles along the dashed white lines in (b) and (d), respectively. (h) The cross-sectional profiles along the dashed white lines in (f). The arrows indicate the corners.

References

1. M. Ohtsu, K. Kobayashi, T. Kawazoe, S. Sangu, and T. Yatsui, "Nanophotonics: design, fabrication, and operation of nanometric devices using optical near fields," *IEEE Journal of Selected Topics in Quantum Electronics* **8**, 839-862 (2002).

2. T. Kawazoe, K. Kobayashi, S. Sangu, and M. Ohtsu, "Demonstration of a nanophotonic switching operation by optical near-field energy transfer," *Appl. Phys. Lett.* **82**, 2957-2959 (2003).
3. M. L. Brongersma, J. W. Hartmann and Harry A. Atwater, "Electromagnetic energy transfer and switching in nanoparticle chain arrays below the diffraction limit," *Phys. Rev. B* **62**, R16356-R16359 (2000).

Adiabatic and nonadiabatic nanofabrication by localized optical near fields

Tadashi Kawazoe^a, Motoichi Ohtsu^{a,b}

^aExploratory Research for Advanced Technology, Japan Science and Technology Agency,
687-1 Tsuruma, Machida, Tokyo 194-0004, Japan, e-mail: kawazoe@ohtsu.jst.go.jp

^bInterdisciplinary Graduate School of Science and Engineering, Tokyo Institute of Technology,
4259 Nagatsuta, Midori-ku, Yokohama 226-8502, Japan

ABSTRACT

Near-field optical chemical vapor deposition (NFO-CVD), proposed by us, is a kind of optical CVD using the optical near field (ONF). Its application to nanostructure fabrication has the potential to realize high-density nanometric structures with extremely high accuracies in size and position. The localized property of ONF also causes a unique photochemical reaction. Conventional optical CVD is based on the adiabatic photochemical process and requires the UV light in order to excite molecules from the ground electronic state to the excited state for dissociation. For NFO-CVD, however, nonadiabatic photodissociation can take place, *i.e.*, even by a visible light, which arises from the steep spatial gradient of optical power of ONF. We succeeded to deposit nanometric Zn dots by using this nonadiabatic process, which can be explained by the exciton-phonon polariton model. According to this model, ONF generated at the apex of the fiber probe can directly excite the molecular vibrational state with its photon energy. Such nonadiabatic process rejects the requirement of resonant light for photochemical reaction. This unique process makes it possible to use visible lights and optically inactive gas sources to deposit a variety of nanometric materials, and is also applicable to other photochemical processes, *e.g.*, photolithography.

Keywords: Optical near field, photochemical reaction, optical CVD, nonadiabatic process, photolithography

1. INTRODUCTION

An advanced nanofabrication technique is required that realizes high spatial resolution, high precision in controlling size and position, and is applicable to various materials. Self-organized growth has been employed for nanofabrication [1]; however, its spatial precision is not sufficiently high to meet this requirement. To improve the precision, an e-beam [2], scanning tunneling microscope (STM) [3], and surface modification [4] are used for site-control of the substrate. In situ patterning of nanoscale structures using a scanning probe microscope, such as STM [5], has also been investigated; however, it has a fatal disadvantage in that it limits the materials that can be deposited because it cannot deal with insulators. By the conventional optical chemical vapor deposition (CVD), vapors of organometallic molecules are dissociated by the photochemical reaction with the far-field light; however, it is difficult to deposit subwavelength-sized materials due to the diffraction limit of light.

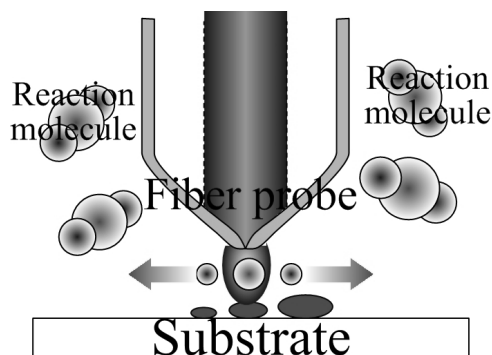


Fig.1. Principle of the NFO-CVD. Vapors of the organometallic molecules are dissociated by the photochemical reaction with the optical near-field on the probe tip.

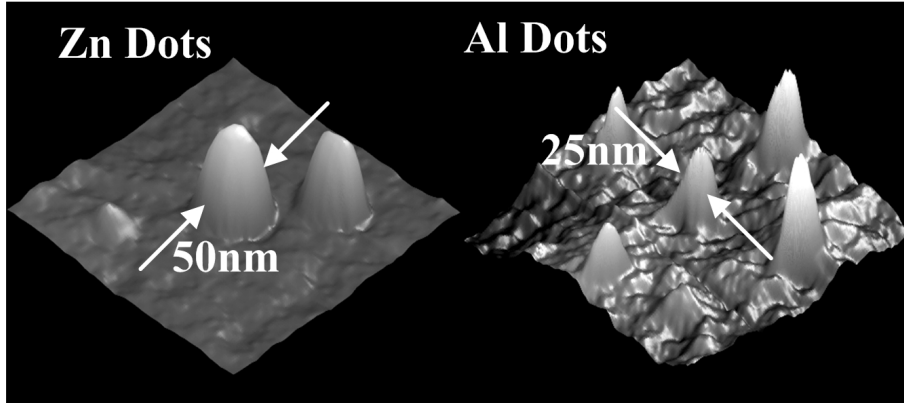


Fig.2. Shear-force topographic images of Zn dots and Al dots deposited by NFO- CVD.

Fig. 1 shows the principle of near-field optical CVD (NFO-CVD), which has been proposed by the authors in order to solve these problems by utilizing high spatial resolution capability of the optical near field. Nanometric Zn, Al, and ZnO dots and loops have been successfully deposited by this method [6]-[9]. As an example, Fig. 2 shows the shear-force topographic images of the deposited Zn and Al dots, whose sizes are less than 50 nm. It has been confirmed from these results that the precision of the deposited position was as high as about 1 nm [8]. As an outstanding advantage, we recently found that the photodissociation can take place even in nonresonant conditions to electronic transition of molecules, which is due to the nonadiabatic process comes from inherent properties of the optical near field [10]. Conventional optical CVD utilizes a two-step process: photodissociation and adsorption. For photodissociation, far-field light must resonate the reacting molecular gasses in order to excite molecules from the ground state to an excited electronic state [11]. The Franck-Condon principle holds that this resonance is essential for excitation. The excited molecules then relax to the dissociation channel, and the dissociated atoms adsorb to the substrate surface. However, the nonadiabatic photodissociation process, which is observed in NFO-CVD under the nonresonant condition, is able to violate the Franck-Condon principle. This is because the Franck-Condon principle is approved at an adiabatic process. In this paper, we discuss nonadiabatic NFO-CVD of nanometric Zn dots and explain the experimental results based on the features of the ONF and the exciton-phonon polariton model. According to our model, the nonadiabatic photochemical reaction is a universal phenomenon and is applicable to many other photochemical processes. We also report the application of this nonadiabatic near-field photochemical reaction to the photolithography.

2. NEAR-FIELD OPTICAL CVD

Figure 3 shows the experimental setup for NFO-CVD. Ultra-high purity argon (Ar) was used as a buffer gas and diethylzinc (DEZn) as a reacting molecular gas source. The second harmonic ($\lambda = 244$ nm) of an Ar^+ laser, which had a photon energy $\hbar\omega$ ($=5.08$ eV), was used as a light source that resonates the absorption band (band edge $E_{\text{abs}}=4.13$ eV) of DEZn [12]. A He-Cd laser ($\lambda=325$ nm) was used as the light source, which had a photon energy $\hbar\omega$ ($=3.81$ eV) that was nearly resonant. The fundamental frequencies of Ar^+ ($\lambda= 488$ nm:2.54 eV) and diode ($\lambda= 684$ nm: 1.81 eV) lasers were used as nonresonant light sources. The fiber probe used for NFO-CVD was a high throughput single tapered fiber probe, which was fabricated by pulling and etching a pure silica core fiber [13]. The cone angle of the fabricated fiber probe was 30 degrees and its apex diameter was 30 nm. In order to investigate the deposition effect of nonresonant far-field light, a fiber probe without the usual metal coating, *i.e.*, a bare fiber probe was used for the deposition. Therefore, the optical far-field was generated by light leaking through the circumference of the fiber probe, while the optical near-field was generated at the apex, as shown in Fig. 3. The separation between the fiber probe and the sapphire substrate was controlled to within several nanometers by using a shear-force technique [13]. The laser output power from the fiber probe was measured with a photo-diode placed behind the sapphire substrate. The sizes of the deposited Zn dots were measured using a shear-force microscope. During deposition, the partial pressure of DEZn was 100 mTorr and the total pressure in the chamber was 3 Torr. Details of the Zn deposition procedures have been reported in a previous work [8]. It should be noted that the deposition of Zn on the fiber probe

and the resultant decrease in the efficiency of optical near-field generation are negligible because the deposition time is sufficiently short, as has been pointed out elsewhere [8].

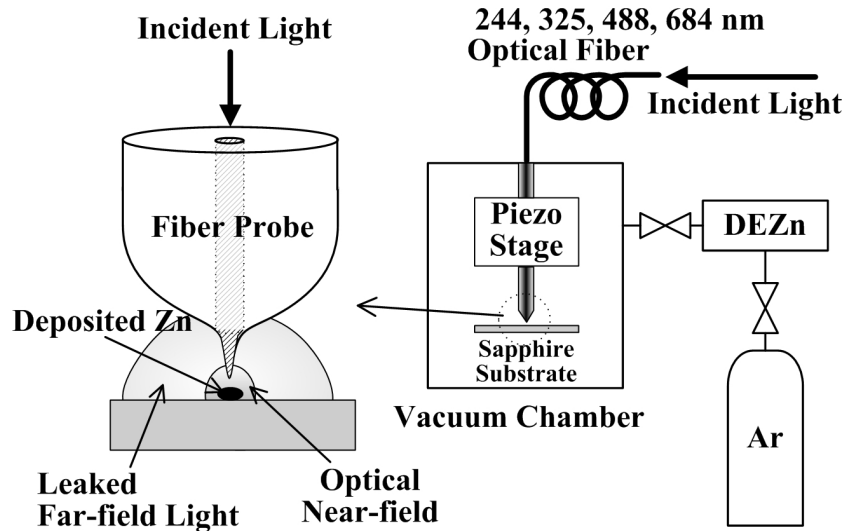


Fig.3. Experimental setup for chemical vapor deposition using an optical near field.

Figure 4 shows the shear-force topographical images after NFO-CVD for the photon energies 5.08 eV ($\lambda = 244$ nm) (a), 2.54 eV ($\lambda = 488$ nm) (b), and their cross sectional profiles (c) of the Zn dot deposited on the sapphire substrate with atomic-level steps [15]. For Fig. 4 (a) ($\hbar\omega = 5.08$ eV), the laser power was $1.6 \mu\text{W}$ and the irradiation time was 60 s. Before NFO-CVD, atomic-level step structures 0.4-nm high on the sapphire substrate were clearly observed, however, after NFO-CVD, the atomic-level steps disappear and a deposited Zn dot less than 50 nm in diameter appears at the center of the image. This occurs because the optical near field deposited the Zn dot directly under the apex of the fiber probe. Furthermore, since the bare fiber probe also leaked strong far-field light and DEZn absorbs the far-field light with this photon energy, a Zn layer that covered the atomic-step structures was deposited. For Fig. 4 (b), the laser power was $150 \mu\text{W}$ and the irradiation time was 75 s. The photon energy ($\hbar\omega = 2.54$ eV) is higher than the dissociation energy of DEZn, but it is still lower than the absorption edge of DEZn [12]. Therefore, it is not absorbed by the DEZn. A Zn dot less than 50 nm in diameter appears at the center of the broken circle of this figure. While the previous work using conventional CVD with a far-field light has claimed that a Zn film cannot be grown using nonresonant light ($\hbar\omega < 4.13$ eV: $\lambda > 300$ nm) [16], we observed the deposition of Zn dots on the substrate just below the apex of the fiber probe using NFO-CVD, even with nonresonant light. The atomic-level steps in this figure are still observed, despite the leakage of far-field light from the bare fiber probe. In Fig. 4(c), the solid curve is a cross sectional profile of the Zn dot deposited at $\lambda = 488$ nm across the dashed line in Fig. 4(b). The dashed curve represents the cross sectional profile of the Zn dot deposited at $\lambda = 244$ nm, taken across the dashed line in Fig. 4(a). These curves confirm that Zn dots with a full width at a half maximum of 30 nm were deposited in the region where the optical near field is dominant. The dashed curve has tails 4-nm high on both sides of the dot. These tails correspond to the deposition by the leaked far-field light. This deposition process is based on the conventional adiabatic photochemical process. On the other hand, the solid curve has no tails; thus, it is clear that the leaked 488-nm far-field light did not deposit a Zn layer. This result agrees with previous work using conventional optical CVD for Zn deposition with a far-field light with $\lambda = 300$ nm [16]. It should be noted that the 30-nm Zn dot without tails was deposited under a nonresonant condition, despite the presence of leaked far-field light.

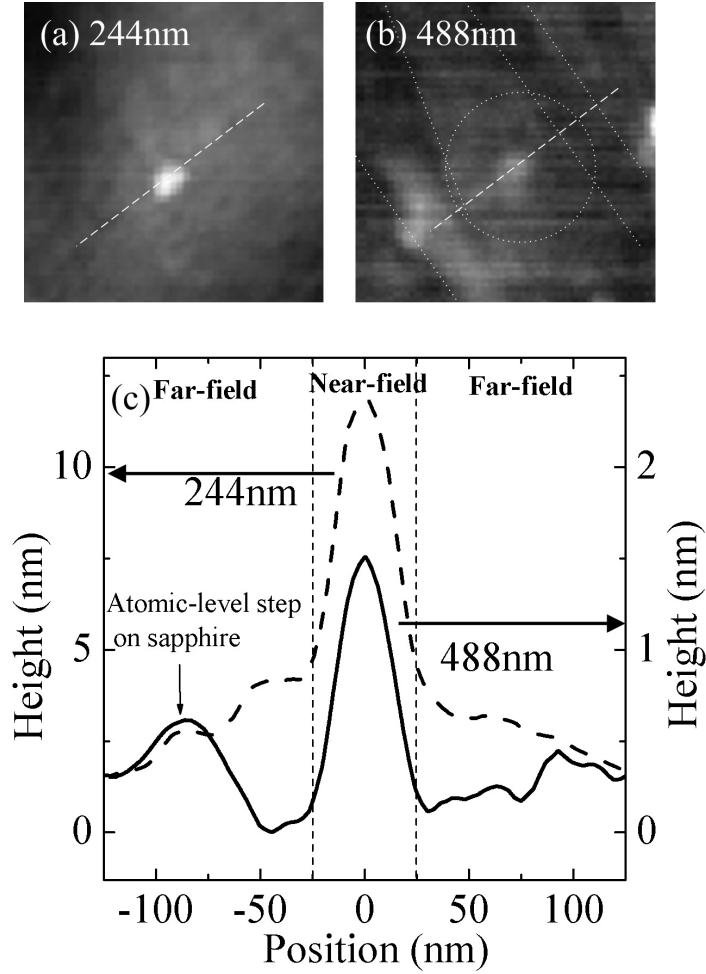


Fig.4. Shear-force topographical images before and after NFO-CVD at photon energies of 5.08 eV ($\lambda = 244$ nm) (a) and 2.54 eV ($\lambda = 488$ nm) (b). The image sizes are 300x300 nm. Cross-sectional profiles of the deposited Zn patterns. (c) Dashed and solid curves represent profiles along the dashed lines on the right-hand side of Figs. (a) and (b), respectively.

Figure 5 shows the shear-force topographical images of the sapphire substrate after NFO-CVD using ONF with photon energies of 3.81 eV ($\lambda=325$ nm) (a), 2.54 eV ($\lambda=488$ nm) (b), and 1.81 eV ($\lambda=684$ nm) (c), respectively. The laser power and the irradiation time were (a) 2.3 μ W and 60 s, (b) 360 μ W and 180 s, and (c) 1 mW and 180 s, respectively. The high purity quality of the deposited Zn was confirmed by X-ray photoelectron spectroscopy, and we observed luminescence from ZnO dots prepared by oxidizing the Zn dots fabricated by NFO-CVD [17]. In Fig. 5 (a), the photon energy, $\hbar\omega$ is higher than the dissociation energy, E_d , of DEZn, and is close to the absorption band edge, E_{abs} , of DEZn, *i.e.*, $\hbar\omega > E_d$ and $\hbar\omega \cong E_{abs}$ [12]. The diameter (FWHM) and height of the topographical image were 45 and 26 nm, respectively. This image has a small tail, as shown by dotted curves. This tail is a Zn layer, less than 2 nm thick, which is deposited by far-field light leaking from the bare fiber probe. This deposition is possible because DEZn absorbs a small amount of light with $\hbar\omega = 3.18$ eV. The very high peak in the image suggests that the ONF enhances the photodissociation rate at this photon energy, because the ONF intensity rapidly increases near the apex of the fiber probe. In Fig.5 (b), the photon energy still exceeds the dissociation energy of DEZn, but it is lower than the absorption band of DEZn, *i.e.*, $E_{abs} > \hbar\omega > E_d$ [12]. The diameter and height of the image were 50 nm and 24 nm, respectively. While some high intensity far-field light leaked from the bare fiber probe, it did not deposit a Zn layer,

so there is no foot at the base of the peak. This confirmed that the photodissociation of DEZn and Zn deposition only occurred with an ONF of $\hbar\omega = 2.54 \text{ eV}$. In Fig.5 (c), $\hbar\omega < E_d$ and $\hbar\omega < E_{abs}$. Even with such low photon energy, we succeeded in depositing of Zn dots. The topographical image showed a diameter and height of 40 nm and 2.5 nm, respectively. Experimental results in Fig. 5 demonstrate that the photodissociation process using nonresonant ONF, which is based on the nonadiabatic photochemical process that violates the Franck-Condon principle.

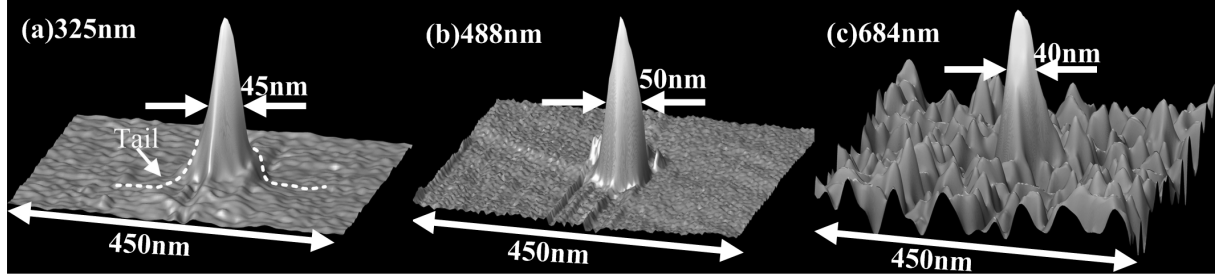


Fig.5. Shear-force topographical images after NFO-CVD at wavelengths of $\lambda = 325$ (a), 488 (b), and 684 (c) nm. The scanning area are 450x450 nm. The observed laser output power and the irradiation time for deposition were 2.3 μW and 60 s (a), 360 μW and 180 s (b), and 1 mW and 180 s (c).

In order to discuss this novel photodissociation process quantitatively, we examine the relationship between the photon-flux, I , and the deposition rate of Zn, R , in Fig. 6. For $\hbar\omega = 3.81 \text{ eV}$ (\bullet), R is proportional to I . For $\hbar\omega = 2.54 \text{ eV}$ (\blacksquare) and 1.81 eV (\blacktriangle), higher-order dependencies appear and are fitted by the third-order function $R = a \cdot I + b \cdot I^2 + c \cdot I^3$. The respective values of $a_{\hbar\omega}$, $b_{\hbar\omega}$, and $c_{\hbar\omega}$ are $a_{3.81} = 5.0 \times 10^{-6}$, $b_{3.81} = 0$, and $c_{3.81} = 0$ for $\hbar\omega = 3.81 \text{ eV}$; $a_{2.54} = 4.1 \times 10^{-12}$, $b_{2.54} = 2.1 \times 10^{-27}$, and $c_{2.54} = 1.5 \times 10^{-42}$ for $\hbar\omega = 2.54 \text{ eV}$; $a_{1.81} = 0$, $b_{1.81} = 4.2 \times 10^{-29}$, and $c_{1.81} = 3.0 \times 10^{-44}$ for $\hbar\omega = 1.81 \text{ eV}$. The fitting results are shown by a solid, a broken, and a dotted curve in Fig.6. These fitting values are used to investigate the physical origin of nonresonant NFO-CVD below.

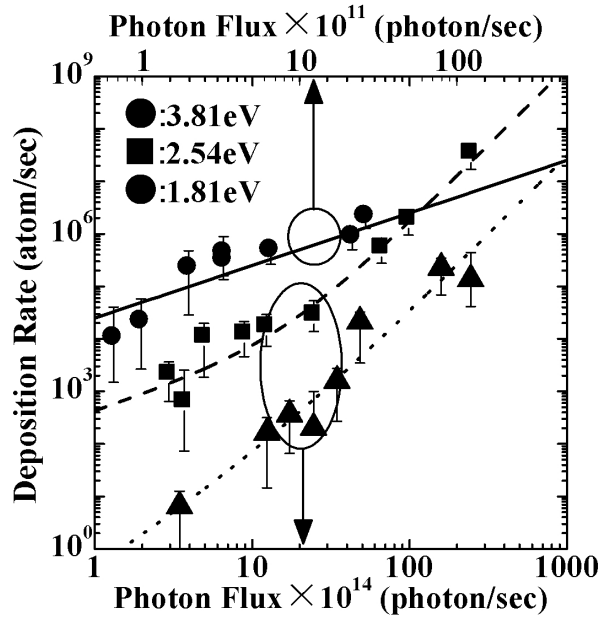


Fig.6. The optical power (photon-flux: I) dependency of the rate R of Zn deposition. The dotted, solid, and broken curves fit the results using $R = a \cdot I + b \cdot I^2 + c \cdot I^3$

3. EXCITON-PHONON POLARITON MODEL

Although we used the bear fiber probe, whose optical field broadens more than 200-nm diameter (FWHM), the Zn dots are deposited directly under the apex of the fiber probe. Any existing photochemical process for optical far field, e.g., Raman process, two-photon absorption, and so on, cannot explain our experimental results. Here, we propose the unique model for ONF in order to explain them.

Figure 7 shows the potential curves of an electron in a DEZn molecular orbital drawn as a function of the inter-nuclear distance of the C-Zn bond, which is involved in photodissociation [12]. The relevant energy levels of the molecular vibration mode are indicated by the horizontal broken lines in each potential curve. When a far-field light is used, photo-absorption (indicated by the white arrow in this figure) triggers the dissociation of DEZn [11]. By contrast, when a nonresonant optical near field is used, there are three possible origins of photodissociation, as we have already proposed [10]. They are (1) the multiple photon absorption process, (2) a multiple step transition process via the intermediate energy level induced by the fiber probe, and (3) the multiple step transition via an excited state of the molecular vibration mode. Possibility (1) is negligible, because the optical power density in the experiment was less than 10 kW/cm^2 , which is too low for multiple photon absorption. Possibility (2) is also negligible, because NFO-CVD was observed for the light in the ultra-violet ~ near-infra red region, although DEZn lacks relevant energy levels for such a broad region. As a result, our experimental results strongly supported possibility (3), i.e., that the physical origin of the photodissociation caused by a nonresonant optical near field is a transition to an excited state via a molecular vibration mode. The three multiple-step excitation processes in Fig. 7, labeled by ①, ②, and ③, contributed to this. Since we consider here the system strongly coupling to the vibration state, the system must be treated as a nonadiabatic system.

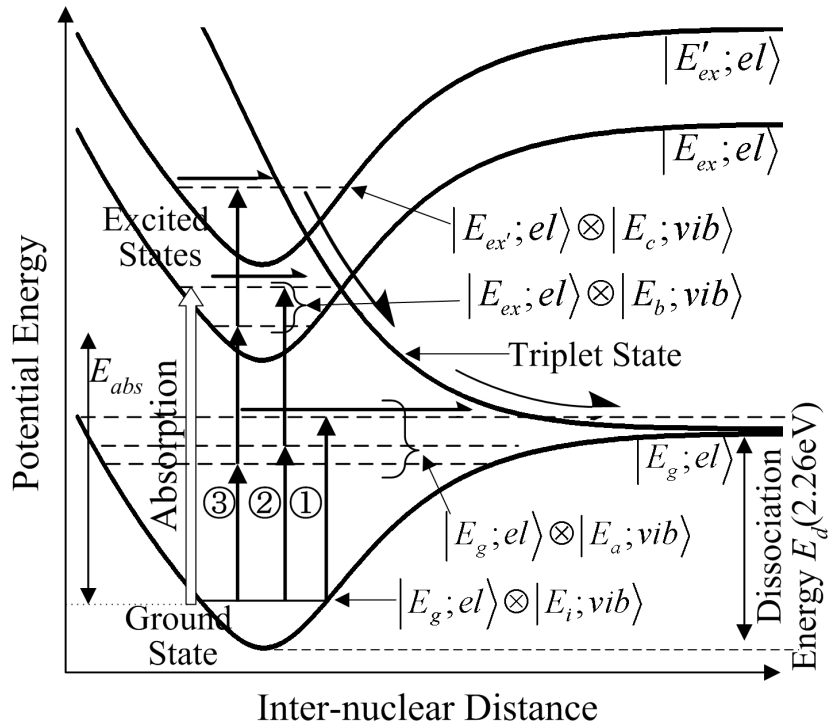


Fig.7. Potential curves of an electron in DEZn molecular orbitals. The relevant energy levels of the molecular vibration modes are indicated by the horizontal broken lines.

To evaluate these contributions, we propose an exciton-phonon polariton model. In the exciton-phonon polariton model, the ONF excite the molecular vibration mode due to the steep spatial gradient of the ONF. Figure 8 illustrates schematics the excitation of the molecular vibration mode by ONF and exciton-phonon polariton schematically. For

an optical far field, the field intensity is uniform in a neutral molecule smaller than the wavelength. Only the electrons in the molecule respond to the electric field with the same phase and intensity. Therefore, an optical far field cannot excite the molecular vibration. By contrast, the field intensity is not uniform in a molecule for an ONF with a steep spatial gradient. The electrons respond non-uniformly, and the molecular vibration modes are excited because the molecular orbital changes and the molecule is polarized as a result of this non-uniform response of the electrons, as shown in Fig. 8(a). We propose the exciton-phonon polariton model to quantify this excitation process. The exciton-phonon polariton is a quasi-particle, which is an exciton polariton trailing the phonon (lattice vibration) generated by the steep spatial gradient of its optical field, as shown in Fig. 8(b). The exciton-phonon polariton model is formulated below.

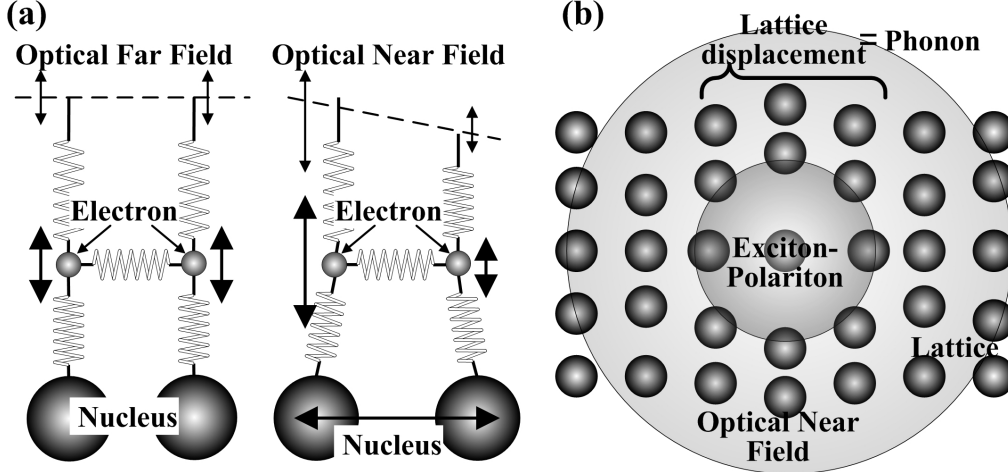


Fig.8. Schematic explanations of the excitation of molecular vibration mode by the optical near field (a) and the exciton phonon polariton (b).

The optical near field generated on the nanometric probe tip [18] is described in terms of the following model Hamiltonian:

$$\begin{aligned}
 H &= \sum_p \hbar \left[\omega_p a_p^\dagger a_p + \omega_p^{\text{ex}} b_p^\dagger b_p + \frac{i\Omega_c}{2} (a_p^\dagger b_p - a_p b_p^\dagger) \right] \\
 &\quad + \sum_p \hbar \Omega_p c_p^\dagger c_p + \sum_{p,q} \{ i\hbar M(p-q) b_p^\dagger b_q [c_{p-q} + c_{q-p}^\dagger] + h.c. \} \\
 &= \sum_p \hbar \omega_p^{\text{pol}} B_p^\dagger B_p + \sum_p \hbar \Omega_p c_p^\dagger c_p + \sum_{p,q} \{ i\hbar M'(p-q) B_p^\dagger B_q [c_{p-q} + c_{q-p}^\dagger] + h.c. \},
 \end{aligned}$$

where the creation (annihilation) operators for a photon, an exciton, a renormalized phonon, and an exciton polariton are denoted as a_p^\dagger (a_p), b_p^\dagger (b_p), c_p^\dagger (c_p), and B_p^\dagger (B_p), respectively, and their respective frequencies are ω_p , ω_p^{ex} , Ω_p , and ω_p^{pol} . The photon-exciton coupling, exciton-phonon coupling, and exciton polariton-phonon coupling are designated Ω_c , $M(p-q)$, and $M'(p-q)$, respectively. The first line of this description expresses the Hamiltonian for a photon-exciton interacting system and is transformed into the exciton-polariton representation in the third line, while the second line represents the Hamiltonian for a phonon-exciton interacting system. Note that the mode coupling and the anharmonic coupling of phonons are considered a renormalized phonon; therefore, multiple phonons can interact with an exciton or an exciton polariton simultaneously.

If the mean field approximation of exciton polaritons near the probe tip is

$$\langle B_{k_0}^\dagger \rangle = \langle B_{k_0} \rangle = \sqrt{I_0(\omega_0)} V,$$

using the unitary transformation

$$\begin{pmatrix} B_p \\ c_{p-k_0} \end{pmatrix} = \begin{pmatrix} iv'_p & u'_p \\ u'_p & iv'_p \end{pmatrix} \begin{pmatrix} \xi_{(-)p} \\ \xi_{(+)p} \end{pmatrix},$$

we can diagonalize the Hamiltonian in the quasi-particle (the exciton-phonon polariton) representation as [19]

$$\begin{aligned}
H &= \sum_p \hbar \omega_p^{\text{pol}} B_p^\dagger B_p + \sum_p \hbar \Omega_p c_p^\dagger c_p + \sum_p \left\{ i \hbar \sqrt{I_0(\omega_0)} V M'(p-k_0) (B_p^\dagger c_{p-k_0} + B_p c_{p-k_0}^\dagger) \right\} \\
&= \sum_p \hbar \omega(p) \xi_p^\dagger \xi_p.
\end{aligned}$$

Here, $I_0(\omega_0)$ is the intensity of an incident photon with frequency ω_0 and momentum $\hbar k_0$, and V represents the volume to be considered. The transformation elements u'_p and v'_p are given by

$$u'_p = \frac{1}{\sqrt{2}} \left[1 + \frac{\Delta}{\sqrt{\Delta^2 + (2Q)^2}} \right]^{\frac{1}{2}}, \quad v'_p = \frac{1}{\sqrt{2}} \left[1 - \frac{\Delta}{\sqrt{\Delta^2 + (2Q)^2}} \right]^{\frac{1}{2}},$$

where the detuning between an exciton polariton and a phonon is denoted as $\Delta = \omega_p^{\text{pol}} - \Omega_{p-k_0}$, and the effective coupling constant is expressed as $Q = \sqrt{I_0(\omega_0)} V M'(p-k_0)$. Therefore, in this model, a molecule located near the probe tip does not absorb simple photons but absorbs exciton-phonon polaritons whose energies are transferred to the molecule, which excites molecular vibrations or induces electronic transitions.

We will now discuss the dissociation probability of a molecule, assuming that the deposition rate of the metal atoms is proportional to the molecular dissociation rate. Since the experimental intensity dependence of the deposition rate shown in Fig. 6 is up to the third order, we consider the following initial and three final states of a system consisting of the optical near-field probe and a molecule:

$$\begin{aligned}
|i\rangle &= |\text{probe}\rangle \otimes |E_g; \text{el}\rangle \otimes |E_i; \text{vib}\rangle, \\
|f_{\text{first}}\rangle &= |\text{probe}\rangle \otimes |E_g; \text{el}\rangle \otimes |E_a; \text{vib}\rangle, \\
|f_{\text{second}}\rangle &= |\text{probe}\rangle \otimes |E_{ex}; \text{el}\rangle \otimes |E_b; \text{vib}\rangle, \\
|f_{\text{third}}\rangle &= |\text{probe}\rangle \otimes |E_{ex'}; \text{el}\rangle \otimes |E_c; \text{vib}\rangle,
\end{aligned}$$

where $|\text{probe}\rangle$, $|E_\alpha; \text{el}\rangle$, and $|E_\beta; \text{vib}\rangle$ represent the probe state, molecular electronic states with energy E_α ($\alpha = g, ex, ex'$), and molecular vibrational states with energy E_β ($\beta = i, a, b, c$), respectively, as shown in Fig. 7. The transitions from the initial to the final states can be formulated using the conventional perturbation method for the interaction Hamiltonian expressed in terms of exciton-phonon polaritons as

$$H_{\text{int}} = - \left\{ \mu^{\text{el}} (e + e^\dagger) + \mu^{\text{nucl}} (v + v^\dagger) \right\} \sum_p i \sqrt{\frac{2\pi \hbar \omega_p}{V}} \left\{ -v_p v'_p (\xi_p - \xi_p^\dagger) \right\} e^{ipr}.$$

Here, μ^{el} and μ^{nucl} are the electronic and vibrational dipole moments, respectively, and the creation (annihilation) operators of the electronic and vibrational excitations are denoted as e^\dagger (e) and v^\dagger (v), respectively. The incident photon frequency and transformation coefficients are ω_p and v_p (v'_p), respectively. Then transition probability of one-, two-, and three-step excitation (labeled ①, ②, and ③ in Fig. 7, and denoted the corresponding final states as $|f_{\text{first}}\rangle$, $|f_{\text{second}}\rangle$, and $|f_{\text{third}}\rangle$) can be written as follows:

$$\begin{aligned}
P_{\text{first}}(\omega_p) &= \frac{2\pi}{\hbar} |\langle f_{\text{first}} | H_{\text{int}} | i \rangle|^2 = \frac{(2\pi)^2}{\hbar} v_p^2 v_p'^2 u_p'^2 (\mu^{\text{nucl}})^2 (\hbar \omega_p) I_0(\omega_p), \\
P_{\text{second}}(\omega_p) &= \frac{2\pi}{\hbar} |\langle f_{\text{second}} | H_{\text{int}} | i \rangle|^2 = \frac{(2\pi)^3}{\hbar} \frac{v_p^4 v_p'^6 u_p'^2}{|\hbar \omega(p) - (E_a - E_i + i\gamma_m)|^2} (\mu^{\text{el}})^2 (\mu^{\text{nucl}})^2 (\hbar \omega_p)^2 I_0^2(\omega_p), \\
P_{\text{third}}(\omega_p) &= \frac{2\pi}{\hbar} |\langle f_{\text{third}} | H_{\text{int}} | i \rangle|^2 \\
&= \frac{(2\pi)^4}{\hbar} \frac{v_p^6 v_p'^{10} u_p'^2}{|\hbar \omega(p) - (E_a - E_i + i\gamma_m)|^2 |\hbar \omega(p) - (E_{ex} - E_g + i\gamma_m)|^2} (\mu^{\text{el}})^4 (\mu^{\text{nucl}})^2 (\hbar \omega_p)^3 I_0^3(\omega_p),
\end{aligned}$$

where u'_p and $I_0(\omega_p)$ represent the transformation coefficient and the incident light intensity, respectively. In addition, E_α ($\alpha = g, ex, ex'$) and E_β ($\beta = i, a, b, c$) represent the molecular electronic and vibrational energies,

respectively, as shown in Fig. 7, and γ_m is the linewidth of the vibrational states. It follows that these near-resonant transition probabilities have the following ratio

$$\frac{P_{\text{second}}(\omega_p)/I_0^2(\omega_p)}{P_{\text{first}}(\omega_p)/I_0(\omega_p)} = \frac{P_{\text{third}}(\omega_p)/I_0^3(\omega_p)}{P_{\text{second}}(\omega_p)/I_0^2(\omega_p)} = \frac{\hbar}{2\pi} \frac{P_{\text{first}}(\omega_p)}{\gamma_m^2 I_0(\omega_p)} \left(\frac{v_p'^2}{u_p'^2} \right) \left(\frac{\mu^{\text{el}}}{\mu^{\text{nucl}}} \right)^2.$$

Using this ratio, we analyze the experimental intensity dependence of the deposition rate to clarify possibility (3). For $\hbar\omega = 2.54$ eV, all the processes (①, ②, and ③) depicted in Fig. 7 are possible, because $\hbar\omega > E_d$ (even though $\hbar\omega < E_{\text{abs}}$). Fitting the experimental value of $P_{\text{first}}(\omega_{2.54}) = a_{2.54} I_0(\omega_{2.54}) = 10^2$ events/s with reasonable values of $\mu^{\text{nucl}} = 1$ Debye, $\mu^{\text{el}} = 10^{-3}$ Debye, $\gamma_m = 10^{-1}$ eV, and $v_p'^2/u_p'^2 = 0.02$, we obtain the following value for the ratio

$$\frac{P_{\text{second}}(\omega_{2.54})/I_0^2(\omega_{2.54})}{P_{\text{first}}(\omega_{2.54})/I_0(\omega_{2.54})} = \frac{P_{\text{third}}(\omega_{2.54})/I_0^3(\omega_{2.54})}{P_{\text{second}}(\omega_{2.54})/I_0^2(\omega_{2.54})} = \frac{\hbar}{2\pi} \frac{P_{\text{first}}(\omega_{2.54})}{\gamma_m^2 I_0(\omega_{2.54})} \left(\frac{v_p'^2}{u_p'^2} \right) \left(\frac{\mu^{\text{el}}}{\mu^{\text{nucl}}} \right)^2 \simeq 10^{-15},$$

which is in good agreement with the experimental values $b_{2.54}/a_{2.54} \simeq c_{2.54}/b_{2.54} \simeq 10^{-15}$ (see Fig.6). For $\hbar\omega = 1.81$ eV, dissociation occurs via either ② or ③ shown in Fig. 7, because $\hbar\omega < E_d$ (E_{abs}). The ratio can be evaluated as

$$\frac{P_{\text{third}}(\omega_{1.81})/I_0^3(\omega_{1.81})}{P_{\text{second}}(\omega_{1.81})/I_0^2(\omega_{1.81})} = \frac{\hbar}{2\pi} \frac{P_{\text{first}}(\omega_{1.81})}{\gamma_m^2 I_0(\omega_{1.81})} \left(\frac{v_p'^2}{u_p'^2} \right) \left(\frac{\mu^{\text{el}}}{\mu^{\text{nucl}}} \right)^2 \simeq 10^{-15},$$

which is also in good agreement with the experimental value $c_{1.81}/b_{1.81} \simeq 10^{-15}$. For the theoretical estimation, we use the experimental value for $P_{\text{first}}(\omega_{1.81}) \simeq a_{2.54} I_0(\omega_{2.54}) = 10^2$ events/s because both transitions for light with the photon energies of 1.84 and 2.54 eV are attributed to the coupling between phonons in the probe and molecular vibrations. The overall agreement between the theory and experimental results suggests that the exciton-phonon polariton model provides a way to understand the physical origin of the near-field photodissociation process. For $\hbar\omega = 3.81$ eV, the direct absorption by the electronic state is much stronger than in other cases, because the light is near resonant for DEZn. This is why we did not observe higher-order power dependence of the deposition rate in the optical power region that we observed.

4. APPLICATIONS OF NONADIABATIC PHOTOCHEMICAL PROCESS

According to our model, the nonadiabatic photochemical reaction is a universal phenomenon and is applicable to many other photochemical processes. In this section we show the deposition of nanometric Zn dots by NFO-CVD using the metal-organic gas zinc-bis(acetylacetonate) ($\text{Zn}(\text{acac})_2$), which is not usually used for conventional optical CVD due to its low optical activity, and demonstrated the patterning by near-field photolithography using a 672-nm laser.

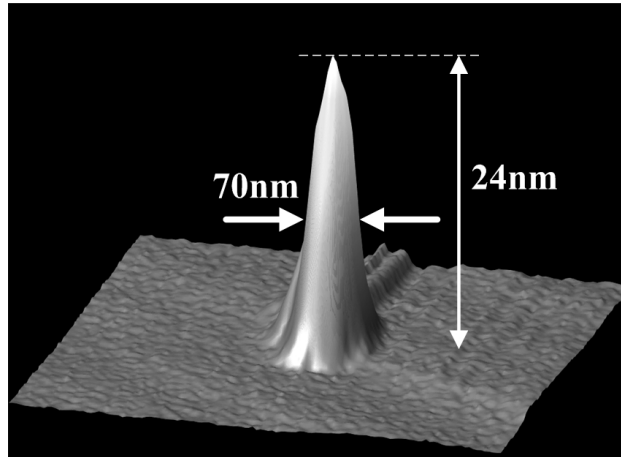


Fig.9. Shear-force topographical images after NFO-CVD using $\text{Zn}(\text{acac})_2$ at wavelengths of $\lambda = 457\text{nm}$. The scanning area are 750×750 nm. The observed laser output power and the irradiation time for deposition were 1 mW and 15 s.

Figure 9 shows the shear-force topographical image of the sapphire substrate after NFO-CVD using optical near fields of $\lambda=457$ nm (Ar^+ laser). In the experiment, $\text{Zn}(\text{acac})_2$ was used as the gas source of reactant molecules. During deposition, the partial pressure of $\text{Zn}(\text{acac})_2$ was maintained at 70 mTorr. The laser power and the irradiation time were 1 mW and 15 s, respectively. The diameter and height of the Zn dot were 70 nm and 24 nm, respectively. $\text{Zn}(\text{acac})_2$ is not usually used for conventional optical CVD due to its low optical activity. However, in case of NFO-CVD, the optical near field can activate the molecule. In NFO-CVD, its deposition rate was almost the same as that of deposition in which DEZn gas was used, although for the conventional optical CVD, we carried out that DEZn has a deposition rate of more than 1000 times higher than that of $\text{Zn}(\text{acac})_2$. We consider that the physical origin of the photodissociation of $\text{Zn}(\text{acac})_2$ is also the nonadiabatic photochemical process by ONF.

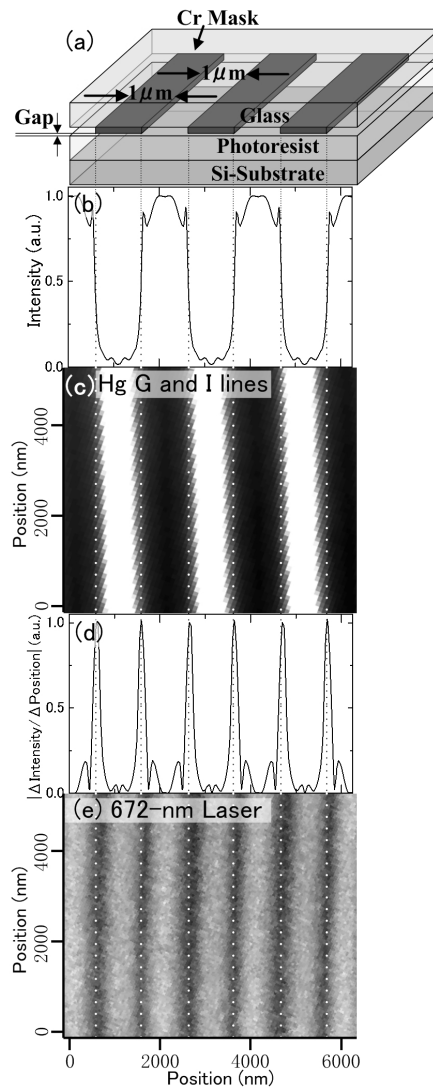


Fig.10. (a) The schematic configuration of the used photo-mask and the Si-substrate spin-coated with the photoresist (OFPR-800) at the exposure process. (b) The cross-sectional distribution of the optical energy at the contact plane between the photo-mask and the photoresist calculated by FDTD. (c) AFM images of photoresist by g and i lines of Hg lamp after development. (d) The spatial gradient of the cross-sectional distribution of the optical energy (Fig.1(b)). (e) AFM images of photoresist by 672-nm laser after development.

Figure 10(a) shows the schematic configuration of the used photo-mask and the Si-substrate spin-coated with the photoresist (OFPR-800) at the exposure process in contact mode. We adjusted the gap between the photo-mask and photoresist to become as narrow as possible. Figures 10(c) and (e) show the atomic force microscope images of the photoresist surface after development by g and i lines of Hg lamp and 672-nm laser, respectively. Figures 10(b) and (d) show the cross-sectional distribution of the optical energy and its spatial gradient at the contact plane between the photo-mask and the photoresist calculated by the finite difference time domain (FDTD) Method. By g and i lines, the conventional exposure process forms the corrugation whose size corresponds to the optical intensity distribution generated by the photo-mask pattern, i.e., lines and spaces $1\mu\text{m}$ (Figs. 10(b) and (c)), because the used photoresist is active to the g and i lines. The 672-nm laser also developed the corrugation pattern on the photoresist though this photoresist must be inactive to the 672-nm light. The width and depth of the groove in the corrugation pattern were 200nm and 25nm, respectively. The period (lines and spaces) of the corrugation by the 672-nm laser is different from that by g and i lines and is a half that. This result can be explained by our proposed nonadiabatic photochemical process. The exposure process cannot occur by direct irradiation of 672-nm light. However, the optical near field causes the exposure process due to the nonadiabatic photochemical reaction. This unique photochemical reaction is induced by the steep spatial gradient of the optical energy. Since the optical near field is strongly generated at around the edges of the Cr-mask, the spatial gradient of the optical energy is large at the edges as shown in Fig. 10(d). Such spatial gradient of the optical energy increases in the coupling between photons and molecules of photoresist. Thus our proposed photochemical process, which was mentioned in Sec.3. must be applied. The developed pattern by the 672-nm laser agrees well with the distribution of the gradient (Figs. 10(d) and (e)). This agreement confirms the nonadiabatic photochemical process occurs due to the steep spatial gradient of the optical energy. This novel process for photolithography is one of the promising techniques for nanofabrication, because it does not require the expensive vacuum UV light source and optics for the nano-photolithography.

5. CONCLUSION

In conclusion, we demonstrated NFO-CVD of nanometric Zn dots based on the photodissociation of gas-phase diethylzinc using an optical near field under nonresonant conditions. To clarify the physical origin of this process, the optical power and photon energy dependencies of the deposition rates were measured. We explain the dependencies using multiple-step excitation process via the molecular vibration mode and the exciton-phonon polariton model. In this model, the enhanced coupling between the optical field and molecular vibration originates from the steep spatial gradient of the optical power of the optical near field. Such a nonadiabatic photochemical process violates the Franck-Condon principle, and it can be applied to other photochemical phenomena. The process involved in the photochemical reaction based on an optical near field reported here will open new method in nanotechnology. As applicable examples of this nonadiabatic photochemical reaction, we demonstrated the deposition of nanometric Zn dots by NFO-CVD using the metal-organic gas zinc-bis(acetylacetonate) ($\text{Zn}(\text{acac})_2$), which is not usually used for conventional optical CVD due to its low optical activity, and the patterning by the near-field photolithography using a 672-nm laser. The experimental results of the near-field photolithography also strongly support the nonadiabatic photochemical process and the exciton-phonon polariton model.

ACKNOWLEDGMENTS

We thank Drs. K. Kobayashi, and S. Sangu at Japan Science and Technology Agency for their useful discussions. We also thank Mr. S. Takubo at Tokyo Institute of Technology for his experimental supports.

REFERENCES

1. D. Leonard, M. Krishnamurthy, C. M. Reaves, S. P. Denbaars, and P. M. Petroff, "Direct formation of quantum-sized dots from uniform coherent islands of InGaAs on GaAs surfaces," *Appl. Phys. Lett.*, **63**, 3203, 1993.
2. T. Tsutsui, K. Kawasaki, M. Mochizuki, and T. Matsubara, "Site controlled metal and semiconductor quantum dots on epitaxial fluoride films," *Microelectron. Eng.*, **47**, 135, 1999.
3. S. Kohmoto, H. Nakamura, T. Ishikawa, and K. Asakawa, "Site-controlled self-organization of individual InAs quantum dots by scanning tunneling probe-assisted nanolithography," *Appl. Phys. Lett.*, **75**, 3488, 1999.

4. E. Kuramochi, J. Temmyo, T. Tamamura, and H. Kamada, "Perfect spatial ordering of self-organized InGaAs/AlGaAs box-like structure array on GaAs (311)B substrate with silicon nitride dot array," *Appl. Phys. Lett.*, **71**, 1655, 1997.
5. R. Wiesendanger, "Fabrication of nanometer structures using STM," *Appl. Surf. Sci.*, **54**, 271, 1992.
6. V. V. Polonski, Y. Yamamoto, M. Kourogi, H. Fukuda, and M. Ohtsu, "Nanometric patterning of zinc by optical near-field photochemical vapor deposition," *J. Microsc.*, **194**, 545, 1999.
7. V. V. Polonski, Y. Yamamoto, J. D. White, M. Kourogi, and M. Ohtsu, "Vacuum Shear-force microscopy application to high resolution work," *Jpn. J. Appl. Phys.*, pt. 2, **38**, L826, 1999.
8. Y. Yamamoto, M. Kourogi, M. Ohtsu, V. Polonski, and G. H. Lee, "Fabrication of nanometric Zinc pattern with photodissociated gas-phase diethylzinc by optical near-field," *Appl. Phys. Lett.*, **76**, 2173, 2000.
9. G. H. Lee, Y. Yamamoto, M. Kourogi, and M. Ohtsu, "Fabrication of ZnO nanostructure using near-field optical technique," *Proc. SPIE-Int. Soc. Opt. Eng.*, **3791**, 132, 1999.
10. T. Kawazoe, Y. Yamamoto, and M. Ohtsu, "Fabrication of a nanometric Zn dot by nonresonant near-field optical chemical vapor deposition," *Appl. Phys. Lett.*, **79**, 1184, 2001.
11. J. G. Calvert and J. N. Patts Jr., *Photochemistry*, 1996, Wiley, New York.
12. R. L. Jacson, "Vibrational energy of the monoalkyl zinc product formed in the photodissociation of dimethyl zinc, diethyl zinc, and dipropyl zinc," *J. Chem. Phys.*, **96**, 5938, 1992.
13. M. Ohtsu, *Near-Field Nano/Atom Optics and Technology*, 1998, Springer, Tokyo, Berlin, Heidelberg, New York.
14. M. Ohtsu, K. Kobayashi, H. Ito, and G. Lee, "Nanofabrication and atom manipulation by optical near-field and relevant quantum optical theory," *Proc. IEEE*, **88**, 1499, 2000.
15. M. Yoshimoto, T. Maeda, T. Ohnishi, H. Koinuma, O. Ishiyama, M. Shinohara, M. Kubo, R. Miura, and A. Miyamoto, "Atomic-scale formation of ultrasmooth surfaces on sapphire substrates for high-quality thin film fabrication," *Appl. Phys. Lett.*, **67**, 2615, 1995.
16. M. Shimizu, H. Kamei, M. Tanizawa, T. Shiosaki, and A. Kawabata, "Low temperature growth of ZnO film by photo-MOCVD," *J. Cryst. Growth*, **89**, 365, 1988.
17. T. Yatsui, T. Shimizu, Y. Yamamoto, M. Kourogi, G. H. Lee, and M. Ohtsu, "Near-field ultraviolet photoluminescence spectroscopy for evaluating the crystallinity of polycrystalline zinc oxide," *Appl. Phys. Lett.*, **79**, 2369, 2001.
18. K. Kobayashi, S. Sangu, H. Ito, and M. Ohtsu, "Near-field potential for a neutral atom," *Phys. Rev. A*, **63**, pp. 0138061-1-9, 2001.
19. J. J. Hopfield, "Theory of the Contribution of Excitons to the Complex Dielectric Constant of Crystals", *Phys. Rev.* **112**, 1555, 1958.

Nanophotonics: Devices, fabrications, and systems

M. Ohtsu*

*Interdisciplinary Graduate School of Science and Technology,
Tokyo Institute of Technology*

The word “nanophotonics” was proposed by Ohtsu in 1994. Nanophotonics is not to realize nanometer-sized optical science and technology but to realize “novel functions and phenomena originated from the localized nature of optical near fields”¹⁾. These novel functions and phenomena are possible by noting that the nanometric system is buried in a macroscopic heat bath. Energy non-conservation can be observed in the nanometric system due to energy exchange between the two systems. Further, higher order effects, e.g., magnetic dipole or electric quadrupole transitions are not neglected due to localized nature of optical near fields. True nature of nanophotonics is to utilize these “novel functions and phenomena originated from the localized nature of optical near fields”, which is impossible by propagating lights.

Based on the consideration mentioned above, nanophotonics is defined as “the technology for fabricating and operating nanophotonic devices by using the optical near field as signal carrier and small numbers of nanoparticles as device materials”. The essential features of these devices are their novel functions and phenomena. In addition, their sizes are far smaller than the diffraction limit of light.

Recent progress of our research is reviewed. They are; (1) nanophotonic devices (optical switches²⁾, etc.) and optical input/output terminals, (2) nanophotonic fabrication (size-and position-controlled photochemical vapor deposition and non-adiabatic process, etc.), and (3) future prospect to realize nanophotonic systems (optical fiber communications, optical memory, photon computing, etc.).

1) M. Ohtsu et al., IEEE J. Selected Topics in Quantum Electron., **8**, 839-862 (2002).

2) T. Kawazoe, et al., Appl. Phys. Lett., **82**, 2957-2959 (2003).

M8.26

Fabrication of 20-nm Zn nanocrystallites by the selective photodissociation of adsorption-phase diethylzinc using a near-field optical chemical vapor deposition

J. Lim,^{a)} T. Yatsui,^{b)} and M. Ohtsu^{a), b)}

^{a)} Interdisciplinary Graduate School of Science and Engineering, Tokyo Institute of Technology, Kanagawa, Japan.

^{b)} Ohtsu Localized Photon Project, ERATO, Japan Science and Technology Corporation, Tokyo, Japan.

Future optical transmission system require ultrahigh integration of photonic devices. To meet this requirement, we have proposed nanophotonic integrated circuits that consist of nanometer-scale dots. To fabricate this, nanometer-scale dots must be deposited on a substrate with nanometer-scale controllability in size and position. To achieve this level of controllability, we demonstrated the feasibility of nanometer-scale chemical vapor deposition (CVD) using optical near-field techniques. However, conventional photo-CVD uses a light source that resonates the absorption band of metalorganic (MO) vapor and has a photon energy that exceeds the dissociation energy. Thus, it utilizes a two-step process; gas-phase photodissociation and subsequent adsorption. However, we found that the dissociated MO molecules migrate on the substrate before adsorption, which limits the minimum lateral size of deposited dots. To overcome this difficulty, we demonstrate here a deposition of Zn dots using the selective photodissociation of adsorption-phase diethylzinc (DEZn) with a nonresonant optical near field, where the photon energy is lower than that of the absorption band edge of gas-phase DEZn and higher than that of the absorption edge of adsorption-phase DEZn.

Since the absorption band edge energy (E) of the gas-phase DEZn was 4.6 eV, we used He-Cd laser light ($E = 3.81$ eV) as the light source; it is nonresonant to gas-phase DEZn. Using a sharpened UV fiber probe, we achieved selective dissociation of adsorbed DEZn, as a results, we successfully fabricated 20-nm Zn dots with 75-nm separation on (0001) sapphire substrate. Furthermore, since the nonresonant propagating light that leaked from the probe did not dissociate the gas-phase DEZn, the atomic-level sapphire steps around the deposited dots were clearly observed after the deposition. Since high-quality ZnO nanocrystallites can be obtained by oxidizing Zn nuclei, this technique could be used to produce high-quality ZnO nanocrystallites, which is promising material for nanophotonic devices.

T3.16

Observation of an optical near-field energy transfer between closely spaced ZnO/ZnMgO multiple-quantum-well nanorods for nanophotonic devices.

T. Yatsui,^{a)} J. Lim,^{b)} T. Kawazoe,^{a)} K. Kobayashi,^{a)} M. Ohtsu,^{a), b)} W. I. Park,^{c)} and G.-C. Yi^{c)}

^(a) Ohtsu Localized Photon Project, ERATO, Japan Science and Technology Corporation, Tokyo, Japan.

^(b) Interdisciplinary Graduate School of Science and Engineering, Tokyo Institute of Technology, Kanagawa, Japan.

^(c) Department of Materials Science and Engineering, POSTECH, Kyungbuk, KOREA

For future optical transmission systems, we have proposed nanometer-scale photonic devices. These devices consist of nanometer-scale dots, and an optical near-field is used as the signal carrier. ZnO nanocrystallites is a promising material for realizing these devices at room-temperature, due to its large exciton binding energy. To confirm the promising optical properties of ZnO nanocrystallites, we measured the photoluminescence (PL) spectra using an optical near-field microscope. In this measurement, we found anti-correlation features in PL spectra between closely spaced ZnO/ZnMgO multiple-quantum-well (MQW) nanorods, which we attributed to optical near-field energy transfer from one nanorod to the other.

We used the MQW nanorods which consist of ten periods of 3-nm ZnO/6-nm ZnMgO as samples. These were grown on the ends of ZnO nanorods with a 40-nm mean diameter. In the near-field PL spectra at 15 K, several sharp peaks were observed. The number of the sharp peaks and their energy values (E_1 : 3.420 eV, E_2 : 3.426 eV, E_3 : 3.436 eV) in each spectrum showed strong position dependence. To investigate their origins, we measured spatial distribution of PL intensity for individual ZnO/ZnMgO MQW nanorods with a spatial resolution of 50 nm. The outstanding feature was the anti-correlation in the PL intensity of E_1 (I_1) and I_2 ; I_1 was suppressed while I_2 was enhanced in one nanorod, and I_1 was enhanced while I_2 were suppressed in a closely adjacent nanorod. Furthermore, since the degree of the anti-correlation was larger for more closely spaced pair of nanorods, such an anti-correlation feature is due to energy transfer phenomena induced by optical near field between two resonant energy levels in a ZnO/ZnMgO MQW and its adjacent ZnO/ZnMgO MQW. This phenomenon can be used to realize nanophotonic devices, such as the switching mechanism confirmed by the authors in CuCl quantum cubes.

Nanophotonics; for size- and position- controlled nanofabrication by optical near fields

Takashi Yatsui^{1,#} and Motoichi Ohtsu^{1,2}

¹ Ohtsu Localized Photon Project, ERATO, Japan Science and Technology Corporation, Japan

² Interdisciplinary Graduate School of Science and Engineering, Tokyo Institute of Technology, Japan

ABSTRACT

This paper reviews the recent progress of application of interactions between optical near-fields and nanoscale material. Ultrahigh integration of photonic matrix switching devices is necessary to increase data transmission rates and capacity of future optical transmission system. To support this increase, we proposed and demonstrated the feasibility of nanometer-scale optical chemical vapor deposition using optical near-field techniques, which enables the fabrication of nanometer-scale structures. By the use of an UV optical near field we demonstrated the fabrication of various materials, including metals (Al and Zn) and semiconductors (ZnO and GaN) with nanometer-scale shapes. Novel near-field effect of the optical chemical vapor deposition was also demonstrated using a nonresonant light, i.e., using visible light. Furthermore, we report that optical near-field desorption can dramatically regulate the growth of Zn nanoparticles during optical chemical vapor deposition. The trade off between the deposition and desorption allowed the fabrication of a single 15 nm Zn dot, while regulating its size and position. The possibilities of applying such a near-field desorption to other deposition technique without the fiber probe were also demonstrated, which enables mass-production of nanometric structures.

Topic Category: Nanophotonics, Optical near field, Nanofabrication.

Optical transmission systems require increased integration of photonic switching devices. To support this increase, it is estimated that the size of photonic matrix switching devices should be reduced to less than 100 nm by the year 2015. To realize this, we have proposed nanometer-scale photonic devices and their integration (i.e., integrated nanophotonic devices, see Fig. 1).¹ These devices consist of nanometer-scale dots, and an optical near field is used as the signal carrier (see Fig. 2). As a representative device, a nanophotonic switch can be realized by controlling the dipole forbidden optical energy transfer among resonant energy states in nanometer-scale quantum dots via an optical near field.² It is composed of sub-100-nm scale dots and wires, and their size and position must be controlled on a nanometer

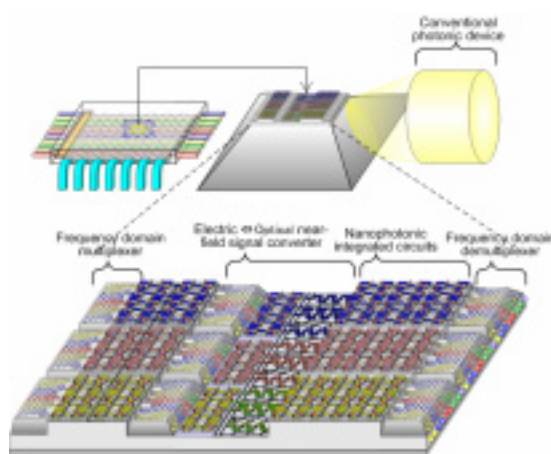


Fig. 1 Integrated nanophotonic devices

scale to fabricate the device.

In order to realize this level of controllability, we proposed and demonstrated near-field optical chemical vapor deposition (NFO-CVD, see Fig. 3), which enables

Corresponding Author :

Email : yatsui@ohtsu.jst.go.jp

Tel. +81-42-788-6030; Fax +81-42-788-6031

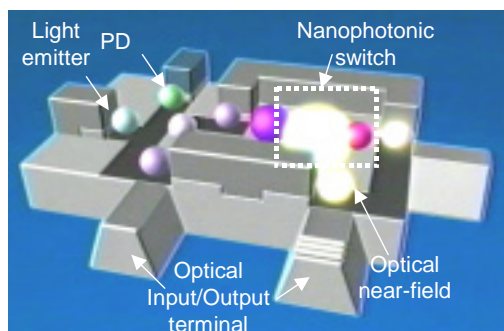


Fig. 2 Single cell of integrated nanophotonic devices.

the fabrication of nanometer-scale structures, while precisely controlling their size and position.³⁻⁵ In this process, resonant photons excite metal-organic (MO) molecules from the ground state to the excited electronic state and the excited molecules relax to the dissociation channel, and then the dissociated metal atoms adsorb to the substrate.⁶ Due to the photochemical reaction between the reactant molecules and the optical near field generated at the tip of an optical fiber probe, NFO-CVD is applicable to various materials, including metals,

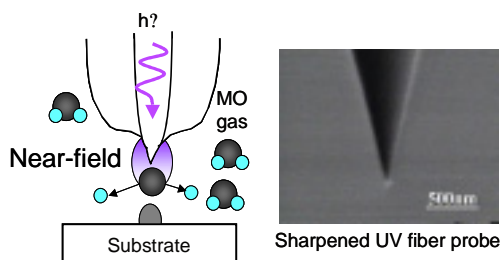


Fig. 3 Schematics of NFO-CVD.

semiconductors, and insulators with various shapes [see Figs. 4(a), (b), and (c)]. By changing the reactant molecules during deposition, nanometric Zn and Al dots were successively deposited on a sapphire substrate with high precision (see Fig. 4(d)).⁷

For photodissociation, the far-field light must resonate the reacting molecular gasses in order to excite molecules from the ground state to excited electronic state. The *Frank-Condon* principle claims that this resonance is essential for excitation. The conventional MO gas source for optical CVD has the excited electron state in the ultraviolet region. For NFO-CVD, however,

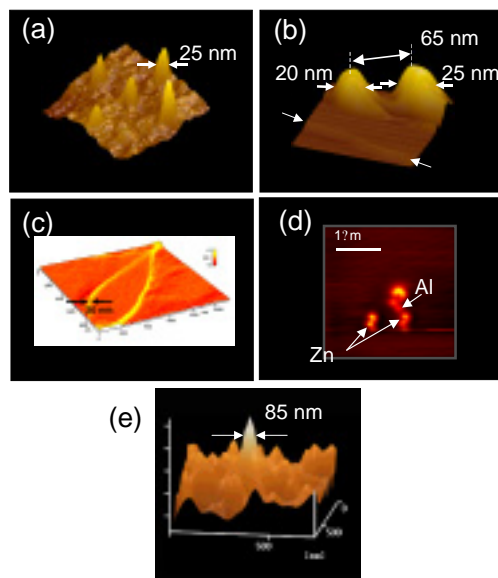


Fig. 4 Shear-force images of deposited Al dots (a), Zn dots (b), Zn looped shape (c), and Zn and Al dots (d). (e) Photoluminescence image of single deposited ZnO dot.

photodissociation can take place under nonresonant conditions, i.e., using visible light, due to the inherent properties of optical near-fields.⁸ Since the optical near field has a very large spatial gradient with a nanometric decay length, it can interact with the polarization of molecule. As a result of this interaction, atoms in the molecule can be translated directory.

In order to confirm that the deposited dots are Zn, we fabricated UV-emitting ZnO dots by oxidizing Zn immediately after deposition. Laser annealing was employed for this oxidation. The deposited Zn dot was irradiated with a pulse of ArF excimer-laser in a high-pressure oxygen environment. To evaluate the optical properties of the oxidized dot, the photoluminescence (PL) intensity distribution was measured using an illumination and collection mode (IC-mode) near-field optical microscope. Figure 4(e) shows the PL intensity distribution of the oxidized dot integrated for the wavelength region longer than 360 nm. The low collection efficiency due to the IC-mode configuration did not establish the spectrum. However, in the case of a ZnO thin film deposited using the same CVD process, except the optical near-field was replaced by the far-field light, we found that the PL intensity of the spontaneous

emission from the free exciton was ten times greater than that of the deep-level green emission. From this result, we concluded that the luminescence in this figure originated from spontaneous emission from the free exciton in ZnO nano-dot. This is the first observation of PL from a single deposited ZnO nanocrystallite.⁵

In order to realize further controllability in size, we studied dependence of nanoparticle formation on photon energy used for the NFO-CVD. As the light source for the photodissociation of diethylzinc (DEZn), a He-Cd laser [photon energy $E_p = 3.81$ eV] was used. This is a resonant light because its photon energy exceeds the band edge energy of DEZn. Figure 5(a) shows topographical image of Zn deposited on a (0001) sapphire substrate by NFO-CVD.

In order to control the size distribution, we introduced Ar^+ ($E_p = 2.54$ eV) or He-Ne ($E_p = 1.96$ eV) lasers, in addition to the He-Cd laser. Their photon energies are lower than the absorption band edge energy of DEZn, i.e., they are nonresonant light sources for the dissociation of DEZn. Figures 5(b) and 5(c) show topographical images of Zn deposited by NFO-CVD with irradiation at $E_p = 3.81$ and 2.54 eV and at $E_p = 3.81$

and 1.96 eV, respectively. The respective FWHMs were 60, 30, and 15 nm; i.e., a lower photon energy gave rise to smaller particles.

The dependency of fabricated size on the photon energy is due to plasmon resonance of optical absorption in a metal nanoparticle,⁸⁻¹¹ which strongly depends on particle size. This can induce the desorption of the deposited metal nanoparticles.¹² As the deposition of metal nanoparticles proceeds in the presence of light, the growth of the particles is affected by a trade off between deposition and desorption, which determines their size, and depends on the photon energy.

These results suggest that the additional light controls the size of the dots and reduces the size fluctuation, i.e., size regulation is realized. Furthermore, the position can be controlled accurately by controlling the position of the fiber probe used to generate the optical near field. The experimental results and the suggested mechanisms described above show the potential advantages of this technique in improving the regulation of size and position of deposited nanodots. Furthermore, since our deposition method is based on a photodissociation reaction, it could be widely used for nanofabrication of the other material for example GaN, GaAs, and so on.

In order to realize mass-production of nanometric structures, we will also discuss possibilities of applying such a near-field desorption to other deposition technique, which does not use fiber probe .

Acknowledgement

The authors thank Dr. H. Tamaru, University of Tokyo, for valuable discussions.

References

1. M. Ohtsu, K. Kobayashi, T. Kawazoe, S. Sangu, and T. Yatsui, "Nanophotonics: Design, Fabrication, and Operation of Nanometric Devices Using Optical Near Fields," IEEE J. Sel. Top. Quantum Electron. IEEE J. Selected Topics in Quantum Electron., Vol.8, No.4, pp.839-862, 2002.
2. T. Kawazoe, K. Kobayashi, S. Sangu, and M. Ohtsu, "Demonstration of a nanophotonic switching operation by optical near-field energy transfer,"

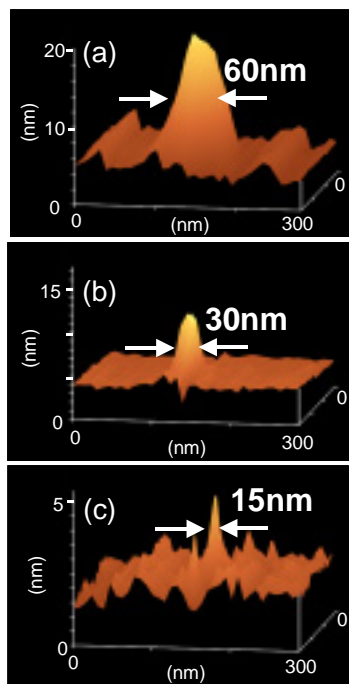


Fig. 4 Bird's-eye views of shear-force topographical images of Zn deposited by NFO-CVD with (a) $E_p = 3.81$ eV, (b) $E_p = 3.81$ and 2.54 eV, and (c) $E_p = 3.81$ and 1.96 eV, respectively.

- Appl. Phys. Lett., Vol.82, No.18, pp. 2957-2959, 2003.
3. V. V. Polonski, Y. Yamamoto, M. Kouroggi, H. Fukuda, and M Ohtsu, "Nanometric patterning of zinc by optical near-field photochemical vapour deposition," *J. Microscopy*, Vol.194, pt.2/3, pp. 545-551, 1999.
4. Y. Yamamoto, M. Kouroggi, M. Ohtsu, V. Polonski, and G. H. Lee, "Fabrication of nanometric zinc pattern with photodissociated gas-phase diethylzinc by optical near field," *Appl. Phys. Lett.*, Vol.76, No.16, pp. 2173-2175, 2000.
5. T. Yatsui, T. Kawazoe, M. Ueda, Y. Yamamoto, M. Kouroggi, and M. Ohtsu, "Fabrication of nanometric single zinc and zinc oxide dots by the selective photodissociation of adsorption-phase diethylzinc using a nonresonant optical field," *Appl. Phys. Lett.*, Vol.81, No.19, pp. 3651-3653, 2002.
6. R. L. Jackson, "Vibrational energy of monoalkylzinc product formed in the photodissociation of dimethyl zin, diethyl zinc, and dipropyl zinc," *J. Chem. Phys.*, Vol. 96, pp. 5938-5951, 1992.
7. Y. Yamamoto, M. Kouroggi, M. Ohtsu, and T. Kawazoe, "Lateral Integration of Zn and Al Dots with Nanometer-Scale Precision by Near Field Optical Chemical Vapor Deposition Using a Sharpened Optical Fiber Probe," *IEICE Trans. Electron.*, Vol.E85-C, No.12, pp. 2081-2085, 2002.
8. T. Kawazoe, Y. Yamamoto, and M. Ohtsu, "Fabrication of nanometric Zn dots by nonresonant near-field optical chemical-vapor deposition," *Appl. Phys. Lett.*, Vol.79, No.8, pp. 1184-1186, 2001.
9. G. T. Boyd, Th. Rasing, J. R. R. Leite, and Y. R. Shen, "Local-field enhancement on rough surfaces of metals, semimetals, and semiconductors with the use of optical second-harmonic generation," *Phys. Rev. B*, Vol. 30, No. 2, pp. 519-526, 1984.
10. H. Kuwata, H. Tamaru, H. Miyazaki, and K. Miyano, "Resonant light scattering from metal nanoparticles: Practical analysis beyond Rayleigh approximation," *Appl. Phys. Lett.* (2003) in press.
11. R. G. Yarovaya, I. N. Shklyarevsklii, and A. F. A. El-Shazly, "Temperature dependence of the optical properties and the nergy spectrum of zinc," *Sov. Phys. JETP*, Vol. 38, No. 2, pp. 331-334, 1974.
12. K. F. MacDonald, V. A. Fedotov, S. Pochon, K. J. Ross, G. C. Stevens, N. I. Zheludev, W. S. Brocklesby, and V. I. Emel'yanov, "Optical control of gallium nanoparticle growth," *Appl. Phys. Lett.* Vol. 80, No. 9, pp. 1643-1645, 2002.
13. *Near-Field Nano/Atom Optics and Technology*, edited by M. Ohtsu, (Springer, Tokyo, 1999) Chap. 3.

Fabrication of 20-nm Zn nanocrystallites by the selective photodissociation of adsorbed diethylzinc molecules using a near-field optical chemical vapor deposition

J. Lim,^{a)} T. Yatsui,^{b)} and M. Ohtsu^{a), b)}

^{a)} Interdisciplinary Graduate School of Science and Engineering, Tokyo Institute of Technology, Kanagawa 226-8502, Japan.

^{b)} SORST, Japan Science and Technology Agency, Tokyo 194-0004, Japan.

Future optical transmission systems require ultrahigh integration of photonic devices. To meet this requirement, we have proposed nanophotonic integrated circuits that consist of nanometer-scale dots.^[1] To fabricate them, nanometer-scale dots must be deposited on a substrate with nanometer-scale controllability in size and position. To achieve this level of controllability, we demonstrated the feasibility of nanometer-scale chemical vapor deposition (CVD) using optical near-field techniques. Conventional photo-CVD uses a light source that resonates the absorption band of metalorganic (MO) vapor and has a photon energy that exceeds the dissociation energy. Thus, it utilizes a two-step process; gas-phase photodissociation and subsequent adsorption. However, we found that the dissociated MO molecules migrate on the substrate before adsorption, which limits the minimum lateral size of deposited dots.

To overcome this difficulty, we demonstrate here the deposition of Zn nanocrystallites using the selective photodissociation of adsorbed diethylzinc (DEZn) molecules with a nonresonant optical near field, where the photon energy is lower than that of the absorption band edge of gas-phase DEZn molecules and higher than that of the absorption edge of adsorbed DEZn molecules.^[2]

Since the absorption band edge energy (E_{ab}) of the gas-phase DEZn molecules was 4.6 eV, we used He-Cd laser light ($E_{ab}=3.81$ eV) as the light source; it is nonresonant to gas-phase DEZn molecules. Note that the photon energy remained higher than the dissociation energy of DEZn (2.26 eV).

Using a sharpened UV fiber probe, we achieved selective dissociation of adsorbed DEZn, as a result, we successfully fabricated 20-nm Zn dots with 65-nm separation on a sapphire substrate with high controllability in size and position (see Fig.1). Furthermore, since the nonresonant propagating light that leaked from the probe did not dissociate the gas-phase DEZn molecules, the atomically steps of sapphire substrate (step height = 0.3nm) around the deposited nanocrystallites were clearly observed after the deposition. Since high-quality ZnO nanocrystallites can be obtained by oxidizing Zn nuclei, this technique could be used to produce high-quality ZnO nanocrystallites, which is a promising material for nanophotonic devices.

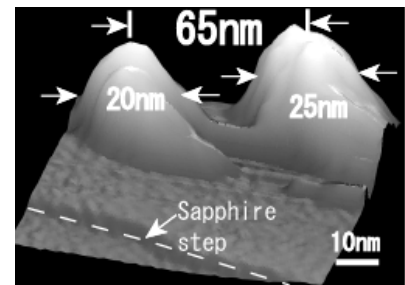


Fig.1: Shear-force image of Zn nanocrystallites on sapphire substrate

References

- [1] M.Ohtsu *et al.*, IEEE Journal of Selected Topics in Quantum Electronics. **8**, 839 (2002).
- [2] T. Yatsui *et al.*, Appl. Phys. Lett. **81**, 3651 (2002).

Photolithography using a visible light based on the nonadiabatic near-field photochemical reaction

Ryoichi HAGA¹, Tadashi KAWAZOE², Motoichi OHTSU^{1,2}

¹Tokyo Institute of Technology, ²Japan Science and Technology Agency

E-mail: r-haga@ae.titech.ac.jp

The spatial locality of the optical near field leads to novel physical phenomena such as optically forbidden energy transfer [1] and giant second harmonic generation. Previously, we found another novel phenomenon, *i.e.*, the photodissociation of metal organic molecules using a nonresonant optical near field with photon energy lower than the energy gap of the electronic state of the molecule [2]. This unique photochemical reaction seems to violate the Franck-Condon principle. We succeeded to explain the photodissociation by the exciton-phonon polariton model and nonadiabatic process based on the spatial locality of the optical near field [3]. In this presentation, we report the application of this nonadiabatic near-field photochemical reaction to the photolithography.

Figures 1 (a) and (b) show the atomic force microscope images of the photoresist (OFPR-800) surface after development for UV light source and 672nm laser, respectively. The schematic drawings are the used photo-mask. Although this photoresist is not active to the 672nm light, the patterns developed on the photoresist and the ditches, fabricated on the photoresist for 672 nm, were 250 nm wide and 25 nm deep. This result can be explained by the optical near-field effect. For UV light the exposure process occurs conventionally and the exposed area correspond to the photo-mask pattern (Fig.1(a)). Since the photoresist has no photosensitivity for 672 nm light source. Therefore, the exposure process cannot occur by direct irradiation of 672 nm light. However, the optical near field enhances the photosensitivity and causes the exposure process using the nonresonant photochemical reaction by the optical near field. Since the optical near field is strongly generated at around the edge of the photo-mask pattern, the fabricated ditches were limited at narrow areas along the edges of the photo-mask pattern, whose spaces are a half of the photo-mask pattern (Fig.1(b)).

This novel process for photolithography is one of the promising techniques for nanofabrication, because this technique enables conventional systems without using the expensive vacuum UV light source and optics for the nanophotolithography.

[1] T. Kawazoe, K. Kobayashi, J. Lim, Y. Narita, and M. Ohtsu, *Phys. Rev. Lett.*, **88**, pp.067404 (2002).

[2] T. Kawazoe, Y. Yamamoto, and M. Ohtsu, *Appl. Phys. Lett.*, **79**, pp.1184 (2001).

[3] T. Kawazoe, K. Kobayashi, S. Takubo, and M. Ohtsu, Technical digest of QELS QWA12 (2003).

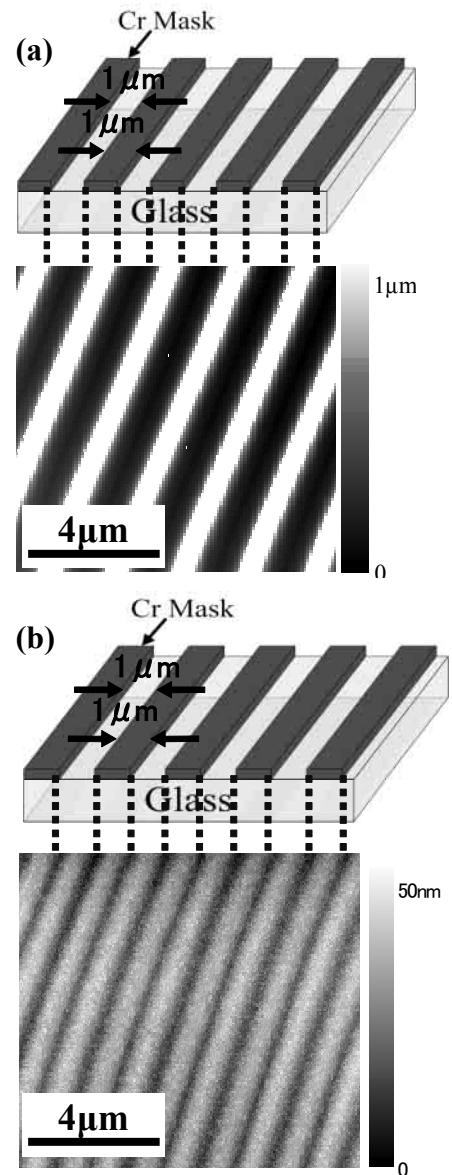


Fig.1. AFM images of photoresist after the development.

Exciton Dynamics in a Quantum Dot System and Local Manipulation by Optical Near Fields

K.Kobayashi¹⁾, S. Sangu¹⁾, A. Shojiguchi¹⁾, T. Kawazoe¹⁾ and M. Ohtsu^{1), 2)}

1) ERATO Localized Photon Project, Japan Science and Technology Agency, 687-1 Tsuruma, Machida, Tokyo 194-0004, Japan

2) Interdisciplinary Graduate School of Science and Engineering, Tokyo Institute of Technology, 4259 Nagatsuta-cho, Midori-ku, Yokohama, Kanagawa 226-8502, Japan

Much attention has been paid to the miniaturization of photonic devices, and near-field optical approaches have been actively investigated theoretically and experimentally [1]. In this paper, we examine exciton dynamics in a three-quantum dot system driven by an optical near field [2,3], as schematically shown in Fig. 1, and experimentally demonstrate a switching operation [4] as well as a theoretical proposal of logic gates and a state selection from entangled states prepared by the optical near field [5].

Figure 2 shows an experimental result of a nanophotonic switch using three CuCl quantum dots (switching time ~ 100 ps with a repetition of 80 MHz), which is consistent with the theoretical estimation. As an extension of this kind of switch, we can show AND- and XOR-gates by considering temporal evolution of excitons prepared in quantum dots by an optical near field probe.

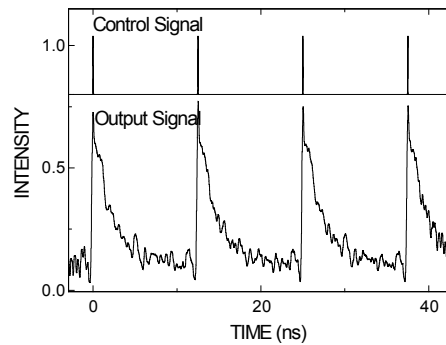
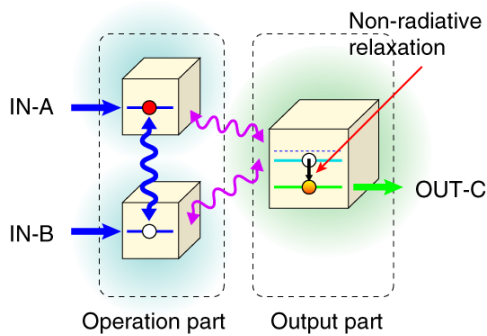


Fig. 1: A three-quantum dot system **Fig. 2:** Nano-switch operation using CuCl quantum dots

Figure 3 illustrates how to measure the coefficient of entangled states in symmetrically and asymmetrically configured three-quantum dot systems, where the initial state is prepared by the optical near fields. The selection is based on the difference in coupling strengths for symmetric and asymmetric states.

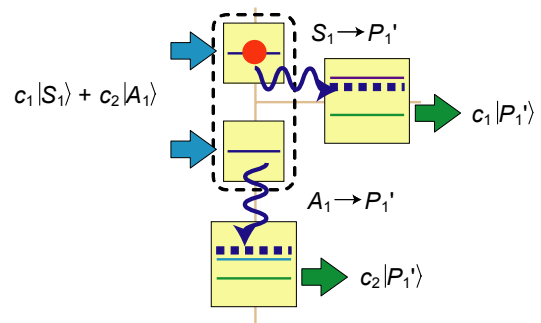


Fig. 3: State selection from entangled states

References

- [1] M. Ohtsu, K. Kobayashi, T. Kawazoe, S. Sangu, and T. Yatsui, IEEE J. Sel. Top. Quant. Electron. **8**, 839 (2002).
- [2] K. Kobayashi, S. Sangu, A. Shojiguchi, T. Kawazoe, K. Kitahara and M. Ohtsu, J. Microsc. **210**, 247 (2003).
- [3] S. Sangu, K. Kobayashi, T. Kawazoe, A. Shojiguchi, and M. Ohtsu, J. Appl. Phys. **93**, 2937 (2003).
- [4] T. Kawazoe, K. Kobayashi, S. Sangu, and M. Ohtsu, Appl. Phys. Lett. **82**, 2957 (2003).
- [5] S. Sangu, K. Kobayashi, A. Shojiguchi, and M. Ohtsu, submitted to Phys. Rev. B.

Magnetic circular dichroism and large Faraday rotation of Au/Fe/Au/Fe optical fiber probe

Syinya MARUYAMA¹, Tadashi KAEAZOE², Motoichi OHTSU^{1,2}

Tokyo Institute of Technology¹, Japan Science and Tech. Agency²

maruyama@ae.titech.ac.jp, kawazoe@ohtsu.jst.go.jp, ohtsu@ae.titech.ac.jp

Optical fiber transmission systems require increased integration of photonic devices because data transmission rate is required as high as 40T bit/s by the year 2015. To support this increase, it is estimated that the size of photonic device should be reduced to a sub-wavelength scale. To meet this requirement, we have succeeded in the nanophotonic switching operation by optical near-field energy transfer^[1].

The polarization is one of the important degree of freedom for optical near field and brings additional functions to the optical devices. We consider these advantages to utilize the polarization are equivalent for the nanophotonic devices. This presentation reports the fabrication of an Au/Fe/Au/Fe-layer coated fiber probe and the experimental result of the polarization control of optical near field.

We fabricated the Au/Fe/Au/Fe (10nm/ 2nm/ 80nm/ 100nm) coated fiber probe as shown in Fig.1^[2]. The magneto-optical effect of the fiber probe is increased by an Au/Fe/Au quantum well structure^[3]. Figure2 shows the magnetic circular dichroism of the fiber probe. We achieved the extinction ratio of 6.0 in the external magnetic field of 0.22T, and the preserved extinction ratio of 5.5 after removing the external magnetic field by the favor of the magnetized layer.

The Au/Fe/Au/Fe coated fiber probe also has large Faraday effect. We achieved the Faraday rotation angle of 70 degree in the external magnetic field of 0.4T, and confirmed it is preserved even after removing the external magnetic field (Fig.3).

These experimental results show that our proposed optical fiber probe is promising for the polarization measurement of optical near field and nanophotonic device, such as nanophotonic polarizer, isolator, and so on.

[1] T. Kawazoe, K. Kobayashi, S. Sangu, and M. Ohtsu, Appl. Phys. Lett. 82, 2957 (2003)

[2] J. Lim, T.Kawazoe, T.Yatsui, M.Ohtsu, IEICE TRANS. ELECTRON., Vol.E85-C, No.12, pp.2077-2080, 2002

[3] S. Maruyama et al., JSAP, The 64th autumn meeting, 1am-Q-5,2003

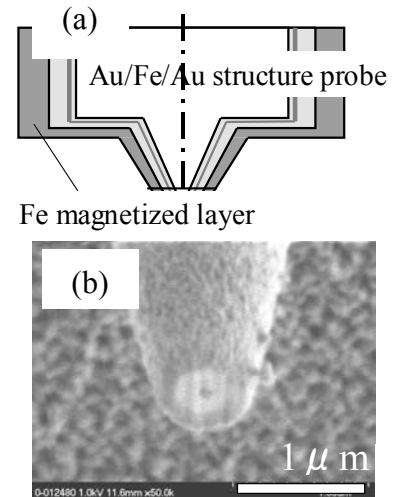


Fig.1. Fe/Au/Fe/Au coated fiber probe

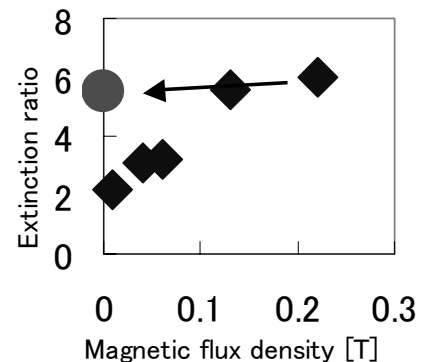


Fig.2. Magnetic circular dichroism of the fiber probe

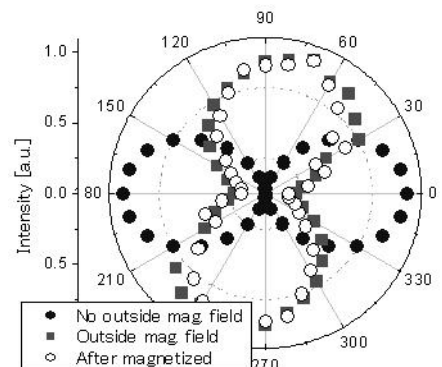


Fig.3. Faraday rotation of the fiber probe

ナノフォトニクス：デバイス、加工、システム

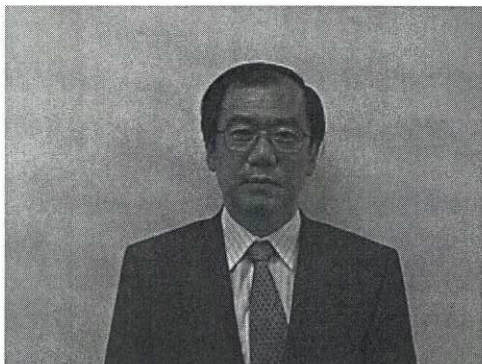
Nanophotonics: Devices, Fabrications, and Systems

教授 大津 元一、東京工業大学 大学院総合理工学研究科 電子機能システム専攻
Prof. Dr. Motoichi Ohtsu
Interdisciplinary Graduate School of Science and Engineering, Tokyo Institute of
Technology

スピーチ要約:

ナノフォトニクスとは大津が 1994 年に提案した述語であり、「近接場光を信号キャリア、少数個のナノ物質を材料として用いてナノ寸法の光デバイスを加工し、動作させる技術」と定義される。ナノフォトニクスの本質はナノ寸法の光科学技術を実現するというのではなく、近接場光の局在性を利用して通常の伝搬光では到底不可能な機能や現象を実現することである。本講演では最近の研究成果を紹介する。それらは(1)ナノフォトニックデバイス(光スイッチなど)と入出力端子、(2)ナノ光加工(寸法と位置の制御された光化学気相堆積とその非断熱過程)、(3)ナノフォトニックシステムの展望(光通信、光記録、光コンピュータなど)である。

略歴:



大津 元一 1973 年東京工業大学工学部電子工学科卒、1975、1978 年に各々同大学院修士課程、博士課程修了。

1978 年に同大学助手、1982 年助教授。1986～1987 年、米国 AT&T ベル研究所研究員、1991 年、東京工業大学教授に昇進し現在に至る。1983 年より(財)神奈川科学技術アカデミー「フォトン制御プロジェクト」リーダー、1998 年より科学技術振興事業団「局在フォトンプロジェクト」総括責任者、2002 年より経済産業省「大容量光ストレージ開発事業」責任者などを兼任。

発表論文 320 編以上、特許 87 件。出版書籍 39 件(共著含む)。

2000 年に IEEE/LEOS 日本支部の代表、応用物理学会理事。2001 年国際会議 CLEO-PR プログラム委員長、SPIE, OSA 学会などのチュートリアル講師、文部省や経済産業省などの委員会委員などを歴任。

OSA(Optical Society of America)のフェロー、IEEE のシニア会員、等を始めいくつかの学会会員。1984 年に電波科学国際連合より Issac Koga 金メダル、1988 年に日本 IBM 科学賞、1982 年と 1990 年に応用物理学会賞、1999 年に井上科学賞などを受賞。

研究の要約:

大津教授の専門分野はフォトニクス(光エレクトロニクス)と量子エレクトロニクスである。1994 年にナノフォトニクスと呼ばれる光科学技術の新分野を提案し、現在に至るまでその研究を活発に推進している。これは近接場光(そのエネルギーはナノ寸法空間に局在している)を用いたナノ寸法の光加工、光デバイスを実現し、それを次世代の光システムへ応用する研究である。この研究

の本質は従来より使われている伝搬光では実現不可能な新現象、新機能を発現することである。

連絡先:

〒226-8502 横浜市緑区長津田 4259
東京工業大学大学院総合理工学研究科
Tel: 045-924-5455
Fax: 045-924-5599
E-mail: ohtsu@ae.titech.ac.jp
URL: <http://uuu.ae.titech.ac.jp>

Abstract:

The word “nanophotonics” was proposed by Ohtsu in 1994. Nanophotonics is defined as “the technology for fabricating and operating nanophotonic devices by using the optical near field as signal carrier and small numbers of nanoparticles as device materials”. Essential of nanophotonics is not to realize nanometer-sized optical science and technology but to realize “novel functions and phenomena originated from the localized nature of optical near fields” which are impossible by propagating lights. Recent progress of our research is reviewed. They are; (1) nanophotonic devices (optical switches, etc.) and optical input/output terminals, (2) nanophotonic fabrication (size- and position-controlled photochemical vapor deposition and non-adiabatic process, etc.), and (3) future prospect to realize nanophotonic systems (optical fiber communications, optical memory, photon computing, etc.).

Biography:

Motoichi Ohtsu received the B.E., M. E., and Dr. E. degrees in electronics engineering from the Tokyo Institute of Technology, Tokyo, Japan, in 1973, 1975, and 1978, respectively. In 1978, he was appointed a Research Associate, and in 1982, he became an Associate professor at the Tokyo Institute of Technology. From 1986 to 1987, while on leave from the Tokyo Institute of Technology, he joined the Crawford Hill Laboratory, AT&T Bell Laboratories, Holmdel, NJ. In 1991, he became a Professor at the Tokyo Institute of Technology. Since 1993, he has been concurrently the leader of the “Photon Control” project of the Kanagawa Academy of Science and Technology, Kanagawa, Japan. Since 1998, he has been concurrently the leader of the “Localized Photon” project of ERATO (Exploratory Research for Advanced Technology), JST (Japan Science and Technology Corporation), Japan. Since 2002, He is a leader of the national project on “Ultrahigh density optical storage” sponsored by (METI) Ministry of Economy, Trade and Industry. He has written over 320 papers and received 87 patents. He is the author and co-author of 39 books. In 2000, he was the President of the IEEE/LEOS Japan Chapter. From 2000, he is an executive director of the Japan Society of Applied Physics. He served as a Technical Program Co-chair for the 4th Pacific Rim Conference on Lasers and Electro-Optics(CLEO/PR01), 2001. He has been a tutorial lecturer of the SPIE and the OSA. He is a member of several boards of the Ministry of Education, METI, and so on. Dr. Ohtsu is a Fellow of the Optical Society of America, a senior member of IEEE, and member of several academic societies. He has been awarded ten prizes from academic

institutions, including the Issac Koga Gold Medal of URSI in 1984, the Japan IBM Science Award in 1988, two awards from the Japan Society of Applied Physics in 1982 and 1990, and the Inoue Science Foundation Award in 1999.

Prof. Ohtsu's fields of research are photonics and quantum electronics. In 1994, he proposed "nanophotonics", new field of optical science and technology. Based on this proposal, he is actively carries out basic research and development. Nanophotonics is to use optical near fields whose energy is localized in a nanometric dimension, in order to realize novel nanometric fabrication, nanometric photonice device operation, and apply to next-generation photonic systems. Essential feature of nanophotonics is to realize novel functions and operations, which are impossible as long as conventional propagating light is used.

Nanophotonics: Definition and true nature

M. Ohtsu^{1,2}

¹Interdisciplinary Graduate School of Science and Engineering, Tokyo Institute of Technology
4259, Nagatsuda, Midori-ku, Yokohama 226-8502, Japan

Phone: +81-45-924-5455 Fax: +81-45-924-5599 E-mail: ohtsu@ae.titech.ac.jp

²Ohtsu Localized Photon Project, ERATO, Japan Science and Technology Corporation
687-1 Tsuruma, Machida Tokyo 194-0004, Japan

Main purpose of this invited talk is to review the definition and true nature of nanophotonics. After the word "nanophotonics" was proposed by Ohtsu in 1994, the nanophotonics technical group was organized by OITDA (Optical Industry Technology Development Association, Japan) to discuss future direction of optical science, technology, and industry.

Nanophotonics is not to realize nanometer-sized optical science and technology but to realize "novel functions and phenomena originated from the localized nature of optical near fields" [1, 2]. These novel functions and phenomena are possible by noting that the nanometric system (composed of nanometric particles and optical near field) is buried in a macroscopic heat bath. Energy non-conservation can be observed in the nanometric system due to energy exchange between the two systems. Further, higher order effects, e.g., magnetic dipole or electric quadrupole transitions are not neglected due to localized nature of optical near fields. True nature of nanophotonics is to utilize these "novel functions and phenomena originated from the localized nature of optical near fields", which is completely impossible by propagating lights (Fig.1).

Based on the consideration mentioned above, nanophotonics is defined as "the technology for fabricating and operating nanophotonic devices by using the optical near field as signal carrier and small numbers of nanoparticles as device materials". The essential features of these devices are their novel functions and phenomena. In addition, their sizes are far smaller than the diffraction limit of light. Conventional photonic devices, e.g., quantum dot lasers, photonic crystals, and optical MEMS do not have these features because they use the diffraction-limited propagating light as a signal carrier.

Nanophotonics defined above has been developed by my research group. In this talk, their recent progress is reviewed. They are; (1) nanophotonic devices (switches, AND/XOR gates, delay gate, super-radiant-type pulsed

generator) and optical input/output terminals, (2) nanophotonic fabrication (size- and position-controlled photochemical vapor deposition and non-adiabatic process, desorption and self-organization based on size-dependent resonance, application of non-adiabatic process to photo-lithography), and (3) future prospect to realize nanophotonic systems (optical fiber communications, optical memory, optical data processing, and so on).

References

- [1] M. Ohtsu et al., IEEE J. Selected Topics in Quantum Electron., Vol.8, No.4, pp. 839-862 (2002)
- [2] M. Ohtsu and K. Kobayashi, *Optical Near Fields*, Springer-Verlag, Berlin, to be published, September 2003.

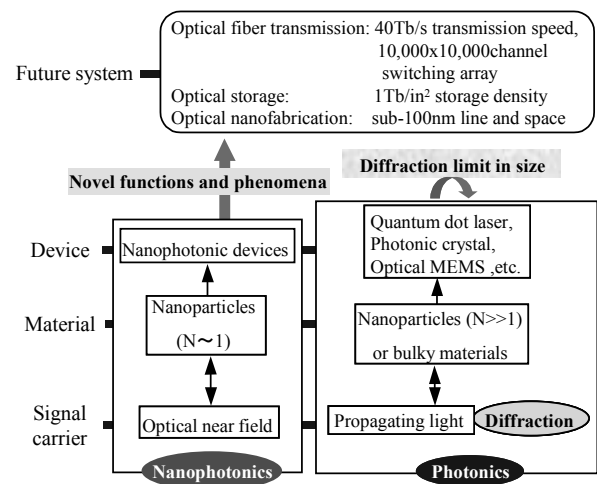


Fig.1. True nature of nanophotonics

The optical nano-fountain, which uses energy transfer to concentrate optical energy to a 10-nm region

Tadashi Kawazoe¹, Kiyoshi Kobayashi¹, Motoichi Ohtsu^{1,2}

¹Exploratory Research for Advanced Technology, Japan Science and Technology Corporation, 687-1 Tsuruma, Machida, Tokyo 194-0004, Japan

²Interdisciplinary Graduate School of Science and Engineering, Tokyo Institute of Technology, 4259 Nagatsuta, Midori-ku, Yokohama 226-8502, Japan

1. Introduction

We are currently developing nanophotonic devices to meet the requirements of optical data transmission systems in the near future [1]. We have already demonstrated nanophotonic switching with a 10-nm device [2]. For nanophotonic devices that are smaller than the diffraction limit of light, a nanometric optical concentration device would be advantageous, both to increase the efficiency of operation and for coupling nanophotonic devices with conventional photonic devices.

A perfect lens has been proposed that uses the negative refraction feature of metal to focus light to a spot that is tens of nanometers in size [3]. However, efficiency is low, due to the short penetration depth of metal. We consider a novel operating mechanism to realize a highly efficient nanometric optical concentration device. In this paper, we propose a new nanophotonic device that we call the “optical nano-fountain”, which uses optical near-field energy transfer among quantum dots and demonstrate its operation.

2. Optical nano-fountain

Recently, we reported energy transfer among quantum dots via an optical near field [4]. The energy transfer occurs from a higher energy level to a lower energy level, *i.e.*, from smaller to larger quantum dots. This unidirectional energy transfer can be applied to optical concentration. Figure 1 (a) shows a schematic explanation of the optical nano-fountain, which is composed of many different-sized quantum dots. When these quantum dots have resonant energy sublevels of carriers, the energy transfer occurs via the optical near field as illustrated by the arrows in Fig. 1(a). Light incident to the optical nano-fountain is ultimately concentrated at the largest quantum dot, the size of which is the focal spot size of this device. Therefore, this device realizes nanometric optical concentration. Since the mechanism of the optical nano-fountain is similar to that of the light trapping system in the photosynthesis bacteria [5], the operation of the optical nano-fountain is a biomimetic action. From experimental tests of nanophotonic switch operation, It is expected that the concentration efficiency of this device will be close to 1

[2].

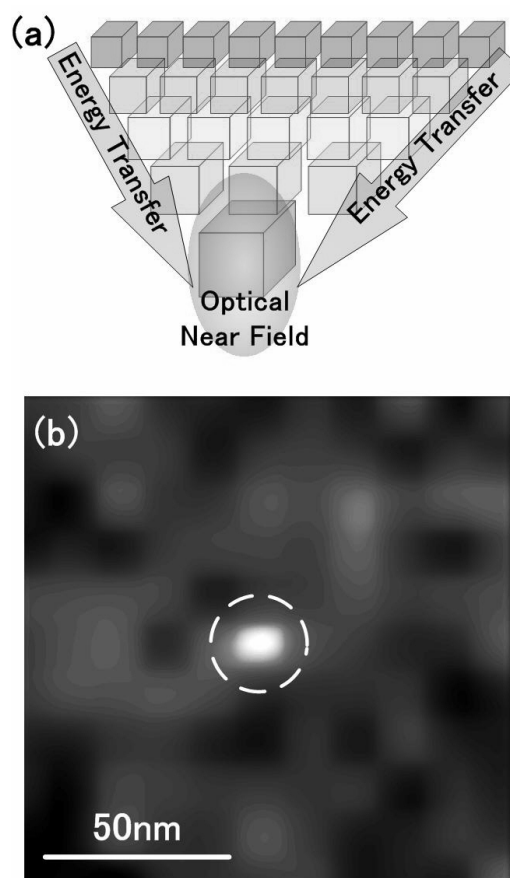


Fig.1. (a) Schematic explanation of the optical nano-fountain. (b) The luminescence intensity distribution of CuCl quantum dots, which operate as the optical nano-fountain.

To demonstrate an optical nano-fountain, we used CuCl cubic quantum dots embedded in a NaCl matrix. This has an inhomogeneous size distribution and a random arrangement of quantum dots. Therefore, in some areas of the sample, the quantum dots are arranged to act as an optical nano-fountain. In the experiment, we maintained the sample temperature at 40 K, as at too low a temperature the resonant condition becomes tight, due to narrowing of the homogeneous linewidth, while at too high a temperature unidirectional energy transfer is

obstructed by thermal activation of excitons in the quantum dots. A 325-nm He-Cd laser was used as the excitation light source.

Figure 1 (b) shows the luminescence intensity distribution of a sample observed with an optical near-field spectrometer. Here, the collected luminescence photon energy was from 3.350 eV to 3.215 eV, which corresponded to the luminescence from 2- to 10-nm quantum dots, respectively. The bright spot surrounded by a broken circle is the focal spot of the optical nano-fountain.

3. Discussion

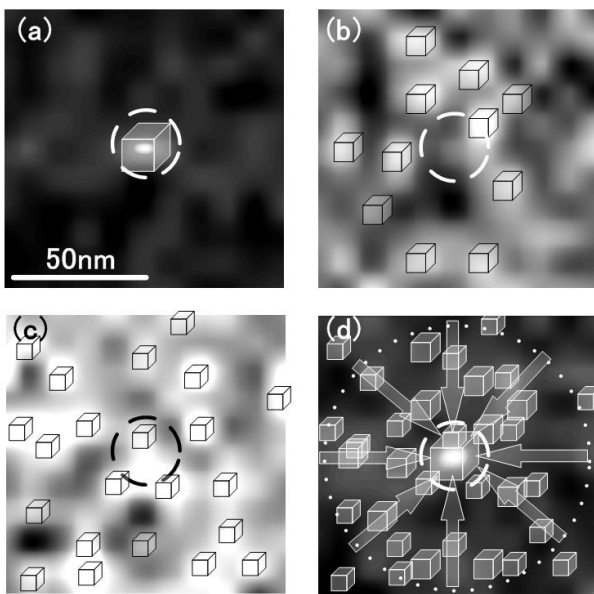


Fig.2. Luminescence intensity distribution of CuCl quantum dots of (a) 6-10, (b)4-6, (c) 2-4, and (d) 2-10 nm.

To investigate the optical energy transfer from smaller to larger quantum dots, we show the selective luminescence intensity distribution by size, *i.e.*, by photon energy, in Figs. 2(a), 2(b), and 2(c). The broken circles show the focal spots, and the scanning areas are the same as in Fig. 1(b). The brightness and darkness indicate the luminescence intensity, and the normalized scales are (a) 0-0.6, (b) 0-0.2, (c) 0-0.1, and (d) 0-1. The schematic drawings of cubic quantum dots show their positions estimated from the luminescence intensity distribution. In Fig. 2(a), the observed quantum dots are 6 to 10 nm in size, and only one quantum dot exists at the focal position. In Figs. 2(b) and 2(c), the observed quantum dots are 4 to 6 nm and 2 to 4 nm, respectively, and many smaller quantum dots exist around the focus. Figure 2(d) shows the luminescence intensity distribution obtained as the

total of Figs. 2(a), 2(b), and 2(c). The bright spot agrees with the position of the largest quantum dot and the smaller quantum dots are distributed around it. The luminescence intensity at the bright spot is several times stronger than that from a single isolated 10-nm quantum dot. Conversely, the luminescence intensities of surrounding smaller quantum dots are weaker than those of the isolated quantum dots. This indicates that energy is transferred from smaller quantum dots to larger quantum dots and is concentrated at the largest quantum dot.

This is the first demonstration of this new nanometric optical condensation device, the optical nano-fountain. Its optical concentration diameter was more than 100 nm and the focal spot size was 10 nm. This device also functions in frequency selection, based on the resonant frequency of quantum dots. This additional function is applied to frequency domain demultiplexing in our proposed nanophotonic integrated circuit.

4. Summary

We proposed a new nanophotonic device, the optical nano-fountain, which uses energy transfer among quantum dots, and demonstrated its operation using CuCl quantum dots embedded in a NaCl matrix. The nanophotonic device concentrated the optical field energy from a 100-nm area and focused it in a 10-nm spot.

References

- [1] M. Ohtsu, K. Kobayashi, T. Kawazoe, S. Sangu, and T. Yatsui, *IEEE J. Sel. Top. Quant. Electron.*, **8** No.4 (2002) p.839.
- [2] T. Kawazoe, K. Kobayashi, S. Sangu, and M. Ohtsu, *Appl. Phys. Lett.*, **82** No.18 (2003) p.2957
- [3] J. B. Pendry, *Phys. Rev. Lett.* **85** No. 18, (2003) p.3966.
- [4] T. Kawazoe, K. Kobayashi, J. Lim, Y. Narita, and M. Ohtsu, *Phys. Rev. Lett.*, **88** No.6 (2002) pp. 067404.
- [5] K. Mukai, S. Abe, and H. Sumi, *J. Phys. Chem. B* **103**, (1999) p.6096.

Development of optical far/near field conversion devices

Takashi Yatsui,¹ Wataru Nomura,² Motonobu Kouroggi,² and Motoichi Ohtsu^{1,2}

¹ Ohtsu Localized Photon Project, ERATO, Japan Science and Technology Corporation
687-1 Tsuruma, Machida Tokyo 194-0004, Japan

Phone: +81-42-788-6030 Fax: +81-42-788-6031 E-mail: yatsui@ohtsu.jst.go.jp

² Interdisciplinary Graduate School of Science and Engineering, Tokyo Institute of Technology
4259, Nagatsuda, Midori-ku, Yokohama 226-8502, Japan

1. Introduction

For future optical transmission systems, nanophotonic integrate circuits [1], which are composed of sub-100 nm scale dots, are necessary to increase data transmission rates and capacity. As a representative device, a nanophotonic switch can be realized by controlling the dipole forbidden optical energy transfer among resonant energy states in nanometer-scale quantum dots via an optical near field [2]. To operate this, coupling them with external conventional diffraction-limited photonic devices is required by using a nanometer-scale optical waveguide for far/near -field conversion. To realize this, we have reported plasmon-polariton waveguide using a metallized silicon wedge structure that converts far-field light to optical near field via metallic core waveguide [3]. To obtain higher efficiency of coupling with plasmon-polariton mode, we propose here a plasmon-polariton condenser with nano-dot coupler.

2. Plasmon-Polariton condenser with nano-dot coupler

Figure 1 shows a schematic of plasmon-polariton condenser with nano-dot coupler. The condenser consists of several hemispheres and they are positioned on an arc, and works as a "phased array" [4]. A nano-dot coupler consists of chains of closely spaced metal nanoparticles. Energy transport in the nano-dot coupler relies on near-field coupling between plasmon-polariton modes of neighboring particles [5]. In comparison with metallic waveguide, the use of nano-dot coupler is expected to realize lower energy loss due to the reduced metal content. Furthermore, since metal nanoparticles act as a scatterer,

high conversion efficiency from two-dimensional surface plasmon-polariton (2D SPP) to plasmon-polariton mode in a chain of metal nanoparticles is expected due to the scattering coupling [6].

3. Experiment

As a plasmon-polariton condenser and nano-dot coupler, carbon hemispheres were aligned by focused ion beam (FIB) on 10- μm Si substrate. Furthermore, to excite 2D SPP mode and increase the efficiency of scattering at metal nanoparticles, 100-nm-thick gold film was coated.

First, we checked whether the metallized carbon columns led to efficient scattering and resultant focusing 2D SPP. The spatial distributions of optical near-field energy were observed by the collection mode near-field optical microscope taken at $\lambda = 785 \text{ nm}$ and arrangement for 2D SPP mode excitation by grating coupling. In this set-up, 2D SPP propagate as long as 50 μm and focused by the condenser to couple the waveguide. As a collection probe, we used a sharpened fiber probe with thin gold coating. Figure 2 shows the spatial distribution of optical near field for the plasmon-polariton condenser without nano-dot coupler. One can see that 2D SPP was focused efficiently. And by optimizing the number of dots and the position, we obtained focused 2D SPP as small as 400 nm (see Fig. 2(c)).

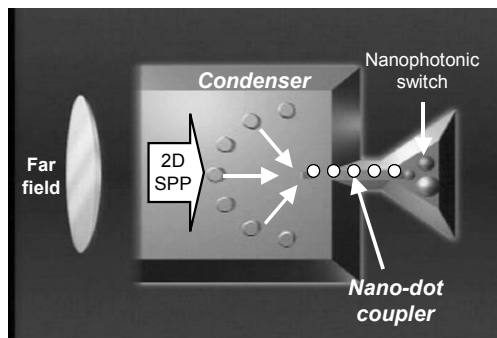


Fig.1 Plasmon-polariton condenser with nano-dot coupler for optical far-/near- field conversion devices.

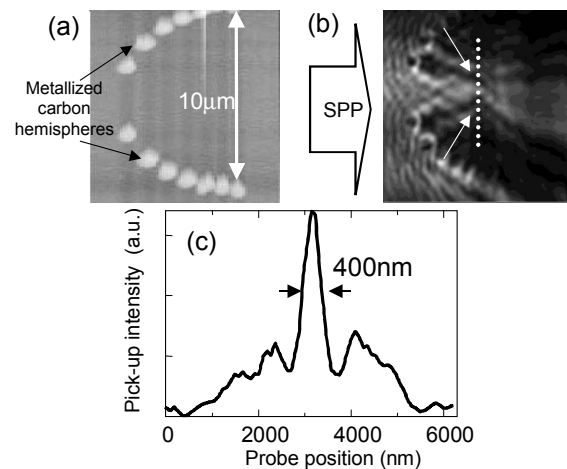


Fig.2 (a) Shear-force image of plasmon-polariton condenser. (b) Intensity distribution of optical near-field of (a). (c) Cross-sectional profiles along the dashed white line in (b).

Next, we compared spatial distributions of optical near field between nano-dot coupler and metallic waveguide. They were aligned at focal point of the plasmon-polariton condenser. As a metallic waveguide, carbon line (instead of the carbon hemispheres chains) was deposited by FIB between the carbon silts and coated with 100-nm thick gold film. By introducing the chains of closely spaced metal nanoparticles inside the slit, the coupled plasmon-polariton mode along the nano-dot coupler was excited efficiently (see Fig. 3(b)). In the case of nano-dot coupler with 250-nm dots and 50-nm separation, we found plasmon-polariton transfer along the nano-dot coupler as long as 4 μm . The full width at half maximum (FWHM) of the tangential cross section of Fig. 3(b) was as small as 250 nm, which is comparable to the dot size. Since the present dot size is determined by the resolution of deposited carbon hemispheres by FIB, the value of FWHM of the coupled plasmon-polariton mode can be decreased by the decreasing the dots size, which will be realized by using electron beam lithography. Furthermore, the energy loss of nano-dot coupler was 10-fold lower than that of metallic waveguide (see Fig. 3(e)).

4. Conclusions

In through our proposal, we fabricated plasmon-polariton condenser with nano-dot coupler as far-field and near-field converter. Efficient excitation of plasmon-polariton mode along the chains of closely spaced metal nanoparticles was observed. These results confirm that it will be possible to create the optical far-/near-field conversion devices required by future systems.

References

- [1] M. Ohtsu, K. Kobayashi, T. Kawazoe, S. Sangu, and T. Yatsui, *IEEE Journal of Selected Topics in Quantum Electronics* **8**, 839 (2002).
- [2] T. Kawazoe, K. Kobayashi, S. Sangu, and M. Ohtsu, *Appl. Phys. Lett.* **82**, 2957 (2003).
- [3] Yatsui, M. Kourogi, and M. Ohtsu, *Appl. Phys. Lett.* **79**, 4583 (2001).
- [4] I. I. Smolyaninov, D. L. Mazzoni, J. Mait, and C. C. Davis, *Phys. Rev. B* **56**, 1601 (1997).
- [5] M. L. Brongersma, J. W. Hartmann and Harry A. Atwater, *Phys. Rev. B* **62**, R16356 (2000).
- [6] T. Yatsui, M. Kourogi, and M. Ohtsu, *Appl. Phys. Lett.* **71**, 1756 (1997).

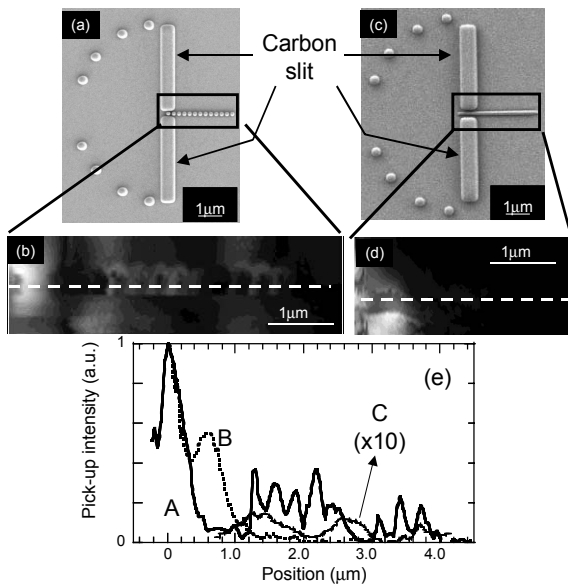


Fig. 3 (a) SEM image of plasmon-polariton condenser with nano-dot coupler. (b) Spatial distribution of optical-near field intensity of (a). (c) SEM image of plasmon-polariton condenser with metallic waveguide. (d) Spatial distribution of optical-near field intensity of (c). (e) Curves A and B show cross-sectional profiles through the dashed white line in (b) and (d), respectively. Curve C shows magnified profile of curve B.

Growth control of Ga and In nanodots by photochemical reactions for applications to group III nitrides-based nanophotonic devices

T.-W. Kim¹, S. Yamazaki², T. Nagira², T. Kawazoe¹, T. Yatsui¹, and M. Ohtsu^{1,2}

¹ Japan Science and Technology Corporation, 687-1, Tsuruma, Machida, Tokyo194-0004, Japan

² Interdisciplinary Graduate School of Science and Engineering, Tokyo Institute of Technology, Yokohama, Kanagawa 226-8502, Japan

Email: twkim90@ohtsu.jst.go.jp

Abstract

We present the growth control of gallium (Ga) and indium (In) nanodots using photochemical reactions of metallorganic reagents for applications to group III nitrides-based nanophotonic devices. Ga and In nanodots less than 30 nm in the typical size on substrate via the photodissociation of Ga(CH₃)₃ (trimethyl gallium (TMG)) and In(CH₃)₃ (trimethyl indium (TMI)) using 5th harmonic generation ($\lambda = 213$ nm) of a Nd:YAG laser pulse. In addition, we have controlled the arrangement of the nanodots, i.e., nanodots array and nanodots square loops, by selecting substrate material.

Characteristic mechanism of molecular dissociation and nanofabrication using optical near fields

Kiyoshi Kobayashi and Tadashi Kawazoe

ERATO Localized Photon Project
Japan Science and Technology
687-1 Tsuruma, Machida, Tokyo 194-0004, Japan
kkoba@ohtsu.jst.go.jp

Motoichi Ohtsu

Interdisciplinary Graduate School of
Science and Engineering
Tokyo Institute of Technology
4259 Nagatsuta-cho, Midori-ku, Yokohama, Japan

Abstract—A quasi particle (exciton-phonon polariton) model, as a simple model of an optical near-field probe, is proposed to investigate an unresolved problem on characteristic (non-adiabatic) mechanisms in photochemical processes. Incident photon energy and intensity dependences of Zn deposition rates are analyzed and good agreement between the theoretical and experimental results is obtained. It suggests that the probe system plays an important role in non-adiabatic transitions as well as electronic transitions in photodissociation processes, and that the couplings between the optical near field and molecular vibrations are enhanced to permit a non-resonant photodissociation inherent in the optical near field.

Keywords—molecular dissociation; probe model; quasi particles; optical near field; characteristic mechanism; nanofabrication

I. INTRODUCTION

Photonic devices must be ultrahighly integrated in order to fulfill the demands for an increase in communication capacity and information processing, and thus the size of each functional block will be so small that it is far beyond the diffraction limit of incident light. We have studied how to fabricate, operate, and control such nanophotonic devices, and reported to fabricate, for example, a Zn-dot or a few dots in a sub-50 nm, using an optical near-field method [1-3]. However, the mechanism of the dissociation and deposition of molecules is not clearly understood. For example, it is not known why an incident photon with less energy than the dissociation energy of a molecule can resolve it into composite atoms and deposit them as a nanometric dot [2]. It is essential to understand this process in order to fabricate nanometric dots while controlling position and size; pairs of such dots could then be used to build nanophotonic devices such as those that we proposed in our previous study [1,4]. In this paper, we address this issue, propose a simple model of an optical near-field probe, and clarify the mechanism of the photochemical processes involved in using such a probe, comparing the theoretical results with Zn-dot deposition data.

The paper is organized as follows. Section II outlines our simple model for an optical near-field probe. In Sec. III, molecular dissociation processes using optical near field are theoretically analyzed, and the results are compared with

experimental data on the deposition rates of Zn dots. Finally concluding remarks are presented in Sec. IV.

II. MODEL

We propose a quasi particle (exciton-phonon polariton) model as a simple model of an optical near-field probe, in order to investigate the physical mechanisms of the chemical vapor deposition using optical near field (NFO-CVD). The optical near field generated on the nanometric probe tip, which is a highly mixed state with material excitation rather than the propagating light field [5], is described in terms of the following model Hamiltonian:

$$\begin{aligned}
 H &= \sum_p \hbar \left[\omega_p a_p^\dagger a_p + \omega_p^{\text{ex}} b_p^\dagger b_p + \frac{i\Omega_c}{2} (a_p^\dagger b_p - a_p b_p^\dagger) \right] \\
 &+ \sum_p \hbar \Omega_p c_p^\dagger c_p + \sum_{p,q} \left\{ i\hbar M(p-q) b_p^\dagger b_q [c_{p-q} + c_{q-p}^\dagger] + h.c. \right\} \\
 &= \sum_p \hbar \omega_p^{\text{pol}} B_p^\dagger B_p + \sum_p \hbar \Omega_p c_p^\dagger c_p \\
 &+ \sum_{p,q} \left\{ i\hbar M'(p-q) B_p^\dagger B_q [c_{p-q} + c_{q-p}^\dagger] + h.c. \right\},
 \end{aligned} \tag{1}$$

where the creation (annihilation) operators for a photon, an exciton, a renormalized phonon, and an exciton polariton are denoted as a_p^\dagger (a_p), b_p^\dagger (b_p), c_p^\dagger (c_p), and B_p^\dagger (B_p), respectively, and their frequencies are ω_p , ω_p^{ex} , Ω_p , and ω_p^{pol} , respectively. Each coupling between a photon and an exciton, a phonon and an exciton, and an exciton polariton and a phonon is designated as Ω_c , $M(p-q)$, and $M'(p-q)$, respectively. The first line of this description expresses the Hamiltonian for a photon-exciton interacting system and is transformed into the exciton-polariton representation as shown in the third line [6], while the second line represents the Hamiltonian for a phonon-exciton interacting system. Note that the mode-mode couplings or the anharmonic couplings of phonons are taken into account as a renormalized phonon; therefore, multiple phonons in the

original representation can interact with an exciton or an exciton polariton simultaneously.

Assuming the mean field approximation of exciton polaritons near the probe tip as

$$\langle B_{k_0}^\dagger \rangle = \langle B_{k_0} \rangle = \sqrt{I_0(\omega_0)}V, \quad (2)$$

and using the unitary transformation as

$$\begin{pmatrix} B_p \\ c_{p-k_0} \end{pmatrix} = \begin{pmatrix} iv'_p & u'_p \\ u'_p & iv'_p \end{pmatrix} \begin{pmatrix} \xi_{(-)p} \\ \xi_{(+)p} \end{pmatrix}, \quad (3)$$

we can diagonalize the Hamiltonian in the exciton-phonon polariton representation as [7]

$$\begin{aligned} H &= \sum_p \hbar\omega_p^{\text{pol}} B_p^\dagger B_p + \sum_p \hbar\Omega_p c_p^\dagger c_p \\ &+ \sum_p \left\{ i\hbar\sqrt{I_0(\omega_0)}VM'(p-k_0) \left(B_p^\dagger c_{p-k_0} + B_p c_{p-k_0}^\dagger \right) \right\} \\ &= \sum_p \hbar\omega(p) \xi_p^\dagger \xi_p. \end{aligned} \quad (4)$$

Here the creation (annihilation) operator for an exciton-phonon polariton and the frequency are denoted as ξ_p^\dagger (ξ_p) and $\omega(p)$, respectively. In addition, $I_0(\omega_0)$ is the intensity of an incident photon with frequency ω_0 and momentum $\hbar k_0$, and V represents the volume to be considered. The transformation coefficients u'_p and v'_p are given by

$$u_p'^2 = \frac{1}{2} \left(1 + \frac{\Delta}{\sqrt{\Delta^2 + (2Q)^2}} \right), \quad v_p'^2 = \frac{1}{2} \left(1 - \frac{\Delta}{\sqrt{\Delta^2 + (2Q)^2}} \right), \quad (5)$$

where the detuning between an exciton polariton and a phonon is denoted as $\Delta = \omega_p^{\text{pol}} - \Omega_{p-k_0}$, and the effective coupling constant is expressed as $Q = \sqrt{I_0(\omega_0)}VM'(p-k_0)$.

Therefore, in this model, a molecule located near the probe tip does not absorb simple photons but absorbs exciton-phonon polaritons whose energies are transferred to the molecule, which excite molecular vibrations or induce electronic transitions.

We now discuss the dissociation probability of a molecule, postulating that the deposition rate of the metal atoms is proportional to the molecular dissociation rate. Since the experimental intensity dependence of the deposition rate is up to the third order [8], we consider multiple-step transitions via vibrational levels in the electronic ground state. For the purpose, the following initial and three final states of a system

consisting of the optical near-field probe and a molecule are prepared:

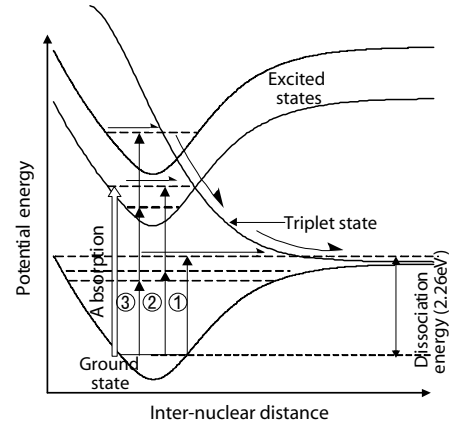


Figure 1. Potential energy of a diethylzinc molecule as a function of inter-nuclear distance. The solid curves depict the electronic ground state and three excited states while the dashed lines denote the vibrational levels. Three labeled transitions marked by the arrows are considered for the dissociation of the molecules.

$$\begin{aligned} |i\rangle &= |\text{probe}\rangle \otimes |E_g; \text{el}\rangle \otimes |E_i; \text{vib}\rangle, \\ |f_{\text{first}}\rangle &= |\text{probe}\rangle \otimes |E_g; \text{el}\rangle \otimes |E_a; \text{vib}\rangle, \\ |f_{\text{second}}\rangle &= |\text{probe}\rangle \otimes |E_{ex}; \text{el}\rangle \otimes |E_b; \text{vib}\rangle, \\ |f_{\text{third}}\rangle &= |\text{probe}\rangle \otimes |E_{ex'}; \text{el}\rangle \otimes |E_c; \text{vib}\rangle, \end{aligned} \quad (6)$$

where $|\text{probe}\rangle$, $|E_\alpha; \text{el}\rangle$, and $|E_\beta; \text{vib}\rangle$ represent a probe state, molecular electronic and vibrational states with energy E_α ($\alpha = g, ex, ex'$) and E_β ($\beta = i, a, b, c$), respectively, as shown in Fig. 1. The transitions from the initial to the final states can be formulated using the conventional perturbation method of the interaction Hamiltonian expressed in terms of the exciton-phonon polaritons as

$$\begin{aligned} H_{\text{int}} &= -\left\{ \mu^{\text{el}} (e + e^\dagger) + \mu^{\text{nuc}} (v + v^\dagger) \right\} \\ &\cdot \sum_p i \left(\frac{2\pi\hbar\omega_p}{V} \right)^{1/2} \left\{ -v_p v_p' (\xi_p - \xi_p^\dagger) \right\} e^{ipr}. \end{aligned} \quad (7)$$

Here μ^{el} and μ^{nuc} are the electronic and vibrational dipole moments, respectively, and the creation (annihilation) operators of the electronic and vibrational excitations are denoted as e^\dagger (e) and v^\dagger (v), respectively. Transition

probability of one-, two-, and three-step excitation (labeled ①, ②, and ③ in Fig. 1) can be written as follows;

$$P_{\text{first}}(\omega_p) = \frac{2\pi}{\hbar} |\langle f_{\text{first}} | H_{\text{int}} | i \rangle|^2 = \frac{(2\pi)^2}{\hbar} v_p^2 v_p'^2 u_p'^2 (\mu^{\text{nucl}})^2 (\hbar\omega_p) I_0(\omega_p), \quad (8)$$

$$P_{\text{second}}(\omega_p) = \frac{2\pi}{\hbar} |\langle f_{\text{second}} | H_{\text{int}} | i \rangle|^2 = \frac{(2\pi)^3}{\hbar} v_p^4 v_p'^6 u_p'^2 (\mu^{\text{el}})^2 (\mu^{\text{nucl}})^2 (\hbar\omega_p)^2 I_0^2(\omega_p), \quad (9)$$

$$P_{\text{third}}(\omega_p) = \frac{2\pi}{\hbar} |\langle f_{\text{third}} | H_{\text{int}} | i \rangle|^2 = \frac{(2\pi)^4}{\hbar} \frac{v_p^6 v_p'^{10} u_p'^2 (\mu^{\text{el}})^4 (\mu^{\text{nucl}})^2 (\hbar\omega_p)^3 I_0^3(\omega_p)}{|\hbar\omega(p) - (E_a - E_i + i\gamma_m)|^2 |\hbar\omega(p) - (E_{\text{ex}} - E_g + i\gamma_m)|^2}, \quad (10)$$

where v_p and γ_m are the transformation coefficient from a photon to an exciton polariton and the linewidth of a vibrational level, respectively. The lower polariton frequency is represented as $\omega(p)$. Note that the energy locally transferred to a molecule is conserved, while the momentum is not conserved.

III. RESULT

It follows from (8) to (10) that the near-resonant transition probabilities have the following ratio

$$\frac{P_{\text{second}}(\omega_p)}{P_{\text{first}}(\omega_p)} = \frac{P_{\text{third}}(\omega_p)}{P_{\text{second}}(\omega_p)} = \frac{\hbar}{2\pi} \frac{P_{\text{first}}(\omega_p)}{\gamma_m^2} \left(\frac{v_p'^2}{u_p'^2} \right) \left(\frac{\mu^{\text{el}}}{\mu^{\text{nucl}}} \right)^2. \quad (11)$$

Using this ratio (11) and experimental deposition data for Zn dots dissociated from diethylzinc molecules, we analyze the intensity dependence of the deposition rate to clarify the origin of the near-field photochemical processes, i.e., the multiple-step transition via an excited state of a molecular vibrational mode. As a test case, two cases are examined: (i) the incident photon energy, 2.54 eV, corresponding to the wavelength of $\lambda = 488$ nm, is larger than the dissociation energy of a diethyl zinc (DEZn) molecule, 2.26 eV, but much smaller than the energies of the electronic excited states, and (ii) the incident photon energy, 1.81 eV, corresponding to the wavelength of $\lambda = 684$ nm, is smaller than both the dissociation and

electronic excitation energies required. In the first case, all the processes (①, ②, and ③) depicted in Fig. 1 are possibly allowed. Fitting $P_{\text{first}}(\omega_{488})$ to one experimental value shown in Fig. 2 as $P_{\text{first}}(\omega_{488}) = a_{488} I_0(\omega_{488}) = 10^2$ events/s with reasonable values of $\mu^{\text{nucl}} = 1$ Debye, $\mu^{\text{el}} = 10^{-2}$ Debye, $\gamma_m = 10^{-2}$ eV, and $v_p'^2/u_p'^2 = 0.2$, we obtain the following ratio

$$\frac{P_{\text{second}}(\omega_{488})}{P_{\text{first}}(\omega_{488})} = \frac{P_{\text{third}}(\omega_{488})}{P_{\text{second}}(\omega_{488})} = \frac{\hbar}{2\pi} \frac{P_{\text{first}}(\omega_{488})}{\gamma_m^2} \left(\frac{v_p'^2}{u_p'^2} \right) \left(\frac{\mu^{\text{el}}}{\mu^{\text{nucl}}} \right)^2 \simeq 10^{-15}, \quad (12)$$

which is in good agreement with the experimental values [8] $b_{488}/a_{488} \simeq c_{488}/b_{488} \simeq 10^{-15}$. Here the experimental deposition rate R is fitted as $R = a_\lambda I_0(\omega_\lambda) + b_\lambda I_0^2(\omega_\lambda) + c_\lambda I_0^3(\omega_\lambda)$, (shown in Fig. 2), and it is assumed to be proportional to the transition probability as $a_\lambda \propto P_{\text{first}}(\omega_\lambda)$, $b_\lambda \propto P_{\text{second}}(\omega_\lambda)$, and $c_\lambda \propto P_{\text{third}}(\omega_\lambda)$. In the second case, the dissociation occurs via either the ② or ③ process shown in Fig. 1. The ratio can be evaluated as

$$\frac{P_{\text{third}}(\omega_{684})}{P_{\text{second}}(\omega_{684})} = \frac{\hbar}{2\pi} \frac{P_{\text{first}}(\omega_{684})}{\gamma_m^2} \left(\frac{v_p'^2}{u_p'^2} \right) \left(\frac{\mu^{\text{el}}}{\mu^{\text{nucl}}} \right)^2 \simeq 10^{-15}, \quad (13)$$

which is also in good agreement with the experimental value $c_{684}/b_{684} \simeq 10^{-15}$. For the theoretical estimation, we have used

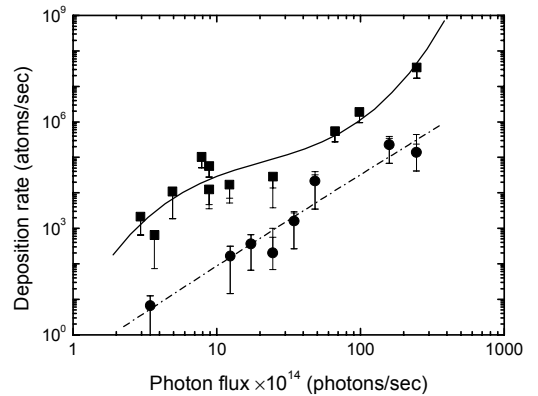


Figure 2. Zn deposition rate as a function of photon flux. Experimental data for photon energy 2.54 eV and 1.81 eV are represented by the rectangles and circles, respectively. The solid and dashed curves fit the results using the formula (see text).

the same experimental value as $P_{\text{first}}(\omega_{684}) \simeq a_{488} I_0(\omega_{488}) = 10^2$ events/s because both transitions are attributed to the coupling between phonons in the probe and molecular vibrations. The overall agreement between the theory and experimental results suggests that the exciton-phonon polariton model provides a possible way to understand the physical origin of the near-field photodissociation processes; the probe effect or the enhanced coupling between the optical near field and molecular vibration originates from the steep spatial gradient of the optical near field, and it cannot be described by the conventional perturbation method of the propagating light field-matter and the electron-phonon interactions.

IV. CONCLUSION

To clarify the physical origin of the NFO-CVD of nanometric Zn dots based on the photodissociation process of gas-phase diethylzinc under non-resonant conditions, we theoretically investigated incident photon energy and intensity dependence of the deposition rates. We analyzed the dependence, using multiple-step excitation process via the molecular vibrational levels as well as the exciton-phonon polariton model of an optical near-field probe proposed here. The overall agreement between the theory and experimental results was obtained. The enhanced coupling between the optical near field and the molecular vibration originates from the steep spatial gradient of the field. Such a non-adiabatic photochemical process can be applied to other near-field phenomena, and will be open up a new way in nanoscale science and technology.

ACKNOWLEDGMENT

The authors gratefully acknowledge valuable comments from H. Hori (Yamanashi Univ.), A. Shojiguchi, S. Sangu, T. Yatsui (Japan Science and Technology), H. Ito, and S. Takubo (Tokyo Inst. Tech.).

REFERENCES

- [1] M. Ohtsu, K. Kobayashi, T. Kawazoe, S. Sangu, and T. Yatsui, "Nanophotonics: design, fabrication, and operation of nanometric devices using optical near fields," *IEEE J. Selected Topics in Quantum Electronics*, vol. 8, pp. 839–862, 2002.
- [2] T. Kawazoe, Y. Yamamoto, and M. Ohtsu, "Fabrication of a nanometric Zn dot by nonresonant near-field optical chemical-vapor deposition," *Appl. Phys. Lett.*, vol. 79, pp. 1184–1186, 2001.
- [3] T. Yatsui, M. Ueda, Y. Yamamoto, T. Kawazoe, M. Kourogi, and M. Ohtsu, "Fabrication of nanometric single zinc and zinc oxide dots by the selective photodissociation of adsorption-phase diethylzinc using a nonresonant optical near field," *Appl. Phys. Lett.*, vol. 81, pp. 3651–3653, 2002.
- [4] S. Sangu, K. Kobayashi, A. Shojiguchi, T. Kawazoe, and M. Ohtsu, "Excitation energy transfer and population dynamics in a quantum dot system induced by optical near-field interaction," *J. Appl. Phys.*, vol. 93, pp. 2937–2945, 2003; T. Kawazoe, K. Kobayashi, S. Sangu, and M. Ohtsu, "Demonstration of a nanophotonic switching operation by optical near-field energy transfer," *Appl. Phys. Lett.*, vol. 82, pp. 2957–2959, 2003; K. Kobayashi, S. Sangu, A. Shojiguchi, T. Kawazoe, K. Kitahara, and M. Ohtsu, "Excitation dynamics in a three-quantum dot system driven by optical near-field interaction: towards a nanometric photonic device," *J. Microsc.*, vol. 210, 2003, in press.
- [5] K. Kobayashi, S. Sangu, H. Ito, and M. Ohtsu, "Near-field optical potential for a neutral atom," *Phys. Rev. A*, vol. 63, pp. 013806-1–9, 2001.
- [6] J. J. Hopfield, "Theory of the contribution of excitons to the complex dielectric constant of crystals," *Phys. Rev.*, vol. 112, pp. 1555–1567, 1958.
- [7] A. L. Ivanov, H. Haug, and L.V. Keldysh, "Optics of excitonic molecules in semiconductors and semiconductor microstructures," *Phys. Rep.*, vol. 296, pp. 237–336, 1998.
- [8] T. Kawazoe, private communications.

Functional Operations Using a Near-Field Optically Coupled Quantum-Dot System

Suguru Sangu, Kiyoshi Kobayashi
and Akira Shojiguchi
ERATO Localized Photon Project
Japan Science and Technology Corporation
687-1 Tsuruma, Machida
Tokyo, 194-0004 Japan
Email: sangu@ohtsu.jst.go.jp

Motoichi Ohtsu
Interdisciplinary Graduate School
of Science and Engineering
Tokyo Institute of Technology
4259 Nagatsuta-cho, Midori-ku, Yokohama
Kanagawa, 226-8502 Japan
Email: ohtsu@ae.titech.ac.jp

Abstract—We investigate the population dynamics in a three quantum-dot system coupled via an optical near field, which consists of a coherent operation part and an output part. We analytically show that a resonance condition between the two parts depends on initial excitation in the coherent operation part. Using this feature, AND- and XOR-gate operations are demonstrated in the case of symmetrically arranged quantum dots. We also evaluate the effects of asymmetric arrangement on these operations, and show that the coherence plays an important role in an asymmetric system.

I. INTRODUCTION

Conventional optical devices have been restricted in miniaturization and functional operations due to the diffraction limit of light. Nanophotonics, in which an optical near field instead of the far-field light plays important roles for signal input, output, and control, enables us to access nanometric elements individually in such a device far beyond the diffraction limit, and to bring about novel device technologies.

Together with development in nanofabrication techniques, one should consider a design for a nanophotonic device system. So far, we have proposed a nanophotonic switch which consists of a few quantum dots with discretized energy levels for resonant optical near-field coupling and with non-radiative relaxation to guarantee unidirectional signal transfer [1]. A characteristic feature in such a system is to use both of the coherent and incoherent process. As a typical example, in this paper, we consider a three quantum-dot system which is clearly separated into the coherent operation part and (incoherent) output part, and evaluate the characteristic dynamics for device operations.

Figure 1 is an illustration of the three quantum-dot system. Two identical quantum dots (QD-A and B) are resonantly coupled with each other via optical near-field interaction. The dynamics of a pair of quantum dots has been already investigated by various researchers [2], [3]. The energy transfer between two quantum dots is expressed as a Förster process [4], and nutation of excitation occurs in the strongly coupled or resonant energy levels. We call this coherently coupled two quantum-dot system a *coherent operation part*. By using an optical near field, initial excitation in each quantum dot

can be prepared independently because of the spatially high resolution. The coherent operation part makes certain excitation modes depending on the initial excitations. We briefly expect that specified excitation modes can be attracted if an energy level of the QD-C is set to resonantly couple to such excitation modes. The third quantum dot is named an *output part*, which involves non-radiative relaxation process due to exciton-phonon interaction in order to guarantee unidirectional energy or signal transfer.

For this system, we evaluate the dynamics of exciton population by using the density matrix formalism. This problem can be analytically solved in the case of a three quantum-dot system with symmetric arrangement, and we show in Sec. II that logical operations of AND- and XOR-gates can be achieved by adjusting energy configuration in the system. We also investigate the effects of asymmetric arrangement numerically, and discuss interesting aspects regarding to quantum states in the coherent operation part in Sec. III. Finally, the concluding remarks are presented in Sec. VI.

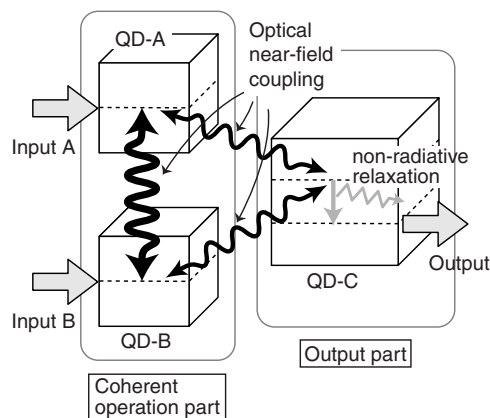


Fig. 1. A three quantum-dot system coupled via an optical near field.

II. POPULATION DYNAMICS AND FUNCTIONAL OPERATIONS

Here, we restrict our discussion to a symmetric system. A model Hamiltonian for this system is given by

$$\hat{H}_0 = \hbar\Omega\hat{A}^\dagger\hat{A} + \hbar\Omega\hat{B}^\dagger\hat{B} + \hbar\sum_{i=1}^2\Omega_{C_i}\hat{C}_i^\dagger\hat{C}_i, \quad (1a)$$

$$\hat{H}_{\text{int}} = \hbar U(\hat{A}^\dagger\hat{B} + \hat{B}^\dagger\hat{A}) + \hbar U'(\hat{B}^\dagger\hat{C}_2 + \hat{C}_2^\dagger\hat{B} + \hat{C}_2^\dagger\hat{A} + \hat{A}^\dagger\hat{C}_2), \quad (1b)$$

where creation and annihilation operators of an exciton in the QD-A, B, and C are described as $(\hat{A}^\dagger, \hat{A})$, $(\hat{B}^\dagger, \hat{B})$, and $(\hat{C}_i^\dagger, \hat{C}_i)$, respectively, and the subscripts $i = 1$ and 2 correspond to the lower and higher energy levels. The optical near-field interaction is denoted as U between the QD-A and B (coherent operation part) and U' between the QD-B and C or QD-A and C (output part). Equation of motion for the density operator is represented in Born-Markov approximation as

$$\dot{\hat{\rho}}(t) = -\frac{i}{\hbar}[\hat{H}_0 + \hat{H}_{\text{int}}, \hat{\rho}(t)] + \frac{\Gamma}{2} \left[2\hat{C}_1^\dagger\hat{C}_2\hat{\rho}(t)\hat{C}_2^\dagger\hat{C}_1 - \hat{C}_2^\dagger\hat{C}_1\hat{C}_1^\dagger\hat{C}_2\hat{\rho}(t) - \hat{\rho}(t)\hat{C}_2^\dagger\hat{C}_1\hat{C}_1^\dagger\hat{C}_2 \right], \quad (2)$$

where non-radiative relaxation is denoted as Γ . Radiative relaxation due to the coupling between excitons and free photons is omitted because the time scale of the optical near-field interaction and the exciton-phonon interaction is much faster than the spontaneous emission lifetime which is in the order of a few ns.

From the symmetry of the system, the following bases are suitable for describing the dynamics by using the smallest number of the density matrix elements:

$$|S_1\rangle = (|A^*BC_1C_2\rangle + |AB^*C_1C_2\rangle)/\sqrt{2}, \quad (3a)$$

$$|A_1\rangle = (|A^*BC_1C_2\rangle - |AB^*C_1C_2\rangle)/\sqrt{2}, \quad (3b)$$

$$|P_1'\rangle = |ABC_1^*C_2^*\rangle, \quad |P_1\rangle = |ABC_1^*C_2\rangle, \quad (3c)$$

when an exciton exists in the three quantum-dot system, which we call *one-exciton states*. The asterisk A^* denotes the exciton level in the QD-A. Similarly, *two-exciton states* mean that two excitons stay in the system. The suitable bases for the two-exciton states without occupation of the lower energy level in the QD-C are expressed as

$$|S_2'\rangle = (|A^*BC_1C_2^*\rangle + |AB^*C_1C_2^*\rangle)/\sqrt{2}, \quad (4a)$$

$$|A_2'\rangle = (|A^*BC_1C_2^*\rangle - |AB^*C_1C_2^*\rangle)/\sqrt{2}, \quad (4b)$$

$$|P_2'\rangle = |A^*B^*C_1C_2\rangle, \quad (4c)$$

and with occupation of the lower energy level as

$$|S_2\rangle = (|A^*BC_1^*C_2\rangle + |AB^*C_1^*C_2\rangle)/\sqrt{2}, \quad (5a)$$

$$|A_2\rangle = (|A^*BC_1^*C_2\rangle - |AB^*C_1^*C_2\rangle)/\sqrt{2}, \quad (5b)$$

$$|P_2\rangle = |ABC_1^*C_2^*\rangle, \quad (5c)$$

where $|S\rangle$ and $|A\rangle$ represent symmetric and asymmetric states in the coherent operation part, respectively, and the subscripts

1 and 2 on the left hand sides in (3), (4), and (5) denote the one- and two-exciton states. Applying the bases of (3) and (4) to (2) and substituting (1), the density matrix elements for the symmetric system read the following simultaneous differential equations:

$$\dot{\rho}_{S_1, S_1}(t) = i\sqrt{2}U'(\rho_{S_1, P_1'}(t) - \rho_{P_1', S_1}(t)), \quad (6a)$$

$$\dot{\rho}_{S_1, P_1'}(t) = [i(\Delta\Omega - U) - \Gamma/2]\rho_{S_1, P_1'}(t) + i\sqrt{2}U'(\rho_{S_1, S_1}(t) - \rho_{P_1', P_1'}(t)), \quad (6b)$$

$$\dot{\rho}_{P_1', S_1}(t) = [-i(\Delta\Omega - U) - \Gamma/2]\rho_{P_1', S_1}(t) - i\sqrt{2}U'(\rho_{S_1, S_1}(t) - \rho_{P_1', P_1'}(t)), \quad (6c)$$

$$\dot{\rho}_{P_1', P_1'}(t) = -i\sqrt{2}U'(\rho_{S_1, P_1'}(t) - \rho_{P_1', S_1}(t)) - \Gamma\rho_{P_1', P_1'}(t), \quad (6d)$$

$$\dot{\rho}_{P_1, P_1}(t) = \Gamma\rho_{P_1', P_1'}(t), \quad (6e)$$

and

$$\dot{\rho}_{S_2', S_2'}(t) = i\sqrt{2}U'(\rho_{S_2', P_2'}(t) - \rho_{P_2', S_2'}(t)) - \Gamma\rho_{S_2', S_2'}(t), \quad (7a)$$

$$\dot{\rho}_{S_2', P_2'}(t) = [-i(\Delta\Omega + U) - \Gamma/2]\rho_{S_2', P_2'}(t) + i\sqrt{2}U'(\rho_{S_2', S_2'}(t) - \rho_{P_2', P_2'}(t)), \quad (7b)$$

$$\dot{\rho}_{P_2', S_2'}(t) = [i(\Delta\Omega + U) - \Gamma/2]\rho_{P_2', S_2'}(t) - i\sqrt{2}U'(\rho_{S_2', S_2'}(t) - \rho_{P_2', P_2'}(t)), \quad (7c)$$

$$\dot{\rho}_{P_2', P_2'}(t) = -i\sqrt{2}U'(\rho_{S_2', P_2'}(t) - \rho_{P_2', S_2'}(t)), \quad (7d)$$

where the density matrix element $\langle\alpha|\hat{\rho}(t)|\beta\rangle$ is abbreviated as $\rho_{\alpha, \beta}(t)$, and the energy difference $\Omega_{C_2} - \Omega$ is replaced by $\Delta\Omega$. The equations of motion for the bases of (5) are not shown, but are similarly derived. Although the other matrix elements relating to the asymmetric states $|A\rangle$ also appear in the equations of motion, they are decoupled from the above equations and do not affect the population dynamics in the case of a symmetric system. Note that the states $|S_1\rangle$ and $|P_1'\rangle$ or $|S_2'\rangle$ and $|P_2'\rangle$ are coherently coupled with each other as seen in (6) and (7). Moreover, in comparison of the dynamics between the one- and two-exciton states, the energy difference in (6) and (7) differently contributes as $\Delta\Omega - U$ and $\Delta\Omega + U$. These terms determine the resonance conditions between the coherent operation part and the output part, which enables us to selectively pick out the information of either the one-exciton states or two-exciton states, i.e., the information about initial excitations in the coherent operation part. Therefore, logical operations are expected even in this simple system.

The analytic solutions of (6) and (7) can be readily obtained on the basis of the Laplace transformation. The results are plotted in Fig. 2 by using typical parameters for CuCl quantum cubes and our estimated optical near-field interactions [3]. Figure 2(a) shows the temporal evolution of the output population $\rho_{P_1, P_1}(t)$ for three typical energy differences $\Delta\Omega = -U, 0$, and U in the case of the one-exciton state. We find that the energy transfer is observed most efficiently at the condition $\Delta\Omega = U$, where the population can reach a half of the maximum value. The reason is as follows; the coherent

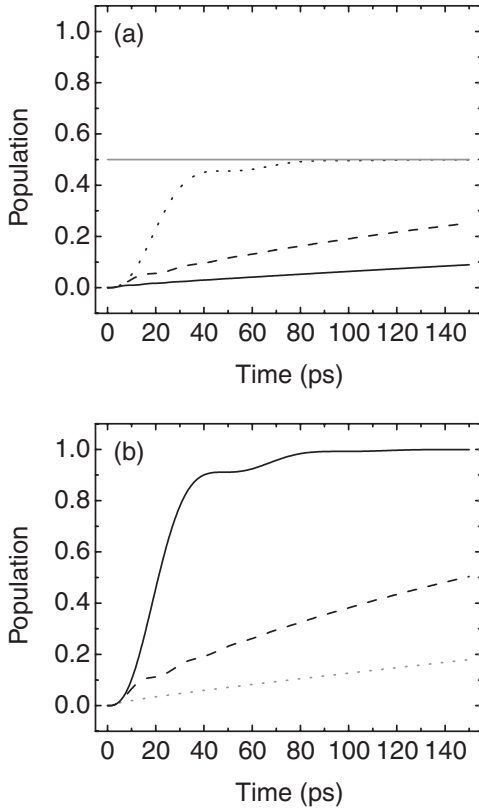


Fig. 2. Temporal evolution of output populations in the cases of (a) one-exciton state and (b) two-exciton state. The solid, dashed, and dotted curves represent for the energy difference $\Delta\Omega = -U$, 0 , and U , respectively. The fixed parameters are set as $U^{-1} = 3.3$ ps, $U'^{-1} = 20$ ps, and $\Gamma^{-1} = 10$ ps.

operation part couples with the output part in the one-exciton state through the states $|S_1\rangle$ and $|P_1\rangle$. However, when we use the initial condition as the only one quantum dot is excited, the state $|S_1\rangle$ is not fully excited. In other words, the state $|A_1\rangle$ which decouples with the state $|P_1\rangle$ in the symmetric system is simultaneously excited, and the population remains in the state $|A_1\rangle$ without temporally evolving. On the other hand, in the case of the two-exciton states (Fig. 2(b)), the energy transfer occurs under the resonance condition $\Delta\Omega = -U$, and the population can reach a unit value because the initial state is independent of the state $|A'_2\rangle$.

We summarize the results in Table I. When we set the energy difference as $\Delta\Omega = -U$, this system operates as an AND-gate. In contrast, for $\Delta\Omega = U$, it provides an XOR-like-gate operation. The value 0.5 means that the signal can be detected in the probability 1/2 against the initial excitation of the QD-A or B. In this stage, we proposed to realize the functional operations inherent in nanophotonic devices by assembling coherent and incoherent process.

III. EFFECTS OF ASYMMETRY ON POPULATION DYNAMICS

To consider the dynamics in an asymmetric quantum-dot system is meaningful for fabrication of the system mentioned above and/or to realize the other functional operations inherent

TABLE I
RELATION BETWEEN INPUT AND OUTPUT POPULATIONS

INPUT		OUTPUT	
A	B	$\Delta\Omega = -U$	$\Delta\Omega = U$
0	0	0	0
1	0	0	0.5
0	1	0	0.5
1	1	1	0

in nanophotonic devices. In this section, we investigate the effects of the asymmetry by means of numerically calculation. There are two types of asymmetry; the one originates from energy difference between the QD-A and B, and the other from the arrangement of three quantum dots. For simplicity, we pay our attention to only the effects of the latter one on temporal evolution of the excitation. In this case, the density matrix elements related to the asymmetric states $|A_i\rangle$ can be coupled to the states $|S_i\rangle$ and $|P_i\rangle$. Comparing to (6) and (7), the optical near-field interaction U' is replaced by the average value $\bar{U}' = (U_{BC} + U_{CA})/2$ in the asymmetrically arranged quantum-dot system, and the additional terms related to difference of the coupling strength $\Delta U' = (U_{BC} - U_{CA})/2$ appear, where U_{BC} and U_{CA} represent the coupling between the QD-B and C, and the QD-A and C, respectively. In order to examine the effects of the arrangement, the average coupling strength \bar{U}' is fixed so that the energy transfer between the coherent operation part and the output part maintains the same time evolution as the symmetric system. Here, an asymmetry factor is defined by the ratio of $\Delta U'$ to \bar{U}' . This factor varies from 0 (the symmetric system) to 1 (the maximumly asymmetric system).

Figure 3 is the plot of temporal evolution for the energy difference $\Delta\Omega = -U$ (an AND-gate) with and without the asymmetric arrangement. In the case of the one-exciton states (Fig. 3(a)), the asymmetric arrangement strongly affects the dynamics. This is caused that the resonant condition between the states $|S_1\rangle$ and $|P_1\rangle$ is opposite to that between the states $|A_1\rangle$ and $|P_1\rangle$. Therefore, the one-exciton states, which are off-resonant in the symmetric system, is quite sensitive to the asymmetric arrangement. In contrast, the effect of asymmetric arrangement is not observed in the two-exciton state. (See Fig. 3(b)) Similarly, in the case of an XOR-gate ($\Delta\Omega = U$), the two-exciton states correspond to the off-resonant states, and the excitation leaks the output energy level in the QD-C as the asymmetry factor becomes large, which is shown in Fig. 4(b). Consequently, the XOR-operation is reversed in the large asymmetric system, and the difference of the functional operations between $\Delta\Omega = -U$ and U disappears.

Finally, we discuss application of an asymmetric system to inherent nanophotonic functions. As mentioned above, the effect of asymmetry is based on the coupling to the states $|A_i\rangle$. In other words, populations of the states $|S_i\rangle$ and $|A_i\rangle$ can be taken out selectively by adjusting the arrangement of some quantum dots. Note that both states are expressed

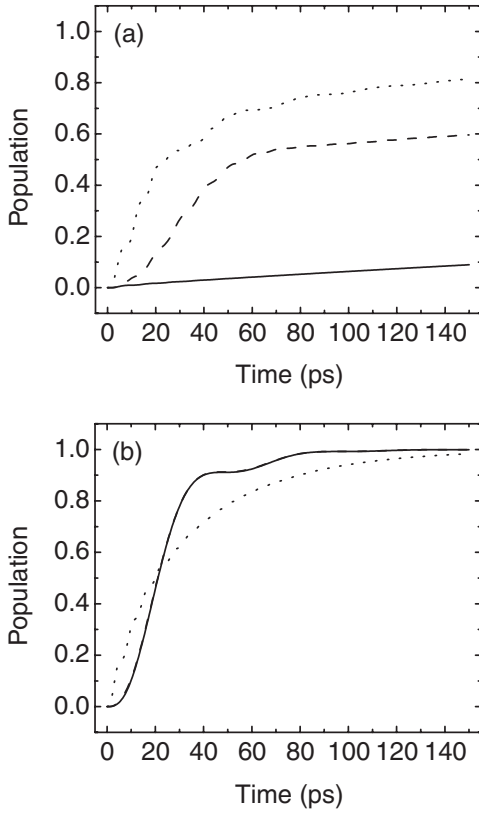


Fig. 3. Temporal evolution of output populations where the energy difference is set as $\Delta\Omega = -U$. Top and bottom figures are in the cases of (a) one-exciton state and (b) two-exciton state, respectively. The solid, dashed, and dotted curves represent for the asymmetry factor $\Delta U'/\bar{U}' = 0, 0.1, \text{ and } 1$, respectively. In the bottom figure (b), the solid and dashed curves are almost identical.

by superposition of eigenstates in isolated quantum dots. Therefore, the system constructed by only three quantum dots operates not only to choose some information depending on initially prepared excitations but also to do that reflecting the initial quantum state in the coherent operation part. From this point of view, information processing related to the coherence of the states may be developed by using such nanophotonics devices.

IV. CONCLUSION

In this paper, we have proposed inherent nanophotonic operations by using a three quantum-dot system. Such a system consists of a coherent operation part and an output part, and the excited states in the coherent operation part can be read out selectively by adjusting the energy level in an output quantum dot. First, we have obtained analytical solutions of the population dynamics in a symmetric system, and predicted that the system operates as an AND-gate at the energy difference being set as $\Delta\Omega = -U$ and an XOR-gate for $\Delta\Omega = U$. Then, we have numerically investigated the effects of asymmetric arrangement of the quantum dots. Although the asymmetric arrangement decreases the signal to noise ratio in the AND- and XOR-gates operations, it gives us a possibility to manipulate the information about quantum states

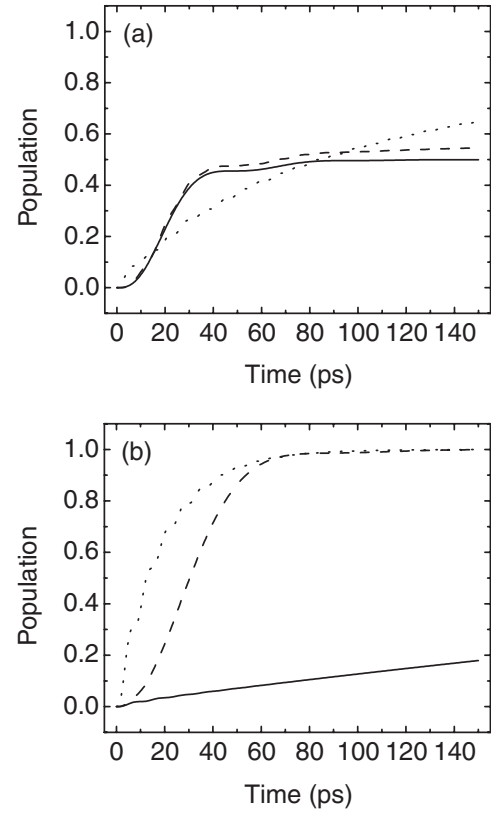


Fig. 4. Temporal evolution of output populations where the energy difference is set as $\Delta\Omega = U$. Top and bottom figures are in the cases of (a) one-exciton state and (b) two-exciton state, respectively. The solid, dashed, and dotted curves represent for the asymmetry factor $\Delta U'/\bar{U}' = 0, 0.1, \text{ and } 1$, respectively.

or coherence. In conclusion, we have proposed the functional operations by using a near-field optically coupled quantum-dot system as well as characteristic device operations inherent in nanophotonics including the coherent and incoherent process. Such a system can open up a novel way to nanoscale science and technology.

ACKNOWLEDGMENT

The authors thank Dr. T. Kawazoe (Japan Science and Technology Corporation) for kindly providing experimental information about CuCl quantum dots and the dynamics driven by the optical near-field interaction.

REFERENCES

- [1] M. Ohtsu, K. Kobayashi, T. Kawazoe, S. Sangu, and T. Yatsui, "Nanophotonics: design, fabrication, and operation of nanometric device using optical near fields," *IEEE J Sel. Top. Quant. Electron.*, vol. 8, pp. 839–862, July/August 2002.
- [2] E. Biolatti, R. C. Iotti, P. Zanardi, and F. Rossi, "Quantum information processing with semiconductor macroatoms," *Phys. Rev. Lett.*, vol. 85, pp. 5647–5650, December 2000.
- [3] S. Sangu, K. Kobayashi, A. Shojiguchi, T. Kawazoe, and M. Ohtsu, "Excitation energy transfer and population dynamics in a quantum dot system induced by optical near-field interaction," *J. Appl. Phys.*, vol. 93, pp. 2937–2945, March 2003.
- [4] Th. Förster, "Delocalized excitation and excitation transfer," in *Modern Quantum Chemistry*, O. Sinanoğlu, Ed. New York: Academic, 1965, pp. 93–137.

Cold-Atom Output from a Near-Field Optical Funnel

Akifumi Takamizawa¹, Haruhiko Ito², Shungo Yamada², Motoichi Ohtsu^{1,2}

¹ ERATO, Japan Science and Technology Corporation, 687-1 Tsuruma, Machida 194-0004, Japan

² Interdisciplinary Graduate School of Science and Engineering, Tokyo Institute of Technology, 4259 Nagatsuta-cho, Midori-ku, Yokohama 226-8502, Japan
e-mail: takami@ae.titech.ac.jp

Abstract— We demonstrated an atom funnel using blue-detuned near-field light. Cold Rb atoms generated by a magneto-optical trap (MOT) were introduced into the funnel and the output atoms were counted by an accumulative MOT detection system. The number of cold Rb atoms outputted from a 200- μm exit hole was maximal at a blue detuning of 1.2 GHz under Sisyphus cooling. The flux intensity was estimated to be 10^5 atoms/ cm^2s . To increase the flux intensity up to 10^{13} atoms/ cm^2s , we made an atom funnel with a 2- μm exit hole.

Keywords— component; atom funnel; cold atomic beam; dipole force; Sisyphus cooling

I. INTRODUCTION

Motion of atoms can be controlled by resonant forces of light. Indeed, reflection [1], deflection [2], diffraction [3], trapping [4] and cooling [5] of atoms have been demonstrated. Moreover, patterning of periodical micro/nano-structure has been conducted by channeling atoms with standing waves [6--8]. However, the conventional atom-optical methods using propagative light cannot precisely control atoms due to diffraction effects, so that it is difficult to make a nanostructure of an arbitrary shape including single dots. To manipulate atoms with high spatial accuracy beyond the diffraction limit, we use near-field light. Since near-field light decays as a Yukawa function, it exerts a strong dipole force on atoms.

We are developing a couple of near-field optical devices using the dipole force. One is a slit-type atom deflector that controls direction of atomic motion, where near-field light is induced in an edge of a 100-nm-wide slit [9]. The other is a single-atom trap using a sharpened fiber probe, where an atom is trapped near the nanometric tip by balance of a repulsive dipole force from blue-detuned near-field light with an attractive van der Waals force from a dielectric surface [10]. These techniques are used for optical nanofabrication and studies of quantum-mechanical phenomena relative to optical near field. For instance, they can be applied to atom-by-atom deposition [10] and detail study of interactions between atom and near-field light in a mesoscopic scale. We can also conduct non-demolition measurement of near-field light by using the atom-deflection method [10].

The above atom manipulation uses nanometric near-field light. Consequently, many atoms must come into the near-field region very slowly for the effective dipole interaction. If the near-field light is localized in a 10-nm region, the atomic flux density of 10^{12} $\text{s}^{-1}\text{cm}^{-2}$ and the atomic speed of less than 1 m/s (equals 100 μK in terms of temperature) are required. In order

to generate such cold atoms, we have developed an atom funnel composed of blue-detuned near-field light (evanescent light) [11].

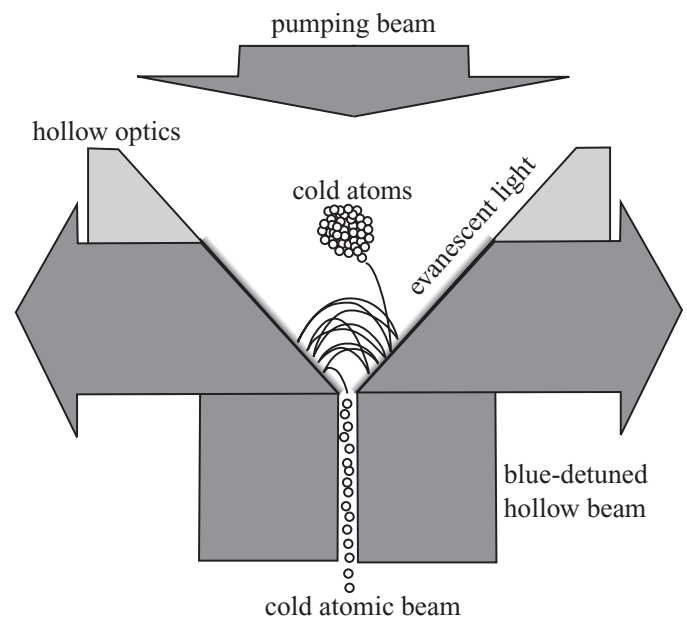


Figure 1. Sketch of a near-field optical funnel.

Figure 1 schematically shows the atom funnel. Cold atoms are first produced by a magneto-optical trap (MOT) [4] inside a reverse triangular hollow optics with a small exit hole at the bottom, and then released from MOT. A blue-detuned hollow light beam shone upward induces evanescent light on the inner-wall surface via total-internal reflection. The atoms that divergently fall by gravity are reflected every approaching the inner-wall surface by a repulsive dipole force from the evanescent light. Note that alkali-metal atoms such as Rb are regarded as the Λ -type three-level system composed of two hyperfine ground states and an excited state. When the light frequency is blue-detuned with respect to both ground states, the reflection potential for the lower ground state is higher than that for the upper ground state, since the light-shift energy is inversely proportional to the frequency detuning. If the atom in the lower ground state is transferred to the upper ground state in reflection, it loses the kinetic energy by the amount of potential difference. The energy-loss process is repeated (Sisyphus cooling [12, 13]) by returning the reflected atom to the lower ground state with an additional weak pumping light shone downward. Due to the Sisyphus cooling, atoms are

collected at the bottom and go out of the exit hole. Multi-loading of cold atoms from MOT forms a cold atomic beam with high flux intensity.

There are some advantages of the atom funnel, compared to the conventional methods using far-field light [14--16]. First, the Sisyphus cooling induced by near-field light compensates heating of atoms by gravity. Second, the small exit hole increases the flux intensity. Third, the fixed output of a cold atomic beam is controllable, so that the funnel can supply cold atoms to a point aimed at. Thus, the near-field optical funnel is a convenient source of a cold atomic beam for precise manipulation.

In our previous work [17], we observed multireflection of cold Rb atoms inside the funnel and estimated the optimum frequency detuning and excitation-light beam diameter from measurements of the reflection efficiency. In this paper, we report the first observation of cold atoms outputted from the funnel. Here, we detected atoms using an accumulative MOT system [18]. The number of funneled atoms was a function of the frequency detuning.

II. EXPERIMENT

Figure 2 shows an experimental setup with a double MOT configuration. The upper MOT generates cold ^{87}Rb atoms inside the funnel, while the lower MOT placed 25 cm below collects the output atoms. A reverse triangular hollow optics, hereafter we call funnel prism, is shown in Fig. 3. It consists of three quartz glass plates combined at right angle each other. Each plate has a 15-mm-long and 3-mm-thick side, and the refractive index $n = 1.45$ for the Rb resonant wavelength of 780 nm. The funnel prism is placed on the glass tube in a vacuum chamber. The bottom corner is ground flat and a triangular hole with a side of $320\ \mu\text{m}$ is made in the center.

Three orthogonal pairs of counterpropagating circularly-polarized ($\sigma^+ - \sigma^-$) laser beams for the upper MOT is applied through each plate of the funnel prism. The intensity and diameter of each cooling beam are $7\ \text{mW}/\text{cm}^2$ and 1 cm, respectively. The cooling beams are red-detuned by 10 MHz with respect to the $5S_{1/2}, F = 2 \rightarrow 5P_{3/2}, F = 3$ transition. Repumping laser beams tuned to the $5S_{1/2}, F = 1 \rightarrow 5P_{3/2}, F = 2$ transition are superimposed over the cooling beams to transfer ^{87}Rb atoms to the $5S_{1/2}, F = 2$ upper ground state. The intensity and diameter of each repumping beam are $5\ \text{mW}/\text{cm}^2$ and 1 cm, respectively. Vapor of Rb atoms is introduced into the upper chamber under a background pressure of 10^{-9} torr. A pair of anti-Helmholtz coils generates a quadrupole magnetic field with a gradient of 10 G/cm and spatially modulates the atomic Zeeman sublevels. The upper MOT produces a bright cloud of cold ^{87}Rb atoms. After 2 s, polarization gradient cooling [19] is conducted by turning off the magnetic field and stepwise changing the red-detuning to 80 MHz during 10 ms, so that the ^{87}Rb atoms are cooled down to the mean temperature of 9 μK . Then, they are released from the upper MOT by turning off all laser beams.

After release, the bottom of the funnel prism is illuminated by a $\text{Ti:Al}_2\text{O}_3$ laser beam with a power of 110 mW and the waist (full width of $1/e^2$ maximum) of 4 mm. Here, for

simplicity, we use a Gaussian beam instead of a hollow beam. In addition, for Sisyphus cooling, a $7\text{-}\mu\text{W}/\text{cm}^2$ pumping laser beam, which is red-detuned by 10 MHz with respect to the $5S_{1/2}, F = 2 \rightarrow 5P_{3/2}, F = 2$ transition, is shone downward to transfer ^{87}Rb atoms to the $5S_{1/2}, F = 1$ lower ground state. In order to avoid influence of the pumping beam on the output atoms from the funnel, we introduce it along a thalweg of the funnel prism. After illuminating with the excitation and pumping beams for 1 s, the generation of cold ^{87}Rb atoms by the upper MOT begins again. The generation and funneling of cold atoms are repeated 50 times.

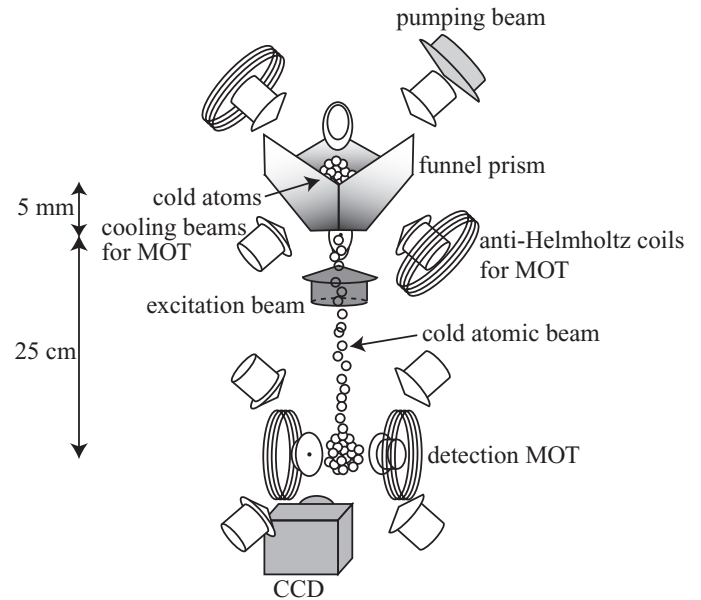


Figure 2. Experimental setup for a near-field optical funnel.

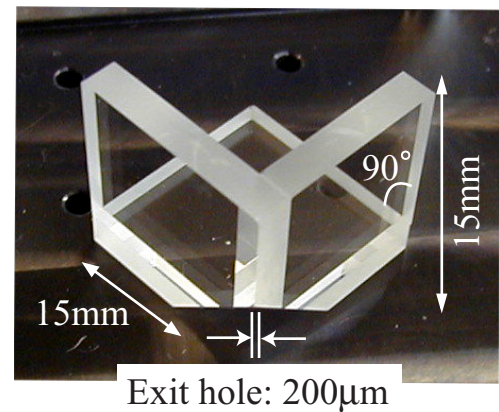


Figure 3. Photograph of a funnel prism.

^{87}Rb atoms coming out of the exit hole are captured by the lower MOT under a background pressure of 10^{-11} torr. Since the lower MOT is separated from the upper MOT by the hollow optics and the glass tube, it detects only the output atoms without background atoms. The cooling and repumping beams of the lower MOT have the same diameters of 2 cm so that all atoms coming through the connection tube can enter the capture region of the lower MOT. The intensity of each beam

is 1 mW/cm^2 . The cooling beams are red-detuned by 17 MHz with respect to the $5S_{1/2}, F = 2 \rightarrow 5P_{3/2}, F = 3$ transition. The other conditions of the lower MOT are the same as those of the upper MOT. The capture efficiency is 0.6 and ^{87}Rb atoms are trapped for 270 s [18]. Consequently, the lower MOT can accumulate the output ^{87}Rb atoms over funneling of the 50 times.

The number of trapped atoms is estimated from the intensity of resonant fluorescence measured with a charge-coupled device (CCD) camera. Figure 4 shows the result as a function of the frequency detuning measured with respect to the $5S_{1/2}, F = 1 \rightarrow 5P_{3/2}, F = 0$ transition. Note that some atoms escape the funnel prism straightforward without reflection. Then, in order to estimate the net number of funneled atoms, we subtract the number obtained without the pumping beam (no Sisyphus-cooling case) from that obtained with it (Sisyphus-cooling case). As you see, the number of funneled atoms is maximal at the blue detuning of +1.2 GHz, at which the funneled atoms occupy 50 % of the total outputted atoms.

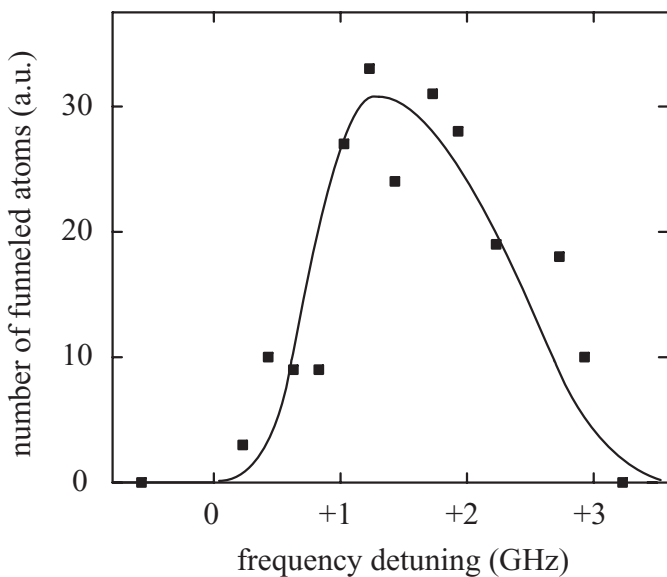


Figure 4. Number of funneled atoms plotted as a function of the frequency detuning of the excitation light beam.

III. DISCUSSION

The dipole force has a dispersion character with respect to an atomic resonant frequency [20]. It becomes attractive in the red-detuning region, while repulsive in the blue-detuning region. The maximum value of the reflection potential depends on the light intensity and the frequency detuning. Figure 4 shows the detuning dependence in the atomic funnel. Bounce to the area without near-field light and adherence to the inner-wall surface result in the loss of atoms.

A cold atomic beam is generated by multiloading from the upper MOT. In order to estimate the flux intensity, we first average the number of outputted atoms obtained at the blue detuning of +1.2 GHz over accumulation time of 50 s, and then divide the averaged value by the area of the exit hole. As a result, we get a flux intensity of $10^5 \text{ atom/cm}^2\text{s}$. On the other hand, according to the Monte-Carlo simulations we made, the

flux intensity reaches $4 \times 10^{11} \text{ atom/cm}^2\text{s}$ for a 200- μm exit hole [17]. For the small flux intensity in our experiment, we consider three reasons. First, the number of trapped atoms in the upper MOT is smaller than that we expect (10^8 atoms in a popular MOT) in the numerical simulations by two orders of magnitude. It may influence of the funnel prism. The center of the upper MOT is only 3 mm away from each glass plate. Second, the power of the excitation laser beam is weaker than that we assume by an order of magnitude. Third, we did not use a hollow light beam in the experiment. It led to heating on atoms due to scattering of the excitation laser beam. If the hollow light beam can be used, the light power will be increased. The experiment with a hollow excitation beam is now in progress. The hollow light beam also works as a guide of outputted atoms, in which atoms are confined by the repulsive dipole force [21].

IV. SUMMARY AND FUTURE

We conducted experiments of the atom funnel supported by blue-detuned evanescent light and observed cold Rb atoms outputted from the funnel with an MOT detection system. The flux intensity is estimated to be $10^5 \text{ atom/cm}^2\text{s}$.

For atom manipulation using 10 nm-sized near-field light, the flux intensity of more than $10^{12} \text{ atom/cm}^2\text{s}$ is required. To increase the flux density, we are going to perform experiments using a hollow excitation light beam. In addition, we have made a new funnel prism with a 2- μm exit hole by photolithography and anisotropic chemical etching of a silicon-on-insulator substrate [22], and drilling with a focused ion beam. In this case, the flux intensity and the mean temperature are estimated to be $6 \times 10^{13} \text{ atom/cm}^2\text{s}$ and 20 μK , respectively. Such a cold atomic beam will be used for precise control using near-field light.

References

- [1] V. I. Balykin, V. S. Letokhov, Yu. B. Ovchinnikov, and A. I. Sidorov, "Quantum-state-selective mirror reflection of atoms by laser light," *Phys. Rev. Lett.*, vol. 60, pp 2137-2140, 1988.
- [2] J. E. Bjorkholm, R. R. Freeman, and D. B. Pearson, "Efficient transverse deflection of neutral atomic beams using spontaneous resonance-radiation pressure," *Phys. Rev. A*, vol. 23 pp. 491-497, 1981.
- [3] P. E. Moskowitz, P. L. Gould, S. R. Atlas, and D. E. Pritchard, "Diffraction of an atomic beam by standing-wave radiation," *Phys. Rev. Lett.*, vol. 51, pp. 370-373, 1983.
- [4] E. L. Raab, M. Prentiss, A. Cable, S. Chu, and D. E. Pritchard, "Trapping of neutral sodium atoms with radiation pressure," *Phys. Rev. Lett.*, vol. 59, pp. 2631-2634, 1987.
- [5] S. Chu, L. Hollberg, J. E. Bjorkholm, A. Cable, and A. Ashkin, "Three-dimensional viscous confinement and cooling of atoms by resonance radiation pressure," *Phys. Rev. Lett.*, vol. 55, pp. 48-51, 1985.
- [6] G. Timp, R. E. Behringer, D. M. Tennant, J. E. Cunningham, M. Prentiss, and K. K. Berggren, "Using light as a lens for submicron, neutral-atom lithography," *Phys. Rev. Lett.*, vol. 69, pp. 1636-1639, 1992.
- [7] R. W. McGowan, D. M. Giltner, and S. A. Lee, "Light force cooling, focusing, and nanometer-scale deposition of aluminum atoms," *Opt. Lett.*, vol. 20, pp. 2535-2537, 1995.
- [8] C. Salomon, J. Dalibard, A. Aspect, H. Metcalf, and C. Cohen-Tannoudji, "Channeling atoms in a laser standing wave," *Phys. Rev. Lett.*, vol. 59, pp. 1659-1662, 1987.

- [9] K. Totsuka, H. Ito, K. Suzuki, K. Yamamoto, M. Ohtsu, and T. Yatsui, "A slit-type atom deflector with near-field light," *Appl. Phys. Lett.*, vol. 82, pp. 1616-1618, 2003.
- [10] H. Ito, and M. Ohtsu, "Near-field nano/atom optics and technology," M. Ohtsu Ed., Tokyo: Springer, 1998, pp. 217-266.
- [11] H. Ito, K. Sakaki, W. Jhe, and M. Ohtsu, "Atomic funnel with evanescent light," *Phys. Rev. A*, vol. 56, pp. 712-718, 1997.
- [12] J. Söding, R. Grimm, and Yu. B. Ovchinnikov, "Gravitational laser trap for atoms with evanescent-wave cooling," *Opt. Commun.*, vol. 119, pp. 652-662, 1995.
- [13] Yu. B. Ovchinnikov, I. Manek, and R. Grimm, "Surface Trap for Cs atoms based on Evanescent-Wave Cooling," *Phys. Rev. Lett.*, vol. 79, pp. 2225-2228, 1997.
- [14] E. Riis, D. S. Weiss, K. A. Moler, and S. Chu, "Atom funnel for the production of a slow, high-density atomic beam," *Phys. Rev. Lett.*, vol. 64, pp. 1658-1661, 1990.
- [15] K. Dieckmann, R. J. C. Spreeuw, M. Weidemüller, and J. T. M. Walraven, "Two-dimensional magneto-optical trap as a source of slow atoms," *Phys. Rev. A*, vol. 58, pp. 3891-3895, 1998.
- [16] Z. T. Lu, K. L. Corwin, M. J. Renn, M. H. Anderson, E. A. Cornell, and C. E. Wieman, "Low-velocity intense source of atoms from a magneto-optical trap," *Phys. Rev. Lett.*, vol. 77, pp. 3331-3334, 1996.
- [17] A. Takamizawa, H. Ito, and M. Ohtsu, "Multireflection of cold atoms in a near-field optical funnel," *Jpn. J. Appl. Phys.*, vol. 41, pp. 6215-6218, 2002.
- [18] A. Takamizawa, H. Ito, S. Yamada, and M. Ohtsu, "Accumulative atom detection by magneto-optical trap for near-field optical funnel," *Jpn. J. Appl. Phys.*, in press.
- [19] J. Dalibard, and C. Cohen-Tannoudji, "Laser cooling below the Doppler limit by polarization gradients: simple theoretical models," *J. Opt. Soc. Am. B*, vol. 6, pp. 2023-2045, 1989.
- [20] C. S. Adams, M. Sigel, and J. Mlynek, "Atom optics," *Physics Reports*, vol. 240, pp. 143-210, 1994.
- [21] S. Kuppens, M. Rauner, M. Schiffer, K. Sengstock, W. Ertmer, F. E. van Dorselaer and G. Nienhuis, "Polarization-gradient cooling in a strong doughnut-mode dipole potential," *Phys. Rev. A*, vol. 58, 3068-3079, 1998.
- [22] T. Yatsui, M. Kourogi, K. Tsutsui, M. Ohtsu, and J. Takahashi, "High-density speed optical near-field recording reading with a pyramidal silicon probe on a contact slider," *Opt. Lett.*, vol. 25, pp. 1279-1281, 2000.

Nano-optical CVD and Nanophotolithography using an Optical Near-Field Nonresonant to Electronic Transition

Tadashi Kawazoe, and Kiyosi Kobayashi

ERATO Localized Photon Project,
Japan Science and Technology Corporation
687-1 Tsuruma, Machida-shi, Tokyo 194-0004, Japan
e-mail: kawazoe@ohtsu.jst.go.jp

Motoich Ohtsu

Tokyo Institute of Technology
4259 Nagatsuta-cho, Midori-ku,
Yokohama, Kanagawa 226-8502, Japan

Abstract—In near-field optical chemical vapor deposition (NFO-CVD), photodissociation can take place under nonresonant conditions, *i.e.*, with visible light, due to the inherent properties of the optical near field. We succeeded the deposition of the nanometric Zn dots 70 nm wide and 24 nm high by NFO-CVD using the metal-organic gas $\text{Zn}(\text{acac})_2$, which is not usually used for conventional optical CVD due to its low optical activity. This technique makes it possible to use various light and gas sources to deposit a variety of nanometric materials. This peculiar photochemical reaction of an optical near field is not limited to optical CVD, but can be applied to general photochemical reactions. We demonstrate near-field photolithography using a 532 nm laser. The pattern fabricated on photoresist was 150 nm wide and 25 nm deep.

Keywords; Near-field optical CVD, Photo-chemical reaction, Photolithograph

I. INTRODUCTION

Optical near-fields have been applied to high-resolution optical microscopy, high-density optical memory, atom manipulation, and so on [1]. The spatial locality also leads to novel physical phenomena such as optically forbidden energy transfer [2] and giant second harmonic generation. These phenomena occur because optical near fields do not obey some of the physical principles of the optical far fields. We have studied the application of optical near field to nanostructure fabrication, by applying the novel properties of optical near field to photochemical reactions, and have demonstrated the feasibility of chemical vapor deposition (CVD) of Zn dots using optical near-field techniques [6-8]. We have used the high spatial resolution capability of optical near fields to deposit Zn wires 20 nm wide [3] and Zn dots 25 nm in size [4].

Conventional optical CVD utilizes a two-step process: photodissociation and adsorption. For photodissociation, far-field light must resonate the reacting molecular gasses in order to excite molecules from the ground state to an excited electronic state. The Franck-Condon principle holds that this resonance is essential for excitation. The excited molecules then relax to the dissociation channel, and the dissociated Zn atoms adsorb to the substrate surface. For near-field optical

CVD (NFO-CVD), however, photodissociation can take place under nonresonant conditions, due to the inherent properties of optical near fields. Recently, we succeeded in the photodissociation of metal organic molecules and the deposition of Zn dots using a nonresonant optical near field with a photon energy lower than the energy gap of the electronic state of the molecule [5]. This photochemical reaction is one of the unique phenomena that originate from the steep spatial gradient of the optical near field. In addition to optical CVD, these phenomena can be applied to many other photochemical nanotechnologies. In this paper, we report the deposition of nanometric Zn dots by NFO-CVD using the metal-organic gas diethylzinc (DEZn) and zinc-bis(acetylacetonate) ($\text{Zn}(\text{acac})_2$), which is not usually used for conventional optical CVD due to its low optical activity, and demonstrated the patterning by near-field photolithography using a 532 nm laser.

II. PHOTODISSOCIATION PROCESS

Figure 1 shows the potential curves of an electron in a DEZn molecular orbital drawn as a function of the internuclear distance of the C-Zn bond, which is involved in photodissociation [6]. The relevant energy levels of the molecular vibration mode are indicated by the horizontal broken lines in each potential curve. When a far-field light is used, photo-absorption (indicated by the white arrow in this figure) triggers the dissociation of DEZn. By contrast, when a nonresonant optical near field is used, there are three possible origins of photodissociation, as we have already proposed [5]. They are (1) the multiple photon absorption process, (2) a multiple step transition process via the intermediate energy level induced by the fiber probe, and (3) the multiple step transition via an excited state of the molecular vibration mode. Possibility (1) is negligible, because the optical power density in the experiment was less than 10 kW/cm^2 , which is too low for multiple photon absorption. Possibility (2) is also negligible, because NFO-CVD was observed for the light in the ultra-violet ~ near-infrared region, although DEZn lacks relevant energy levels for such a broad region. As a result, our experimental results strongly supported possibility (3), *i.e.*, that the physical origin of the photodissociation caused by a nonresonant optical near field is a transition to an excited state

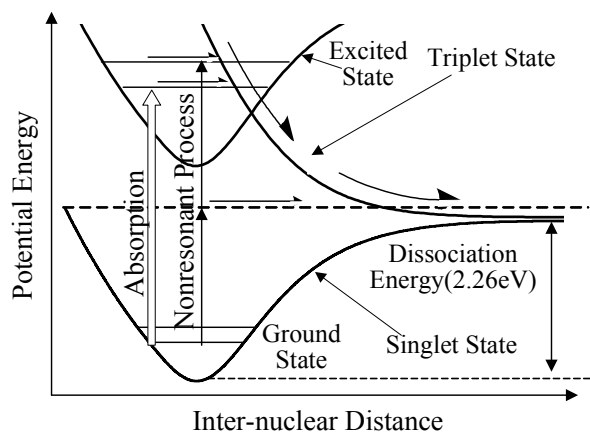


Fig. 1. Potential curves of an electron in DEZn molecular orbitals. The relevant energy levels of the molecular vibration modes are indicated by the horizontal lines.

via a molecular vibration mode. The multiple-step excitation processes in Fig. 1, indicated by the arrows (Nonresonant Process) contributed to this. To evaluate these contributions, we proposed an exciton-phonon polariton model. In this model, a light field in a nanometric structure can donate coherent phonons directly to a molecule, and the molecular vibration mode is excited by the coherent phonons. Multi-step excitation via the molecular vibration modes can make the nonresonant photodissociation possible. The detailed discussion of this model is presented by co-author Kobayashi in the paper_ID 17689.

III. NONRESONANT NFO-CVD

For NFO-CVD, the used fiber probe was high-throughput, single taper UV fiber probe that was fabricated by pulling and etching a pure silica core fiber [1], the cone angle and apex diameter were 30 degrees and less than 30 nm, respectively. To investigate deposition by nonresonant far-field light and an optical near field simultaneously, a fiber probe without an opaque metal coating, *i.e.*, a bare fiber probe, was used for deposition. An optical far field was generated by light leaking through the circumference of the fiber probe, while the optical near field was generated at the apex. The separation between the fiber probe and the sapphire substrate was regulated to within a few nanometers using a shear-force technique [1]. The optical power from the fiber probe was measured with a photo-diode placed behind the sapphire substrate. The size of the Zn dots deposited was measured with a shear-force microscope using the fiber probe used for deposition. Ultra-high purity argon (Ar) was used as the buffer gas and DEZn as the gas source of reactant molecules. A He-Cd laser ($\lambda=325$ nm) was used as the light source, that was nearly resonant with the absorption band edge of DEZn. Ar^+ ($\lambda=488$ nm) and diode ($\lambda=684$ nm) lasers were used as nonresonant light sources. During deposition, the partial pressure of DEZn and the total pressure in the chamber were maintained at 100 mTorr and 3 Torr, respectively. The chamber and substrate were kept at room temperature.

Figure 2 shows the shear-force topographical images of the sapphire substrate after NFO-CVD using optical near fields of $\lambda=325$ nm (a), $\lambda=488$ nm (b), and $\lambda=684$ nm (c). The laser

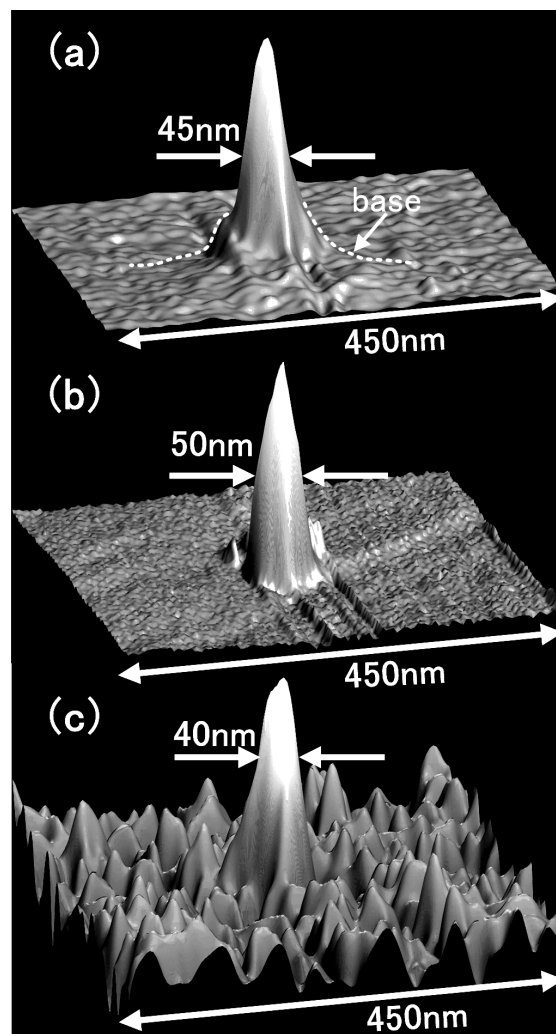


Fig. 2. Shear-force topographical images after NFO-CVD at wavelengths of $\lambda = 325$ (a), 488 (b), and 684 (c) nm. The scanning area are 450×450 nm. The observed laser output power and the irradiation time for deposition were $2.3 \mu\text{W}$ and 60 s (a), $360 \mu\text{W}$ and 180 s (b), and 1 mW and 180 s (c).

power and the irradiation time were (a) $2.3 \mu\text{W}$ and 60 s, (b) $360 \mu\text{W}$ and 180 s, and (c) 1 mW and 180 s, respectively. While the previous work using conventional CVD with a far-field light has claimed that a Zn film cannot be grown using nonresonant light ($\lambda > 300$ nm) [7], we observed the deposition of Zn dots on the substrate just below the apex of the fiber probe using NFO-CVD, even with nonresonant light. The chemical composition of the deposited material was confirmed by X-ray photoelectron spectroscopy; Zn was the principal ingredient. In Addition, we observed luminescence from nanometric ZnO dots, which were prepared by oxidizing the Zn dots fabricated by NFO-CVD. This experimental result implies that the purity of the Zn was high.

In Fig. 2 (a), the photon energy at $\lambda=325$ nm is higher than the dissociation energy of DEZn, and is close to the absorption band edge of DEZn. The diameter (full width at half maximum (FWHM)) and height of the topographical image were 45 and

26 nm, respectively. This image has a wide based, as shown by dotted curves. This base is a Zn layer, less than 2 nm thick, which is deposited by far-field light leaking from the bare fiber probe. This deposition is possible because DEZn absorbs a small amount of light with $\lambda=325$ nm. The very high peak in the image suggests that the optical near field enhances the photodissociation rate at this photon energy, because the optical near-field intensity rapidly increases near the apex of the fiber probe.

In Fig.2 (b), the photon energy still exceeds the dissociation energy of DEZn, but it is lower than the absorption edge of DEZn. The diameter and height of the image were 50 nm and 24 nm, respectively. While some high intensity far-field light leaked from the bare fiber probe, it did not deposit a Zn layer, so there is no foot at the base of the peak. This confirmed that the photodissociation of DEZn and Zn deposition only occurred with an optical near field of $\lambda=488$ nm.

In Fig.2 (c), even with such low photon energy at $\lambda=684$ nm, we succeeded in depositing of Zn dots. The topographical image showed a diameter and height of 40 nm and 2.5 nm, respectively. Experimental results in Fig. 2 demonstrate that the photodissociation process using a nonresonant optical near field violates the Franck-Condon principle.

IV. NFO-CVD OF $Zn(acac)_2$ AND PHOTOLITHOGRAPHY

Figure 3 shows the shear-force topographical image of the sapphire substrate after NFO-CVD using optical near fields of $\lambda=457$ nm (Ar^+ laser). In the experiment, $Zn(acac)_2$ was used as the gas source of reactant molecules. During deposition, the partial pressure of $Zn(acac)_2$ was maintained at 70 mTorr. The laser power and the irradiation time were 1 mW and 15 s, respectively. The diameter and height of the Zn dot were 70 nm and 24 nm, respectively. $Zn(acac)_2$ is not usually used for conventional optical CVD due to its low optical activity. However, in case of NFO-CVD, the optical near field can activate the molecule. In NFO-CVD, its deposition rate was

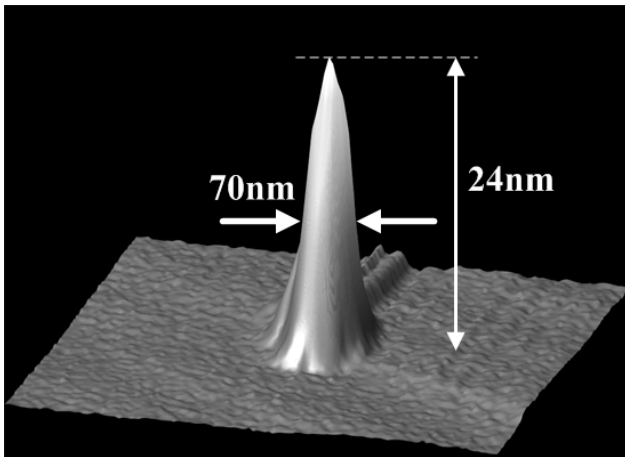


Fig. 3. Shear-force topographical images after NFO-CVD using $Zn(acac)_2$ at wavelengths of $\lambda = 457$ nm. The scanning area are 750×750 nm. The observed laser output power and the irradiation time for deposition were 1 mW and 15 s.

almost the same as that of deposition in which DEZn gas was used. For the conventional optical CVD, we carried out that DEZn has a deposition rate 1000 times higher than that of $Zn(acac)_2$. We suppose that the physical origin of the photodissociation of $Zn(acac)_2$ is same as it for DEZn in NFO-CVD.

This peculiar photochemical reaction of an optical near field is not limited to optical CVD, but can be applied to general photochemical reactions. We applied it to the photolithography.

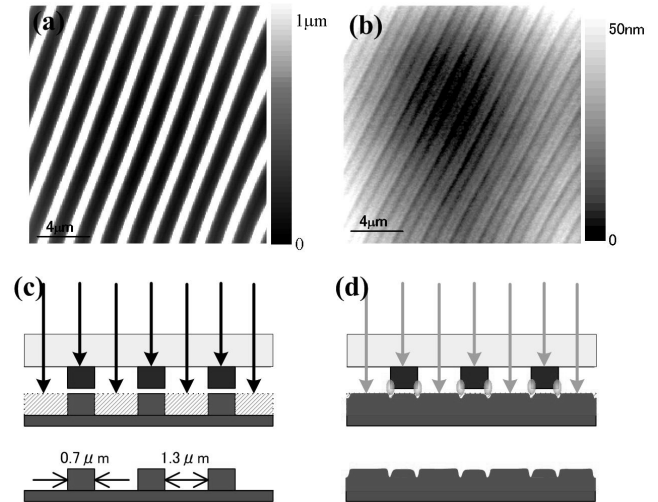


Fig. 4. (a) and (b) show atomic force microscope images of the photoresist after development for UV light source and 532nm laser, respectively. (c) and (d) show the schematic drawings of the exposure process in the UV and 532nm cases, respectively.

Figure 4 (a) and (b) show the atomic force microscope images of the photoresist (OFPR-800) surface after development for UV light source and 532nm laser, respectively. Although we used same photo-mask for them, the patterns developed on the photoresist were different each other. The ditch, fabricated on the photoresist for 532 nm, was 150 nm wide and 25 nm deep. We consider this result can be explained by the optical near-field effect. Figure 4 (c) and (d) show the schematic drawings of the exposure process using the UV and 532nm light source, respectively. For UV light the exposure process is conventional. For 532nm light source, although the photosensitivity is lower than it for UV light, the optical near field enhances the photosensitivity and photochemical reaction due to the same origins as the NFO-CVD. It can be readily supposed that the optical near field is strongly generated at around the edge of the mask pattern. Thus, the ditches were fabricated along the edges of the photo-mask pattern, as shown in Fig. 4(d).

V. CONCLUSION

In conclusion, we demonstrated NFO-CVD of nanometric Zn dots based on the photodissociation of gas-phase DEZn and $Zn(acac)_2$ using an optical near field under nonresonant conditions. The physical origin of the nonresonant optical CVD can be explained the multiple-step excitation process via

the molecular vibration mode and the exciton-phonon polariton model. In this model, the enhanced coupling between the optical field and molecular vibration originates from the steep spatial gradient of the optical power of the optical near field. Such a non-adiabatic photochemical process violates the Franck-Condon principle, and it can be applied to other photochemical phenomena. We demonstrated the near-field photolithography using 532nm light source, and confirmed the optical near field enhances the photosensitivity of the photoresist. The process involved in the photochemical reaction based on an optical near field reported here will open new method in nanotechnology.

- [1] M. Ohtsu, Ed., "Near-Field Nano/Atom Optics and Technology", Tokyo, Berlin, Heidelberg: Springer-Verlag, 1998.
- [2] T. Kawazoe, K. Kobayashi, J. Lim, Y. Narita, and M. Ohtsu, "Direct observation of optically forbidden energy transfer between CuCl

quantum cubes via near-field optical spectroscopy," *Phys. Rev. Lett.*, vol. 88, no. 6, pp. 067404-1-4, 2002.

- [3] V. V. Polonski, Y. Yamamoto, M. Kouroggi, H. Fukuda, and M. Ohtsu, "Nanometric patterning of zinc by optical near-field photochemical vapor deposition," *J. Microsc.*, vol. 194, pp. 545-551, 1999.
- [4] T. Yatsui, M. Ueda, Y. Yamamoto, T. Kawazoe, M. Kouroggi, M. Ohtsu, "Fabrication of nanometric single zinc and zinc oxide dots by the selective photodissociation of adsorption-phase diethylzinc using nonresonant optical near field" *Appl. Phys. Lett.* 81. 3651-3653 (2002).
- [5] T. Kawazoe, Y. Yamamoto, and M. Ohtsu, "Fabrication of a nanometric Zn dot by nonresonant near-field optical chemical vapor deposition," *Appl. Phys. Lett.*, vol. 79, pp. 1184-1186, 2001.
- [6] R. L. Jacson, "Vibrational energy of the monoalkyl zinc product formed in the photodissociation of dimethyl zinc, diethyl zinc, and dipropyl zinc," *J. Chem. Phys.*, vol. 96, pp. 5938-5951, 1992.
- [7] M. Shimizu, H. Kamei, M. Tanizawa, T. Shiosaki and A. Kawabata, "Low temperature growth of ZnO film by photo-MOCVD," *J. Crystal Growth*, vol. 89, pp. 365-370, 1988.

Observation of an optical near-field energy transfer in closely spaced ZnO/ZnMgO multiple-quantum-well nanorods for nanophotonic devices

T. Yatsui,^{a)} J. Lim,^{b)} T. Kawazoe,^{a)} K. Kobayashi,^{a)} M. Ohtsu,^{a),b)} W. I. Park,^{c)} and G.-C. Yi^{c)}

^(a) Ohtsu Localized Photon Project, ERATO, Japan Science and Technology Corporation, Tokyo, JAPAN
yatsui@ohtsu.jst.go.jp

^(b) Interdisciplinary Graduate School of Science and Engineering, Tokyo Institute of Technology, Kanagawa, JAPAN

^(c) Department of Materials Science and Engineering, POSTECH, Pohang, Kyungbuk, KOREA

Abstract—The optical properties of ZnO/ZnMgO multiple-quantum-well (MQW) nanorods were investigated by the optical near-field technique. Using a thin metal coated UV fiber probe, we performed spatially- and spectrally-resolved photoluminescence imaging of individual ZnO/ZnMgO MQW with a spatial resolution of 40 nm. Furthermore, we observed an anti-correlation feature in the PL intensity distributions. This is attributed to an optical near-field energy transfer in closely spaced pairs of ZnO/ZnMgO MQW nanorods.

ZnO/ZnMgO multiple-quantum-well, nanorod, optical near field, energy transfer

I. INTRODUCTION

For future optical transmission systems with high data transmission rates and capacity, we have proposed nanometer-scale photonic devices (i.e., nanophotonics devices) and a method of integrating them [1]. These devices consist of nanometer-scale dots, and an optical near-field is used as the signal carrier. As a representative device, a nanophotonic switch can be realized by controlling the dipole forbidden optical energy transfer among resonant energy states in nanometer-scale quantum dots via an optical near field [2]. It is composed of sub-100-nm scale dots and wires, and their size and position must be controlled on a nanometer-scale to fabricate the device. A nanometer-scale ZnO dot is a promising material for realizing these devices at room-temperature, due to its large exciton binding energy (60 meV). To confirm the promising optical properties and crystallinity of ZnO nanocrystallites, we measured the photoluminescence (PL) spectra using a low temperature optical near-field microscope. In this measurement, we found anti-correlation features in PL spectra between closely spaced ZnO/ZnMgO multiple-quantum-well (MQW) nanorods, which we attributed to optical near-field energy transfer.

II. ZNO/ZNMGO MQW NANORODS

We used the MQW nanorods which consist of ten periods of 3-nm ZnO/6-nm Zn_{0.8}Mg_{0.2}O as samples (a schematic

diagram of the MQW nanorods is shown in Fig. 1). These were grown on the ends of ZnO nanorods with a 40-nm mean diameter [3]. Using metalorganic vapor phase epitaxy (MOVPE), ZnO and Zn_{0.8}Mg_{0.2}O heterostructure were grown epitaxially with homogeneous in-plane alignment and a c-axis orientation on sapphire substrates without using any metal catalysts. This growth method ensures minimal intermixing, since no dissolution is required in a catalyst particle, and it creates sharp interfaces.

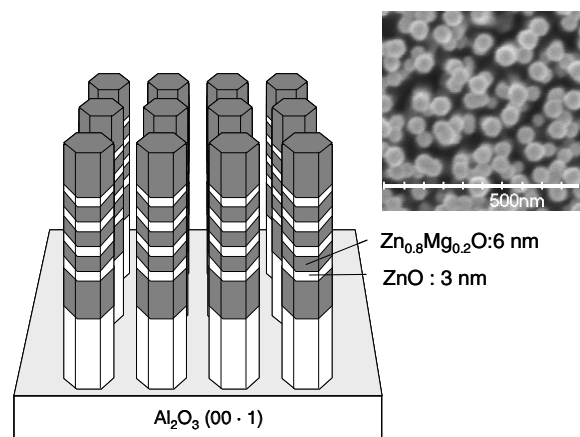


Figure 1. Schematic of multiple-quantum-well (MQW) nanorods consisting of 10 periods of ZnMgO/ZnO on the tips of ZnO nanorods. SEM image of the MQW nanorods (instet)

III. NEAR-FIELD SPECTROSCOPY

We investigated the optical properties in ZnO/ZnMgO MQW using a low-temperature scanning near-field optical microscopy (SNOM) system in collection-mode. UV fiber probe coated with 50-nm thick aluminum film was used for

scanning. He-Cd laser light ($\lambda = 325 \text{ nm}$) was employed to excite the ZnO nanocrystallites. The PL signal was collected by the fiber probe and detected by a cooled charge coupled device through a monochromator. The fiber probe was kept in close proximity to the sample surface ($\sim 10 \text{ nm}$) by the shear-force feedback technique.

In the far-field PL spectra taken at 15 K, blue-shifted PL emission peak was observed at 3.42 eV marked as an open square with a shoulder marked as an open triangle (solid line in Fig. 2). The value of the blue shift was consistent with the theoretical value of the quantum confinement effect in the ZnO well layer [4]. Furthermore, it is noted that the emission from well-known neutral-donor bound excitons (D_0, X ; 3.36 eV) in the ZnO nanorods is suppressed due to the good quality of crystallinity in the ZnO nanorods. While, in the near-field PL spectra obtained at 15 K, several sharp ($< 10 \text{ meV}$) peaks were observed in addition to the emission from D_0, X and free exciton (3.365 eV) in the ZnO nanorods. The number of the sharp peaks and their energy values (A_1 : 3.389 eV, A_2 : 3.402 eV, E_1 : 3.420 eV, E_2 : 3.426 eV, E_3 : 3.436 eV) in each spectrum showed strong position dependence.

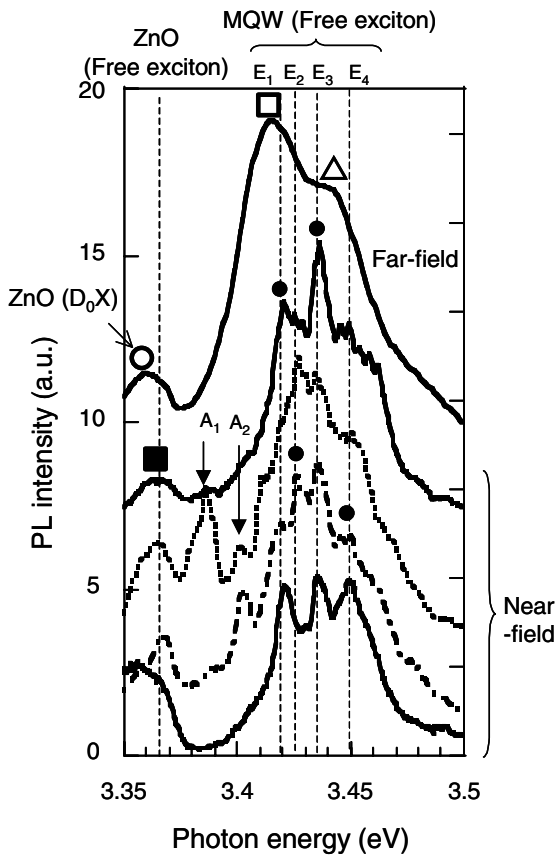


Figure 2. Far- and near-field PL spectra from ZnO/ZnMgO MQW nanorods.

To investigate their origins, we measured spatial distributions of PL intensity for individual ZnO/ZnMgO MQW nanorods the spectroscopy with a spatial resolution of 40 nm (see Figs. 4 and 5).

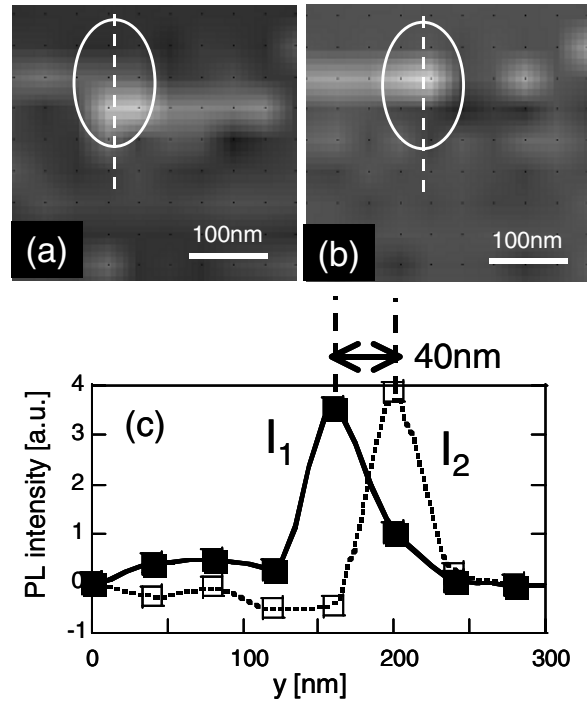


Figure 3. Monochromatic PL images of ZnO/ZnMgO MQW nanorods obtained at photon energy of (a) 3.420 and (b) 3.426 eV. (c) Closed and open squares represent cross-sectional profiles along the dashed lines in (a) and (b).

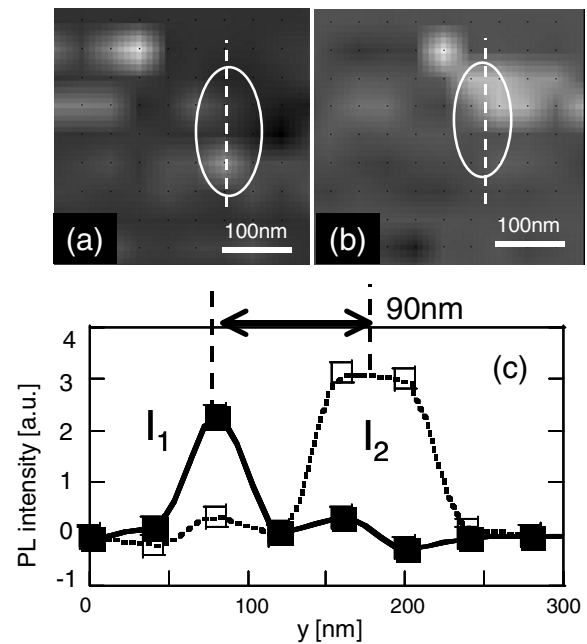


Figure 4. Monochromatic PL images of ZnO/ZnMgO MQW nanorods obtained at photon energy of (a) 3.420 and (b) 3.426 eV. These images are obtained at different position from those shown in Fig. 3. (c) Closed and open squares represent cross-sectional profiles along the dashed lines in (a) and (b).

Considering the energy differences among the excited states of electron and hole in the ZnO/ZnMgO MQW, E_1 and E_2 are originated from the ground state and excited state of holes in ZnO/ZnMgO MQW, respectively. It is noted that emission from E_2 is enhanced only in the near-field spectra, accompanied by the emissions from A_1 and A_2 .

From the above results, we consider a model in the PL process from closely spaced pairs of ZnO/ZnMgO MQW. Figure 5 illustrates the energy diagram of ZnO/ZnMgO MQW, where the emission from E_1 is expected to be dominant. Due to a deep potential depth to the vacuum of 4 eV [5], carrier tunneling between the nanorods can be neglected. Although the excited state E_2 is the dipole forbidden state and can not be detected in the far-field, it can be detected by optical fiber probe due to the near-field coupling of the probe and ZnO/ZnMgO MQWs (denoted by γ). This is supported by the facts that I_2 is suppressed in the far-field spectra. Furthermore, the emission from the ground state E_1 (denoted by the open square in Fig. 2) is dominated and the emission from the excited state E_3 (denoted by the open triangle in Fig. 2), while the excited states E_2 and E_3 were enhanced in the near-field spectra. Since A_1 and A_2 were obtained only in the close proximity of the probe, the charge transfer rate of α is smaller than the decay rate of E_1 without probe.

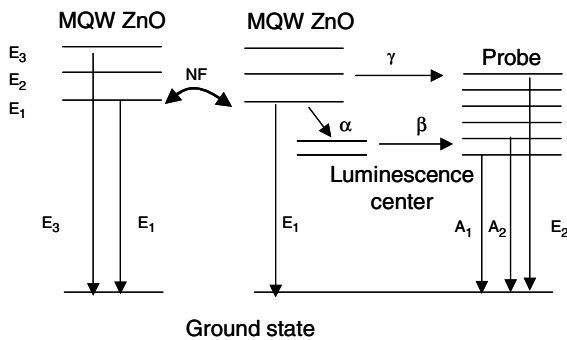


Figure 5. Model for closely spaced pairs of ZnO/ZnMgO MQW nanorods.

The outstanding feature was the anti-correlation in the PL intensity of E_1 (I_1) and I_2 ; I_1 was suppressed, while I_2 was enhanced in one nanorod, and I_1 was enhanced, while I_2 was suppressed in a closely adjacent nanorod. Furthermore, since the degree of the anti-correlation was larger for more closely spaced pair of nanorods, such an anti-correlation feature might be due to the optical near-field coupling between ZnO/ZnMgO MQW (denoted by NF in Fig. 5), *i.e.*, energy transfer phenomena induced by optical near field between two resonant energy levels in a ZnO/ZnMgO MQW and its adjacent ZnO/ZnMgO MQW.

IV. CONCLUSION

We performed spatially- and spectrally-resolved photoluminescence imaging of individual ZnO/ZnMgO MQW with a spatial resolution of 40 nm. We observed an anti-correlation feature in the PL intensity distributions, which is attributed to an optical near-field energy transfer in closely spaced pairs of nanorods. This phenomenon can be used to realize nanophotonic devices, such as the switching mechanism confirmed by the authors in CuCl quantum cubes [2].

ACKNOWLEDGMENT

Research by Park and Yi was supported by the Korea Research Foundation Grant (KRF-2002-041-C00098).

REFERENCES

- [1] M. Ohtsu, K. Kobayashi, T. Kawazoe, S. Sangu, and T. Yatsui, "Nanophotonics: Design, fabrication and operation of nanometric devices using optical near field," IEEE Journal of Selected Topics in Quantum Electronics **8**, 2002, pp.839-862.
- [2] T. Kawazoe, K. Kobayashi, S. Sangu, and M. Ohtsu, "Demonstration of a nanophotonic switching operation by optical near-field energy transfer," Appl. Phys. Lett. **82**, 2003, pp.2957-2959.
- [3] W. I. Park, G.-C. Yi, M. Kim, and S. J. Pennycook, "Quantum confinement observed in Zn/ZnMgO nanorod heterostructures," Adv. Mater., vol. 15, 2003, pp.526-529.
- [4] S. L. Chuang, in Physics of Optoelectronic Devices (Eds: J. W. Goodman), Wiley, New York, 1995, Ch. 4.
- [5] N.W. Wang, J. O. McCaldin, J. F. Swenberg, T. C. McGill, and R. J. Hauenstein, Appl. Phys. Lett. **66**, 1995, pp. 1974-1976.

[III] REVIEW PAPERS



特集：光微細加工技術とその応用 解説

ナノフォトンクス：近接場光による寸法・位置制御ナノ光加工

Nanophotonics: Size- and Position-Controlled Nanofabrication Using Optical Near Field

八井 崇*・大津元一*,**

Takashi YATSUI* and Motoichi OHTSU*,**

要旨 本稿では近接場光とその検出の原理について概説した後、物質間の近接場光のエネルギー移動の特異性について解説する。そして、近接場光のエネルギー移動を利用した加工技術であるナノフォトンクスを用いることで、伝搬光では原理的に不可能な形態の微細光加工の実際について列挙する。

Abstract This paper reviews the specific nature of nanophotonics, i.e., a novel optical nano-technology, utilizing local electromagnetic interactions between a small number of nanometric matters and optical near field. The size- and position-controlled fabrication of nano-scale structures is demonstrated using near-field optical chemical vapor deposition and size-dependent optical desorption.

キーワード：近接場光，ナノフォトンクス，ナノ光加工，寸法・位置制御ナノ光加工

Key words: optical near field, nanophotonics, size- and position-controlled nanofabrication

1. まえがき

従来の光技術では光の波動的性質を使っているが、この光の波は空間的に広がろうとする性質（回折）を持つ。従ってそれを凸レンズで集めても焦点面上での光のスポット径は波長程度以下にはならない。これが光リソグラフィなどの微細加工における加工可能最小寸法の限界を与えている。この限界（回折限界と呼ばれている）は加工のみでなく、光メモリの高密度化、光デバイスの微小化、高集積化の限界も与える。最近では光技術全般でこの回折限界に達しつつあり、ブレークスルーのための革新技术が待望されている。ナノフォトンクスはこの期待にこたえる技術であり、それは「近接場光のエネルギー移動を活用して微細な光加工を行ったり光デバイス機能を発現する技術」と定義されている^{*1}。

この技術では近接場光と呼ばれる小さな光を使うが、これは次節に概説するように近接場光とは物質表面近傍の、光の波長に比べ十分近い位置に発生する電磁場である。本稿では物質の寸法が波長に比べずっと小さい場合を考えるが、その表面に発生する近接場光のエネルギーを利用するとナノ寸

法の光加工が可能となる。また、近接場光を信号の担い手として使い、そのエネルギーをナノ寸法物質間で移動させると、新しい光デバイス機能が発現する。この方法により光の波長より小さい寸法をもつ光デバイス、すなわちナノフォトンクデバイス¹⁾が実現する。

ナノフォトンクスは光の波長以下でナノ寸法の光加工や光デバイス動作を実現する。しかし光の回折限界を超えたナノ寸法を実現することがナノフォトンクスの本質ではないことに注意されたい。本質的なことは「物質間の近接場光のエネルギー移動の性質が伝搬光のエネルギー移動の性質とは異なることを用いて、伝搬光では原理的に不可能な形態の微細光加工、光デバイス機能を実現する」ことであり、これにより光技術のパラダイムシフトが実現する。

本稿では材料技術を専門とする読者諸氏のために、まず2節で近接場光について概説した後、3節以降ではナノフォトンクスでのみ可能になるナノ寸法の光加工について列挙する。尚、ナノフォトンクスの基礎および近接場光の詳細については参考文献2-4などを参照されたい。

平成 16 年 5 月 19 日受付・受理 Received and accepted 19th, May 2004

*科学技術振興機構 SORST ナノフォトンクスチーム 〒194-0004 東京都町田市鶴間 687-1 天幸ビル 17 4 階
SORST, Japan Science and Technology Agency, 687-1 Tsuruma, Machida-shi, Tokyo 194-0004, Japan

**東京大学大学院工学系研究科電子工学専攻 〒113-8656 東京都文京区本郷 7-3-1
School of Engineering, The University of Tokyo, 7-3-1 Hongo, Bunkyo-ku, Tokyo 113-8656, Japan

*1「ナノフォトンクス」は筆者が 1993 年頃に命名したものであり、従来の光技術において伝搬光のエネルギー移動を利用して加工、光デバイス機能を発現させるのが「フォトンクス」であることに対応している。このアイデアに基づき、筆者が代表幹事となり（財）光産業技術振興協会では 1995 年～2003 年にわたり「ナノフォトンクス懇談会」が運営され、ナノフォトンクスに関連する技術の基礎、応用、実用化に関する産官学の活動があった。

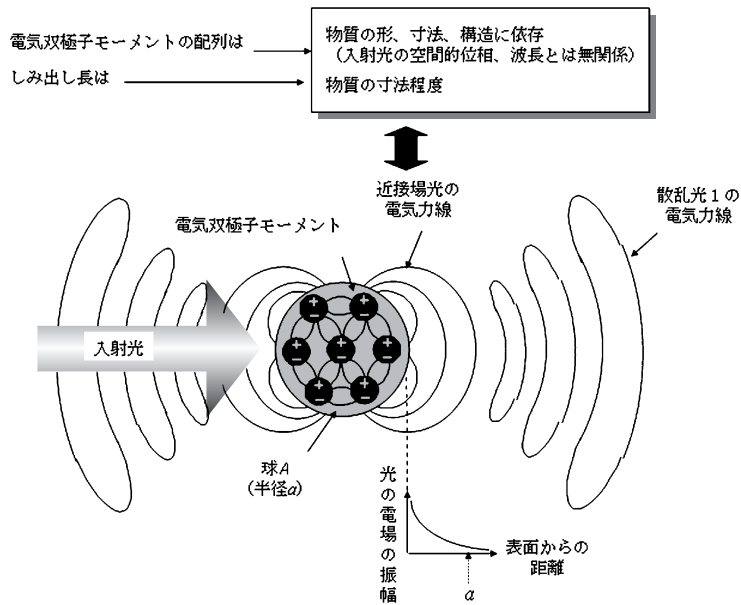


Fig. 1 近接場光の発生の様子.

2. 近接場光とその検出

近接場光とは物質表面近傍の、光の波長に比べ十分近い位置に発生する電磁場である。ここでは物質の寸法が波長にくらべずっと小さい場合を考える。近接場光は (a) 非伝搬 (物質表面に局在している), (b) エネルギーは物質表面から遠ざかるにつれ減少 (その減少の割合を表す「しみ出し長」は物質の寸法程度), という 2 つの性質を持つ。

Fig. 1 は近接場光の発生の様子を示している。すなわち半径 a の電的に中性な物質 (球 A) に光が入射したとき、その中の多数の原子に時間的に振動する電気双極子モーメントが誘起され、その電気双極子モーメントから電磁場が発生する。この電磁場を表す電気力線は電気双極子モーメント同士を結び、その一部は球 A の外にしみ出している。このしみ出した電気力線が表す光が近接場光である。この電気力線は電気双極子モーメントから発して電気双極子モーメントに終端しているので非伝搬であることを表している (性質 (a) に対応)。その外側にある閉曲線状の電気力線は遠方へと回折しながら伝搬する光を表すが、これは従来の光技術で使われている光である (散乱光 1 と呼ぶ)。半径 a が入射光の波長にくらべずっと小さい場合、発生する多数の電気双極子モーメントの配列の仕方は入射光の空間的位相、波長とは無関係となり、球 A の形、寸法、構造に依存するので、近接場光のしみ出し長は球 A の半径 a 程度となる (性質 (b) に対応)*2。

近接場光は非伝搬なので、近接場光の発生 (Fig. 1) のみの

考察では不十分で、検出についての考察が必須である。検出するためには Fig. 2 のように近接場光の中に第二の球 B を置くことによって近接場光を乱す。乱された近接場光は散乱光 2 (散乱光 2 と呼ぶ) となって遠くに伝搬するので、光検出器を用いれば散乱光 2 のパワーを測定できる。これが近接場光の検出過程である。

Fig. 2 のように近接場光に起因する電気力線が 2 つの球を結びつけているということは近接場光が 2 つの球により多重

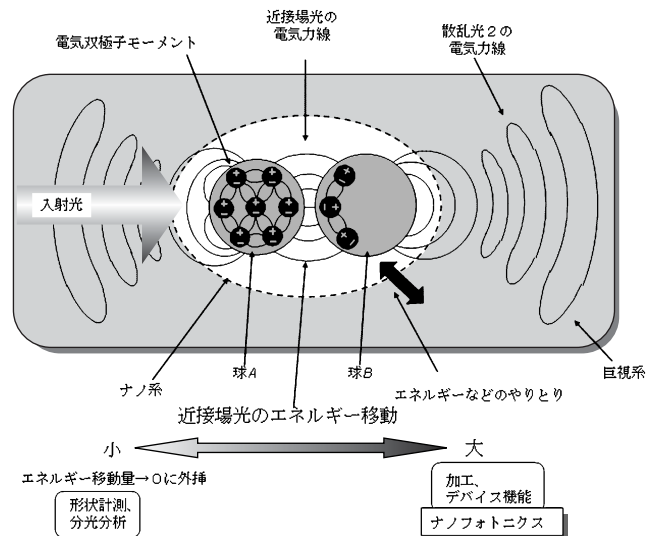


Fig. 2 近接場光の測定の様子。破線の楕円はナノ系と巨視系との間の境界を表す。

*2 無限平面境界をはさんで 2 つの物質が接するとき屈折率の高い物質から屈折率の低い物質へと光が伝搬すると全反射が起こる。このとき境界面にエバネッセント光と呼ばれる表面波が発生する。その性質は近接場光の性質とよく似ているが、そのしみ出し長は光の波長程度である。この違いは電気双極子モーメントの配列の仕方に起因する。これらの電気双極子モーメントの配列の仕方は入射する光と反射光の空間的位相によって決まり、規則正しく周期的に無限に並ぶ (その周期は入射光と反射光の波長に他ならない)。これらの電気双極子モーメント同士をつなぐ物質表面付近の電気力線がエバネッセント光を表す。これらの電気力線の総和から決まるエバネッセント光のしみ出し長は電気双極子モーメントの配列の仕方と同様に入射光の空間的位相に依存し、光の波長程度となる。近接場光を使うと光の回折限界を超えたナノ寸法の光技術が可能になるのは電気双極子モーメントの配列の仕方が入射光の空間的位相とは無縁だからである。この点においてエバネッセント光は依然として従来の光学の枠組みの中に留まっており、近接場光とは異なる。

散乱されることを意味している。いいかえると近接場光のエネルギーが2つの球の間を移動している。このように近接場光の検出の過程で発生するエネルギー移動を積極的に利用すると球Aを用いて球Bを加工したり、新しい光デバイス機能を発現させることができる。即ち一方の球が他方の球の光学的特性、構造、形状を変化させる。近接場光はこのような応用に適している。

一方、物質の形状や構造を測定する顕微鏡、分光分析装置などへの応用では測定試料の状態を乱してはいけないので近接場光のエネルギー移動が少ない状態で用い、得られたデータの解析の際にはエネルギー移動が0の状態を推定する。しかし実際にはこのような極限状態への外挿は非常に困難なので、無理のある使い方である。以上の関係を Fig. 2 の下部に示す。

ナノフォトニクスで本質的なことは「物質間の近接場光のエネルギー移動の性質が伝搬光のエネルギー移動の性質とは異なることを用いて、伝搬光では原理的に不可能な形態の微細な光加工、光デバイス機能を実現する」ことである。これは(1)近接場光のエネルギーが光の波長よりもずっと小さい寸法の空間に局在していること、(2)Fig. 2に示すように近接場光、微粒子からなるナノ寸法の系が熱浴(入射光、散乱光、基板、などからなる巨視的寸法の系)の中に埋もれており、両系の間でエネルギーなどのやりとりがあること、などに起因する。なお、これらの考え方は互いに共通する内容を別の表現で述べているにすぎない。これらを統一的に記述するには波動光学の枠組みでは不十分で、特に微小物質との電磁気学的相互作用をとりいれ、さらに巨視系の中に埋もれたナノ系としての振る舞いを記述するために量子論が必要となる。これらの詳細の議論は参考文献2, 3を参照されたい。

以上で述べた近接場光の性質、現象は普遍的である。これらを利用することにより光技術のパラダイムシフトを実現することがナノフォトニクスの本質である。波長に比べずっと小さな光技術を実現することは副次的な成果にすぎない。以下の節ではナノフォトニクスの特徴を利用したナノ光加工について列挙する。

3. 近接場光によるナノ光加工

3.1 化学気相堆積法

ナノフォトニックデバイスに代表されるナノ寸法のデバイス製作手法として、露光装置とエッチングを用いる加工法(トップダウン)と原子・分子を積み上げる加工法(ボトムアップ)が挙げられる。トップダウンは、近年X線や電子線を用いたリソグラフィにより20 nm以下の精度の加工が可能であるが⁵⁾、「削る」ことによる加工が主となるため基板などの損傷が問題となる。これに対してボトムアップは「積み上げる」加工のため損傷は回避できる。近年、量子ドットレーザーなど、量子ドットが高密度に形成されたデバイスを作製

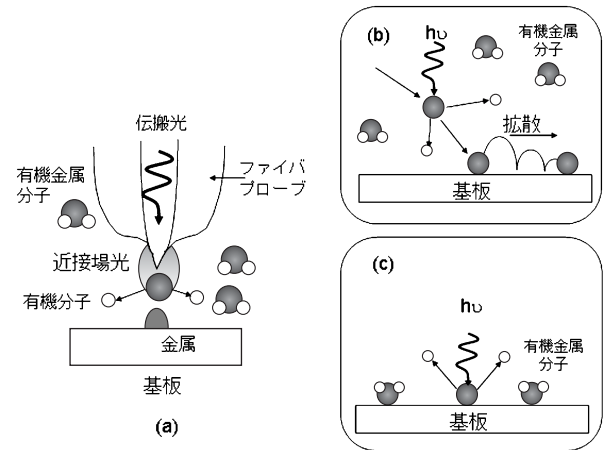


Fig. 3 (a) 近接場光化学気相堆積法 (NFO-CVD). (b) 気相分子による堆積. (c) 吸着分子による堆積.

するために自己組織化による方法が広く用いられている。これは材料原子・分子と基板との相互作用および熱力学的平衡状態を利用して大面積にわたり様に量子構造を作製する手法である⁶⁾。しかし、この方法では所望の寸法の量子ドットを所望の位置に配置することや、異種ドットを隣接して配置することは困難である。

これに対して、原料分子を光により解離し、堆積させる光化学気相堆積法(光CVD法)は、様々な材料を任意の場所に高精度に堆積することが可能である⁷⁾。通常、光は回折限界により波長寸法以下に絞ることはできないため、光CVD法における加工精度は光の波長程度であるが、近接場光を用いることで光の波長より遥かに小さな寸法の微細加工が可能である。この近接場光CVD法(NFO-CVD)を用いれば、ナノ寸法の構造物を高精度に配置し、任意の大きさ・異種の構造体を組み合わせて堆積することができる。

NFO-CVDの例としてファイバプローブ先端に発生する近接場光により金属亜鉛^{*3}(Zn)を堆積する場合を説明する(Fig. 3(a))⁸⁾。

Znの原料として有機金属分子(ジエチル亜鉛: $\text{Zn}(\text{C}_2\text{H}_5)_2$)を用い、これを光により解離し、析出したZn原子を基板に堆積する。ここで問題となるのが、気相中で解離された金属原子の拡散である。これは、解離された金属分子が堆積する基板上で吸着し核となるまでに基板上を拡散してしまうため、堆積されるドットの寸法がファイバプローブ先端に発生する近接場光エネルギーの空間的分布よりも大きくなってしまふ(Fig. 3(b))。この問題を解決する為、基板に吸着した分子の吸収スペクトルが気体分子のそれに対して長波長側にシフトする性質⁹⁾を利用し、吸着分子を選択的に解離し堆積する方法が試みられている(Fig. 3(c))。実験は、原料である $\text{Zn}(\text{C}_2\text{H}_5)_2$ の気相分子の吸収スペクトル端($\lambda=270\text{ nm}$)よりも僅かに長い波長325 nmの光源を用いて行った。この結果、気相分子に対して強い吸収を有する波長244 nmでの堆積物(Fig. 4(a), および Fig. 4(c)の破線)と比較して、波長325 nm

*3 金属亜鉛を酸化した酸化亜鉛は古くから使われているが、最近では室温で動作するナノフォトニックデバイスの材料としても期待されている。

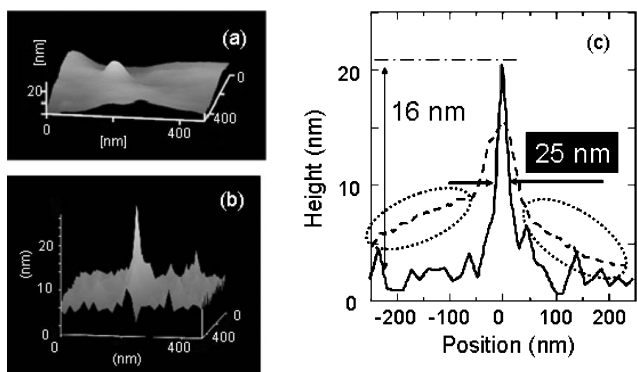


Fig. 4 波長 (a) 244 nm・(b) 325 nm を用いて NFO-CVD により堆積された Zn ドット. (c) (a) 及び (b) の断面図.

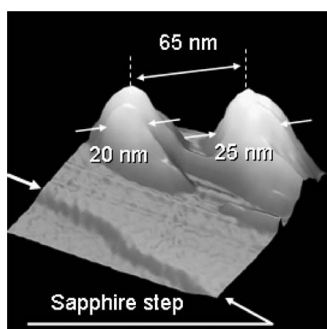


Fig. 5 NFO-CVD による Zn 微粒子の堆積結果.

を用いて堆積した結果、幅 25 nm・高さ 16 nm の高アスペクト比を有する Zn の堆積 (Fig. 4 (b), および Fig. 4 (c) の実線) が確認されている¹⁰⁾. さらには、このようなナノ寸法微粒子を堆積させる際にファイバプローブを走査して複数箇所に固定することで、30 nm 以下の Zn 微粒子の作製が 65 nm の間隔で可能となっている (Fig. 5)¹¹⁾.

ここで、堆積速度の特性について考えるために、サファイヤ基板上に堆積された Zn 微粒子の堆積速度の測定値を Fig. 6 (a) に示す. 図中の■印、●印は各々ファイバプローブへの入射光パワーが 10 μW, 5 μW の場合の測定結果であるが、縦軸は入射光パワーで規格化した堆積速度の値を表している. 横軸は Zn 微粒子の基板面内の寸法である. また図中の $2a_p$ (=9 nm) はファイバプローブ先端の曲率直径である. この結果から、Zn 微粒子の寸法が $2a_p$ に一致したときに、堆積速度が極大となっていることがわかる. つまり、基板上での Zn 微粒子の成長過程において、この堆積された Zn 微粒子とファイバプローブ先端との近接場相互作用は、微粒子寸法が $2a_p$ となったときに最も強くなり、それが堆積速度の極大となって現れている. すなわち堆積速度は物質寸法に依存して共鳴的に増加する. この共鳴効果は、双極子間相互作用の理論から定量的に説明される. 近似としてファイバプローブ先端と Zn 微粒子を各々球 A および球 B 中の双極子により近似し (Fig. 6 (b) 参照), これらの球同士での双極子間相互作用を算出する (詳細は参考文献 2 の第 4 章を参照されたい). ここで、球 A の直径を 9 nm (= $2a_p$) とし、Zn 微粒子である球 B の大きさ ($2a_s$) を変化させた時の、球同士での近接場によ

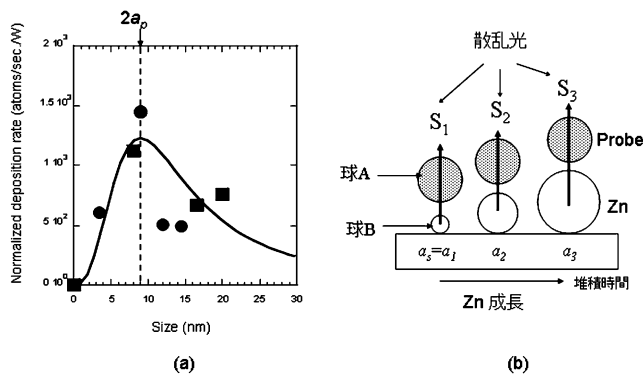


Fig. 6 (a) 入射光パワーで規格化された堆積速度. 横軸は堆積された Zn 微粒子の基板面内寸法. 実線は双極子間相互作用により求められた散乱光 2 の強度 (図 (b) の $S_1 \sim S_1$) を示す. ■印および●印は各々入射光パワーが: 10 μW, 5 μW の場合の測定結果である. (b) 微粒子が堆積されその寸法が増加する様子の説明図.

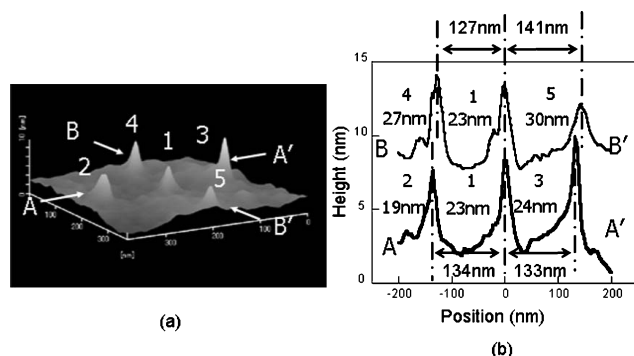


Fig. 7 NFO-CVD により堆積された Al 微粒子の (a) 形状像, および (b) 断面像.

り結合された双極子間相互作用から求められる散乱光強度 (Fig. 2 の散乱光強度 2 および Fig. 6 (b) の $S_1 \sim S_3$) を求めた結果を Fig. 6 (a) の実線に示す. Fig. 6 (a) に示されるように、堆積速度の実験結果と双極子間相互作用による散乱光強度との良い一致から、堆積過程におけるプローブ先端と微粒子との物質寸法に依存し共鳴する効果が観測されたことが確認できる¹²⁾.

次に、位置制御性について考えるために、Fig. 7 に波長 244 nm の光によりトリメチルアルミニウム ($\text{Al}(\text{CH}_3)_3$) 分子を解離してアルミニウム (Al) の微粒子をサファイヤ基板上に近接して 5 つ作製した結果を示す. これは直径 25 nm の Al の微粒子を間隔 130 nm で形成するためにファイバプローブ先端の寸法、位置を調節した結果である. 5 つの微粒子の直径は 25 ± 6 nm, 間隔は 130 ± 4 nm となっており、寸法、位置とも誤差 10 nm 以内で設計値に合致しており、高い精度が得られていることがわかる¹³⁾.

さらには、堆積中に有機金属分子を入れ替えることで異種の金属 (Zn および Al) を隣接して堆積することにも成功している (Fig. 8)¹³⁾. このように異種の物質を任意の位置にかつナノ寸法で隣接して堆積された結果は、他の手法では実現不可能な NFO-CVD の特長的な結果の一つである.

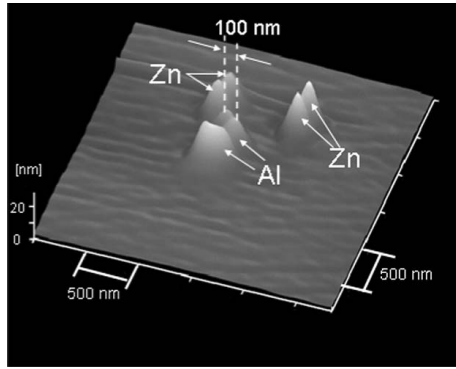


Fig. 8 NFO-CVDにより近接して堆積されたZnおよびAl微粒子の形状像.

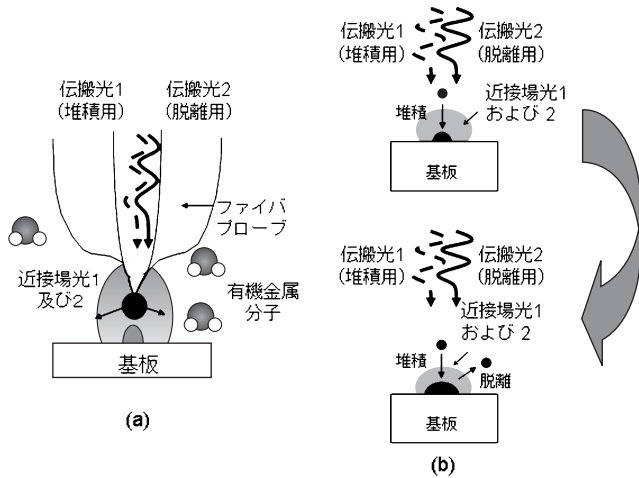


Fig. 9 物質寸法に依存する光脱離法による寸法制御の原理図.

3.2 物質寸法に依存する光脱離法による寸法制御

前節では説明を簡単にするためにファイバプローブを用い、その先端に近接場光を発生させ、ファイバプローブを走査することで微小な物質を堆積する場合について記した。しかし近接場光の特徴をさらに積極的に使うと寸法精度、加工速度などの向上、さらには伝搬光を用いたのでは不可能な新しい微細加工が可能となる。

NFO-CVDでは堆積速度がファイバプローブ先端の寸法に依存する共鳴効果を示すことが確認された。本節ではこれとは別に堆積物自身で生じる共鳴効果を用い、近接場光の光子エネルギーの値を制御することにより、形成されるパターンの寸法精度をさらに向上させる手法について解説する。

そのためには Fig. 9 (a) に示すように2種類の近接場光(近接場光1および2)をファイバプローブ先端に発生させる。近接場光1は光CVDによる堆積のために用いる。このとき同時に近接場光2を発生させて基板に照射し、堆積された物質を一部脱離させる。この脱離の現象は、堆積される金属微粒子が近接場光2を吸収し、この光エネルギー吸収量が金属微粒子同士の吸着エネルギーよりも大きくなる場合に発生する。この脱離の現象とそれによる寸法制御は次の過程により実現する¹⁴⁾。

- (1) 近接場光2により金属微粒子中の自由電子が振動する。

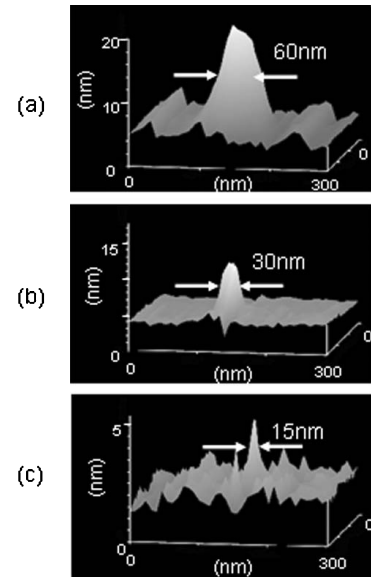


Fig. 10 物質寸法に依存する光脱離法により作製されたZn微粒子の形状像. 堆積用(近接場光1)の光の波長は325 nm. 脱離用(近接場光2)の光の波長は(a) 325 nm, (b) 488 nm, (c) 633 nm. 形状の半値全幅は各々(a) 60 nm, (b) 30 nm, (c) 15 nm.

同時に近接場光1により堆積が進むので、微粒子寸法は次第に増加する。その寸法が自由電子の平均自由行程より大きくなると、電子は微粒子全体を動くことができなくなるために、微粒子端での多重反射による微粒子内部での電子の固有振動が立ちにくくなり、電子振動のスペクトル中心周波数(固有振動周波数)が変化するとともにスペクトル幅が広がる。言い換えるとドラーデモデルにおいて電子振動の緩和定数が増加する。この固有振動周波数の変化、スペクトル幅が、緩和定数の増加は微粒子が小さいときは近似的にその寸法に比例すると考えて良い¹⁵⁾。

- (2) このように変化した固有振動周波数が近接場光2の周波数と一致したとき、言い換えると微粒子寸法がある特定の値になったとき、微粒子に吸収される近接場光2のエネルギーは極大をとる。すなわち物質寸法に依存した光共鳴吸収が起こる。
- (3) その結果、この特定の寸法のときに脱離が顕著になり、Fig. 9 (b) に示すように近接場光1による堆積との釣り合いによりこれ以上の寸法の増加が停止する^{14) 16)}。これにより基板上に形成される物質の寸法はファイバプローブ先端の寸法ではなく、近接場光2の光子エネルギーの値によって決まるので、物質の寸法を高い精度で制御することができる。

このように本方法は物質寸法に依存する緩和により誘起される光脱離現象を用い、寸法制御された微粒子を作製するので「物質寸法に依存する光脱離法」と呼ばれている¹⁶⁾。

Fig. 10はサファイヤ基板上にZnを堆積した実験結果であるが、近接場光1用の光源波長はいずれも325 nmである。一方近接場光2用の光源波長は各々325 nm(Fig. 10 (a)), 488 nm

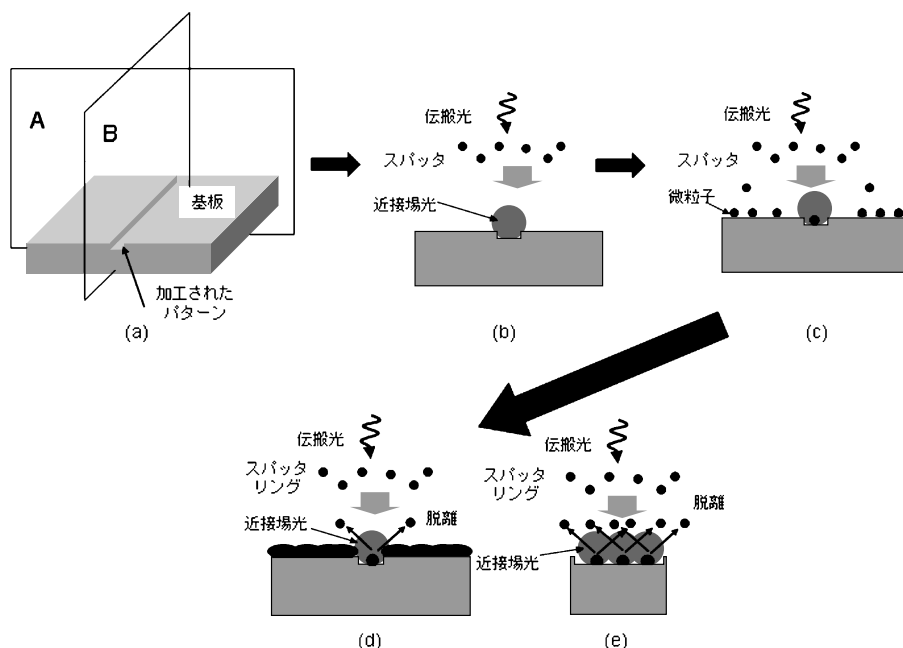


Fig. 11 プローブを用いない自己組織的作製法による微粒子列作製の原理図。(a) 堆積前加工基板。面 A および B はそれぞれ溝に対して垂直および平行。(b) (c) 堆積初期段階：パターン端部での近接場光発生 (A における断面図)。(d) (e) 物質寸法に依存する光脱離の効果による金属微粒子列の作製。(それぞれ面 A および B での断面図)。

(Fig. 10 (b)), 633 nm (Fig. 10 (c)) である。形成された Zn 微粒子の寸法はこの光子エネルギーに依存しており、各々 60 nm, 30 nm, 15 nm となっている¹⁴⁾。

3.3 物質寸法に依存する光共鳴脱離による自己組織的作製法

前節の結果によれば、形成されるパターンの寸法は近接場光の光子エネルギーの値によって決定されるので、ファイバプローブ先端の寸法や堆積時間などの精度が低くとも、高い寸法制御性が得られることがわかる。従ってファイバプローブの代わりに他の近接場光発生用デバイス (たとえばフォトマスク) を使ってもよい。さらには形状加工基板を近接場光発生用デバイスとして用いることで、フォトマスクなどが不要となりマスクと基板との密着性などの問題点が回避できる。また、近接場光発生用デバイスを通して多色の近接場光を発生させることで、それらの光子エネルギーに応じた複数寸法の物質が同一基板上に一括形成できる。これらの利点は寸法精度の向上のみでなく加工速度の向上にもつながる。さらに、金属微粒子中での物質寸法に依存する光脱離は一般的な現象であるので光 CVD 以外の様々な微細加工法にも応用が可能である。そのような応用例として、本節では自己組織的ナノ微粒子列形成法について紹介する。

金属微粒子薄膜を直接堆積する方法の一種であるスパッタリング法を例にとり、金属微粒子列の作製原理について説明する (Fig. 11)。ここでは、堆積された微粒子を脱離するための近接場光 (Fig. 9 の近接場光 2) 発生用に前節で用いていたファイバプローブの代わりに基板の一部にあらかじめナノ寸法の微細パターン (溝など) を加工しておく (Fig. 11 (a))。また、本方法では金属微粒子を直接堆積させる為、堆積用の光源 (Fig. 9 の近接場光 1) は必要とはならない。スパッタリ

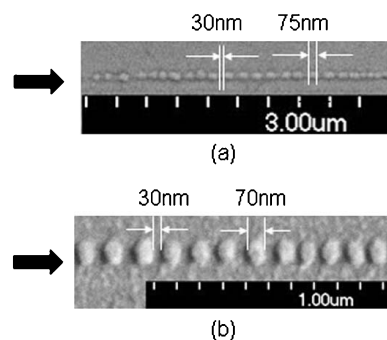


Fig. 12 プローブを用いない自己組織的作製法による (a) Au および (b) Al 微粒子列の電子顕微鏡写真。

ングの際に伝搬光 (Fig. 9 の伝搬光 2) をこのような基板に照射すると、このパターンの端部に局所的に強い近接場光 (Fig. 9 の近接場光 2) が発生する (Fig. 11 (b))。これが 3.2 節で記した脱離を誘起し、寸法制御された金属微粒子がパターン近傍に形成される。その後引き続き伝搬光照射を続けても、この微粒子の表面では脱離の効果により成長進行しないため、これにより微粒子同士が繋がることなく第二の金属微粒子が高い寸法制御性にて形成される。これが繰り返され最後には寸法制御された金属微粒子の列が形成される。このように本方法は寸法制御された微粒子を自動的に作製するので「自己組織的作製法」と呼ばれている。

Fig. 12 はそのようにして形成された Au (Fig. 12 (a)) および Al (Fig. 12 (b)) 微粒子の一次元配列である¹⁷⁾。ここでは物質寸法に依存する光脱離を実現するためにスパッタリング中にそれぞれ波長 678 nm および 532 nm の光を照射した。その結果、直径約 70 nm の半球状の Au および Al 微粒子が微粒子間隔 30 nm で、全長 20 μm にわたって一列に形成されている。

直径および間隔の値は光子エネルギーおよびあらかじめ形成された基板パターン形状により、全長は照射スポット径及び基板パターン形状により決まる。このようにして作製したいパターンに応じて、その自己組織的形成を引き起こす種となる近接場光を発生させるための形状、寸法をもつパターンを基板の一部に作製しておくことにより、フォトリソ不要な一括加工が可能となり、加工速度が著しく向上する。このような金属微粒子列構造は、高効率かつナノ寸法のビーム径が得られるナノ光配線として期待される¹⁸⁾。さらには伝送路の担い手である近接場光による脱離により自動的に作製された金属微粒子列は、近接場光の伝送路としても高効率になると予想される。

4. あとがき

本稿ではナノフォトリクスにおいてのみ観測可能な現象およびそれを用いたナノ寸法の光加工について解説した。本方法は、光化学反応を利用したものであるため、ここで示した金属微粒子以外に半導体微結晶 (ZnO, GaN, GaAs 等) の作製にも応用可能である。さらに、形状に起因して局在する近接場光の性質を用いることは、これまでナノ寸法加工に必要とされていたプローブやマスクが不要となるため、多品種多量生産が求められる将来の社会的要求に答えられる革新的な技術である。さらには、近接場特有な局在性を利用することで従来紫外線にのみ感光性を有するフォトリソストに対して可視光によっても加工可能となるなど¹⁹⁾、光技術のパラダイムシフトが期待される。

また、従来のナノ微細加工技術としては、半導体微細加工などに用いられている電子ビームリソグラフィなどが一般であるが、これらの技術においても「加工する」とこと、デバイスとして「動作させる」とことは別の技術であり、ナノ寸法のデバイスを実現させるためには大きな技術的・機能的限界が存在する。これに対し、近接場光による加工は単にナノ寸法の微細加工が可能ということではなく、近接場光で動作するナノフォトリックデバイスを作製する手法としては、

作製後デバイスとしての動作を保証する自己完結的手法であると期待される。

参 考 文 献

- 1) M. Ohtsu, K. Kobayashi, T. Kawazoe, S. Sangu, T. Yatsui, *IEEE J. Selected Topics in Quantum Electron.*, **8**, 839 (2002).
- 2) 大津元一, 小林 潔, “近接場光の基礎”, オーム社, pp. 1-244 (2003).
- 3) M. Ohtsu, K. Kobayashi, “Optical Near Fields”, Springer-Verlag, Tokyo, 2003, pp. 1-200.
- 4) 大津元一監修, “ナノフォトリクスへの挑戦”, 米田出版, pp. 1-183 (2003).
- 5) P. B. Fischer, S. Y. Chou, *Appl. Phys. Lett.*, **62**, 1414 (1993).
- 6) D. Leonard, M. Krishnamurthy, C. M. Reaves, S. P. Denbaars, P. M. Petroff, *Appl. Phys. Lett.*, **63**, 3203 (1993).
- 7) D. J. Ehrlich, R. M. Osgood, Jr., T. F. Deutsch, *J. Vac. Sci. Technol.*, **21**, 23 (1982).
- 8) Y. Yamamoto, M. Kourogi, M. Ohtsu, V. Polonski, G. H. Lee, *Appl. Phys. Lett.*, **76**, 2173 (2000).
- 9) C. J. Chen, R. M. Osgood, *Chem. Phys. Lett.*, **98**, 363 (1983).
- 10) T. Yatsui, T. Kawazoe, M. Ueda, Y. Yamamoto, M. Kourogi, M. Ohtsu, *Appl. Phys. Lett.*, **81**, 3651 (2002).
- 11) 林 定植, 八井 崇, 大津元一, 第 64 回秋季応用物理学関係連合講演会予稿集, No. 3, 925 (2003).
- 12) 林 定植, 八井 崇, 大津元一, 第 51 回春季応用物理学関係連合講演会予稿集, No. 3, 1137 (2004).
- 13) Y. Yamamoto, M. Kourogi, M. Ohtsu, G. H. Lee, T. Kawazoe, *IEICE Trans. Electron.*, **E85-C**, 2081, (2002).
- 14) T. Yatsui, S. Takubo, J. Lim, W. Nomura, M. Kourogi, M. Ohtsu, *Appl. Phys. Lett.*, **83**, 1716 (2003).
- 15) C. Sönnichsen, T. Franzl, T. Wilk, G. von Plessen, J. Feldmann, *Phys. Rev. Lett.*, **88**, 077402 (2002).
- 16) K. F. MacDonald, V. A. Fedotov, S. Pochoon, K. J. Ross, G. C. Stevens, N. I. Zheludev, W. S. Brocklesby, V. I. Emel'yanov, *Appl. Phys. Lett.*, **80**, 1643 (2002).
- 17) 野村 航, 八井 崇, 興梠元伸, 大津元一, 第 50 回春季応用物理学関係連合講演会予稿集, No. 3, 1110 (2003).
- 18) 八井 崇, 野村 航, 大津元一, *光学*, **33**, 174 (2004).
- 19) T. Kawazoe, K. Kobayashi, M. Ohtsu, *Proceedings of the Third IEEE Conference on Nanotechnology*, San Francisco, 561 (2003).

ナノ光加工： 光加工のパラダイムシフト

東京工業大学大学院総合理工学研究科 大津 元一

科学技術振興事業団 創造科学技術推進事業 大津局在フォトンプロジェクト*

川添 忠, 八井 崇

1. まえがき

ナノ寸法物質表面にエネルギーが局在する近接場光を使うとナノ寸法の加工が可能となる。本稿の題名の「ナノ光加工」とは近接場光によるこのような微細加工を意味する。この技術は主に

①ナノフォトニックデバイスの製作

②既存のフォトニックデバイスの製作

をめざして開発されたものである。特に①のナノフォトニックデバイスの必要性は筆者の解説記事^{1~3)}にも記してある。例えば今後ますます伝送容量が増大する光ファイバー通信システムを支える光スイッチ配列において、そのチャンネル数の増加の要求に応えるため(2015年には入出力チャンネル数1万以上)⁴⁾、光スイッチデバイスの寸法を100nm以下に微小化する必要がある。ただしこの寸法は光の回折限界*を超えている。さらにそれ以上に重要な要求として低消費電力化がある。これらの要求を満たすのが近接場光を情報キャリアとして動作するナノフォトニックデバイスであるが、それを作製するには位置および寸法精度がナノ寸法であることが不可欠となる。そのためにはナノ光加工が必須である。一方②については、既存の光リソグラフィー**、ステッパー***

技術では対応できない多品種少量加工などをはじめとする要求に応えることを目的としている。これについては本特集号の他稿でも記されているので詳細は省く。

しかし①、②に共通して本稿で記したいことは、ナノ光加工は単にナノ寸法の位置、寸法精度が実現できることではなく、図1に示すように伝搬光を用いたのではまったく不可能であった、新規な加工が可能ということである。例えば、新規な光化学反応が起こるので紫外線を使わなくとも加工できる、といった特徴であり、光加工のパラダイムシフトである。以下の各節でこれらについて述べる。

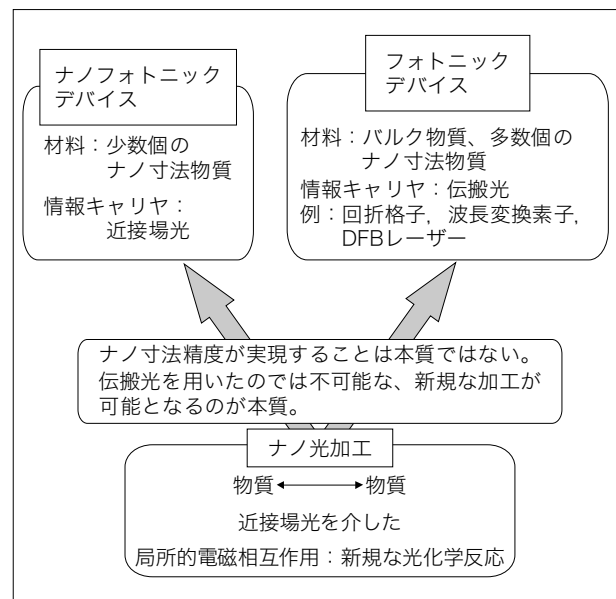


図1 ナノ光加工の本質とデバイス製作への応用

* 光がその波長程度の寸法を持つ穴を通り抜けると、広がろうとする性質のために光を凸レンズで集光してもそのスポット径は波長程度以下にはならず、したがって波長程度以下の寸法の小さな領域に光を閉じ込めることができない。この閉じ込めの下限を回折限界という。

** 半導体製造の際、微細な回路パターンを基板表面に光を照射し転写する技術の総称。

*** 集積回路の製造で、回路パターンを比例縮小して基板上に露光転写する装置。

おおつ もといち, かわぞえ ただし, やついで たかし

* 現 科学技術振興機構 戦略的創造研究推進事業継続研究課題 ナノフォトニクスチーム

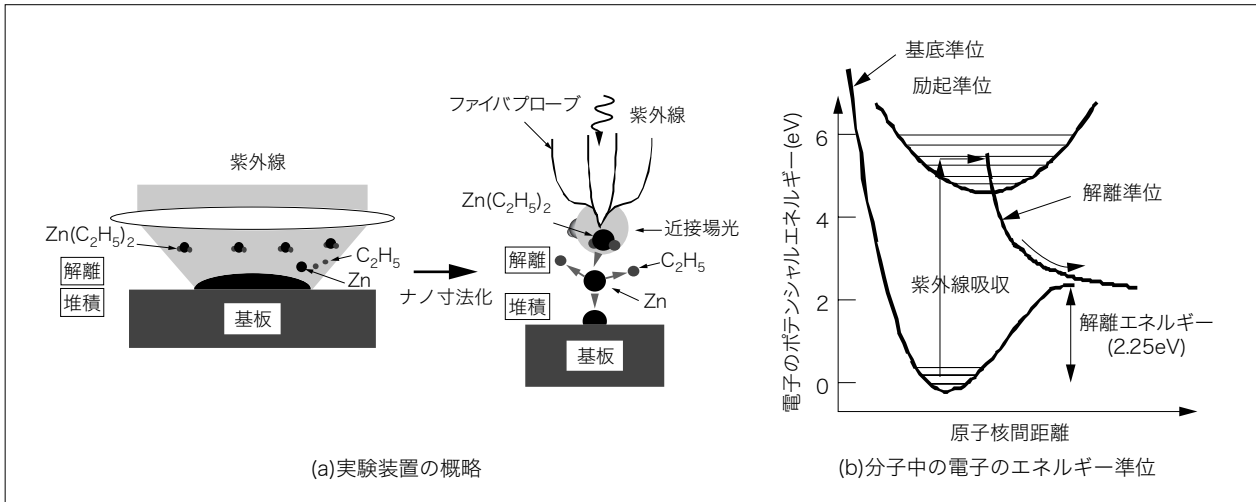


図2 光を使った化学気相堆積の原理

2. 紫外線は本当に必要か？

2.1 まず光化学気相堆積法を例に

図2は光を使った化学気相堆積（CVD：Chemical Vapor Deposition）の原理である。ここでは金属亜鉛の堆積を例にとっている。ジエチル亜鉛分子（ $Zn(C_2H_5)_2$ ）を光により解離し、析出した亜鉛原子を基板に堆積する。分子内の電子は光を吸収して、基底準位から励起準位へ遷移し、励起された電子は励起準位と縮退する解離準位へと緩和して、分子が解離する。このような電子励起を経た解離のためには分子の解離エネルギーや電子の励起エネルギーより高い光子エネルギーをもつ光、すなわち紫外線を用いる必要がある。このとき伝搬光の代わりに近接場光を使えば、基板にはナノ寸法の高精度で亜鉛パターンが形成される。これまでに亜鉛、アルミニウム、などのナノ寸法の金属微粒子、酸化亜鉛などが形成され、特に酸化亜鉛からは青色発光が確認されている^{5)~7)}。

ところで以上のような寸法、位置精度の高いことは決して近接場光を用いたナノ加工の本質ではないことを指摘したい。本質的なのは1節でも述べたように、伝搬光を用いたのではまったく不可能な、新規な加工が可能なことである。その例として図3には紫外線よりもずっと低い光子エネルギーをもつ近接場光、すなわち可視光を用いても分子が解離し、亜鉛が堆積した結果を示す⁸⁾。図中(a)、(b)は青、赤色の近接場光を使った結果であり、特に(b)の赤色の光子エネルギーは分子の解離エネルギーよりも低く、このような解離・堆積は伝搬光を用いた

のでは実現不可能である。この解離の原因は2光子吸収などの非線形光学効果によるものではなく、近接場光のエネルギーがナノメートル寸法の空間に局在していることに起因する⁹⁾。すなわちこの局在性のために近接場光は急峻な光強度勾配を持ち、この急勾配により分子振動が励振され分子は解離したのである（波長程度の領域で均一な光強度をもつ伝搬光ではこのような分子振動は到底励振できない）。すなわち非断熱過程が誘起されており、もはやFranck-Condon原理が有効でなくなっている。

このような新規な現象は

- ①紫外光源が不要なので、設備上の自由度が増え、経済性が上がること、
- ②従来の光学活性な分子ガスのみでなく、不活性分子ガスの使用も可能となるので、材料上の自由度が増え、環境問題の改善が図れること、

などの際だった特徴を持ち、微細加工のパラダイムシフトを引き起こす。例えば②の特徴を活かした例として、爆発性のない安全な優良材料であるビスアセチルアセトナト亜鉛（ $Zn(acac)_2$ ）分子（これは有機金属CVDなどではよく使われているが、光学不活性であるために従来の光CVDではまったく使われていなかった）を近接場光により解離することが可能となり、これにより亜鉛のナノ寸法微粒子が堆積されている¹⁰⁾。

2.2 リソグラフィー用フォトレジスト*が可視光にも感光

2.1節の非断熱過程は近接場光と物質との相互作用に

*露光によって薬品への耐性変化を持つ高分子の総称。

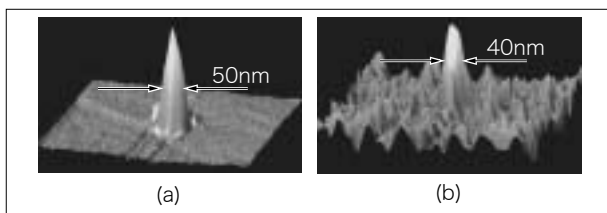


図3 可視光による亜鉛の化学気相堆積の結果。基板はサファイア。各図は堆積した亜鉛微粒子の原子間力顕微鏡像を表す。光の波長は488nm(a), 684nm(b)である。形状の半値全幅は50nm(a), 40nm(b) (ただし原子間力顕微鏡の分解能値を含む)。

おいて一般的に見られる現象なので光CVD以外の加工にも適用できる。その代表例として光リソグラフィーを例にとる。近接場光によるリソグラフィーについては本特集号の他稿で紹介されているが、本稿では赤色光を使う点が大きく異なる。伝搬光を使った既存の光リソグラフィーでは作製パターンをより微細化するために紫外線などの短波長光を使うので、そのためのフォトレジスト材料も紫外線に強く感光する特性をもっている。言い換えると赤色光には感光しない。しかし赤色光であっても、それが近接場光ならばフォトレジストはそれに感光するのである。その結果微細パターンが描け、さらにそのパターンの寸法は紫外線を使った場合より小さくすることが可能となる。

一例として図4(a)に示すように、石英ガラス基板に回折格子状のクロムパターンを作製し、これを近接場光発生用のフォトマスクとする。基板の裏面に光を照射する

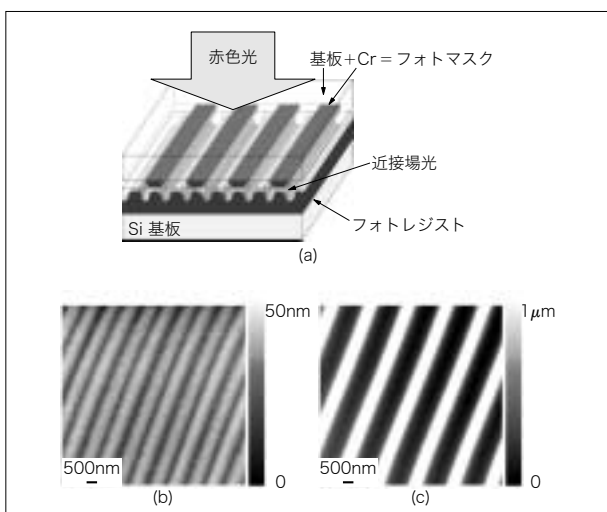


図4 赤色光の近接場光を用いたリソグラフィー。(a)実験配置の断面図。使用したフォトレジストはOFPR-800。光の波長は672nm。(b)感光したフォトレジストパターンの原子間力顕微鏡像。(c)比較のための紫外光源(水銀ランプ)を用いたときの結果。

とフォトマスクを通して近接場光が発生する。特にフォトマスクの端部に近接場光のエネルギーが集中する。その下にはシリコン基板上に塗布されたフォトレジスト(型名OFPR-800:水銀ランプg線(436nm), i線(365nm)用)がある。この図の実験では赤色光を使っているのでこのフォトレジストは感光しないはずである。しかし図4(b)の実験結果にあるように感光し、微細なパターンが形成される。このように赤色光で感光するのは2.1節の非断熱過程に起因している¹⁰⁾。このパターンの幅は用いた光源の波長の1/5程度であり、光の回折限界を超えている。これはフォトマスク端部に発生する近接場光の寸法に相当し、同じマスクを用いた紫外線(水銀ランプ)の伝搬光によるパターン(図4(c))より小さい。

この光リソグラフィーは回折格子などの既存の多様な光デバイスを作製するために有望な加工法と考えられ、特に高価格の紫外光源や光学素子を必要とせず既存の露光装置と安価な光源が利用できるため高い経済効果が期待される。

3. 加工の高速化をめざして

3.1 プローブからフォトマスクへ

2.1節では原理説明のためにプローブを用いて近接場光を発生させ、そのプローブを走査することで任意形状の物質を堆積していた。いわば一筆書き加工である。しかし加工の高速化の点からは基板面内での一括加工が有利である。すでに2.2節の光リソグラフィーではプローブを排除しフォトマスクを用いて近接場光を発生させ一括加工を行っているが、近接場光の特徴を積極的に使うとさらに新しい(伝搬光を用いたのでは不可能な)一括加工が可能となる。

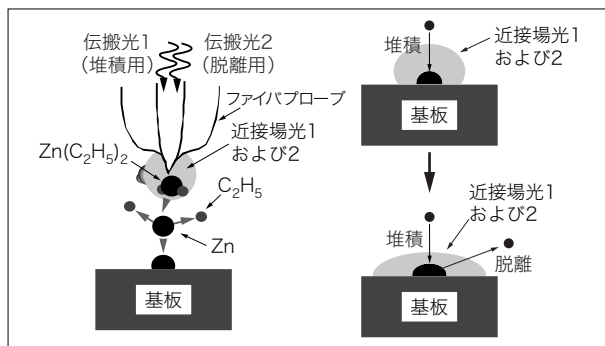


図5 光による脱離を併用して堆積物質の寸法精度を上げる原理図

例えば2.1節の光CVDにおいて、図5に示すように近接場光1によって堆積しながら近接場光2を基板に照射すると、堆積した物質は特定の寸法になった時に脱離を開始する。この脱離開始に必要な光エネルギー吸収過程が物質寸法依存の共鳴現象を示すため¹¹⁾、堆積が進行する過程において堆積物質が近接場光2の光子エネルギーによって決まる寸法まで大きくなると脱離が始まり、近接場光1による堆積と近接場光2による脱離との釣り合いにより成長が停止する¹²⁾。これにより堆積物質の寸法を高い精度で制御することができる。図6(a)~(c)は紫外用ファイバースコープ先端に発生する近接場光によりサファイア基板上に亜鉛を堆積した実験結果であるが、堆積用の近接場光1を発生させる光源波長はいずれも325nmである。一方脱離用の近接場光2には波長325nm(図6(a))、488nm(図6(b))、633nm(図6(c))の光を使っている。作製された亜鉛微粒子寸法はこの光子エネルギーに依存しており、おのおの60nm、30nm、15nmとなっている。

以上の結果は、作製したいパターン寸法に応じて多色

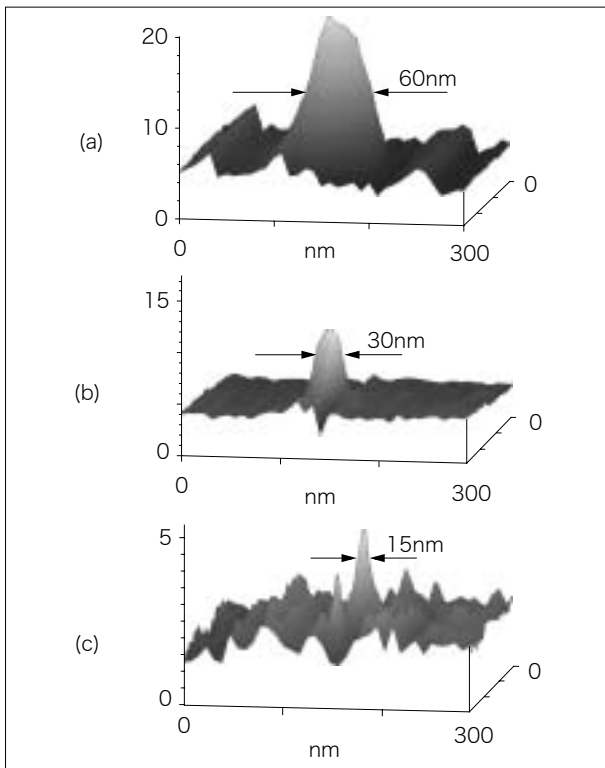


図6 光による脱離を併用して堆積した亜鉛の原子間力顕微鏡像。基板はサファイア。堆積用(近接場光1)の光の波長は325nm。脱離用(近接場光2)の光の波長は325nm(a)、488nm(b)、633nm(c)。形状の半値全幅は各々60nm(a)、30nm(b)、15nm(c)。

光を光源として用い(実際には白色光をフィルターにて分光すればよい)、フォトマスクを通して近接場光2を発生すれば、その光子エネルギーに応じた寸法の物質が同一基板上に一括形成できることを示唆している。さらに、パターンの寸法は近接場光を発生させるフォトマスク寸法や形状ではなく近接場光2の光子エネルギーによって決まるので、複数の光源又はフィルターを使うことで近接場光発生用のマスク寸法精度に対する要求が緩和されるという利点がある。以上述べた金属微粒子中での物質寸法依存光共鳴吸収過程はナノ微粒子において一般的な現象であるので光CVD以外のさまざまな堆積方法にも応用が可能である(3.2節参照)。

3.2 さらにフォトマスクさえも不要とするために

2.2節の光リソグラフィーの例に示されたように、近接場光を用いた加工法により大面積にわたる微細加工が可能となった。その際、フォトマスク下面の近接場光のエネルギーのしみ出し長さは面内広がり幅と同程度であるため、フォトレジスト表面とフォトマスクの距離がこの値以内となるよう調整をする必要がある。しかし、フォトマスクを用いた密着露光法を大量生産に用いる場合、マスクの劣化やゴミの混入等の問題が予想されるためフォトマスク不要のナノ光加工が望ましい。そのために近接場光の特徴を積極的に利用した自己組織的形成法が提案されている¹³⁾。

この一例としてスパッタリング法による金属パターン

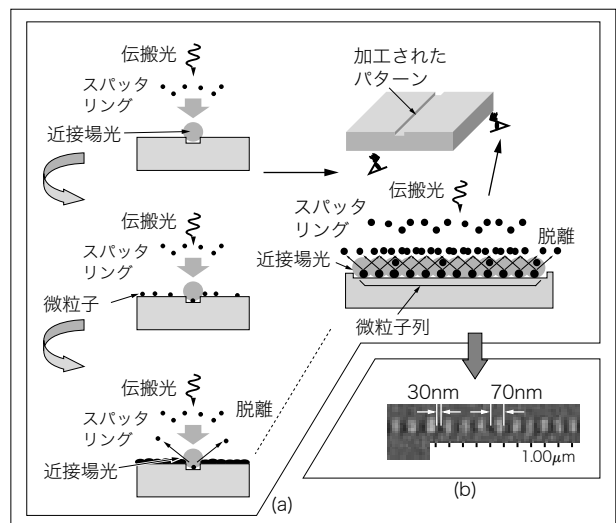


図7 パターン加工された基板と光による脱離を使った自己組織的ナノパターン形成法。(a)原理図。(b)堆積したアルミニウム微粒子列の電子顕微鏡像。基板は石英。脱離用の光の波長は532nm。

形成の場合を例にとり図7(a)により原理説明する。スパッタリングにより基板に金属を堆積する際、基板の1部にあらかじめ適当なナノ寸法の微細パターン（溝など）を加工しておく。スパッタリングの際に伝搬光をこのような基板に照射すると、このパターンの端部に局所的に強い近接場光が発生する。これが3.1節で記した脱離を誘起し、寸法制御された金属微粒子がパターン近傍に形成される。伝搬光照射を続けた場合でもこの微粒子の表面では脱離により堆積が進行しないため、これにより微粒子同士が繋がることなく第2の金属微粒子が高い寸法制御性にて形成される。これが繰り返され最後には寸法制御された金属微粒子の列が形成される。図7(b)はそのようにして形成されたアルミニウムの微粒子列である。ここではアルミニウム微粒子における寸法依存光共鳴吸収を実現するためにスパッタリング中に波長532nmの光を照射した。このようにして作製したいパターンに応じて、その自己組織的形成を引き起こす種となる形状、寸法のパターンを基板の1部に加工しておくことにより、フォトマスク不要な一括加工が可能となる。

4. あとがき

本稿では伝搬光を用いたのではまったく不可能であった、新規な加工が可能となる技術としてのナノ光加工を概説した。これは近接場光のエネルギーがナノメートル寸法の空間に局在することに起因する非断熱過程などの新規な光化学過程を利用している。ナノ寸法の加工精度が得られることは副産物にすぎない。尚、ナノ光加工も含め本特集号で取り扱うナノ加工技術の展開の方向はどのようなデバイスを作るために用いるかに強く依存する。DRAM (Dynamic Random Access Memory) 用半導体の加工のように少品種多量生産のためには大きな処理速度が要求されてきたが、今後のシステムの多様化とともにデバイスの多品種少量生産の必要性が高まっている。この場合には加工技術に関する従来の指導原理は有効でなくなり、別の観点から新しい微細加工技術を開発しなくてはならない。

本稿のナノ光加工はまさにこのような観点による革新

技術である。最近ではナノ光加工の技術ロードマップ策定も行われており、光加工のパラダイムシフトが始まりつつある¹⁴⁾。21世紀の高度情報社会、高度福祉社会を支えるための光システム、それを構成するための光デバイスの生産のためにナノ光加工技術の急速な進展に期待したい。

参考文献

- 1) 大津元一：「ナノフォトニクスとナノ光集積デバイス」、O plus E, Vol. 24, No. 1, pp. 28～32 (2002)
- 2) 大津元一：「ナノフォトニクス」、電子情報通信学会, 第85巻, 第11号, pp. 834～838 (2002)
- 3) M. Ohtsu, K. Kobayashi, T. Kawazoe, S. Sangu, and T. Yatsui : IEEE J. Sel. Top. Quant. Electron, Vol. 8, No. 4, pp. 839～862 (2002)
- 4) 財団法人光産業技術振興協会編：「光テクノロジーロードマップ報告書—情報通信分野—」、財団法人光産業技術振興協会, p. 34 (1998)
- 5) V. V. Polonski, Y. Yamamoto, M. Kourogi, H. Fukuda, and M. Ohtsu : J. Microsc. Vol. 194, No. 2/3, pp. 545～551 (1999)
- 6) Y. Yamamoto, M. Kourogi, M. Ohtsu, V. Polonski, and G. H. Lee, Appl. : Phys. Lett. Vol. 76, No. 16, pp. 2173～2175 (2000)
- 7) T. Yatsui, T. Kawazoe, M. Ueda, Y. Yamamoto, M. Kourogi, and M. Ohtsu : Appl. Phys. Lett. , Vol. 81, No. 19, pp. 3651～3653 (2002)
- 8) T. Kawazoe, Y. Yamamoto, and M. Ohtsu : Appl. Phys. Lett. Vol. 79, No. 8, pp. 1184～1186 (2001)
- 9) T. Kawazoe, A. Takubo, K. Kobayashi, S. Sangu, and M. Ohtsu : Technical Digest of the Quantum Electronics & Laser Science Conference, QELS 2003, Technical Digest, Optical Society of America, New York, paper number QWA12 (2003)
- 10) T. Kawazoe, K. Kobayashi, and M. Ohtsu : Proceedings of IEEE-Nano 2003, THL3 (2003)
- 11) G. T. Boyd, Th. Rasing, J. R. R. Leite, and Y. R. Shen : Phys. Rev. B, Vol. 30, No. 2, pp. 519～526 (1984)
- 12) T. Yatsui, S. Takubo, J. Lim, W. Nomura, M. Kourogi, and M. Ohtsu : Appl. Phys. Lett. , Vol. 83, No. 9, pp. 1716～1718 (2003)
- 13) 野村 航, 八井 崇, 興梠 元伸, 大津 元一：第50回春季応物予稿集, No. 3, p. 1110 (2003)
- 14) 財団法人光産業技術振興協会編：「ナノ光加工技術報告書」、財団法人光産業技術振興協会, p. 1 (1998)

[V] PUBLISHED BOOKS

